



University
of Glasgow

Millar, Colin Anderson (1976) Evanescent field coupling of thin film and fibre optical waveguides. PhD thesis.

<http://theses.gla.ac.uk/5409/>

Copyright and moral rights for this thesis are retained by the author

A copy can be downloaded for personal non-commercial research or study, without prior permission or charge

This thesis cannot be reproduced or quoted extensively from without first obtaining permission in writing from the Author

The content must not be changed in any way or sold commercially in any format or medium without the formal permission of the Author

When referring to this work, full bibliographic details including the author, title, awarding institution and date of the thesis must be given.

EVANESCENT FIELD COUPLING OF THIN FILM
AND FIBRE OPTICAL WAVEGUIDES.

A Thesis

Submitted to the Faculty of Engineering
of the University of Glasgow
for the degree of

Doctor of Philosophy

by

Colin Anderson Millar, B.Sc.

October 1976.

212341
2124
11903

LIBRARY
UNIVERSITY OF GLASGOW

PAGE
NUMBERING
AS ORIGINAL

BEST COPY

AVAILABLE

Variable print quality

A C K N O W L E D G E M E N T S

I wish to thank Professor J. Lamb for his supervision and for the use of the facilities of the laboratories of the Department of Electrical Engineering.

I am greatly indebted to Dr. P.J.R. Laybourn for closely supervising the work and for many helpful and stimulating discussions, and also to Mr. R. Hutchins for his help and encouragement.

The assistance of Mr. G. Boyle and Mr. S. Orr in the technical and photographic work was much appreciated. Thanks are also due to Mr. E. Thompson and Mrs. L. McCormick for their able assistance in the computer simulation and graphics, and to Mr. J. McMurray and Mr. G. Stewart for many interesting suggestions and discussions.

I would also like to thank Miss I. Adams, who typed the thesis.

Grateful acknowledgement is made to the Science Research Council for financial support of this work.

Finally I would like to thank my wife and parents for their continual support and encouragement.

DECLARATION

The ray-optics treatment for a slab waveguide directional coupler was developed at the initial stage by Dr. R. Dunsmuir and was finalized with the helpful collaboration of Mr. J.A. McMurray.

Most of the credit for the research into silver ion-exchange in glass slabs and circular clad fibres rests with Mr. George Stewart.

The author declares that the work of this thesis has not been previously submitted for any other degree or award.

SUMMARY

The study described in this thesis relates to the optical evanescent wave coupling between bulk, thin film and fibre structures, with a view to producing efficient interconnecting waveguides for optical communication systems.

A review is presented of the general waveguide and directional coupler theory, surveying the work of other authors and unifying various methods using a common notation. The waveguides encountered in the work are analysed using a ray-optic approach and a description of the wave-vector components and the eigenvalue equations is obtained. The solutions of the coupled wave equations are obtained analytically, and by a digital simulation of the general differential equations. Determination of the coupling coefficient is approached from three different aspects: the general wave, the ray-optic, and the direct or intuitive. The latter two are limited in their general application but are particularly useful in this work to the evaluation of the theoretical coupling coefficient for a coupler consisting of graded-index waveguides.

Methods are described of modifying the cladding material of circular fibres to facilitate transverse coupling, and an example of coupling to a cladde multimode fibre from a thin film waveguide is presented. Qualitative results are obtained for the excitation of cladde fibre waveguide modes at a region of cladding modification. Because of the importance of the technique, firstly to demonstrate transverse coupling in fibre optics, and secondly as a fibre test and evaluation procedure in its own right, a detailed description of the method and an analysis of the results is given. The high-order waveguide mode patterns are presented and discussed, and favourably compared with the theoretical predictions. Further modification of the cladding-treated region allows selective excitation of the

complete mode family (including the HE_{11} mode) of an overmoded clad fibre.

Coupling-fibres of alternative geometries are described, commencing with a review of planar ribbons. The sandwich ribbon optical fibre is introduced and the properties and uses to which it may be put are discussed. The three-dimensional sandwich ribbon fibre is developed and the excitation and the characteristics of the near-rectangular waveguide modes are studied.

Finally the SR fibre is put to use in several experimental coupling configurations. A reciprocal quasi-single-mode directional coupler with a measured transfer efficiency of 97% is obtained by matching the phase velocities of the fibre and film modes. An experimental coupling coefficient of $\frac{\pi/2}{47 \mu m}$ is recorded. A second value for the coupling coefficient, independently obtained by varying the phase mismatch, is $\frac{\pi/2}{69 \mu m}$. These values compare with a theoretical prediction of $\frac{\pi/2}{65 \mu m}$. SR fibres are shown to provide a solution to the problem of interconnecting thin film circuits and coupling integrated optical components to the optical data highway, and the findings of this work are related to the expected trends in system development.

TABLE OF CONTENTS

	<u>Page Number</u>
ACKNOWLEDGEMENTS	I
DECLARATION	II
SUMMARY	III
CONTENTS	V
 <u>CHAPTER 1. INTRODUCTION</u>	
1.1 General.	1
1.1.1 Fibre optics.	1
1.1.2 Integrated optics.	2
1.1.3 The coupling problem.	4
1.2 Motivation and aims of research.	7
1.3 Review of contents of the thesis.	8
 <u>CHAPTER 2. WAVEGUIDE AND DIRECTIONAL COUPLER THEORY.</u>	
2.1 Introduction.	10
PART I: Waveguide theory.	
2.2 Step-index dielectric slab waveguide.	10
2.3 Graded-index dielectric slab waveguide.	15
2.4 Rectangular dielectric waveguide.	18
2.5 Circular dielectric fibre waveguide.	22
2.6 Part I: Summary and conclusions.	25
PART II: Coupling theory.	
2.7 The coupled wave equations.	26
2.7.1 Simulation of the coupled wave equations.	27
2.7.2 Analytic solution of the coupled wave equations.	32
2.7.3 Discussion of analytic solution and comparison with the digital simulation.	36
2.7.4 Conclusions.	38
2.8 The coupling coefficient - wave approach.	39

	<u>Page Number</u>
2.9 The coupling coefficient - ray optics approach.	43
2.9.1 The scattering matrix.	43
2.9.2 New eigenvalue equation.	44
2.9.3 Perturbation.	45
2.10 The coupling coefficient - the 'direct' method.	47
2.10.1 General approach.	47
2.10.2 General five-layer slab structure.	48
2.11 Extension of the slab derivations to rectangular waveguides.	50
2.12 Part II: Summary and conclusions.	52
APPENDIX 2 Derivation of the normalised scattering matrix of a waveguide tunnelling layer.	53
 <u>CHAPTER 3. CLADDING MODIFICATION OF MULTIMODE OPTICAL FIBRES.</u>	
3.1 General Introduction.	58
3.2 Modification of cladding glass by silver/sodium ion exchange.	59
3.2.1 Underlying philosophy.	59
3.2.2 The refractive index profile of a treated cladding.	59
3.2.3 Preliminary results.	60
3.3 Removal of cladding glass by acid etching.	61
3.3.1 Introduction.	61
3.3.2 The materials used.	61
3.3.3 Monitoring the progress of the etch.	63
3.3.4 Results of acid etching.	64
3.3.5 Physical and optical properties of the etched fibre.	64
3.4 Discussion, and comparison of ion-exchanged and acid-etch techniques.	67
3.5 Coupling of a thin film waveguide and a circular fibre at the cladding-modified region.	71
3.5.1 Introductory discussion.	71
3.5.2 Experimental details of thin film/multimode fibre coupler.	72
3.5.3 Theory of thin film/multimode fibre coupling.	74
3.5.4 Comparison between theory and experiment, and conclusions.	81
3.6 Summary and conclusions.	82

CHAPTER 4. CLADDED FIBRE WAVEGUIDE MODES EXCITED BY
A PRISM COUPLER AT A CLADDING-MODIFIED REGION.

4.1	Introduction.	83
4.2	Theory of prism coupling to circular fibres.	84
4.2.1	Synchronous and tilt angles of the prism coupler.	84
4.2.2	Launching efficiency of a prism/fibre coupler.	85
4.3	Coupling to the high-order modes at the treated region.	88
4.3.1	Experimental details.	88
4.3.2	Reflected spot m-line distribution.	88
4.3.3	Near-field patterns of the high-order modes and relation to theory.	89
4.3.4	Theoretical formulation of the far-field distributions of the high order modes.	93
4.3.5	Experimental far-field patterns of high- order modes and comparison with theory.	96
4.4	Further modification of the cladding treated region.	96
4.5	Coupling to the low-order modes at the treated region with further modification.	100
4.5.1	Synchronous coupling.	100
4.5.2	Comparison with the theory of mode propagation in circular fibres.	102
4.5.3	Near-field patterns of low-order modes.	104
4.5.4	Comparison of the actual and expected intensity distributions.	105
4.5.5	Fibre waveguide mode polarization and its implications.	108
4.6	Summary and conclusions.	108
APPENDIX 4	Normalised propagation constant as a function of the normalised frequency V .	111

CHAPTER 5. PLANAR AND SANDWICH-RIBBON FIBRE WAVEGUIDES.

5.1	General Introduction.	112
5.2	Planar ribbon fibre waveguides.	114
5.2.1	A review.	114
5.2.2	Merits and disadvantages of planar ribbons.	117
5.2.3	Planar ribbons in a coupling situation.	118

5.3	Sandwich ribbon fibre waveguides.	120
5.3.1	Introduction.	120
5.3.2	Manufacture of SR fibre waveguides.	120
5.3.3	Cross-section of a single-mode SR fibre waveguide.	121
5.4	Propagation characteristics of SR fibre waveguides.	122
5.4.1	Validity of the slab waveguide approximation.	122
5.4.2	The theoretical dispersion characteristics.	124
5.4.3	Excitation of SR fibre waveguide modes.	124
5.4.4	Experimental example of SR fibre modes.	128
5.4.5	Comparison of theory and experiment.	130
5.4.6	Optical loss of SR fibres.	130
5.5	Uses of the SR fibre.	132
5.5.1	Low-loss short range data highway.	132
5.5.2	Multichannel capacity of SR fibres.	132
5.5.3	SR fibre directional coupler.	133
5.6	Summary and conclusions.	134

CHAPTER 6. THREE-DIMENSIONAL SANDWICH-RIBBON FIBRE WAVEGUIDES.

6.1	Introduction.	136
6.2	Manufacture of three-dimensional SR fibres.	136
6.3	Cross-section of three-dimensional SR fibres.	137
6.4	Three-dimensional SR fibre mode excitation using a prism coupler.	140
6.4.1	Introduction.	140
6.4.2	Theory.	140
6.4.3	Experimental results.	141
6.4.4	Theory of modal power variation with tilt angle.	147
6.4.5	Comparison with experiment.	149
6.4.6	Conclusions.	149
6.5	Near-field patterns of three-dimensional SR fibre waveguide modes.	151
6.5.1	Introduction.	151
6.5.2	Theory of approximate mode field distributions.	151
6.5.3	Description of experiment.	152
6.5.4	Discussion of the results.	153
6.5.5	Near-field patterns of degenerate mode combinations.	156
6.5.6	The $(E_{51} + E_{21})$ degenerate-mode near-field pattern.	157
6.5.7	Theory of the approximate degenerate-mode distributions.	157
6.5.8	Conclusions.	164

6.6	Far-field radiation patterns of three-dimensional SR fibre waveguide modes.	165
6.6.1	Introduction.	165
6.6.2	Theory of far-field patterns due to radiation from SR fibre termination.	165
6.6.3	Observation of far-field patterns and comparison with theory.	167
6.6.4	Conclusions.	170
6.7	Summary and general conclusions.	172
APPENDIX 6	Plane wave excitation of circular fibre modes by end illumination.	174
 <u>CHAPTER 7. EVANESCENT FIELD COUPLING OF RIBBON FIBRES AND THIN FILM WAVEGUIDES.</u>		
7.1	Introduction.	175
7.2	Silver/sodium ion exchanges thin film waveguides.	176
7.2.1	Advantages of silver/sodium IE waveguides.	176
7.2.2	The refractive index profile.	179
7.2.3	Universal mode dispersion graph.	181
7.2.4	Particular solution of the mode dispersion against diffusion time.	182
7.2.5	Selection of the film-mode propagation constant.	182
7.2.6	Discussion and conclusions.	184
7.3	System coupling coefficient.	184
7.3.1	Introduction.	184
7.3.2	Determination of the IE waveguide self-coupling coefficient.	185
7.3.3	Complete expression for the system coupling coefficient.	187
7.4	The experimental coupler - preamble.	187
7.5	Phase matched IE/SR directional coupler.	189
7.5.1	Introduction.	189
7.5.2	Experimental investigation - outline.	189
7.5.3	Experimental investigation - details.	193
7.5.4	Results and analysis.	198
7.5.5	Comparison of the theoretical and experimental coupling coefficients.	201
7.5.6	Summary and conclusions.	201
7.6	Phase mismatched directional coupler.	202
7.6.1	Introduction.	202
7.6.2	Phase mismatched system response: the method of obtaining the coupling coefficient.	202
7.6.3	Results and analysis.	204
7.6.4	Summary and conclusions.	206

	<u>Page Number</u>
7.7 Phase mismatched leakage coupler.	206
7.7.1 Introduction.	206
7.7.2 Antenna formulation - radiation due to travelling waves of current.	208
7.7.3 Rate of leakage.	209
7.7.4 The experimental leakage coupler.	214
7.7.5 Leakage coupler at a film edge.	217
7.7.6 Discussion and conclusions.	217
7.8 Summary and general conclusions.	219
 <u>CHAPTER 8. CONCLUSIONS.</u>	
8.1 General conclusions.	221
8.2 Relation of the results to future system development.	225
8.3 Proposals for future work.	228
APPENDIX 8	230
REFERENCES.	231

1.1 General.

Much human endeavour has been directed towards the transmission and manipulation of electromagnetic energy for the rapid and accurate transfer of information. The historical progression of developments has been one of increasing carrier frequency, from the radio waves of the earlier part of the century, through the microwave bands to the optical region of the spectrum. Most advances have been preceded by the introduction of an efficient power source, and the development of the laser in 1960¹ stimulated the upsurge of interest in optical communication. The large potential bandwidths available, using a highly coherent source in the visible or near-infrared region, has led workers over the past ten years to consider methods of optical waveguide transmission and data processing. Two distinct categories have emerged.

1.1.1 Fibre Optics.

Fibre optics, according to Kapany² is

"the art of active and passive guidance of light (rays and waveguide modes) in the ultraviolet, visible or infrared regions of the spectrum, along transparent fibres through predetermined paths".

In 1966, Kao and Hockham³ proposed the use of glass fibres as a transmission medium for modulated laser light, which focused attention on the communication possibilities of optical fibre waveguides. The bulk loss of the materials, at that time, was in many hundreds of dB/km, preventing transmission over reasonable distances. However, in recent years the considerable research effort has reduced the attenuation dramatically: 20 dB/km was noted by Kapron et.al.⁴ in 1970, 8 dB/km was recorded in 1971 by Ogilvie et.al.⁵ using liquid core fibres, and recently Keck et.al.⁶ at Corning Glass Works in

America and Payne and Gambling⁷ at Southampton University reported losses as low as 2.7 dB/km.

First generation systems comprising light emitting diode (LED) sources and large diameter fibres and fibre bundles were demonstrated at Standard Telecommunications Laboratories⁸ in 1968 and such systems are now on a sound commercial footing. They provide rugged, compact and secure data links, such as manufactured by Thomson - CSF⁹ for application in avionics and short-range telecommunications. The higher bandwidths afforded by semiconductor lasers and single-mode fibres have led to the production of a second generation of systems using direct pulse code modulation (PCM) of the source and avalanche photodiode detection.³⁸ High data rate transmission over long distances will undoubtedly supersede the coaxial microwave systems at present in use. The future of fibre optics is thus assured and the subject has passed beyond the laboratory models to the stage of commercial utilization.

There is projected, however, a third generation of systems in which terminal equipment of a low-loss fibre optical communication link will comprise "integrated optical" devices, which form the second category of current interest.

1.1.2 Integrated Optics.

The term 'integrated optics' introduced by S.E. Miller¹⁰ of Bell Laboratories in 1969, described the miniature form of laser beam circuitry which concentrates light in thin film waveguides deposited inside, or on the surface of, a common substrate. The domain of integrated optics defined by Taylor and Yariv¹¹ is,

"the integration of a number of optical components in a single structure to perform complex functions".

Shubert and Harris¹² discussed the application of surface waves on thin films to integrated data processors. Lenses, prisms and

gratings were demonstrated in thin film form,¹³ and the geometrical optical properties of light beams in the thin films were presented by Ulrich and Martin.¹⁴ The theoretical analysis of propagation in dielectric sheets can be traced back to Hondros and Debye.¹⁵ In 1954 Hatkin¹⁶ described the travelling wave as the addition of two criss-crossing plane-wave components, as did Lotsch.¹⁷ The method was used by Tien¹⁸ to introduce the modes of propagation in thin films. Rectangular dielectric waveguides have been studied theoretically by Goell¹⁹ and Marcatili.²⁰ Goell²¹ and Ihaya²² independently demonstrated a passive thin film directional coupler fabricated using rectangular waveguides. Active thin film devices such as modulators,²³ deflectors,²⁴ integrated lasers^{25,26} and detectors²⁷ have already been demonstrated. Because of their small size, many of these devices are more thermally and mechanically stable than their bulk counterparts, and the high electrical and optical field densities lead to very efficient and compact devices.

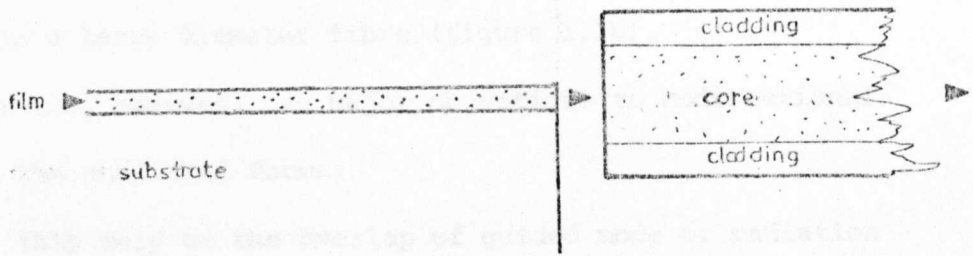
The selective excitation of waveguide modes by a Gaussian laser beam using a high-index coupler was described by Tien et.al.²⁸ and Midwinter²⁹ and other forms of input/output coupling devices such as the tapered film coupler,³⁰ the periodic grating coupler³¹ and the holographic coupler³² are in regular use. These were devised as convenient methods of transferring unconfined optical energy into and out of single active and passive waveguide devices, and would not be used in a practical waveguide-to-terminal configuration. The interconnection of thin film circuits and devices on the same or separate substrates and the coupling of integrated circuits to the optical fibre data highway was recognised as 'the coupling problem'.

1.1.3 The Coupling Problem.

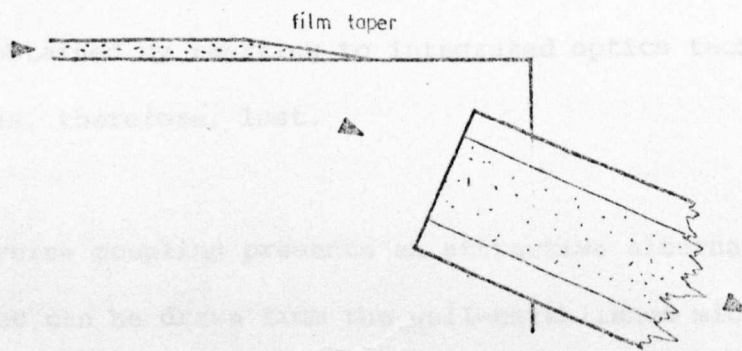
The efficient coupling of optical fibres to integrated waveguides is the basic hindrance to the development of a complete third-generation system. The marriage of the two categories, with their particular and recognised advantages to produce a fibre optic data link between integrated optic terminal equipment, has become a problem of significant proportions. Solutions have been attempted which can be subdivided into separate classes; co-directional and transverse coupling.*

The problems associated with the former approach are formidable. Because of the wide discrepancy in waveguide profiles between thin film optical circuits and circular cladded fibres, butt jointing (figure 1.1a) presents an inherent mismatch of the guided mode fields.. Reflection losses and micropositioning difficulties produce further inefficiencies. It would be advantageous if the fibre could be coupled at any part of the integrated circuit and not solely at the film edge. Boivin³⁴ has produced one of the best examples of a film to fibre coupler, with a transfer efficiency of approximately 30%. Other workers^{35,36} have studied the codirectional coupling from thin film semiconductor lasers to circular fibres, with figures of 66% power transfer reported.

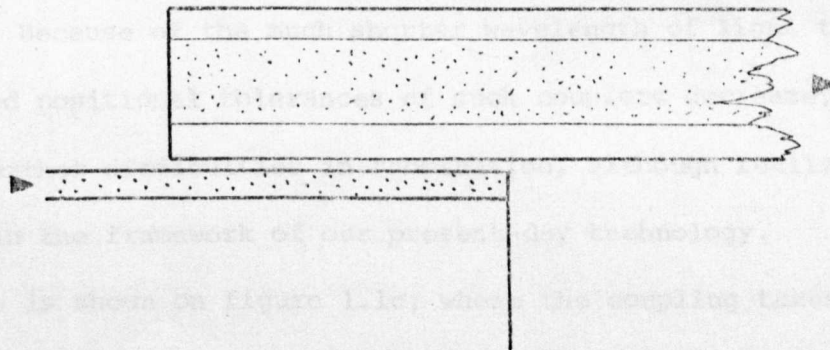
* The terms 'codirectional' and 'transverse' were defined by Arnaud³³. 'Transverse' describes the evanescent field coupling of two or more dielectric waveguides lying side by side, where the transfer of power takes place in the transverse direction. 'Codirectional' applies where the two waveguides are placed end to end, and the transfer of power takes place along the common axis. This term will be expanded in this text to include the coupling of waveguide radiation fields along the direction of power flow.



(a) butt jointing



(b) collection of a radiation field



(c) transverse coupling

FIGURE 1.1 Methods of coupling from planar waveguides to circular fibres .

Tien et.al.³⁷ have converted the guided film mode into a radiation mode in a manner similar to a dielectric rod antenna and collected the energy in a large diameter fibre (figure 1.1b).

There are, however, two major objections to codirectional coupling in the published forms:

- (i) they rely on the overlap of guided mode or radiation mode fields, and are inherently lossy and generally non-reversible;
- (ii) they represent coupling from a single-mode to a multimode waveguide. The advantage of high bandwidth obtained by reërting to integrated optics technology is, therefore, lost.

Transverse coupling presents an attractive alternative solution. Many analogies can be drawn from the well-established microwave technology of directional and distributed couplers,³⁹ and techniques used in them can, in principle, be applied at the higher optical frequencies. Because of the much shorter wavelength of light the dimensional and positional tolerances of such couplers decrease, introducing further difficulties in fabrication, although realization is still within the framework of our present-day technology. The basic approach is shown on figure 1.1c, where the coupling takes place via the interaction of the component waveguide evanescent fields. Bulmer⁴⁰ has studied the distributed coupling between a single-mode fibre and a planar waveguide. The fields of the fibre core were brought to the surface of the fibre by reducing the overall dimensions, and the presence of a phase grating brought about the necessary phase-matching condition for the guided modes. Unwanted interactions were introduced which limited the efficiency of the device. Hammer⁴¹ attempted a similar configuration, this

time with the fibre cladding partially removed. The transfer efficiency was limited to 6%. Dalgoutte⁴² in 1975, utilized a new type of fibre introduced in 1974,⁴³ to couple energy out of a thin film waveguide. To overcome the phase mismatch, a tapered velocity coupler, described by Louisell⁴⁴ and Wilson and Teh⁴⁵ was used, and an efficiency from film to fibre of 70% was reported. All of these couplers can be applied to the coupling of high-refractive-index thin films and low-refractive-index glass fibres. The major advantages to be gained from transverse coupling are:

- (i) the power transfer can reach a theoretical maximum of 100% in either direction;
- (ii) the coupling is generally between single waveguide modes;
- (iii) the relative cross-sections of the waveguide structures are not required to be the same or similar.

Coupling can take place at any point on the thin film circuit and the amount of power coupled can be varied at will. However, a completely successful and practical coupler has not yet been reported in the literature.

1.2 Motivation and Aims of Research.

At the commencement of this research in September, 1973, few methods of coupling fibres and films were known, although Laybourn in 1972⁴⁶ had proposed the use of thin unclad planar ribbon waveguides⁴⁷ for this purpose, and had qualitatively demonstrated the principle. Thin film waveguide directional couplers were just appearing in the literature,^{22,48} though the phenomenon of spatial beating was well-known in fibre optics⁴⁹ and in microwave transmission lines.^{50,51} Many exciting developments were taking place in integrated optics, particularly in modulation and integrated lasers. Concurrently,

ultra-low-loss optical fibres were being developed.⁷

It was felt that the advances in integrated optics would be of use only when a method of coupling optical circuits together and to the optical data highway, was developed. The aims of the present research were, therefore, set out as follows:

- (i) To develop a theoretical and experimental understanding of evanescent field coupling of thin film and fibre optical waveguides with a view to producing efficient and practical film to fibre waveguide coupling devices for future generations of optical communication systems.
- (ii) To investigate novel forms of optical fibres and coupling configurations, always bearing in mind the future system requirements.

1.3 Review of the Contents of the Thesis.

In Chapter 2, following this introduction, a general treatment of waveguide and directional coupler theory is presented. In Part I, we deal with the waveguides encountered in this work: step-index and graded-index slab waveguides, rectangular waveguides and circular waveguides. A simple plane-wave approach is adopted for clarity, and the notation is made consistent throughout. Part II of Chapter 2 describes the coupled wave solution for two transmission lines, and gives some examples of the expected response with different propagation constants and coupling coefficients. The determination of the coupling coefficient is then discussed and the results of our theoretical predictions are compared with those of other authors.

Chapter 3 introduces the need for cladding modification of circular fibres for the purpose of evanescent field coupling, and two methods of achieving this are described and compared. The uses to which such modified fibres may be put are evaluated in a preliminary coupling experiment.

The principle is further demonstrated in Chapter 4, where the excitation of low - and high - order modes of a clad circular fibre by a high-index prism coupler is described. The work of this chapter leads to a verification of circular fibre mode fields and propagation characteristics, and shows that evanescent field coupling to and from other structures at a suitably treated region of the fibre is possible, though not necessarily practicable.

Chapter 5 describes possible alternatives. The previous work on planar ribbon fibres is reappraised and an improved version - the sandwich ribbon fibre - is described from the manufacturing process to a theoretical and experimental analysis of the structure. The properties and uses of sandwich ribbon fibres are discussed.

Chapter 6 is devoted in its entirety to an extensive study of the three-dimensional sandwich ribbon fibre, an entirely new waveguide for use in the coupling experiments. The results of these experiments are presented in Chapter 7, where the realization of the first single-mode fibre-film optical directional coupler is described, as well as some novel coupling configurations. The theoretical predictions are recalled at relevant points.

In conclusion we present in Chapter 8 some further discussions of the results and relate the findings of our work to expected trends in system development.

There is ample scope for further study, and suggestions for the continuation of the work are given.

2.1 Introduction.

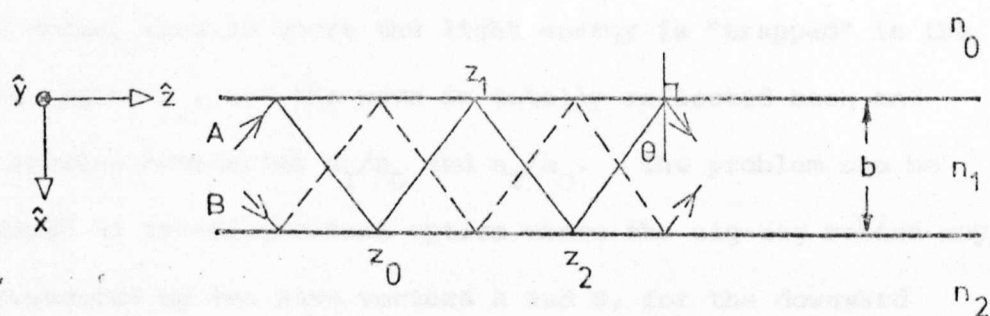
The aim of the chapter is to present a general waveguide and directional coupler theory, reviewing the work of other authors and unifying the various methods using a common notation. Several novel methods of stating the problems and obtaining equivalent solutions will be discussed.

The chapter commences with Part I, containing brief sections outliningⁱⁿ the theory of guided modes of step-index and graded-index slab waveguides, and rectangular and circular waveguides. Though a fuller account of such structures is available in the prescribed literature, the sections will serve to introduce the reader to the coordinate system, the notation and the methodology.

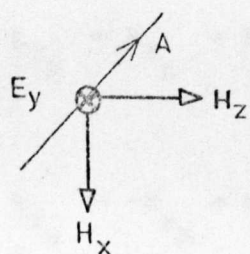
In Part II the coupled wave equations, representing the most general description of the behaviour of coupled modes in transmission lines, are solved analytically. Use is made of a digital simulation of the coupled differential equations and computer solutions are obtained directly. The determination of the coupling coefficient is approached from three different aspects: the general wave solution (in particular for slab waveguides), the ray optics method for coupled slab waveguides, and a direct approach. The results will be summarized in a concluding section.

PART I. WAVEGUIDE THEORY.2.2 Step-index Dielectric Slab Waveguide.

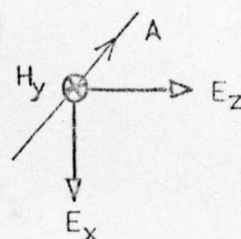
In many integrated optic⁷³ and fibre optic applications^{42,43,47} the waveguide consists of a high-refractive-index layer, n_1 , embedded in low-refractive-index media, n_0 and n_2 as in figure 2.1a. The waveguide is termed 'slab' because it is taken as infinite in the y -directions and the media n_0 (the superstrate) and n_2 (the substrate)



(a) step - index dielectric slab waveguide .



TE



TM

(b) slab waveguide mode polarization

FIGURE 2.1 Plane wave formulation of a step - index slab waveguide .

extend to infinity. The dielectric materials are all assumed to be isotropic. Mathematical solutions of the waveguide show that there exist many possible modes of light-wave propagation which depend on the refractive indices and the thickness, b , of the guiding region. We will, however, restrict our attention to guided modes, that is where the light energy is "trapped" in the guiding region n_1 , and the wave is totally reflected back and forth between boundaries n_1/n_0 and n_2/n_0 . The problem can be considered as two-dimensional optics where the zig-zag motion may be represented by two wave vectors A and B, for the downward travelling and upward travelling plane waves respectively. The z components of A and B are equal, indicating a constant wave velocity in the axial direction, while the x components are equal and opposite. We have

$$k_{z_A} = k_{z_B} = kn_1 \sin \theta = \beta \quad 2.1$$

and

$$k_{x_B} = -k_{x_A} = kn_1 \cos \theta = k_1 \quad 2.2$$

where

$$k = \frac{2\pi}{\lambda} = \frac{\omega}{c} \quad 2.3$$

ω is the angular frequency, c the velocity of light in vacuum, and λ is the free-space wavelength.

The superposition of A and B results in a standing wave across the thickness of the guide.

Consider now a ray, normal to the B wavefront reflecting at a point z_0 on the n_1/n_2 boundary, totally internally reflecting at point z_1 on the n_1/n_0 boundary and returning to a point z_2 . The phase change for the plane wave to cross the thickness b of the guide is $k_1 b$, and between z_0 and z_2 the contribution is $2k_1 b$. At $z = z_0$ the wave experiences a phase change, $-2\phi_{12}$, due to the

total reflection there,¹¹³ and similarly at z_1 of $-2\phi_{10}$. For the waves in the thin film to interfere constructively the total phase change from (just before) z_0 to (just before) z_2 must be equal to an integral number of 2π , so

$$2k_1 b - 2\phi_{12} - 2\phi_{10} = 2m\pi \quad 2.4$$

or

$$k_1 b = m\pi + \phi_{12} + \phi_{10} \quad 2.5$$

Since a plane wave approach is being used, there are two possible wave polarizations, TE and TM, outlined in figure 2.1b. TE waves have components E_y, H_x, H_z and TM waves, E_x, E_z, H_y . The reflection phase changes $-2\phi_{1\rho}$ ($\rho = 0, 2$) are slightly different for each polarization and therefore equation 2.5 will have solutions for TE_m and TM_m modes. Evaluating the phase changes, $-2\phi_{1\rho}$, gives:¹¹³

$$k_1 b = m\pi + \tan^{-1} \epsilon_{1\rho} \frac{k_0}{k_1} + \tan^{-1} \epsilon_{1\rho} \frac{k_2}{k_1} \quad 2.6$$

where

$$k_1^2 = k^2 n_1^2 - \beta^2 \quad 2.7$$

$$k_0^2 = \beta^2 - k^2 n_0^2 \quad 2.8$$

$$k_2^2 = \beta^2 - k^2 n_2^2 \quad 2.9$$

and

$$\epsilon_{1\rho} = \begin{cases} 1 & \text{for TE modes} \\ \left(\frac{n_1}{n_\rho}\right)^2 & \text{for TM modes} \end{cases} \quad \rho = 0, 2$$

Equation 2.6 represents the characteristic or eigenvalue equation for the waveguide modes. A more rigorous analysis,⁷⁴ involving Maxwell's curl equations and application of the boundary conditions at n_1/n_0 and n_1/n_2 , reveals an equivalent solution. In addition one finds that, for guided TE waves,

$$\begin{aligned}
 E_Y(x) &= \hat{E}_Y \cos [k_1(x-b/2)] & b > x > 0 \\
 \text{or} &= \hat{E}_Y \cos \phi_{10} \exp(k_0 x) & -\infty < x \leq 0 \\
 \text{or} &= \hat{E}_Y \cos (\phi_{12} + m\pi) \exp[-k_2(x-b)] & \infty > x \geq b
 \end{aligned} \quad 2.7a,b,c$$

The obvious extensions for TM waves are omitted. The normalized amplitude of the E_Y wave at $x = 0$ is, from equation 2.7b

$$\frac{E_Y(0)}{\hat{E}_Y} = \cos \phi_{10} = \cos \left(\tan^{-1} \frac{k_0}{k_1} \right) = \frac{k_0}{(k_1^2 + k_0^2)^{1/2}} \quad 2.8$$

and at $x = b$, from equation 2.7c

$$\frac{E_Y(b)}{\hat{E}_Y} = \cos \phi_{12} = \cos \left(\tan^{-1} \frac{k_2}{k_1} \right) = \frac{k_2}{(k_1^2 + k_2^2)^{1/2}} \quad 2.9$$

Equations 2.8 and 2.9 have equal signs for even modes ($m = 0, 2, 4$, etc) and opposite signs for odd modes ($m = 1, 3, 5$ etc). There are $(m+1)$ electric field maxima in the x direction. The field is exponentially decaying from the surface amplitudes $E_Y(0)$ and $E_Y(b)$ with decay constants $\frac{1}{k_0}$ and $\frac{1}{k_2}$ ^{in n_0 and n_2} respectively, the so-called evanescent (quickly fading or vanishing) fields.

The propagation factor β , in equation 2.5, is a function of the refractive indices, the guiding region thickness, the wave polarization and the mode order. The important parameter,

$$\frac{\beta}{k} = n_e = n_1 \sin \theta \quad 2.10$$

the 'effective' refractive index, can be found for a particular waveguide system. The plot of n_e against the thickness b , for the different modes is called the 'dispersion curve', and several examples of this characteristic graph are presented in this thesis, for example figure 5.4.

It should be stressed that the analysis has been presented for guided modes only. In fact there is a continuum of radiation modes,¹⁸

where n_e lies outside the bounds of the guiding conditions

$$\begin{array}{ll} n_1 > n_e > n_0 & \text{for } n_0 > n_2 \\ \text{or} & > n_2 \quad \text{for } n_2 > n_0 \end{array} \quad 2.11$$

Using a simple plane wave (ray optic) analysis, the characteristic equation for mode propagation in isotropic step-index slab waveguides has been obtained. The field distributions have been stated, and the concept of an evanescent field has been introduced. The results are well-known, but will find application throughout the work and provide an interesting starting-point from which the concept of a guided wave may evolve.

2.3 Graded-index Dielectric Slab Waveguide.

The ray optics approach may be used to advantage to describe mode propagation in waveguides the solutions of which are not as straightforward as the step-index slab. In this section the method will be applied to a situation of particular relevance: the graded-index slab waveguide, having a refractive index profile $n(x)$ whose maximum value, n_s , occurs at the surface ($x=0$), again embedded in a superstrate n_0 and a substrate n_2 (figure 2.2). If we assume $n_2 > n_0$ then the range of the effective refractive index for guided modes is

$$n_s > n_e > n_2 \quad 2.12$$

The use of a plane-wave approach allows us to employ the well-known WKB approximation,⁷⁶ in which we write

$$k_1 = k_1(x) = k(n^2(x) - n_e^2)^{1/2} \quad 2.13$$

Gedeon⁷⁷ has demonstrated that, for a monotonically decreasing function, the approximation yields n_e values within about 0.01% of the exact values. Again the intuitive formulation can be stated:

$$\left[(\text{phase change over path length}) + (\text{phase changes due to reflections}) \right] \Big|_{\text{round trip}} = 2m\pi \quad 2.14$$

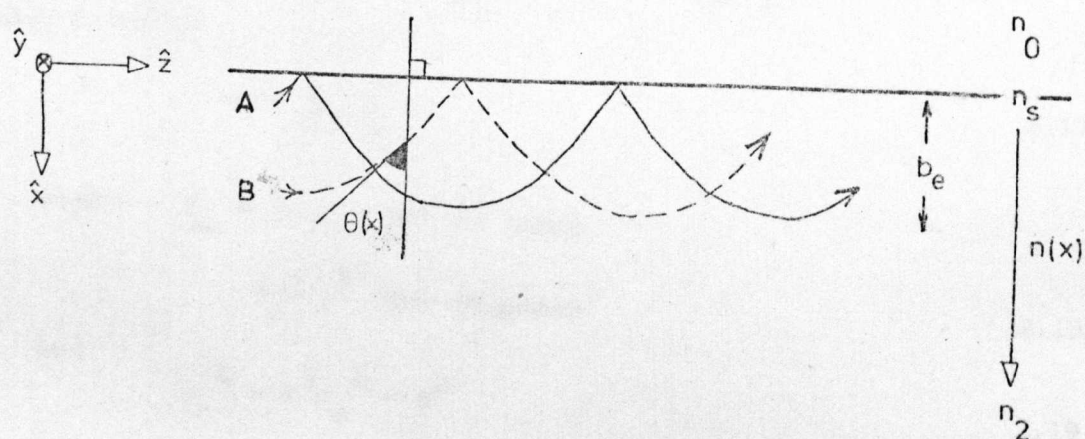


FIGURE 2.2 Graded index dielectric slab waveguide .

If b_e is the turning value of the ray trajectory in the guiding medium where $\theta(x) = \pi/2$, $k_1 = 0$, and, from equation 2.13,

$$n(b_e) = n_e \quad 2.15$$

then the total phase change over the 'round trip' path length is

$$2k \int_0^{b_e} (n^2(x) - n_e^2)^{1/2} dx - \frac{\pi}{2} \quad 2.16$$

The $-\pi/2$ contribution here accounts for the reflection at the WKB turning point.

If the reflection phase-change at the n_s/n_o interface is included, being

$$-2 \tan^{-1} \xi_{so} \frac{k_o}{k_s} \quad 2.17$$

where $\xi_{so} = 1$ for TE modes

$$\left(\frac{n_s}{n_o}\right)^2 \quad \text{for TM modes} \quad 2.18$$

and

$$k_s^2 = k_{n_s}^2 - \beta^2 \quad 2.19$$

we obtain, from equations 2.14, 2.16 and 2.17

$$k \int_0^{b_e} (n^2(x) - n_e^2)^{1/2} dx = m\pi + \frac{\pi}{4} + \tan^{-1} \xi_{so} \frac{k_o}{k_s} \quad 2.20$$

Equation 2.20 is the characteristic equation for the TE_m or TM_m modes of a graded-index slab waveguide, having a slowly-varying refractive index profile $n(x)$. The RHS of equation 2.20 may be solved as a function of n_e analytically or, where appropriate, using methods of numerical integration. The dispersion curves for particular profiles can be constructed and in Chapter 7 of this thesis the example of a linear refractive index profile is discussed.

The wave functions are obtained from Maxwells equations which, for TE modes, reveal⁷⁶

$$\frac{d^2}{dx^2} E_Y(x) + k^2(x) \cdot E_Y(x) = 0 \quad 2.21$$

The eigenfunctions, $E_Y(x)$, may be approximated by ⁷⁷

$$E_Y(x) \approx \left[\frac{k(x)}{k_s} \right]^{-1/2} \cos \left[\int_{b_e}^x k(x) dx - \frac{\pi}{4} \right] \quad 2.22$$

in the range

$$b_e > x > 0 \quad 2.23$$

Outside the bounds of equation 2.23 the fields are exponentially

decaying with decay constants $\frac{1}{k_0}$ and $\sim \frac{1}{k_2}$. At $x = 0$ equation

2.22 becomes

$$E_Y(0) \propto \cos\left(\tan^{-1} \frac{k_0}{k_s}\right) = \frac{k_0}{(k_s^2 + k_0^2)^{1/2}}, \quad 2.24$$

the approximate value of the surface field, normalized with respect

to the field amplitude at the turning value, b_e . Note that the

normalization caters for the cut-off condition $n_e \rightarrow n_2$, where $E_Y(b_e) \rightarrow \infty$

and $E_Y(0)/E_Y(b_e) \rightarrow 0$.

The plane-wave approach has been extended to evaluate the characteristic equation of a general monotonically-decreasing graded-index slab waveguide. The solution of equation 2.20 will be particularly useful in this work where the majority of the thin film waveguides used were silver/sodium ion-exchanged and which have an approximately linear refractive index profile.

2.4 Rectangular Dielectric Waveguide.

In most practical applications the guided wave is not unconfined in the y-direction. The assumption that there is no field variation in that direction does not, therefore, hold and the propagation behaviour of three-dimensional* waveguides is of considerable interest generally

*It is appropriate at this initial stage to clarify the definition of the term 'n-dimensional' used in this context. A slab waveguide is an infinite sheet of dielectric material and is defined as 'two-dimensional' because light may be confined in a beam in any direction within the plane of the sheet. Strictly speaking the field varies transversely in the thickness direction only. The term 'three-dimensional' applies to the situation where the field in the cross-section varies in two directions and the confined energy can propagate in any direction in the complete space.

and of particular interest here. The problem has been tackled theoretically by Goell¹⁹ and Marcatili²⁰. The latter author develops a system of transcendental equations which describe mode propagation in a uniform dielectric waveguide embedded in regions of lower refractive index. The refractive index profile and the coordinate system are shown in Figure 2.3a. The solution is readily obtained in an approximate form by introducing a simplification. It can be assumed that the fields within the four shaded areas are small for reasonably well-guided modes, and that the problem can be thought of as the superposition of two sets of interfering plane waves in the xz and yz planes producing a standing wave in the xy plane and a propagating wave in the z-direction. The plane wave approach developed for slab waveguides may be applied in both the xz and yz planes to give

$$k_x b = m_x \Pi + \tan^{-1} \xi_{10} \frac{k_o}{k_x} + \tan^{-1} \xi_{12} \frac{k_2}{k_x} \quad 2.25$$

$$k_y a = m_y \Pi + \tan^{-1} \xi_{10'} \frac{k_{o'}}{k_y} + \tan^{-1} \xi_{12'} \frac{k_{2'}}{k_y} \quad 2.26$$

where m_x and m_y are the mode orders in the x- and y- directions respectively.

If the substitutions

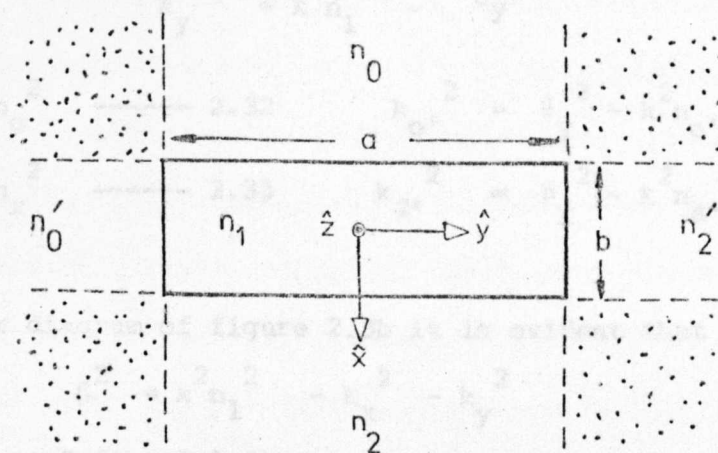
$$q = (m_x + 1) \quad 2.27$$

$$p = (m_y + 1) \quad 2.28$$

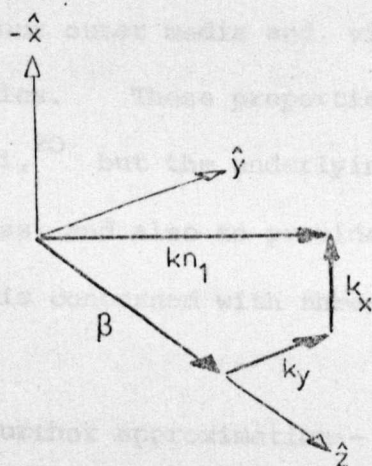
are made, q and p indicate the number of extrema of the electric or magnetic fields in the x and y directions, and the equations of Marcatili²⁰ result. The modes are of the TEM kind and can be grouped into two families E_{pq}^x and E_{pq}^y where

$$\xi_{1p} = \left(\frac{n_1}{n_p} \right)^2 \quad \text{for } E^y \text{ modes} \\ = 1 \quad \text{for } E^x \text{ modes} \quad p = 0, 2$$

$$\xi_{1p'} = 1 \quad \text{for } E^y \text{ modes} \\ = \left(\frac{n_1}{n_{p'}} \right) \quad \text{for } E^x \text{ modes} \quad p' = 0', 2'$$



(a) coordinates and definitions



(b) vector diagram

FIGURE 2.3 Rectangular dielectric waveguide .

In equations 2.25 and 2.26 above it is convenient to introduce two further propagation constants β_x and β_y such that

$$k_x^2 = k_{n_1}^2 - \beta_x^2 \quad 2.30$$

$$k_y^2 = k_{n_1}^2 - \beta_y^2 \quad 2.31$$

$$k_o^2 = \beta_x^2 - k_{n_o}^2 \quad 2.32$$

$$k_{o'}^2 = \beta_y^2 - k_{n_{o'}}^2 \quad 2.34$$

$$k_2^2 = \beta_x^2 - k_{n_z}^2 \quad 2.33$$

$$k_{2'}^2 = \beta_y^2 - k_{n_{z'}}^2 \quad 2.35$$

From the vector diagram of figure 2.3b it is evident that

$$\beta^2 = k_{n_1}^2 - k_x^2 - k_y^2 \quad 2.36a$$

or from equations 2.30 and 2.31

$$\beta^2 = \beta_x^2 + \beta_y^2 - k_{n_1}^2 \quad 2.36b$$

Using working similar to equations 2.6 to 2.9, it is a simple matter to evaluate the expected waveguide field distributions, the magnitudes of the evanescent waves in the four outer media and, via equation 2.36, the mode dispersion characteristics. These properties have been adequately described by Marcatili,²⁰ but the underlying philosophy is presented here for completeness, and also to provide a background to the work of Chapter 6, which is concerned with three-dimensional sandwich ribbon fibres.

Marcatili introduces a further approximation - the closed form solution - the basis of which is that equations 2.25 and 2.26 are written as

$$k_x = \frac{\text{Ilq}}{b} (1 + S_x)^{-1} \quad 2.37$$

$$k_y = \frac{\text{Ilp}}{a} (1 + S_y)^{-1} \quad 2.38$$

where S_x, S_y are constants $\ll 1$. The \tan^{-1} functions are thus set

independent of n_e , an approximation which will be shown to be the result of ignoring the well-known Goos-Hanchen shifts.⁷⁸

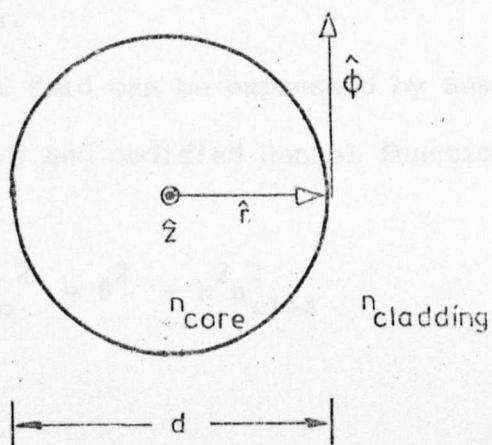
How valid is the closed form approximation? Though Marcatili compares his solution to the exact form of Goell¹⁹ to find good correspondence except at cut-off (where n_e tends to the highest surrounding material refractive index and the Goos-Hanchen shifts become appreciable) some caution must be entertained in applying the approximate results. For example, in the same paper Marcatili develops an expression for the coupling coefficient for a directional coupler, comprising two parallel rectangular waveguides, which is quite erroneous - this topic will be further discussed in Section 2.8.

It is also apparent that it is extremely unlikely that waveguides can be manufactured that are exactly rectangular and with sharp corners.

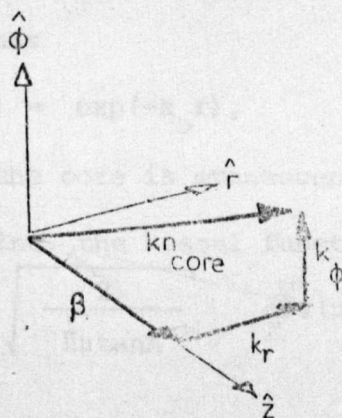
It may be concluded that, by extending the plane wave approach a solution can be found to describe mode propagation in rectangular dielectric waveguides, taking the form of two independent characteristic equations (equations 2.25 and 2.26) the eigenvalues of which are related (through equation 2.36) to give the axial propagation constant, β .

2.5 Circular Dielectric Fibre Waveguide.

Circular fibre waveguides, in the form shown in Figure 2.4a are the most commonly encountered type of transmission medium for optical communication systems. In this section we shall not dwell on the already well-established and complex theory of propagation in cylindrical fibre waveguides, save to refer the reader to some of the more important texts.⁵² However many of the coupling effects under study rely upon the matching of the fibre mode fields to plane waves, for example existing at the base of a high-index prism coupler or in a slab or rectangular waveguide. It would, therefore, be useful to establish approximate relations which allow the guided wave in the fibre to be composed of locally plane waves. As Marcuse points out⁶⁹



(a) fibre cross-section



(b) vector diagram for plane wave composition (high order modes)

FIGURE 2.4 Circular dielectric fibre waveguide .

this can be done for all but the lowest modes in a thick fibre

where

$$k_1 \frac{d}{2} \gg 1 \quad 2.39$$

with

$$k_1^2 = k_{\text{core}}^2 - \beta^2 \quad 2.40$$

and $\frac{d}{2}$ is the fibre radius.

For all modes the transverse field can be expressed by Bessel function

$J(k_1 r)$ inside the fibre core and modified Hankel function $K(k_0 r)$ outside the core,⁶⁹ where

$$k_0^2 = \beta^2 - k_{\text{clad}}^2 \quad 2.41$$

More fully:

$$E \sim J_\mu(k_1 r) e^{j\mu\phi} e^{-j\beta z} \quad \text{for } r < \frac{d}{2} \quad 2.42$$

$$\sim K_\mu(k_0 r) e^{j\mu\phi} e^{-j\beta z} \quad \text{for } r > \frac{d}{2} \quad 2.43$$

In equation 2.42 and 2.43, μ is the azimuthal mode order and the time variation of the field, $\exp(j\omega t)$, is suppressed. For large arguments the modified Hankel function becomes

$$K(k_0 r) \rightarrow \exp(-k_0 r), \quad 2.44$$

indicating that the field outside the core is evanescent. With the conditions of equation 2.39 applying, the Bessel function may be

expanded using¹¹² $J_\mu(\mu \sec A) = \sqrt{\frac{2}{\mu \tan A}} \cos(\mu \tan A - \mu A - \frac{\pi}{4}),$

giving

$$J_\mu(k_1 r) = \frac{\exp(j\psi(r)) + \exp(-j\psi(r))}{\sqrt{2\pi} (k_1^2 r^2 - \mu^2)^{1/4}} \quad 2.45$$

where

$$\psi(r) = r(k_1^2 - (\frac{\mu}{r})^2)^{1/2} - \mu \cos^{-1}(\frac{\mu}{k_1 r}) - \frac{\pi}{4} \quad 2.46$$

Expanding equation 2.46 as the first two terms of a Taylor expansion about $r = \frac{d}{2}$ gives

$$\psi(r) \approx \psi\left(\frac{d}{2}\right) + \left(k_1^2 - \left(\frac{2\mu}{d}\right)^2\right)^{\frac{1}{2}} r + \text{constant} \quad 2.47$$

Ignoring the constant terms it may be seen that the argument of the exponential terms of equation 2.45 is $\left(k_1^2 - \left(\frac{2\mu}{d}\right)^2\right)^{\frac{1}{2}} r$, and that equations 2.42 and 2.43 become,

$$E \sim \exp \left\{ j \left(k_1^2 - \left(\frac{2\mu}{d} \right)^2 \right)^{\frac{1}{2}} r + j\mu\phi - j\beta z \right\} \quad \left(r < \frac{d}{2} \right) \quad 2.48$$

$$\sim \exp \left(k_0 r + j\mu\phi - j\beta z \right) \quad \left(r > \frac{d}{2} \right) \quad 2.49$$

The mode field can be thought of as made up of quasilplane waves with a propagation vector (Figure 2.4b)

$$\vec{K} = k_r \hat{r} + k_\phi \hat{\phi} + \beta \hat{z} \quad 2.50$$

with $k_r^2 = k_1^2 - \left(\frac{2\mu}{d}\right)^2$, 2.51

$$k_\phi = \frac{2\mu}{d} \quad 2.52$$

and

$$|K|^2 = k_r^2 + k_\phi^2 + \beta^2 = k_{n_{\text{core}}}^2 \quad 2.53$$

It is interesting to note the similarity in equations 2.53 and 2.36 where the plane wave approach has been used to describe both circular and rectangular geometries.

The propagation constant β , above, can only be evaluated by solving the characteristic equations presented by Kao and Hockham³ and further described by Gloge⁶⁵ and Snyder.⁷⁹

To summarize, it can be stated that the transverse mode fields for a circular fibre are given by equations 2.42 and 2.43. However, for higher order modes in fibres that support many modes, the fields can be expressed locally by quasi-plane waves with orthogonal vector components k_r , k_ϕ and β , defined in equations 2.50 to 2.53.

2.6 Part I: Summary and Conclusions.

In Part I of this chapter, a short theoretical outline has been made of the waveguiding structures of particular relevance to this work, namely the

1. Dielectric step-index slab waveguide.
2. Dielectric graded-index slab waveguide.
3. Rectangular dielectric waveguide.
4. Circular dielectric fibre waveguide.

Each structure was considered from a plane-wave viewpoint which lends itself to a convenient ray-optical interpretation.

PART II. COUPLING THEORY.

2.7 The Coupled Wave Equations.

An analysis of coupled modes in transmission lines was first given by Albersheim⁸³ and the coupling of guided waves was analysed by Krasnushkin and Khoklov⁵⁰. However the most general analysis was presented in 1954 by S.E. Miller⁵³ which described the effects of wave coupling in dielectric waveguides.

Consider the coupling, by some form of field overlap, of two transmission lines 1 and 2, which is uniform over the interaction length $0 < z < L_1$ and zero elsewhere. The spatial variation of the complex wave amplitudes E_1 and E_2 may be written as⁵³

$$\begin{bmatrix} \dot{E}_1 \\ \dot{E}_2 \end{bmatrix} = \begin{bmatrix} -(\Gamma_1 + k_{11}) & k_{21} \\ k_{12} & -(\Gamma_2 + k_{22}) \end{bmatrix} \begin{bmatrix} E_1 \\ E_2 \end{bmatrix} \quad 2.54$$

where $\dot{E} \equiv \frac{dE}{dz}$

k_{11} , k_{22} represent the reaction of the coupling on the respective lines.

k_{21} , k_{12} are the transfer effects of the coupling.

Γ_1 , Γ_2 are the uncoupled propagation constants of 1 and 2.

$|E_1|^2$ and $|E_2|^2$ represent the power carried by 1 and 2 respectively.

Our case of interest shall be where reciprocity and loose coupling per wavelength hold, and

$$k_{12} = k_{21} = \kappa \quad 2.55$$

$$\text{Introducing} \quad \gamma_1 = \Gamma_1 + k_{11} \quad 2.56$$

$$\gamma_2 = \Gamma_2 + k_{22} \quad 2.57$$

and noting that γ_n differs little from Γ_n , equation (2.54) may be rewritten as

$$\begin{bmatrix} \dot{E}_1 \\ \dot{E}_2 \end{bmatrix} = \begin{bmatrix} -\gamma_1 & \kappa \\ \kappa & -\gamma_2 \end{bmatrix} \begin{bmatrix} E_1 \\ E_2 \end{bmatrix} \quad 2.58$$

Equation 2.58 may be solved in two ways: firstly by obtaining an analytic solution via the Laplace Transformation, or secondly by modelling the system using an analogue computer or an analogue simulation package for a digital computer. The analytic solution is naturally superior for handling practical situations, but the simulation of equation 2.58 gives valuable insight into the coupled wave equations, and may be readily extended to analyse the coupling of any number of transmission lines, where the analytic method becomes cumbersome, if not impossible. Each method is now described.

2.7.1 Simulation of the coupled wave equations.

The system of equation 2.58 may be 'patched' using an analogue computer or investigated using a simulation package for a digital computer.⁸⁰ The former method was found to be less suitable because of the difficulty of maintaining sustained oscillations (uncoupled

conditions) with an analogue computer.* In the latter, numerical integration by a fourth-order Runge-Kutta method⁸¹ was employed on a PDP 11 digital computer and the desired variable was outputted directly on the y-axis of an xy plotter, the independent variable being time on the x-axis corresponding to distance along the coupling region. The "patch diagram" for the analogue simulation and the functional section of the digital simulation programme are shown in Figure 2.5a and 2.5b. Concentrating on the more versatile and reliable digital simulation, the complex propagation constant

$$\gamma_n = \alpha_n + j\beta_n \quad (n = 1, 2) \quad 2.59$$

and the coupling coefficient modulus K may be varied at will. The functions are normalized by setting $\bar{\gamma}_1 = 1$, $\bar{\gamma}_2 = 1 - \frac{\Delta\gamma}{\bar{\gamma}_1} = 1 - \Delta\gamma$ and $\bar{K} = \frac{K}{\bar{\gamma}_1} = K$.

Examples:

(a) When the attenuation of the component waveguides is ignored, that is $\alpha_1 = \alpha_2 = 0$, and the phase constants are equal, that is $\beta_1 = \beta_2$, the condition $K = 0$ results in the generation of two lossless decoupled waves, as one might expect.

(b) With the conditions of (a) applying, but with $K \neq 0$, that is where some coupling is introduced, and with initial conditions

$$\begin{aligned} \bar{E}_1(0) &= 1 &) \\ \bar{E}_2(0) &= 0 &) \end{aligned} \quad , \quad 2.60$$

the spatial power oscillation between the waves is apparent. In Figure 2.6 a & b the result for $\bar{\beta}_n = 1$ and $\bar{K} = 0.1$ is shown.

* In some ways the lack of sustained oscillations in an analogue system is more akin to reality, where the waves in the component guides of an optical coupler are attenuated. However, the presence of 'non-programmed' loss makes interpretation of the results more difficult.

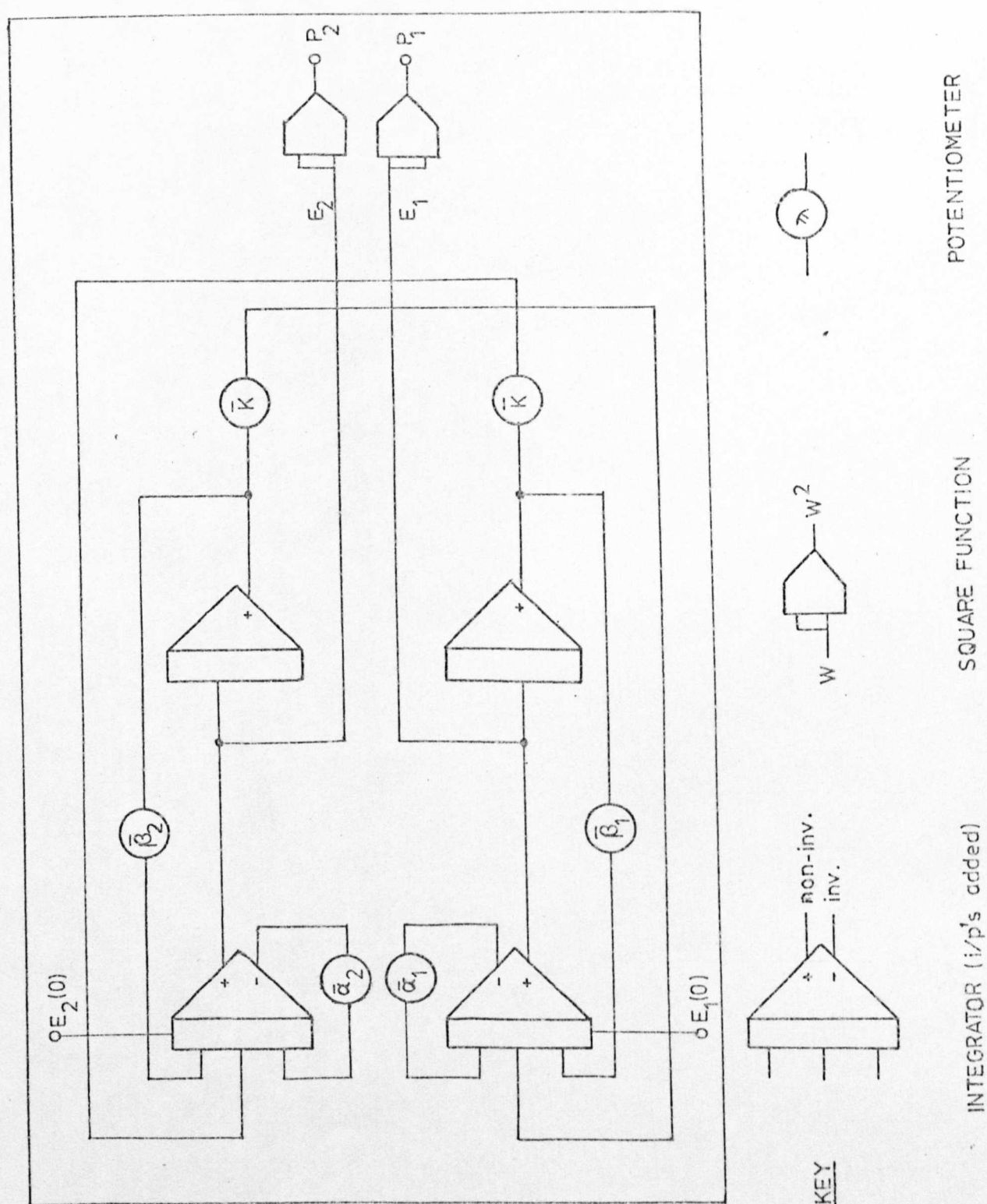


FIGURE 2.5a Patch diagram for the analogue simulation of the coupled-wave equations.

```
CMODV22.FOR
COPTICS
```

```
SUBROUTINE MODEL(VAR,DER,T,M)
COMMON /BLK1/ BA,BB,C,LA,LE
REAL LA,LE
DIMENSION VAR(4),DER(4),DAT(7)
COMMON /V/ DAT

DER(1)=VAR(3)
DER(2)=VAR(4)
DER(3)=-BA*VAR(1)+C*VAR(2)-LA*VAR(3)
DER(4)=-BB*VAR(2)+C*VAR(1)-LE*VAR(4)
A2=VAR(3)**2
B2=VAR(4)**2

IF(M.EQ.0) GOTO 10
DAT(1)=T
DAT(2)=A2
DAT(3)=B2
DAT(4)=VAR(1)
DAT(5)=VAR(2)
DAT(6)=VAR(3)
DAT(7)=VAR(4)
10RETURN
END
```

```
CINIT22.FOR
```

```
SUBROUTINE INIT
REAL LA,LE
DOUBLE PRECISION HEADER(20),H(7)
COMMON /BLK1/ BA,BB,C,LA,LE
COMMON /L/ HEADER
DATA H/'Z','A**2','B**2','JA','JB','A','B'/

DO 1 I=1,7
1HEADER(I)=H(I)

WRITE(7,100)
READ(5,101) BA,BB,C,LA,LE

100FORMAT(1X,'ENTER VALUES FOR BA,BB,C,LA,LE',/)
101FORMAT(6F8.3)
RETURN
END
```

FIGURE 2.5b Central programme for the
digital simulation of the
coupled-wave equations.

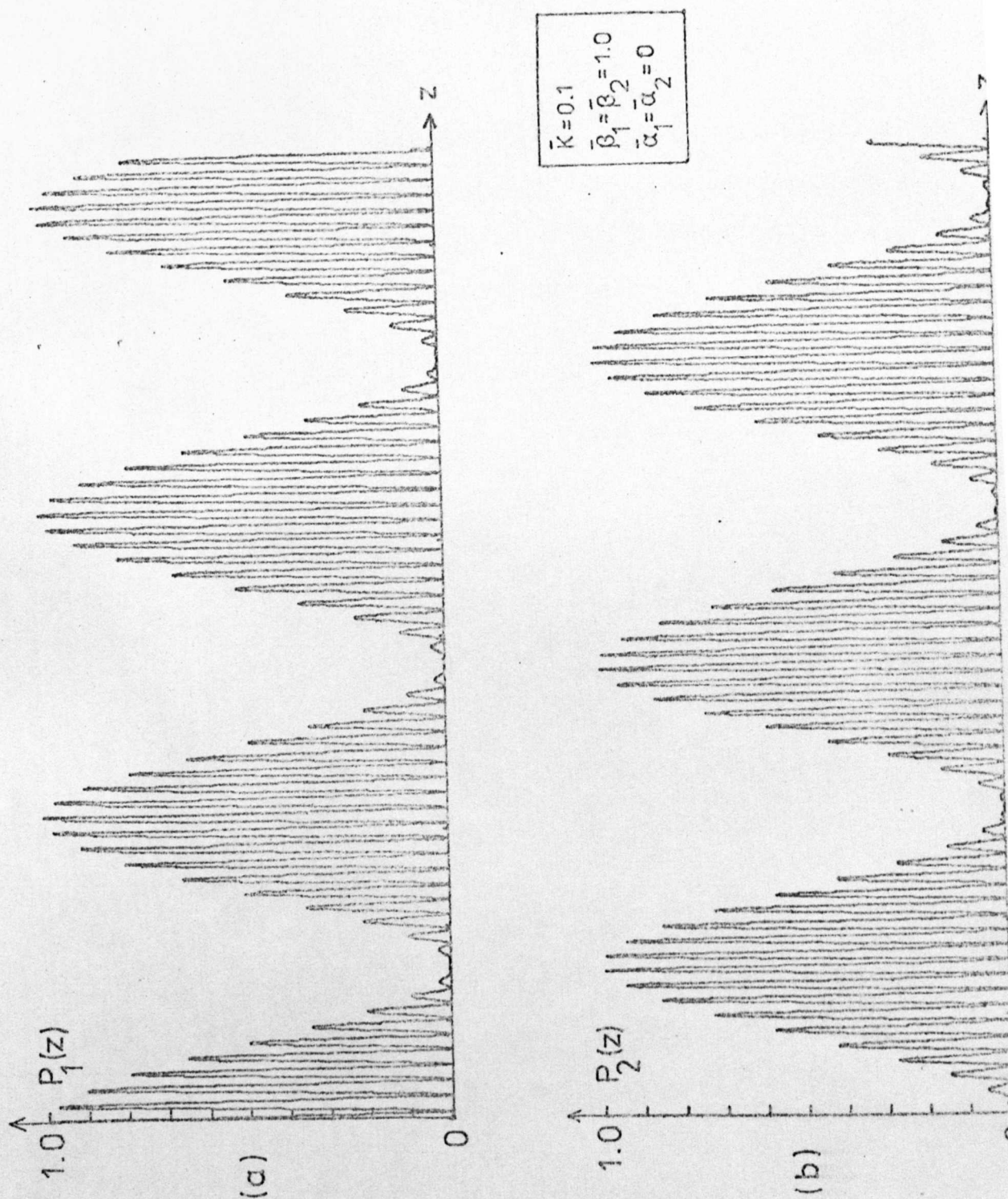


FIGURE 2.6 Digital simulation of the
coupled wave equations
- phase matched coupling.

Clearly a complete transfer of power from one guide to the other occurs in a distance dependent on the magnitude of the coupling coefficient,

$$L = \frac{\bar{\beta}_1 \Pi}{\bar{K} 2} = \frac{\Pi}{2\bar{K}} \quad 2.61$$

(c) With the introduction of a phase mismatch, $\beta_1 \neq \beta_2$, the power transfer becomes incomplete from the driven to the coupled line, and the beat length, L , decreases from the matched case. In Figure 2.7 a & b the simulation results for $\bar{\beta}_1 = 1$, $\bar{\beta}_2 = 0.8$ and $\bar{K} = 0.1$ are shown.

(d) The simulation technique is particularly useful in that any combination of loss, mismatch and coupling coefficient may be modelled without resorting to complex analytical methods. In Figure 2.8a & b we show the simulation results for the situation where

$$\begin{array}{lll} \bar{E}_1(0) = 1 & \bar{\beta}_1 = 1 & \bar{\alpha}_1 = 0.02 \\ \bar{E}_2(0) = 0 & \bar{\beta}_2 = 0.8 & \bar{\alpha}_2 = 0.22 \\ \bar{K} = 0.1 & & \end{array}$$

as investigated by Miller.⁵³ Close examination of this result and that shown in Figures 23 and 24 in reference 53, for $\frac{\bar{\alpha}_2 - \bar{\alpha}_1}{\bar{K}} = 2$, indicates complete agreement.

It can be seen that many diverse situations can be studied by this technique, which could be extended to cover lossy coupling (κ having a real component) and the coupling of more than two modes or waveguide systems, such as the Aueracher coupler.⁸²

2.7.2 Analytical solution of the coupled wave equations.

Taking the Laplace Transform of equation 2.58 and retaining the matrix notation gives

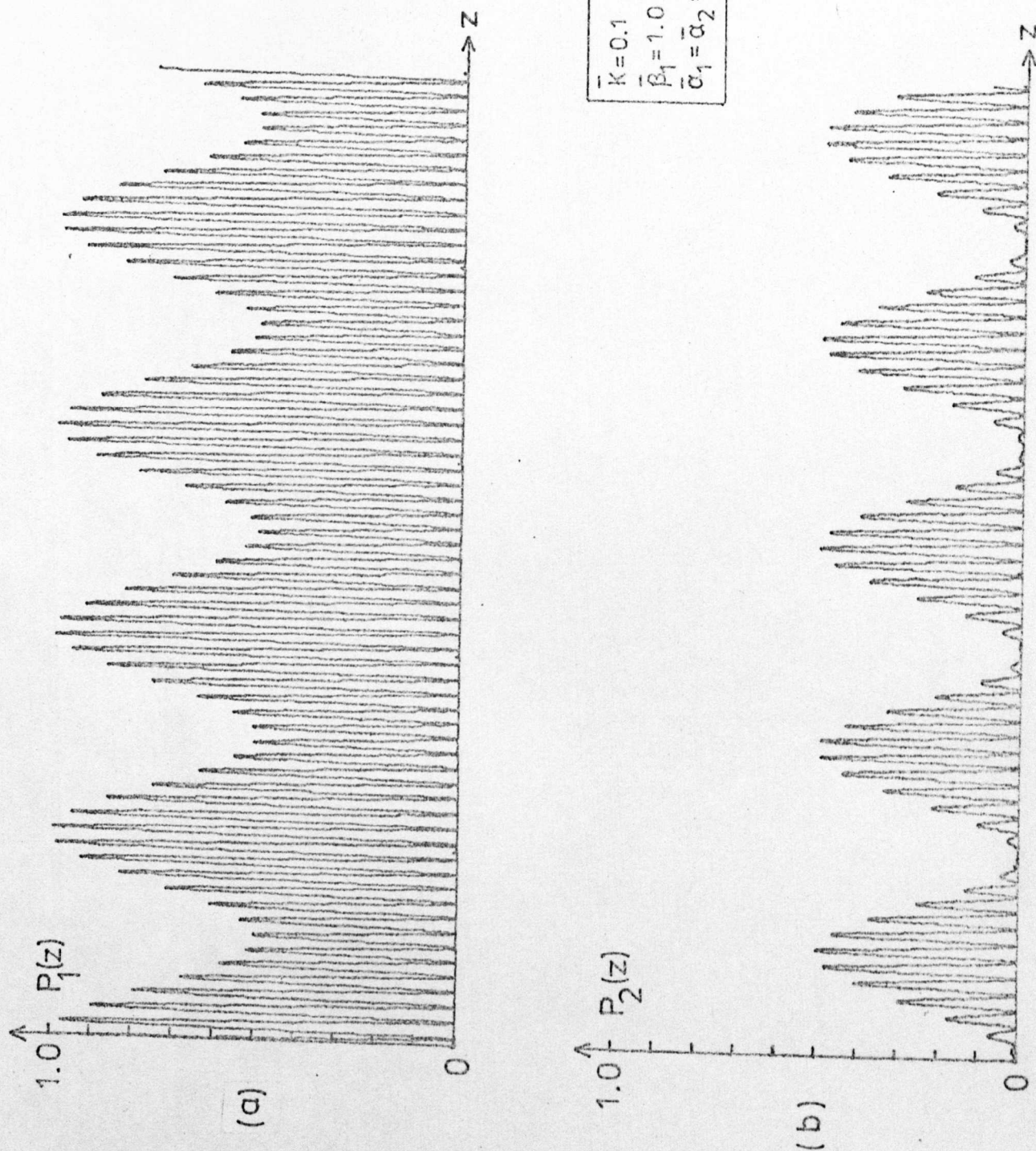


FIGURE 2.7 Digital simulation of the coupled wave equations with phase mismatch.

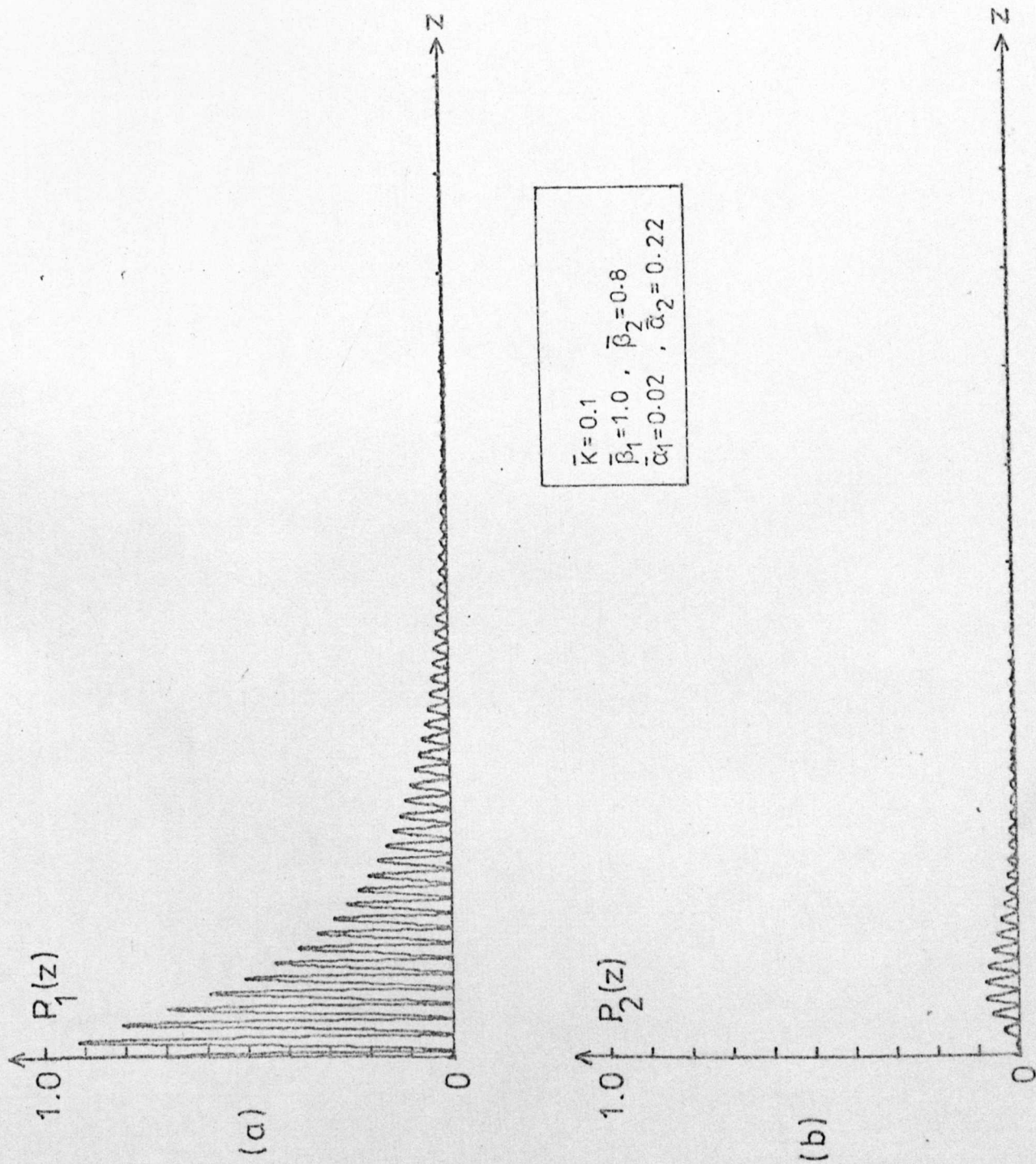


FIGURE 2.8 Digital simulation; coupling with
phase mismatch and
differential loss.

$$\begin{bmatrix} sE_1(s) - E_1(0) \\ sE_2(s) - E_2(0) \end{bmatrix} = \begin{bmatrix} -\gamma_1 & \kappa \\ \kappa & -\gamma_2 \end{bmatrix} \begin{bmatrix} E_1(s) \\ E_2(s) \end{bmatrix} \quad 2.62$$

Solving for $E_1(s)$ and $E_2(s)$ gives

$$(s-s_1)(s-s_2) \begin{bmatrix} E_1(s) \\ E_2(s) \end{bmatrix} = \begin{bmatrix} s + \gamma_2 & \kappa \\ \kappa & s + \gamma_1 \end{bmatrix} \begin{bmatrix} E_1(0) \\ E_2(0) \end{bmatrix} \quad 2.63$$

where

$$s_{1,2} = -\frac{1}{2}(\gamma_1 + \gamma_2) \pm \frac{1}{2}\sqrt{(\gamma_1 - \gamma_2)^2 + 4\kappa^2} \quad 2.64$$

where the upper and lower subscripts correspond to the upper and lower signs.

Taking the inverse Laplace transform of equation 2.63 gives

$$\begin{bmatrix} E_1(z) \\ E_2(z) \end{bmatrix} = (s_1 - s_2)^{-1} \begin{bmatrix} (\gamma_2 + s_1)e^{s_1 z} - (\gamma_2 + s_2)e^{s_2 z} & \kappa(e^{s_1 z} - e^{s_2 z}) \\ \kappa(e^{s_1 z} - e^{s_2 z}) & (\gamma_1 + s_1)e^{s_1 z} - (\gamma_1 + s_2)e^{s_2 z} \end{bmatrix} \begin{bmatrix} E_1(0) \\ E_2(0) \end{bmatrix} \quad 2.65$$

Equation 2.65 represents the most general solution of the coupled wave equations for reciprocal coupling. It may be seen from this equation that the propagation constants of the E_1 and E_2 waves in the coupling region are

$$\gamma_c^{\pm} = s_{1,2} = \frac{1}{2}(\gamma_1 + \gamma_2) \pm \kappa \sqrt{1 + \Delta} \quad 2.66$$

where

$$\Delta = \left(\frac{\gamma_1 - \gamma_2}{2\kappa} \right)^2 \quad 2.67$$

and that the beating effect of the coupled waves is due to the interference of the 'fast' mode γ_c^+ and the 'slow' mode γ_c^- .

For lossless coupling it follows from equation 2.66 that κ must be purely imaginary, or

$$\kappa = jK \quad 2.68$$

Substituting equation 2.68 into equation 2.65, with the initial conditions

$$\begin{aligned} E_1(0) &= E_1(0) \\ E_2(0) &= 0 \end{aligned} \quad 2.69$$

gives

$$P_1(z) = |E_1(z)|^2 = P_1(0) \left| \cos K \sqrt{1+\Delta} z - j \sqrt{\frac{\Delta}{1+\Delta}} \sin K \sqrt{1+\Delta} z \right|^2 \quad 2.70$$

$$P_2(z) = |E_2(z)|^2 = P_1(0) \left| \frac{j}{\sqrt{1+\Delta}} \sin K \sqrt{1+\Delta} z \right|^2 \quad 2.71$$

The term $\exp(-\frac{1}{2}(\gamma_1 + \gamma_2)z)$ is omitted from the latter equations as having no additional contribution to the relative power variation in the coupling region.

It follows from equations 2.70 and 2.71 that

$$\begin{aligned} P_1(z) + P_2(z) &= P_1(0) \left[\cos^2 K \sqrt{1+\Delta} z + \sin^2 K \sqrt{1+\Delta} z \left(\frac{\Delta}{1+\Delta} + \frac{1}{1+\Delta} \right) \right] \\ &= P_1(0) \end{aligned} \quad 2.72$$

and that conservation of energy is maintained.

2.7.3 Discussion of the analytic solution and comparison with the digital simulation.

Throughout this discussion it is assumed that the coupling is non-dissipative and that κ is purely imaginary. The solution is dependent on the parameter Δ defined in equation 2.67. As stated in equation 2.59 the propagation constants consist of real (attenuation) and imaginary (phase) parts and

$$(\gamma_1 - \gamma_2) = \Gamma_1 - \Gamma_2 = (\alpha_1 - \alpha_2) + j(\beta_1 - \beta_2) \quad 2.73$$

Thus

$$= \frac{((\alpha_1 - \alpha_2) + j(\beta_1 - \beta_2))^2}{4\kappa^2} \quad 2.74$$

Let us now compare and contrast the analytic and simulated solutions for the cases (b) - (d) on page 28. Situation (a) is trivial,

where the waves E_1 and E_2 are decoupled.

(b) With $\alpha_1 = \alpha_2 = 0$ and $\beta_1 = \beta_2$ equation 2.74 becomes

$$\Delta = 0$$

and the solutions for the coupling of two degenerate modes in lossless waveguides become, from equations 2.70 and 2.71

$$P_1(z) = P_1(0) \cos^2 Kz \quad 2.75$$

$$P_2(z) = P(0) \sin^2 Kz \quad 2.76$$

A complete spatially periodic power transfer between 1 and 2 takes place with period

$$\left. \begin{array}{l} L \\ \Delta = 0 \end{array} \right| = \frac{\pi}{2K} \quad 2.77$$

This solution corresponds to the simulation output of Figure 2.6a & b.

(c) Introducing the phase mismatch, $\beta_1 \neq \beta_2$, with $\alpha_1 = \alpha_2 \approx 0$ reveals

$$\Delta = \left[\frac{\beta_1 - \beta_2}{2K} \right]^2 \quad 2.78$$

The periodicity of the power transfer decreases, and from equation 2.71

$$\left. \begin{array}{l} L \\ \beta_1 \neq \beta_2 \\ \alpha_1 = \alpha_2 = 0 \end{array} \right| = \frac{\pi}{2K [1 + \Delta]^{\frac{1}{2}}} \quad 2.79$$

The ratio of the coupling length for this case to the ideal case of (b) is

$$[1 + \Delta]^{-\frac{1}{2}} \quad 2.80$$

The maximum attainable power transfer efficiency from 1 to 2 occurs

where

$$K \sqrt{1 + \Delta} z = \frac{\pi}{2}$$

and is, in this case

$$\hat{\eta}_{\alpha_1=\alpha_2=0, \beta_1 \neq \beta_2} = (1 + \Delta)^{-1} \quad 2.81$$

As the output of the corresponding simulation shows (Figure 2.7a & b), for a given mismatch and coupling coefficient the transfer efficiency falls below unity and the frequency of the power oscillations increases.

Equations 2.80 and 2.81 are most important for the analysis of practical couplers where, for the short interaction lengths envisaged, $\alpha_1 = \alpha_2 \approx 0$, and the critical factor affecting the performance is the phase mismatch of the constituent guides.

(d) The analysis of a coupling system with both differential loss and phase characteristics has been tackled in detail by Miller.⁵³ There are three basic situations: equal loss ($\alpha_1 = \alpha_2$) and positive and negative differential loss, or coupling to a less lossy line or to a more lossy line. Substitution of the particular situation into equations 2.74, 2.70 and 2.71 reveals the desired analytic solution which has been shown to produce the equivalent results to the simulation output.

2.7.4 Conclusions.

It may be concluded that there are two equivalent approaches to obtain the theoretical solution of the coupled wave equations, namely by a straightforward simulation of the coupled differential equations or by an analytic formulation. The results of each have been correlated by presenting examples of coupled wave responses for different combinations of the complex propagation constants and coupling coefficient.

The parameter of most interest is the coupling coefficient K , as yet undefined in a physical context, and it will be the purpose of the following sections to determine its magnitude and to predict the response of a practical coupler via equations 2.70 and 2.71. Three methods of doing so are explored - the wave approach, the ray approach, and the direct approach - and each are presented in turn.

2.8 The Coupling Coefficient - Wave Approach.

The wave approach has been used by many authors to determine the coupling coefficient. A most general method was developed by Arnaud³³ using the Lorentz reciprocity theorem, applicable to the coupling of dielectric waveguides of arbitrary shape and refractive index distribution, and with or without loss. Marcuse⁸⁴ approached the problem from a slightly different viewpoint and obtained a coupling coefficient by means of a perturbation theory. The results of both methods were found to be identical for lossless waveguides, and can be summarized for the coupling of degenerate TE modes in dissimilar slabs as

$$K^2 = \frac{(\beta^2 - k_{n_0}^2)}{\beta^2} \cdot \frac{E_1^2 \cdot E_2^2}{\int_{-\infty}^{\infty} E_1^2 dx \int_{-\infty}^{\infty} E_2^2 dx} \quad 2.82$$

$$k = \frac{2\pi}{\lambda}$$

where E_1 and E_2 are the transverse components of the electric field in the isolated guides, evaluated at the same point between the guides.

It should be noted that equation 2.82 could be thought of as the geometric mean of two "self-coupling" coefficients K_1 and K_2 where

$$K_1 = \frac{(\beta^2 - k_{n_0}^2)^{1/2}}{\beta} \cdot \frac{E_1^2}{\int_{-\infty}^{\infty} E_1^2 dx} \quad 2.83$$

$$K_2 = \frac{(\beta^2 - k_0^2 n_0^2)^{1/2}}{\beta} \cdot \frac{E_2^2}{\int_{-\infty}^{\infty} E_2^2 dx} \quad 2.84$$

and

$$K = \sqrt{K_1 K_2} \quad 2.85$$

Both Arnaud and Marcuse continue by developing an expression for the coupling of identical asymmetrical slabs and find^{33,84} in our notation

$$K = \frac{2k_0 \exp(-ck_0)}{\beta(b + \frac{1}{k_0} + \frac{1}{k_2})(1 + (\frac{k_0}{k_1})^2)} \quad 2.86$$

where b is the thickness of a slab, refractive index n_1 embedded in media of lower refractive index, n_0, n_2 . The guides are separated by a distance ' c '. Equivalent statements have been given by Kapany, firstly² using a perturbation method analagous to that of Marcuse, and secondly⁷² from considerations of the eigenvalues associated with the symmetric and antisymmetric modes of a coupled system. Hsu,⁸⁵

in a very complete analysis, developed a similar expression for the coupling coefficient of a block coupler comprising two asymmetric slab waveguides, and Wilson and Reinhart⁸⁶ presented the solution of the general five-layer slab structure. Examination of equation 21 of reference 86 again indicates that the overall coupling coefficient can be formulated by treating each component waveguide separately, as found in equations 2.83 - 2.85 above. The complete expression for the coupling coefficient of degenerate TE modes in the general five-layer slab structure shown in Figure 2.9 is, by the wave approach:

$$K = \frac{2k_0 \exp(-ck_0)}{\beta} \left[b_1^e b_3^e \left(1 + \left(\frac{k_0}{k_1} \right)^2 \right) \left(1 + \left(\frac{k_0}{k_3} \right)^2 \right) \right]^{-1/2} \quad 2.87$$

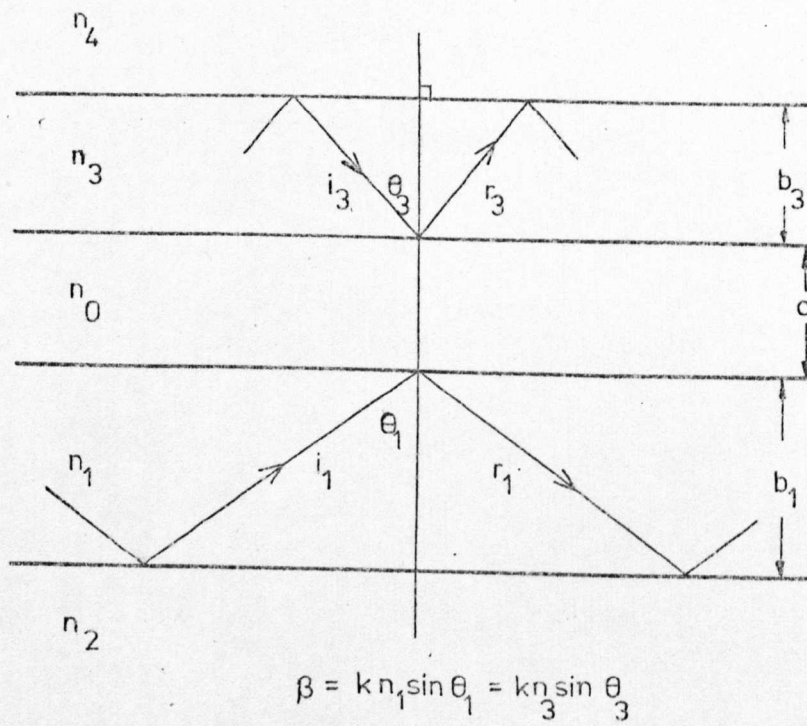


FIGURE 2.9 General phase-matched
five-layer slab coupler.

where

$$\begin{aligned} k_1^2 &= k_{n_1}^2 - \beta^2 & k_2^2 &= \beta^2 - k_{n_2}^2 \\ k_3^2 &= k_{n_3}^2 - \beta^2 & k_4^2 &= \beta^2 - k_{n_4}^2 \end{aligned} \quad 2.88 \quad \begin{pmatrix} a & b \\ c & d \end{pmatrix}$$

$$b_1^e = \text{effective thickness guide 1} = b_1 + \frac{1}{k_0} + \frac{1}{k_2} \quad 2.89 \text{ a}$$

$$b_3^e = \text{effective thickness guide 3} = b_3 + \frac{1}{k_0} + \frac{1}{k_4} \quad 2.89 \text{ b}$$

For identical asymmetric slabs, $k_1 \equiv k_3$ and $b_1^e = b_3^e$, and equation 2.87 reduces to equation 2.86.

For identical symmetric slabs, $k_2 \equiv k_0$ and $b^e = b + \frac{2}{k_0}$

Marcatili²⁰ also develops an expression for K for the coupling of two identical slabs, the result of which is identical in form to equation 2.86 except the effective thickness $(b + \frac{1}{k_0} + \frac{1}{k_2})$ is replaced by the thickness b . This discrepancy is a result of the closed form approximation, equations 2.37 and 2.38, and a consequence of ignoring the effective penetrations of the ray in the zig-zag model, due to the lateral displacements of the reflecting wavefronts by the Goos-Hanchen shift.^{78,87} Kogelnik and Weber⁸⁸ have shown these penetrations to be $\frac{1}{k_0}$ at the n_1/n_0 interface and $\frac{1}{k_2}$ at the n_1/n_2 interface. Marcatili's approximations may allow adequate prediction of the mode propagation characteristics of rectangular fibres, but it can be seen that his expression for the coupling coefficient is inaccurate over the entire range of $\frac{b}{k}$ by a factor

$$\left(1 + \frac{1}{k_0 b} + \frac{1}{k_2 b}\right)^{-1}$$

The correct expression may be obtained by introducing the effective thickness in the direction of the field overlap. Even though the topic of effective thickness in directional couplers has been discussed by Gedeon⁸⁹ and Kapany and Burke,⁷² many authors use the

unmodified expression for the coupling coefficient developed by Marcatili.

The wave-theory result of Arnaud³³ and Marcuse⁸⁴ has been applied to a variety of structures in different situations,^{90,91} and represents the most general formulation of the coupling coefficient. In many cases, however, the wave propagation may be described in terms of a ray optics model and it would be instructive to develop an intuitive picture of the coupling on that basis. The chapter continues by developing, from first principles, the coupling coefficient for a general five-layer slab waveguide structure using a ray-optics approach.

2.9 The Coupling Coefficient - Ray Optics Approach.

We desire to know what happens when the modes of two slab waveguides interact in a directional coupler configuration and if possible to derive a theoretical model using the simple ray-optics approach. The general five-layer slab structure will be considered and the procedure is as follows. Firstly a scattering matrix is constructed for the tunnelling layer using the derived Fresnel formulas for the complex reflection and transmission coefficients for an incident plane wavefront. The phase considerations for each composite waveguide are then introduced to produce an eigenvalue equation for the complete structure. A perturbation analysis finally reveals the coupling coefficient.

2.9.1 The scattering matrix.

In Appendix 2.1 the Fresnel equations are developed and the normalized scattering matrix for the tunnelling layer is derived.⁹² Stating the major results:

$$\begin{bmatrix} r_1 \\ r_3 \end{bmatrix} = (1 - u^2 r_{10} r_{30})^{-1} \begin{bmatrix} r_{10} - u^2 r_{30} & u(1-r_{10}^2)^{\frac{1}{2}}(1-r_{30}^2)^{\frac{1}{2}} \\ u(1-r_{10}^2)^{\frac{1}{2}}(1-r_{30}^2)^{\frac{1}{2}} & r_{30} - u^2 r_{10} \end{bmatrix} \begin{bmatrix} i_1 \\ i_3 \end{bmatrix} \quad 2.90$$

where r_1, r_3 and i_1, i_3 are the reflected and incident waves at the tunnelling layer (Figure 2.9) and

$$r_{mn} = \exp(-j2\phi_{mn}) = \exp(j2 \tan^{-1} \xi \frac{k_n}{k_m}) \quad 2.91$$

$$u = \exp(-ck_0) \quad 2.92$$

2.9.2 New eigenvalue equation.

If the reflections at the n_1/n_2 and n_3/n_4 boundaries are now introduced and the eigenvalue equations of the form of equation 2.4 are invoked for each waveguide,

$$2k_1 b_1 - 2\phi_{10} - 2\phi_{12} = 2m_1 \Pi \quad 2.93$$

$$2k_3 b_3 - 2\phi_{30} - 2\phi_{34} = 2m_3 \Pi \quad 2.94$$

m_1 and m_3 are integers.

With

$$r_1 = i_1 \exp(j2\phi_{10}) = i_1 \exp(j2k_1 b_1 - j2\phi_{12}) \cdot \exp(-j2m_1 \Pi) \quad 2.95$$

$$r_3 = i_3 \exp(j2\phi_{30}) = i_3 \exp(j2k_3 b_3 - j2\phi_{34}) \cdot \exp(-j2m_3 \Pi) \quad 2.96$$

and since

$$\exp(j2m\Pi) = 1 \quad 2.97$$

we find

$$r_1 = i_1 \exp(j2k_1 b_1 - 2\phi_{12}) = i_1 \phi_1 \quad 2.98$$

$$r_3 = i_3 \exp(j2k_3 b_3 - 2\phi_{34}) = i_3 \phi_3 \quad 2.99$$

Substituting into the LHS of equation 2.90 and expanding gives

$$i_{11}^{\phi} = \frac{r_{10}^{-u^2} r_{30}}{1-u^2 r_{10} r_{30}} i_1 + \frac{u(1-r_{10}^2)^{\frac{1}{2}}(1-r_{30}^2)^{\frac{1}{2}}}{1-u^2 r_{10} r_{30}} i_3 \quad 2.100$$

$$i_{33}^{\phi} = \frac{r_{30}^{-u^2} r_{10}}{1-u^2 r_{10} r_{30}} i_3 + \frac{u(1-r_{10}^2)^{\frac{1}{2}}(1-r_{30}^2)^{\frac{1}{2}}}{1-u^2 r_{10} r_{30}} i_1 \quad 2.101$$

Rearranging each equation and cross-multiplying yields

$$\left[\phi_1 - \frac{r_{10}^{-u^2} r_{30}}{1-u^2 r_{10} r_{30}} \right] \left[\phi_3 - \frac{r_{30}^{-u^2} r_{10}}{1-u^2 r_{10} r_{30}} \right] = \frac{u^2 (1-r_{10}^2) (1-r_{30}^2)}{1-u^2 r_{10} r_{30}} \quad 2.102$$

Equation 2.102 represents the eigenvalue equation for the composite waveguide.

2.9.3 Perturbation.

Let us now ignore terms in u^2 as being insignificant, giving

$$(1-\phi_1 r_{10}^{-1}) (1-\phi_3 r_{30}^{-1}) = u(r_{10}^{-1} - r_{10}) \cdot u(r_{30}^{-1} - r_{30}) \quad 2.103$$

Reverting to the exponential notation of equations 2.98, 2.99 and 2.91

we find

$$\phi_1 r_{10}^{-1} = \exp(j(2k_1 b_1 - 2\phi_{10} - 2\phi_{12})) = \exp(jD_1) \quad 2.104$$

$$\phi_3 r_{30}^{-1} = \exp(j(2k_3 b_3 - 2\phi_{30} - 2\phi_{34})) = \exp(jD_3) \quad 2.105$$

and

$$\begin{aligned} r_{10}^{-1} - r_{10} &= -2j \sin 2\phi_{10} \\ r_{30}^{-1} - r_{30} &= -2j \sin 2\phi_{30} \end{aligned} \quad \left. \begin{array}{l}) \\) \\) \end{array} \right\} \quad 2.106$$

Substituting equations 2.104 - 2.106 into 2.104 gives

$$(1-\exp(jD_1)) (1-\exp(jD_3)) = -4u^2 \sin 2\phi_{10} \cdot \sin 2\phi_{30} \quad 2.107$$

Let us define terms F_1 and F_3 such that

$$\begin{aligned} F_1 &= 1 - \exp(jD_1) \\ F_3 &= 1 - \exp(jD_3) \end{aligned} \quad \left. \begin{array}{l}) \\) \\) \end{array} \right\} \quad 2.108$$

Since any phase mismatch can be accounted for in the coupled wave solutions of equations 2.70 and 2.71, no loss of generality is incurred in allowing the guides 1 and 3 to be initially phase matched. For the unperturbed situation, that is where there is no coupling

$$D_1(\beta_0) = D_3(\beta_0) = 2m\pi$$

and consequently

$$F_1(\beta_0) = F_3(\beta_0) = 0$$

If the perturbation about $F_1 = F_3 = 0$ is considered where $\beta \rightarrow \beta_0 + \Delta\beta$, we find

$$1 - \exp(jD_1) = F_1 + \Delta F_1 = \Delta F_1$$

$$1 - \exp(jD_3) = F_3 + \Delta F_3 = \Delta F_3$$

and equation 2.107 becomes

$$\Delta F_1 \Delta F_3 = -4u^2 \sin 2\phi_{10} \sin 2\phi_{30} \quad 2.109$$

It remains to express ΔF_1 and ΔF_3 in terms of $\Delta\beta$

We have, for TE modes,

$$\Delta F_1 = \frac{dF_1}{d\beta} \Delta\beta = -j \frac{dD_1}{d\beta} \Delta\beta = -j \frac{2\beta_0 b_1^\epsilon}{k_1} \Delta\beta \quad 2.110$$

$$\Delta F_3 = \frac{dF_3}{d\beta} \Delta\beta = -j \frac{dD_3}{d\beta} \Delta\beta = -j \frac{2\beta_0 b_3^\epsilon}{k_3} \Delta\beta \quad 2.111$$

Equation 2.109 becomes

$$\Delta\beta^2 = - \frac{4u^2 \sin 2\phi_{10} \sin 2\phi_{30}}{4\beta_0^2 b_1^\epsilon b_3^\epsilon} \cdot k_1 k_3 \quad 2.112$$

Now from equation 2.91, for TE modes,

$$\sin 2\phi_{10} = \frac{2 \frac{k_0}{k_1}}{\left(1 + \left(\frac{k_0}{k_1}\right)^2\right)}$$

$$\sin 2\phi_{30} = \frac{2 \frac{k_0}{k_3}}{\left(1 + \left(\frac{k_0}{k_3}\right)^2\right)}$$

the final answer becomes

$$\Delta\beta = j \frac{2k_0 \exp(-ck_0)}{\beta_0 \sqrt{(1 + (\frac{k_0}{k_1})^2) (1 + (\frac{k_0}{k_3})^2) b_1^{\epsilon} b_3^{\epsilon}}} \quad 2.113$$

The coupling coefficient is defined as $|\Delta\beta|$, and the result is in agreement with equation 2.87 derived by other authors using the wave approach. Repetition of the analysis to cover the case of TM modes will not be carried out.

The ray approach reveals the same result as the wave approach, though of course the method is limited to 'well-behaved' structures such as slabs or rectangular waveguides. Since propagation in the low-order modes of circular fibres cannot be defined in plane wave terms, extension of the technique to the coupling of dielectric cylinders is unlikely.

2.10 The Coupling Coefficient - The 'Direct' Method.

The evaluation of the coupling coefficient will now be attempted in a novel manner which has been coined the 'direct' approach merely to differentiate it from the ray and wave theories. In essence the method is to divide the calculation into two component parts, one dealing with the waveguiding characteristics through the steady-state eigenvalue equation, and the other with the field perturbation in the region of interest.

2.10.1 General approach.

If a waveguiding system with axial propagation constant β is perturbed by some effect, the amount of the disturbance $\delta\beta$ is given by

$$\delta\beta = \sum_r^N \frac{\partial\beta}{\partial\alpha_r} \delta\alpha_r \quad 2.114$$

where α_r is one of the N parameters on which β is dependent and which is also modified by the effect. Implicit, therefore, in the calculation of $\delta\beta$ is the unperturbed eigenvalue equation for the

waveguide:

$$\beta = f(\alpha_r, \alpha_{r+1}, \dots, \alpha_N)$$

The terms $\frac{d\beta}{d\alpha_r}$ for r to N are derived from this eigenvalue equation by differentiation, while the perturbation part of the analysis enters via the evaluation of $\delta\alpha_r$.

This most general statement of the theory is applicable to any phenomenon which perturbs the steady state condition of any waveguide.

2.10.2 General five-layer slab structure.

Let us now consider the case of a general five-layer slab waveguide coupler. Firstly, our experience of Section 2.8 tells us that it is sufficient to reduce the problem to two three-layer structures and evaluate the self-coupling coefficients. The overall coupling coefficient of two dissimilar, but degenerate, structures is the geometric mean of the two self-coupling coefficients (equations 2.85 and 2.87).

The unperturbed eigenvalue equation for a general asymmetrical slab waveguide is (equations 2.6 to 2.9);

$$k_1 b = \tan^{-1} \xi_{10} \frac{k_0}{k_1} + \tan^{-1} \xi_{12} \frac{k_2}{k_1} + m\pi \quad 2.115$$

It may be seen that the solution of β from this transcendental equation depends on the refractive indices of the three media, the guide thickness and the order and polarization of the mode. Therefore

$$\beta = f(k_0, k_1, k_2, b, m, \xi_{10}, \xi_{12}) \quad 2.116$$

For a constant thickness, mode order and polarization

$$\delta\beta = \frac{d\beta}{dk_0} \delta k_0 + \frac{d\beta}{dk_1} \delta k_1 + \frac{d\beta}{dk_2} \delta k_2 \quad 2.117$$

Let us choose evanescent field overlap in a tunnelling layer (region n_0) of thickness c . Equation 2.117 becomes

$$\delta\beta = \frac{d\beta}{dk_0} \delta k_0 = \frac{d\beta}{dn_0} \frac{dn_0}{dk_0} \delta k_0 \quad 2.118$$

since the coupling is assumed weak and the perturbation in regions 1 and 2 are small. Equation 2.118 is a restatement of equation 2.110 with $F \equiv k_0$

(i) evaluation of $\frac{d\beta}{dn_0}$

To obtain $\frac{d\beta}{dn_0}$ both sides of equation 2.115 are differentiated with respect to n_0 . In this instance we may recall the result of Tien,¹⁰⁷

$$\frac{d\beta}{dn_0} = \frac{k_0^2 n_0}{\beta^2 k_0 (1 + (\frac{k_0}{k_1})^2)} \quad 2.119$$

(ii) evaluation of the perturbation term δn_0

Since

$$k_0^2 = \beta^2 - k_1^2 n_0^2$$

we find

$$\frac{\delta n_0}{\delta k_0} = - \frac{k_0}{k_1^2 n_0} \quad 2.120$$

Examining the solution to the wave approach (equations 2.83 to 2.85)

it may be seen that the perturbation part of the derivation was given by

$$\delta\beta = \frac{E_{TOT}^2}{\int_{-\infty}^{\infty} E_{TOT}^2 dx} \quad 2.121$$

evaluated at the same point in the buffer region, $x = \frac{c}{2}$.

In this case, however, our interest lies in the field in the interguide zone only so

$$\delta k_0 = \frac{E_{BUFF}^2}{\int_0^{c/2} E_{BUFF}^2 dx} \quad \text{at } x = \frac{c}{2} \quad 2.122$$

Since

$$E_{\text{BUFF}} = E_0 \exp(-xk_0) \quad 2.123$$

equation 2.122 becomes

$$\delta k_0 = \frac{E_0^2 \exp(-ck_0)}{E_0^2 \left[-\frac{1}{2k_0} \exp(-2k_0 x) \right]_0^{\frac{c}{2}}} = \frac{2k_0 \exp(-ck_0)}{1 - \exp(-ck_0)} \quad 2.124$$

For $\exp(-ck_0) \ll 1$ - the weak coupling approximation - we have

$$\delta k_0 = 2k_0 \exp(-ck_0) \quad 2.125$$

Substitution of equations 2.125, 2.120 and 2.119 into equation 2.118 gives the value of the self-coupling coefficient,

$$\delta \beta = \frac{2k_0 \exp(-ck_0)}{\beta_b^E \left(1 + \left(\frac{k_0}{k_1} \right)^2 \right)} \quad 2.126$$

as before.

The direct approach is thought to be applicable to any waveguiding structure, and will be shown to be particularly useful for such structures as ion-exchanged thin film waveguides. The perturbation analysis is considerably simplified by considering only one section of the total field distribution.

2.11 Extension of the Slab Derivations to Rectangular Waveguides.

Up to this point the results have been presented for slab waveguides only. It is a simple matter to extend the theory to provide a solution for rectangular step-index waveguides. The first postulation is that the evanescent fields in one direction (say y) do not contribute to the coupling in the other direction (x). The second is that the form of the equation for the coupling coefficient for the slab waveguide holds in the direction of the couple. Referring to Figure 2.3, for field overlap in the x-direction (E^y modes) the coupling coefficient is

$$K_x = \frac{2k_0 \exp(-ck_0)}{\beta(b + \frac{1}{k_0} + \frac{1}{k_2})(1 + (\frac{k_0}{k_1})^2)} \quad 2.127$$

However, the terms k_0, k_1, k_2 here differ from the straight-forward slab waveguide values because

$$\begin{aligned} k_0^2 &= \beta_x^2 - k_{n_0}^2 \\ k_2^2 &= \beta_x^2 - k_{n_2}^2 \\ k_1^2 &= k_{n_1}^2 - \beta_x^2 \end{aligned}$$

Using equation 2.36 gives

$$\begin{aligned} k_0^2 &= \beta^2 - k_{n_0}^2 + (k_{n_1}^2 - \beta_y^2) = k_{0s}^2 + k_y^2 & a \\ k_1^2 &= k_{n_1}^2 - \beta^2 - (k_{n_1}^2 - \beta_y^2) = k_{1s}^2 - k_y^2 & b \\ k^2 &= \beta^2 - k_{n_2}^2 + (k_{n_1}^2 - \beta_y^2) = k_{2s}^2 + k_y^2 & c \\ \beta^2 &= \beta_s^2 - k_y^2 & d \end{aligned} \quad 2.128$$

Subscript 's' means the slab values of the variable (when the confinement in the y-direction is zero). k_y is the solution of an eigenvalue equation similar to equation 2.26. It should again be stressed that Marcatili's closed form solution for k_y is unsuitable for use in this context. Substituting equations 2.128 into 2.127 gives

$$K_x = \frac{2(k_{0s}^2 + k_y^2)^{\frac{1}{2}} \exp \left[-(k_{0s}^2 + k_y^2)^{\frac{1}{2}} c \right]}{(\beta_s^2 - k_y^2)^{\frac{1}{2}} \left[b + (k_{0s}^2 + k_y^2)^{-\frac{1}{2}} \right] \left(\frac{k_{1s}^2 + k_{0s}^2}{k_{1s}^2 - k_y^2} + (k_{2s}^2 + k_y^2)^{-\frac{1}{2}} \right)} \quad 2.129$$

k_y is the solution of

$$k_y a = m_y \pi + \tan^{-1} \left(\frac{n_1}{n_0} \right) \frac{k_{0s}}{k_y} + \tan^{-1} \left(\frac{n_1}{n_2} \right) \frac{k_{2s}}{k_1} \quad 2.130$$

Similar expressions hold for K_y (for E^x modes) but with obvious changes in notation. The analyses for K_x for E^x modes and K_y for E^y modes are similar and will be omitted.

In the cases dealt with in this thesis (Chapter 7), the well-guided fundamental transverse mode in a 4:1 aspect ratio guide was used. It is sufficient to set $k_y = 0$ in equation 2.129 and

use the slab waveguide result of equation 2.86.

2.12 Part II - Summary and Conclusions.

In Part II of this chapter, the coupled wave equations were presented and the analytic solution was compared with the direct computer simulation. The results of both were shown to be identical, and the use of the simulation technique was shown to be a powerful time and labour-saving tool to evaluate the coupling of waveguides with any combination of loss and mismatch. Next, the coupling coefficient was discussed and the results of other authors for the general five-layer step-index slab structure were compared with two solutions obtained by the ray optics and a direct method. The following conclusions may be drawn from this work. Firstly, the wave theories represent the most general method of obtaining the coupling coefficient, though the analysis may be cumbersome. The ray approach, while producing the same result as the published prediction, is only applicable to slab or rectangular waveguides, where a plane wave representation may be used. Finally the direct approach simplifies the calculation for slab guides since the perturbation in one region only is considered, though a more rigorous analysis will have to be carried out to test the generality of the method. The extension of the results to the case of rectangular and graded-index waveguides was discussed.

It may be generally concluded that the theoretical description of evanescent field coupling allows us to predict the performance of directional couplers for use in optical electronics.

APPENDIX 2.

A2.1 Derivation of the normalized scattering matrix of a waveguide tunnelling layer.

Consider the diagram of Figure A2.1. A_1 represents the normal to a plane wavefront impinging on the n_1/n_0 boundary, of a three-layer, lossless, isotropic configuration, with $n_1, n_3 > n_0$. B_1 is the reflected wave, A_2 is the evanescent wave in the buffer region of thickness 'c', and B_2 and B_3 are reflected and transmitted waves at the n_0/n_3 boundary respectively. The wave in n_0 decays by a factor

$$u = \exp(-ck_0) \quad \text{A.2.1}$$

across the width. The reflection coefficient r_{mn} , for TE waves (that is with no component of E in the z direction) is⁹³

$$r_{mn} = \frac{k_m - k_n}{k_m + k_n} \quad \text{A2.2}$$

Also the transmission coefficient t_{mn} is

$$t_{mn} = 1 - r_{mn} = \frac{2k_m}{k_m + k_n} \quad \text{A2.3}$$

If k_i ($i = m, n$) is associated with an evanescent wave then

$$k_i^2 = \beta^2 - k_{n_i}^2 \quad \text{A2.4}$$

and if a standing wave

$$k_i^2 = k_{n_i}^2 - \beta^2 \quad \text{A2.5}$$

where $\beta = kn_1 \sin \theta_1$ A2.6

Note from equation A2.2 that $r_{mn} = -r_{nm}$ and, since $\phi_{nm} = \tan^{-1} \frac{k_n}{k_m}$

$$r_{mn} = \exp(2j\phi_{mn}) \quad \text{A2.7}$$

From the fact that the transverse electric field E_y must be continuous we have

$$A_2 = A_1(1 + r_{10}) - B_2 r_{10} \quad \text{A2.8}$$

$$B_1 = A_1 r_{10} + B_2(1 - r_{10}) \quad \text{A2.9}$$

$$B_2 = -r_{30} A_2 u^2 \quad \text{A2.10}$$

$$B_3 = u A_2 (1 - r_{30}) \quad \text{A2.11}$$

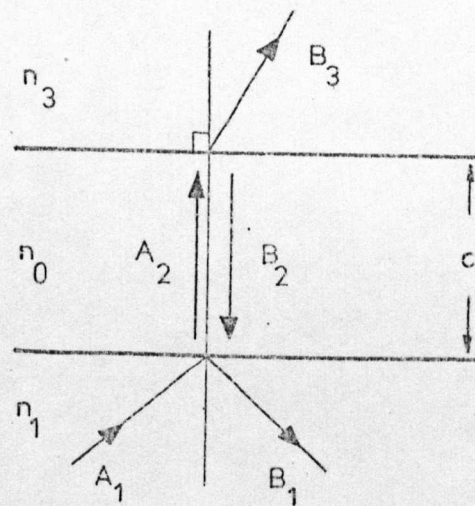


FIGURE A 2.1 Schematic representation of waves in a tunnelling region, with wave A_1 incident on the n_1/n_0 boundary.

Substituting A2.10 into A2.8 gives

$$-\frac{B_2}{r_{30}u^2} = A_1(1+r_{10}) - B_2r_{10} \quad A2.12$$

or

$$B_2 \frac{(r_{10}r_{30}u^2 - 1)}{r_{30}u^2} = A_1(1+r_{10}) \quad A2.13$$

Using equation A2.9 in the form

$$B_2 = \frac{(B_1 - A_1r_{10})}{(1-r_{10})}$$

gives,

$$(A_1r_{10} - B_1)(1-u^2r_{10}r_{30}) = A_1(1+r_{10})(1-r_{10})r_{30}u^2 \quad A2.14$$

Rearranging gives

$$R = \frac{B_1}{A_1} = r_{10} - \frac{(1+r_{10})(1-r_{10})r_{30}u^2}{(1-r_{10}r_{30}u^2)} \quad A2.15$$

Similarly substituting A2.10 into A2.8 gives

$$A_2 = \frac{(1+r_{10})A_1}{(1-r_{10}r_{30}u^2)} \quad A2.16$$

Substituting A_2 from equation A2.11 gives

$$\frac{(1+r_{10})}{(1-r_{10}r_{30}u^2)} A_1 = \frac{B_3}{u(1-r_{30})} \quad A2.17$$

$$T = \frac{B_3}{A_1} = \frac{u(1+r_{10})(1-r_{30})}{(1-r_{10}r_{30}u^2)} \quad A2.18$$

It can be seen that equations A2.15 and A2.18 are in complete agreement with the Fresnel equations⁷⁸

$$R = \frac{r_{10} + r_{03}u^2}{1 + r_{10}r_{03}u^2} \quad A2.19a$$

$$T = \frac{t_{30}t_{01}u}{1 + r_{10}r_{03}u^2} \quad A2.19b$$

It is clear that a wave impinging on the n_3/n_0 interface would produce similar results but with obvious changes in subscripts.

In matrix notation we obtain

$$\begin{bmatrix} r_1 \\ r_3 \end{bmatrix} = (1 - u^2 r_{10} r_{30})^{-1} \begin{bmatrix} r_{10} - u^2 r_{30} & u(1 + r_{30})(1 - r_{10}) \\ u(1 + r_{10})(1 - r_{30}) & r_{30} - u^2 r_{10} \end{bmatrix} \begin{bmatrix} i_1 \\ i_3 \end{bmatrix} \quad \text{A2.20a}$$

where the waves incident on the tunnelling layer from each side are of amplitude i_1 and i_3 , and the corresponding reflected waves are r_1 and r_3 . In shorthand

$$\begin{bmatrix} r_1 \\ r_3 \end{bmatrix} = \begin{bmatrix} s_{11} & s_{13} \\ s_{31} & s_{33} \end{bmatrix} \begin{bmatrix} i_1 \\ i_3 \end{bmatrix} \quad \text{A2.20b}$$

Consider the s_{31} element of this matrix. It represents the ratio of the electric field amplitude in region 3 to the field amplitude of the incident wave in region 1. The fraction of energy incident in region 1 that ends up in region 3 is the TRANSMITTANCE, given as⁹³

$$T = \frac{k_3}{k_1} |T|^2 \quad \text{A2.21}$$

To normalise the matrix, the off-diagonal elements must be multiplied by the factors $\sqrt{\frac{k_1}{k_3}}$ (for s_{13}) and $\sqrt{\frac{k_3}{k_1}}$ (for s_{31}). Using equation A2.2

$$\sqrt{\frac{k_3}{k_1}} = \frac{\sqrt{\frac{k_3}{k_0}}}{\sqrt{\frac{k_1}{k_0}}} = \sqrt{\frac{(1 + r_{30})(1 - r_{10})}{(1 - r_{30})(1 + r_{10})}} \quad \text{A2.22}$$

Such a procedure is customary using a scattering matrix approach⁹⁴ where the normalised voltages and currents are used.

Substituting the normalisation factors into the matrix gives

$$S = (1 - u^2 r_{10} r_{30})^{-1} \begin{bmatrix} r_{10}^{-u^2} r_{30} & u(1 - r_{10}^2)^{\frac{1}{2}} (1 - r_{30}^2)^{\frac{1}{2}} \\ u(1 - r_{10}^2)^{\frac{1}{2}} (1 - r_{30}^2)^{\frac{1}{2}} & r_{30}^{-u^2} r_{10} \end{bmatrix} \quad \text{A2.23}$$

as the normalised scattering matrix for the tunnelling layer.

3.1 General Introduction.

With the realization of ultra low-loss optical fibre waveguides,⁷ the need for highly-efficient connections to and from the thin film terminal circuits becomes acute. Multimode step- and graded-index fibres or single-mode fibres⁵² appear to be the most likely candidates for the optical data highway and each has its own particular advantages in this capacity. However, in terms of coupling to planar waveguides, all have their difficulties. The single-mode fibre does not lend itself to codirectional coupling because of the difficulty of physical alignment. Butt jointing multimode fibres and thin film waveguides also presents an inherent mismatch because of the discrepancy in the waveguide profiles, and generally the codirectional coupling of films and fibres has been unsuccessful.

An alternative method of coupling two guiding structures is by the transverse interaction of the evanescent wave of one guide with the other when the two are placed in close proximity. Irrespective of the component waveguide geometries, directional coupling will take place along the interaction region provided there is a good phase velocity match between the coupled modes and the polarization characteristics are correct. Such a proposal was first put forward by S.E. Miller,⁵³ for the microwave case, in 1954.

However, in all fibre optical waveguides of circular geometry, whether single- or multimode, a cladding material, usually of glass, is provided to protect the surface of the core region, such that the scattering loss caused by external contamination is eliminated. At the cladding/air interface the evanescent field of the guided core mode is very nearly zero, and, because of this necessary design

condition, the clad fibre does not lend itself readily to evanescent field coupling.

In this chapter methods will be described of modifying the cladding material of circular fibres to facilitate transverse coupling. An example of coupling to a multimode fibre at a region of cladding modification will also be presented.

3.2 Modification of Cladding Glass by Silver/sodium Ion Exchange.

3.2.1 Underlying philosophy.

This method of modifying the cladding glass of circular clad fibre waveguides was first proposed by Laybourn and Wilkinson.⁵⁴ The principle of the method is to chemically alter the density of the cladding material and thereby raise its refractive index. The core material is chosen as to be unaffected by the process. The guided core mode enters the cladding whenever the effective refractive index of the guided mode becomes less than the refractive index of the chemically adjusted cladding at the effective core/cladding interface. The fields become evanescent outwards from the cladding/air interface and are available for transverse coupling to other structures or similarly-treated fibres.

The process used to modify the cladding material is one where cations of the glass (Na^+ in the case of soda-lime glass) are exchanged with heavier cations of a diffusant present in a mobile form in a molten salt (Ag^+ in silver nitrate) outside the fibre. Ag^+ ions drift into the cladding glass due to the concentration gradient and replace Na^+ ions in the glass lattice.⁵⁵

3.2.2 The refractive index profile of a treated cladding.

The refractive index profile follows the gradient of the relative density of the material. Clearly the nature of the profile and its dependence on the melt temperature and time of diffusion are important.

Mr. George Stewart of this department has carried out an extensive study into the diffusion of silver ions into soda-lime glass slabs (Chance microscope slides) using a non-destructive optical technique⁵⁶ which requires measurement of the surface refractive index of the diffused samples, n_s , and the effective refractive indices of the modes of the waveguide, n_{e_m} . It has been discovered using this technique that the refractive index profile follows a quadratic variation with depth, x , into the host glass as

$$n(x) = n_s - \Delta \left[\left(\frac{x}{d_d} \right) + f \left(\frac{x}{d_d} \right)^2 \right] \quad 3.1$$

where

$$\Delta = n_s - n_2 = 1.605 - 1.513 = 0.092$$

$$\text{and } f = 0.64$$

d_d is a constant, the value of which depends on the melt temperature and the diffusion time. The graph of $n(x)$ against (x/d_d) is shown in figure 7.2. It has been shown in the same work that the parameter d_d (in microns) is dependent on the diffusion time t (in minutes) and the melt temperature T (in degrees Kelvin) by

$$d_d = 1.19 \times 10^4 t^{1/2} \exp \left[\frac{-1.02 \times 10^4}{2T} \right] \quad 3.2$$

The nature of the diffusion profile for any set of fabrication parameters t and T may be obtained from equations 3.1 and 3.2. The theory outlined here is expanded in section 7.2 which deals in part with the waveguiding properties of ion-exchanged slab waveguides.

The refractive index profile resulting from Ag^+ diffusion into a circular fibre will not be as straightforward as equation 3.1 due to the different geometry, and the effect of the diffusion barrier at the core/cladding interface is unknown.

3.2.3 Preliminary results.

Experiments indicate⁵⁷ that cladding modification using ion exchange is possible, and that for relatively large fibres, equations 3.1 and 3.2 describe the resulting refractive index change. Some

preliminary diffusions into a liquid core[†]/soda lime glass fibre of dimensions 43 μm core diameter and 50 μm overall diameter for 180 minutes at 350°C have successfully demonstrated⁵⁷ that light may be transversely coupled into and out of the core modes of a clad fibre at a region of cladding modified by ion exchange.

3.3 Removal of Cladding Glass by Acid Etching.

3.3.1 Introduction.

In this section a method is described of removing the cladding glass of step-index circular fibres by means of a hydrofluoric acid etch bath, and for the monitoring of the progress of the etch through the core/cladding interface. A similar approach could be used in the general case of removal of a cladding by chemical dissolution or other means; for example the treatment of polymer-clad silica fibre⁵⁸ in an organic solvent bath.

3.3.2 The materials used.

The fibres used in the experiments were machine-drawn at 800°C from a preform consisting of a core glass (Schott, LF5, 1cm diameter, refractive index before pulling = 1.5814 at 589 nm) and a glass cladding (soda-lime glass, inner diameter = 1.1 cm, outer diameter = 1.4 cm, refractive index before pulling = 1.517 at 589 nm). Compaction effects⁵⁹ reduced the refractive indices of the glasses on pulling by a percentage dependent on the glass composition. A typical value for this reduction was found to be -0.4% but could be restored to the bulk value by annealing at 500°C. However, this process was not carried out, and experimental estimates based on mode-angle and Abbé refractometer measurements gave refractive indices at the working wavelength of 633nm of $n_{\text{core}} = 1.577$ and $n_{\text{cladding}} = 1.513$.

[†] Methyl salicylate ($n_D = 1.522$)

The etchant used was buffered hydrofluoric acid having a measured etch rate in soda-lime glass slabs of $2\mu\text{m}/\text{minute}$. Neither the soda-lime glass nor the LF5 core glass suffered significant surface damage subsequent to the action of the acid, although areas of the glass exposed to HF vapour immediately above the surface of the liquid were severely pitted. This problem could have been eliminated by masking the areas where etching was not desired with a perspex film, deposited from an organic solvent solution.

3.3.3 Monitoring the progress of the etch.

The progress of the etch through the fibre was monitored in the following manner. Light was focused into the matched end of the fibre. Any cladding modes were subsequently stripped using a high-index prism clamped to the outer cladding, ensuring that all of the energy was confined to the core. The fibre was then placed in the etch bath and the light output was measured using a photodiode. As the etch progressed through the cladding, little change in the output of the fibre was noted. When the acid encountered the core/cladding junction, the level of scattering from the core increased with an accompanying drop in the fibre output. At this point the fibre was removed from the bath and washed in running water to eliminate excess acid. The apparatus constructed for the purpose of producing an acid-etched region in an unbroken length of clad fibre is shown in Figure 3.1. Laser light was used, though in practice any coherent or incoherent source is suitable for the monitoring procedure. The launching and exit cells were similar to those used by Dakin et al.⁶⁰ The BPY13 photodiode was connected via the biasing chain to a Bryans Southern Instruments' x': time chart recorder. The etch cell, detailed in inset of Figure 3.1, utilized the meniscus of the HF bath and provided an etched length roughly equal to the well diameter, if no masking was provided on the fibre.

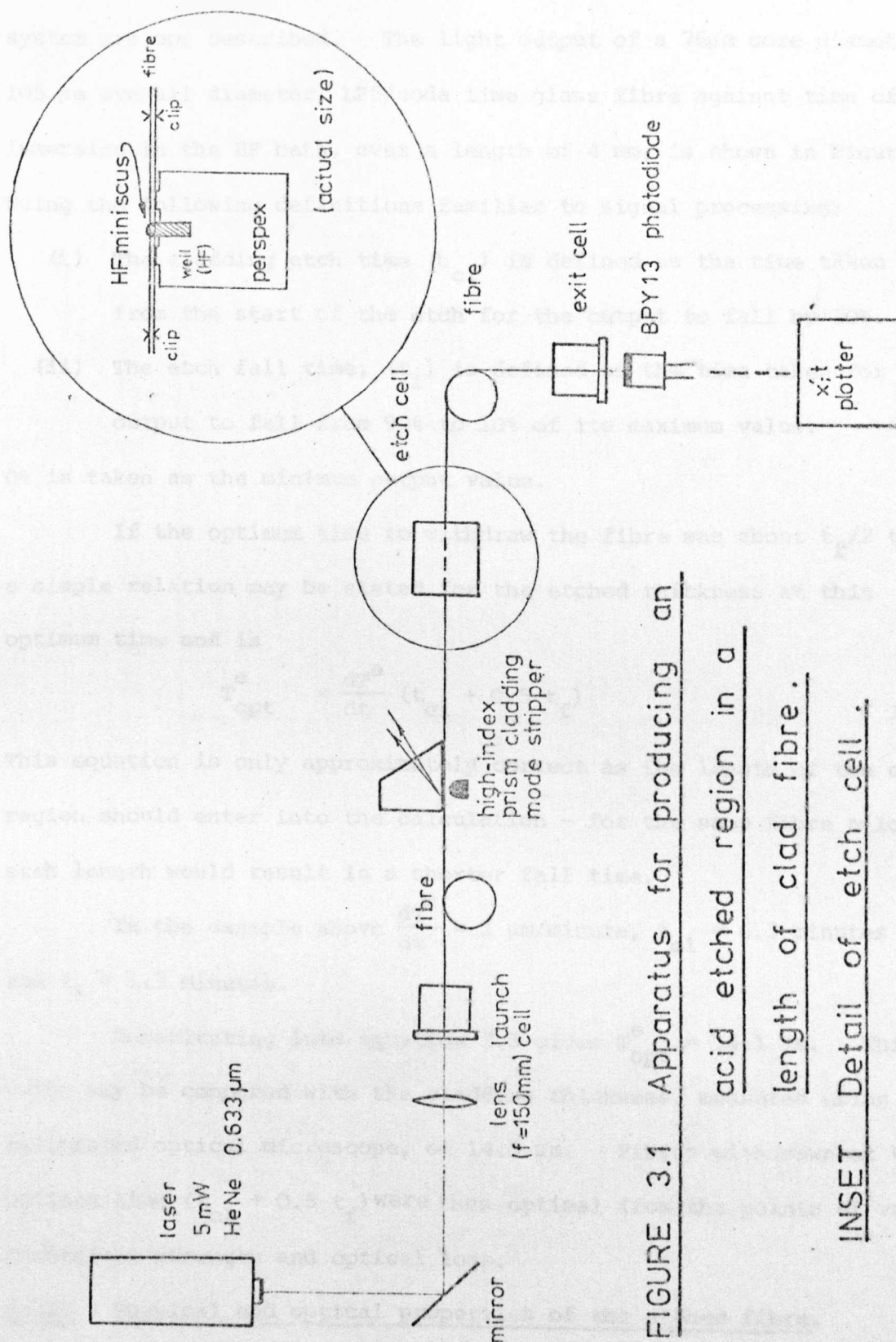


FIGURE 3.1 Apparatus for producing an

acid etched region in a

length of clad fibre.

INSET Detail of etch cell.

3.3.4 Results of acid etching.

Typical results for the acid etching technique using the system are now described. The light output of a 76 μ m core diameter, 105 μ m overall diameter, LF5/soda lime glass fibre against time of immersion in the HF bath, over a length of 4 mm, is shown in Figure 3.2. Using the following definitions familiar to signal processing;

- (i) The cladding etch time (t_{cl}) is defined as the time taken from the start of the etch for the output to fall by 10%.
- (ii) The etch fall time, (t_f) is defined as the time taken for the output to fall from 90% to 10% of its maximum value.

0% is taken as the minimum output value.

If the optimum time to withdraw the fibre was about $t_f/2$ then a simple relation may be stated for the etched thickness at this optimum time and is

$$T_{opt}^e = \frac{dT^e}{dt} (t_{cl} + 0.5 t_f) \quad 3.3$$

This equation is only approximately correct as the length of the etched region should enter into the calculation - for the same fibre a longer etch length would result in a shorter fall time.

In the example above $\frac{dT^e}{dt} = 2 \mu\text{m/minute}$, $t_{cl} = 6.3$ minutes and $t_f = 1.5$ minutes.

Substituting into equation 3.3 gives $T_{opt}^e = 14.1 \mu\text{m}$. This value may be compared with the cladding thickness, measured using a calibrated optical microscope, of 14.5 μm . Fibres withdrawn at the optimum time ($t_{cl} + 0.5 t_f$) were thus optimal from the points of view of mechanical strength and optical loss.

3.3.5 Physical and optical properties of the etched fibre.

A photograph of a typical acid-etched glass fibre is shown in Figure 3.3. The overall diameter in this case was 94 μm and the core diameter was 72 μm . As can be seen, smoothly etched regions were

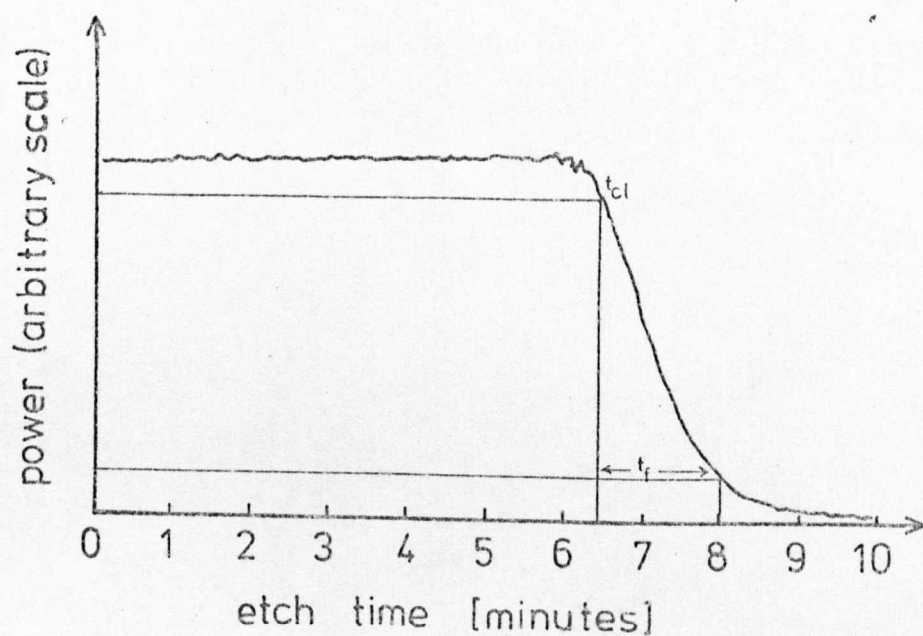


FIGURE 3.2 Light output power of a soda-lime / LF5 fibre as a function of time in an HF bath.

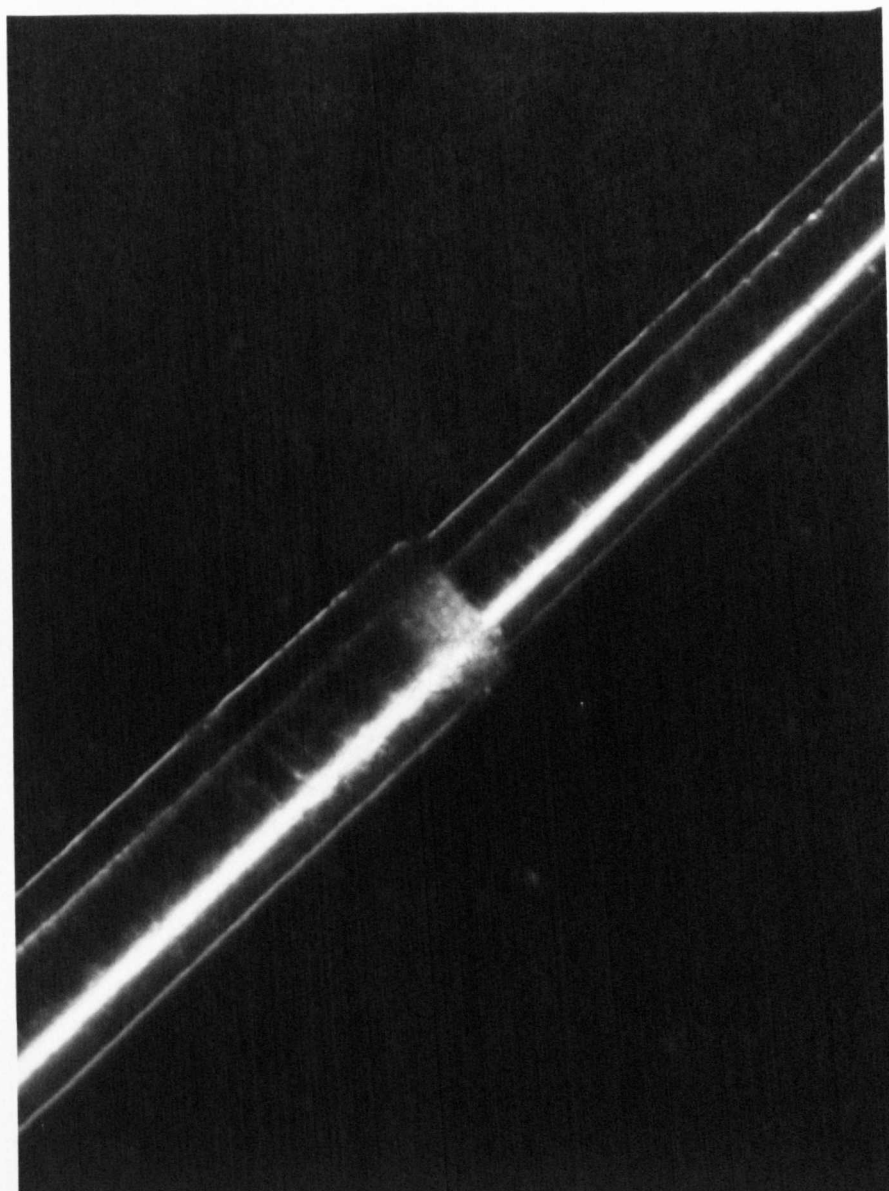
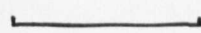


FIGURE 3.3 Photograph of an acid -
etched fibre .


100 μm

produced, which, after washing, showed no increase in light scattering. Some loss was expected at the region of transition from unclad to clad fibre partly due to a mismatch of the field distributions in each region and partly because of radiation from inhomogeneities arising from the etching process. This undesirable loss was dependent on the order of the mode propagating. Because of the relative amplitudes of the fields at the core/cladding boundary, higher order modes were attenuated to a larger extent than low order modes. However, for the lowest order modes in the fibre shown in Figure 3.3, the losses were so small for one short etched region as to be beyond the sensitivity of the available recording apparatus, consisting of a traversing photodiode detecting the forward scattering.

The treated fibres were mechanically weakened by the reduction in the working diameter, and were prone to snap at the cladding discontinuities where the bending load was converted into a shear stress. It is proposed that a suitable soft organic compound such as a plastic or epoxy could be applied at the cladding taper regions to perform the dual functions of index matching and mechanical support.

3.4 Discussion, and comparison of the ion-exchange and acid-etch techniques.

Two methods of modifying cladded glass fibres for evanescent field coupling have been presented, namely the ion-exchange method and the acid-etch method. The former has the following attractions: the material used (silver nitrate) is relatively non-hazardous and, in the small quantities used, is plentiful and inexpensive; the diffusion process is well understood⁵⁶ and documented.^{61,62} The method is one of simple immersion, though the process must be performed within the stable temperature range of silver nitrate,

$$220^{\circ}\text{C} < T < 350^{\circ}\text{C}.$$

The fibres suffer no loss in mechanical strength and in fact gain due to surface hardening effects.⁶³ A major practical disadvantage is that the diffusion time may extend to a period of hours for the refractive index at the core/cladding interface to reach a suitable value. Surface deposits of silver oxide may degrade the fibre with time, as in the case of the planar equivalent,⁶² and increase the scattering losses of the fibre at the cladding-modified region. The outstanding advantages of the diffusion technique are that the physical dimensions of the treated fibre remain unaltered and, more important, that it is applicable to single- or multimode fibres, with graded-index (SELFOC fibres, for example⁶⁴) or step-index cores. However, a word of caution must be sounded at this point. Consider the transition from a single-mode step-index fibre to a region treated by ion exchange, let us say uniformly raised to the core refractive index as in Figure 3.4. The optical energy in the fibre is confined mainly to the core and on entering the treated region the HE_{11} mode diffracts into the field distribution of a mode of the now-multimode fibre at the same phase velocity. This mode in the modified region will not be well-guided, and may be attenuated or scattered into the other modes, although the evanescent wave at the surface will be available for transverse coupling to other waveguide or bulk structures. However, the difficulty arises in the transition from the treated to the untreated region where the field distributions of the guided modes in the different regions are grossly mismatched. It is expected that the guided mode would suffer a large power loss to the cladding modes, thereby limiting the technique to fibres having thick cores and thin claddings.

The acid-etch method has the advantage of being completed in a matter of minutes at room temperature. An important consideration

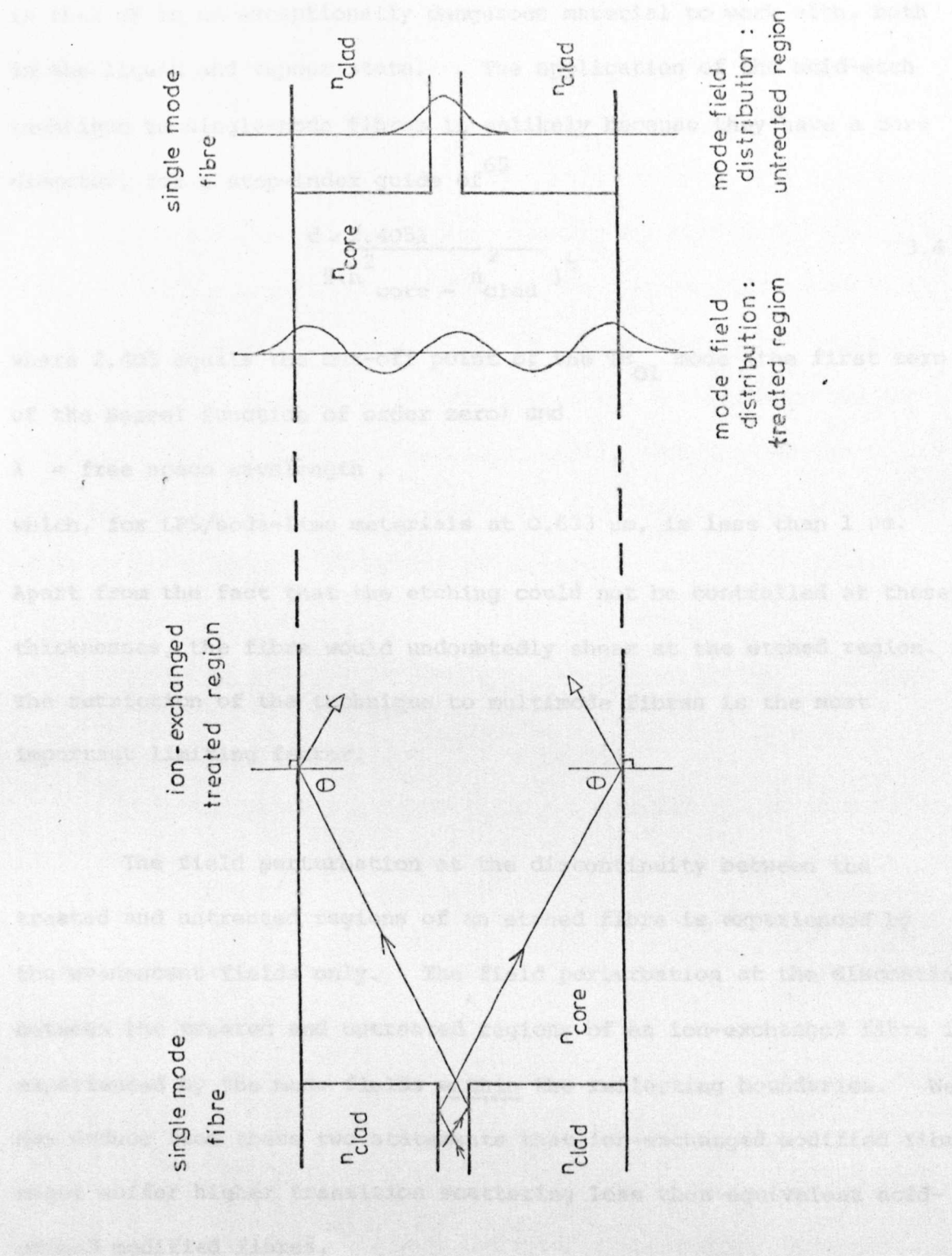


FIGURE 3.4 Diagram to illustrate the expected difficulties of the ion-exchange method applied to single-mode fibres.

is that HF is an exceptionally dangerous material to work with, both in the liquid and vapour state. The application of the acid-etch technique to single-mode fibres is unlikely because they have a core diameter, for a step-index guide of⁶⁵

$$d < \frac{2.405\lambda}{\sqrt{n_{\text{core}}^2 - n_{\text{clad}}^2}} \quad 3.4$$

where 2.405 equals the cut-off point of the TE_{01} mode (the first zero of the Bessel function of order zero) and

λ = free space wavelength ,

which, for LF5/soda-lime materials at 0.633 μm , is less than 1 μm .

Apart from the fact that the etching could not be controlled at these thicknesses, the fibre would undoubtedly shear at the etched region. The restriction of the technique to multimode fibres is the most important limiting factor.

The field perturbation at the discontinuity between the treated and untreated regions of an etched fibre is experienced by the evanescent fields only. The field perturbation at the discontinuity between the treated and untreated regions of an ion-exchanged fibre is experienced by the mode fields within the reflecting boundaries. We may deduce from these two statements that ion-exchanged modified fibres might suffer higher transition scattering loss than equivalent acid-etched modified fibres.

Fibres treated as described may be used to couple optical energy into and out of the data highway using prism or grating couplers or for connecting thin film integrated devices to optical fibres. The coupling of two or more similarly treated fibres may result in fibre directional couplers.

The closest analogy in microwaves is the so-called "Coaxial Bethe-hole directional coupler", developed by Ginzton and Goodwin.⁶⁶

Novel fibre modulators based on the perturbation of the available evanescent fields by electro-optic or similar effects may be proposed.

Cladding removal by chemical etching represents the most direct and easily-controllable method of accessing the waveguide core. It was considered that the research effort should concentrate on this means of cladding modification rather than the less-established ion-exchange method, and to this end experiments, described in the following section, were devised to demonstrate the importance of the principle of evanescent field coupling to cladding-modified multimode fibres.

3.5 Coupling of a thin film waveguide and a circular fibre at the cladding-modified region.

3.5.1 Introductory discussion.

With the principle of coupling to circular fibres at a region of cladding modification established, it was thought that the transverse interaction of the evanescent wave of a fibre with another waveguide - a thin film - would result in a thin film/circular fibre directional coupler. The proposal was simply to press the treated region of the cladding-modified fibre on to the surface of the thin film waveguide, with or without a low-index buffer layer between the two. If the phase velocities of the guided modes were equal then directional coupling would take place along the interaction region where the fields of the guided modes overlapped. Any phase mismatch of the two waves in the structures could be corrected by placing a phase grating³¹ between the fibre and the film, or by the introduction of taper film coupling.⁴⁵ These ideas were embodied in two United Kingdom patents, one of which concerned the coupling using the ion-exchanged modified fibre⁵⁴ and the other using the acid etched fibre.⁶⁷ Hammer⁴¹ has

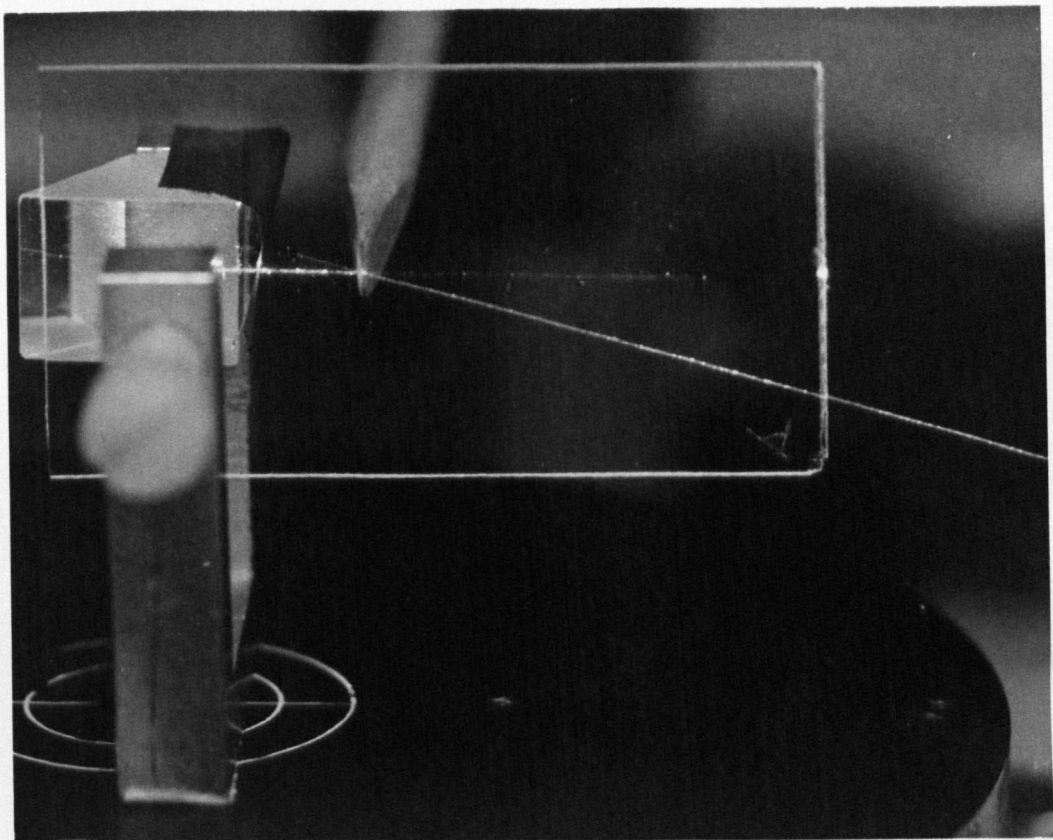
used both the grating and a method of partial cladding removal to attempt to couple from a fibre to a film, and Bulmer⁴⁰ has studied the effects of a periodic grating on the coupling of a repulled section of single-mode fibre to a thin film.

In this section, results are presented for the thin film/multimode fibre coupler. A theory of operation is presented and the difficulties and disadvantages of such a configuration are discussed.

3.5.2 Experimental details of thin film/multimode fibre coupler.

LF5/soda lime glass fibres were used, with the core exposed by acid-etching, typically 90 μm in diameter. The experimental arrangement is shown in Figure 3.5. A laser beam was coupled through a high-index prism coupler into a thin film waveguide, in this case the TE_0 mode in a 1.6 μm thick film of Corning 7059 glass, r.f. sputtered⁶⁸ onto a Fisher microscope slide. The light beam continued in the film until it came into contact with the fibre, the exposed core of which was pressed onto the surface of the film by a chisel-shaped ligneous rod. The fibre axis intersected the beam axis at a synchronous angle ϵ . After the crossing point, the scattering from the light beam in the film was greatly reduced in intensity, the majority of the light coupling into the circular fibre, which had a 76 μm core diameter (LF5 glass) and, with the soda-lime glass cladding, a 105 μm overall diameter. The transition between the unclad and clad regions of the fibre is indicated by the arrow in Figure 3.5.

It was estimated that between 70% and 90% of the light was coupled out of the film by this means. The angle between the beam and the fibre axis was necessary to phase match the waves in the guiding structures and, because of the large number of modes supported by the fibre, phase matching over a wide range of angles was possible.



↑

FIGURE 3.5 Coupling from a thin film waveguide
to a circular clad fibre at a
region of cladding modification .

By observing the near-field patterns of the coupled fibre modes using a low-power optical microscope, it was possible to gain some insight into the operation of the coupler. The following results are for the coupling of an 80 μm diameter unclad LF5 fibre (measured refractive index at 0.633 μm = 1.577), to the TE_1 mode of an ion-exchanged thin film, $\beta/k = 1.571$. Circularly symmetric ring patterns were observed in the near-field, being the high-order modes excited in the fibre by the mode in the film. As the crossover angle ϵ increased, an annular ring pattern, characteristic of spiralling modes, was observed. An example of the spiralling mode pattern, for $\epsilon = 5^\circ$, is shown in Figure 3.6. The zeros of this pattern in the azimuthal direction were not separable, and the other phase distortions in the photograph were due to uneven nature of the fibre termination, which was not properly cleaved. The larger the crossover angle the larger the central area containing only scattered light became.

Unfortunately the considerable experimental difficulties prevented reliable results of a more qualitative nature to be extracted, but we will now determine if these observations are consistent with our theoretical understanding.

3.5.3 Theory of thin film/circular fibre coupling.

(i) Plane wave description of high-order fibre modes.

The coupling effect under study relies upon the phase matching of a slab waveguide mode, which can be considered in terms of plane waves, to the mode field of a circular fibre. It would, therefore, be useful to establish approximate relations which allow the guided wave in the fibre to be composed of locally plane waves. This analysis has been presented in Section 2.5 from the work of Marcuse,⁶⁹ and the results are stated below. For high-order modes, such that

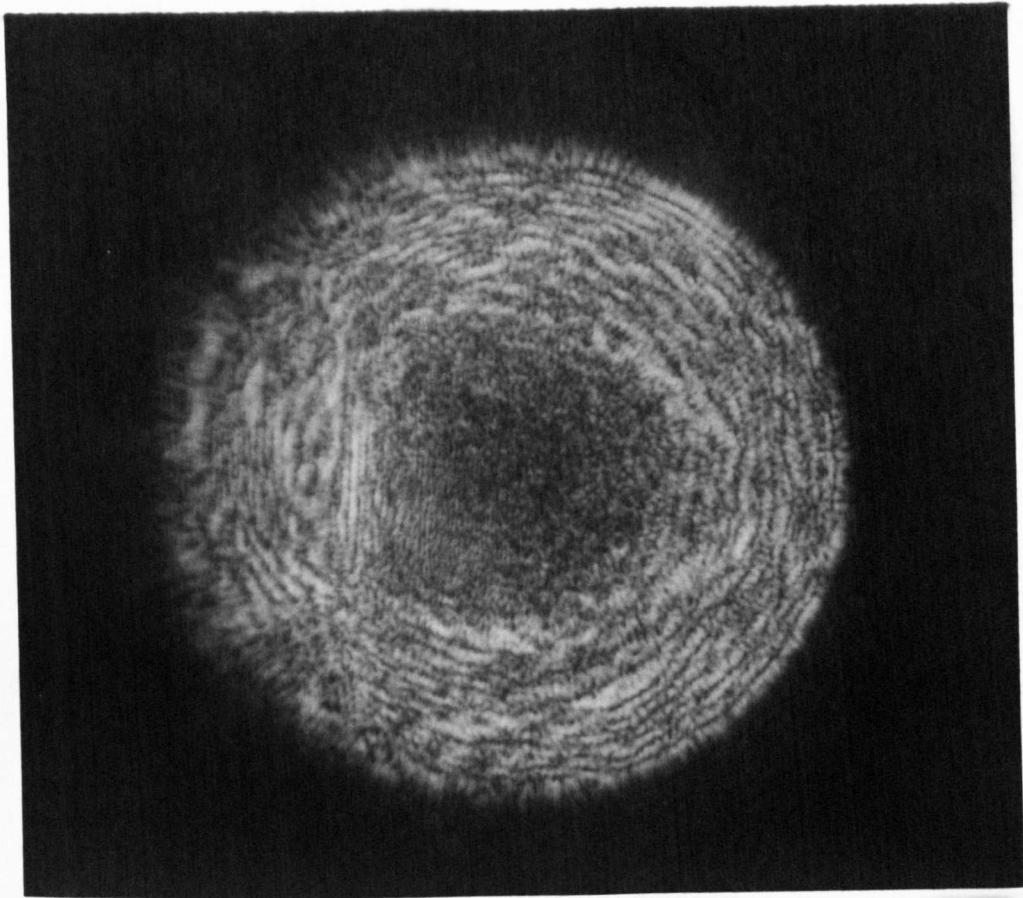


FIGURE 3.6 Near-field pattern of a
spiralling mode coupled from
a thin film waveguide.

$$k_r d/2 \gg 1$$

3.5

the wave in the ^{fibre}guide can be described in plane wave terms with three orthogonal wave-vector components β , k_ϕ and k_r along the axial, azimuthal and radial directions respectively. It has further been shown that

$$k_r^2 = k_{n_{\text{core}}}^2 - \beta^2 - \left(\frac{2\mu}{d}\right)^2 \quad 3.6$$

and

$$k_\phi = \frac{2\mu}{d} \quad 3.7$$

where μ is the azimuthal quantum number.

In practice the fields of the fibre vary as

$$E \rightarrow J_\mu \left((k_{n_{\text{core}}}^2 - \beta^2)^{1/2} r \right) e^{j r \phi} e^{-j \beta z} e^{j \omega t} \quad 3.8$$

inside the fibre core, and

$$E \rightarrow H_\mu^{(1)} \left((j(\beta^2 - k_{n_{\text{clad}}}^2))^{1/2} r \right) e^{j r \phi} e^{-j \beta z} e^{j \omega t} \quad 3.9$$

in the cladding.

J_μ is the Bessel function and $H_\mu^{(1)}$ is the Hankel function, both of the first kind and of order μ .⁷⁰

(ii) Phase matching.

Consider the wave-vector diagram in the yz plane, sketched in Figure 3.7a. Subscripts 1 and 2 denote film and fibre respectively. The coupling takes place by the overlap of the evanescent wave in the film, and the evanescent radial wave in the fibre in the \hat{y} direction. Since the fibre wave vectors are orthogonal we have

$$\vec{\beta}_1 = \vec{\beta}_2 + \vec{k}_{\phi 2} \quad 3.10$$

and

$$\beta_2 = \beta_1 \cos \epsilon \quad 3.11$$

$$k_{\phi 2} = \beta_1 \sin \epsilon \quad 3.12$$

Substituting equations 3.11 and 3.12 into 3.6 and 3.7 gives

$$\mu = d/2 \beta_1 \sin \epsilon \quad 3.13$$

and

$$k_{r2}^2 = k_{n_2}^2 - \beta_1^2 \cos^2 \epsilon - \beta_1^2 \sin^2 \epsilon = k_{n_2}^2 - \beta_1^2 \quad 3.14$$

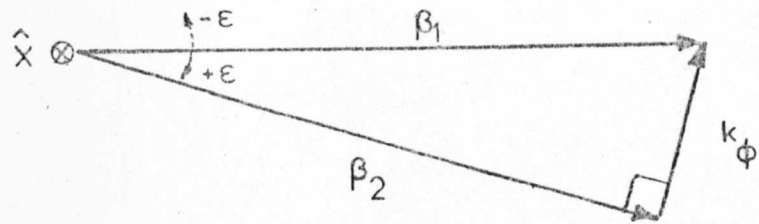


FIGURE 3.7a Wave vector diagram for
film / fibre coupler .

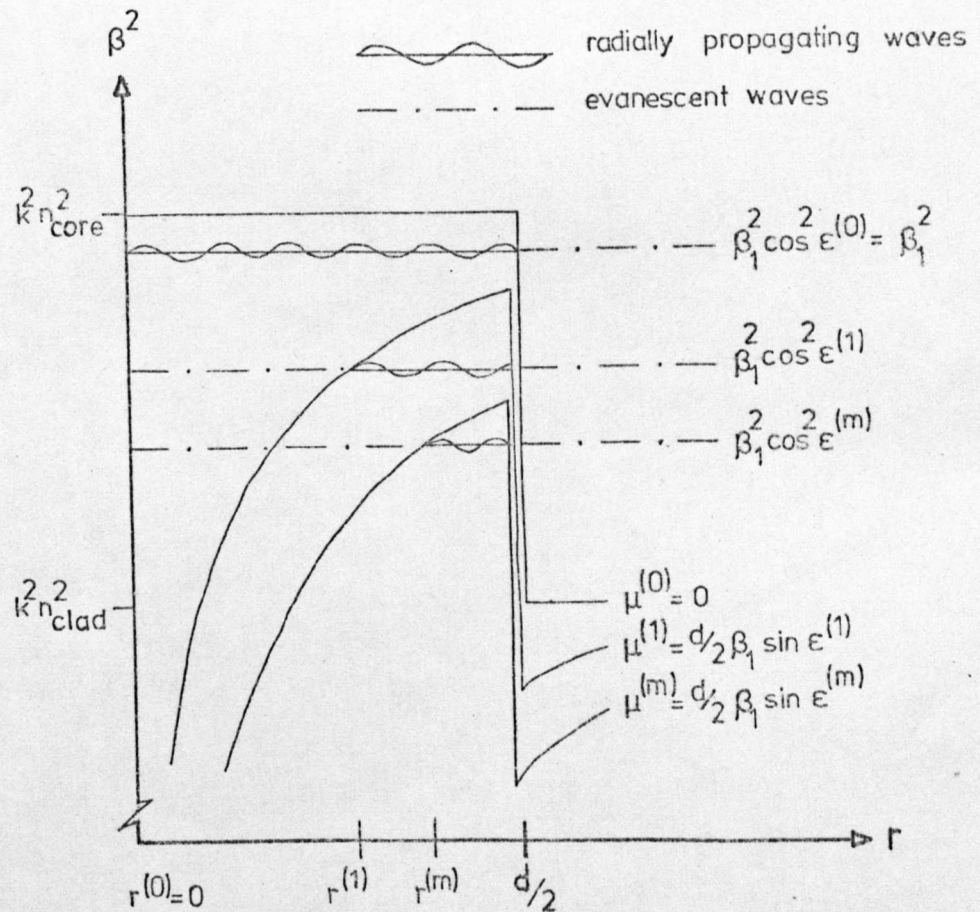


FIGURE 3.7b Fibre propagation constant
(squared) against radius , for
different values of
crossover angle .

(iii) Coupled mode fields.

From equations 3.8 to 3.14, the approximate field distribution of the mode coupled into the fibre is, with the time variation suppressed,

$$\frac{J_d}{2\beta_1 \sin \epsilon} \left[(k_{n_{\text{core}}}^2 - \beta_1^2 \cos^2 \epsilon)^{\frac{1}{2}} r \right] e^{j r \phi} e^{-j \beta_1 \cos \epsilon \hat{z}_1} \quad 3.15$$

inside the core, and

$$\frac{H_d^{(1)}}{2\beta_1 \sin \epsilon} \left[J(\beta_1^2 \cos^2 \epsilon - k_{n_{\text{clad}}}^2)^{\frac{1}{2}} r \right] e^{j r \phi} e^{-j \beta_1 \cos \epsilon \hat{z}_2} \quad 3.16$$

in the cladding.

(iv) Axial and spiralling modes.

As Stewart points out,⁷¹ equation 3.6 may be written as:

$$k^2(r) = k_{n^2}^2(r) - \beta^2 - \left(\frac{\mu}{r}\right)^2 \quad 3.17$$

β is independent of r by definition and β and $\left(\frac{\mu}{r}\right)$ are real.

The description represents a radially propagating wave if $k(r)$ is real.

If $k(r)$ is imaginary, then the wave will be evanescent (increasing or decreasing) in the radial direction. The boundary between these

regions is given by the condition

$$k(r) = 0$$

or

$$\beta^2 = k_{n^2}^2(r) - \left(\frac{\mu}{r}\right)^2 \quad 3.18$$

Three such 'boundary' lines are sketched in Figure 3.7b, which is the

graph of β^2 against r . They are for $\mu^{(0)} = 0$, $\mu^{(1)}$ and $\mu^{(m)}$:

$$0 = \mu^{(0)} < \mu^{(1)} < \mu^{(m)} \quad 3.19$$

Where the mode lines (constant β_2^2) lie below the boundary lines, they

represent radially propagating waves and where they lie above they

represent evanescent waves.

Let us observe the radial variation of the

coupled fibre mode as the synchronous crossover angle is increased

from $\epsilon = 0$.

For the m^{th} value of ϵ ($\epsilon^{(m)}$), equation 3.11 and 3.13 state;

$$\beta_2^{(m)} = \beta_1 \cos \epsilon^{(m)} \quad 3.20$$

and

$$\mu^{(m)} = \frac{d}{2} \beta_1 \sin \epsilon^{(m)} \quad 3.21$$

As the crossover angle increases, β_2 decreases and μ increases.

At $\epsilon^{(0)} = 0$, $\beta_2^{(0)} = \beta_1$ and $\mu^{(0)} = 0$, the mode field is evanescent for $r > d/2$ (Figure 3.7b) and the mode is HE_{1l}

$$l \approx (k^2 n_{\text{core}}^2 - \beta_2^2)^{1/2} d/2 \quad 3.22$$

At $\epsilon_s^{(1)}$, $\beta_2^{(1)} < \beta_1$ and $\mu^{(1)} > 0$, according to Figure 3.7b, the field is evanescent outwards from $d/2$, and also inwards from a radius $r^{(1)}$ given by

$$r^{(1)} = \frac{\mu^{(1)}}{(k^2 n_{\text{core}}^2 - \beta_1^2 \cos^2 \epsilon^{(1)})^{1/2}} \quad 3.23$$

Extending the argument to the m^{th} value, a general expression for the normalized annular ring radius is

$$\frac{r^{(m)}}{d/2} = \frac{\sin \epsilon^{(m)}}{\left[\frac{k^2 n_{\text{core}}^2}{\beta_1^2} - \cos^2 \epsilon^{(m)} \right]^{1/2}} \quad 3.24$$

This ring radius will increase with increasing ϵ until the fibre cut-off condition:

$$\epsilon_{\text{co}} = \cos^{-1} \left[\frac{kn_{\text{clad}}}{\beta_1} \right] \quad 3.25$$

is reached, beyond which the energy will leak into the fibre cladding.

Modes with $\mu > 0$ represent 'spiralling' modes: in the ray optics model of propagation, the ray trajectory never crosses the axis of the fibre. Furthermore the coupling is to only one of the two possible orthogonal degenerate spiralling modes, with clockwise and anticlockwise rotations (viewed in the $+\hat{z}_2$ direction), the former associated with

positive crossover angles and the latter with negative crossover angles (Figure 3.7a). The near field pattern of such a mode rotates as the wave progresses down the fibre. Spiralling modes are characterized by an annular ring pattern in the near field, the inner ring radius of which, as a function of ϵ , is predicted by equation 3.24.

Modes with $\mu = 0$ only occur where $\epsilon = 0$, and are pure axial modes, $HE_{1\ell}$, having no azimuthal field variation.

(v) Directional coupling.

Clearly the introduction of the synchronous angle, ϵ , renders the analysis of the coupler in terms of the classical theory of Chapter 2.7 impossible. Perhaps a better label for this configuration is that of a "spiralling mode coupler". As can be seen from Figure 3.7a the coupling is accompanied by a change in direction of power flow from \hat{z}_1 to \hat{z}_2 . The classical theory of coupled transmission lines only applies when the guides are parallel, that is when $\epsilon = 0$. Otherwise the coupling is a continuous leakage of energy from the film to the fibre and away from the coupling region. If the rate of leakage is fast enough then all of the energy will couple out of the film in a very short distance, and the transfer efficiency will approach 100%.

(vi) Reciprocity.

As Kapany and Burke point out,⁷² the phase factor in equation 3.8,

$$\left[\exp \left(j \left[\frac{k_{\phi} \phi}{\mu} - \beta_2 z_2 \right] \right) \right] \quad 3.26$$

ensures that surfaces of constant phase satisfy the equation

$$z_2 = \frac{k_{\phi} \phi}{\mu \beta_2} + \text{constant} \quad 3.27$$

For $\mu \neq 0$, a given surface of constant phase rotates about the axis of the guide while advancing in the \hat{z}_2 direction. The implications of this statement are far-reaching for the spiralling mode coupler, because the phase-matching conditions to construct the wave in the

film in the reverse direction become dependent on the position of the coupling point along the z_2 axis. Work has not been carried out to evaluate the sensitivity of the fibre-to-film coupling to this positional dependence.

3.5.4 Comparison between theory and experiment, and conclusions.

There was general agreement between the predictions of Section 3.5.3 and the experimental observations. The trend to higher-order spiralling modes with increasing crossover angle was noted and the high efficiencies expected with this 'leakage' type of coupler were recorded. The observation that the coupling appeared to be more efficient with larger fibres was attributed to the leakage occurring over longer effective interaction lengths.

The spiralling modes have been observed in the near-field and their patterns were those expected. The azimuthal variation of the mode fields was not observed, we think due to the coupling over the finite width of the film beam. A filamentary section of the beam in the film couples to a pure spiralling mode at a different point along the fibre axis from another similar section, and the result is a mixture of degenerate modes rotating slightly out of phase with each other. The ordered azimuthal zeros in the near field therefore disappear.

Coupling from a spiralling mode in a multimode fibre to a film mode has not been achieved, presumably because the correct phase synchronism at the coupling point has never been obtained, although there is no reason to suggest that the coupling is not entirely reciprocal.

It can be concluded that this simple and highly-efficient form of film/fibre coupler can be explained using the theoretical model of Section 3.5.3, though the difficulties encountered at the experimental stage of accurately controlling and quantifying the device resulted in poor correlation.

3.6 Summary and Conclusions.

The recognition that highly-efficient coupling between circular fibres and other bulk or waveguiding structures could be achieved by evanescent field coupling led to the study of methods of modifying the cladding material of fibres, such that the insulating effect on the guided mode fields was eliminated. Two methods were investigated: physically removing the cladding, and raising the cladding refractive index by ion-exchange. After a comparison of the methods, the former was chosen as the most suitable.

To demonstrate the principle of evanescent field coupling to cladding-modified multimode fibres an attempt was made to produce a thin-film / circular-fibre coupler, where the exposed core of the fibre was lightly pressed onto the surface of the thin film waveguide. Phase matching occurred at a synchronous crossover angle, such that

$$\cos \epsilon = \frac{\beta_{\text{fibre}}}{\beta_{\text{film}}}$$

The power transfer efficiency from film to fibre was approximately 70% into a single, high-order fibre mode, the coupling taking the form of a continuous leakage of energy away from the coupling region in the spiralling fibre mode. The coupler was studied theoretically by introducing a plane wave approximation for the fibre mode fields and by considering the phase-matching conditions in the plane of the thin film. The excited mode near-field distributions were presented and the apparent non-reversible nature of the coupler was discussed. The coupler was thought to be reciprocal, but depended on the position of the coupling point along the fibre axis.

This type of novel coupler, while being efficient, simple to construct and universally applicable was difficult to control experimentally. Further study must be associated with particularly accurate measuring and recording apparatus.

CHAPTER 4. CLADDED FIBRE WAVEGUIDE MODES EXCITED BY A PRISM COUPLER AT A CLADDING-MODIFIED REGION.

4.1 Introduction.

It is evident from the work of the previous chapter that cladding modification of circular fibres allows transverse coupling to the core modes, and that simple coupling devices based on this principle can be demonstrated. Many difficulties were encountered in controlling accurately the coupling from a film to a fibre and results of a more qualitative nature were required. The simplest and most controllable form of an evanescent field coupler, commonly encountered in integrated optics, is the prism/film coupler.^{28,29} In this chapter the idea is extended to demonstrate the excitation of circular fibre waveguide modes by a high-index prism coupler at a cladding-modified region. A comparison of the experimental results with the established theory of mode propagation in circular dielectric step index fibres will be presented.

Previously, the launching of individual modes in circular fibres was achieved by Kao and Hockham³ and Snitzer and Osterberg⁹⁵ by direct illumination of the fibre end, and an elegant technique by Kapany⁷² was also demonstrated. It was not until early in 1975 that first reports of prism coupling to circular fibres came to the fore, our own⁹⁶ and that of Midwinter.⁹⁷ The latter author developed the technique for fibre testing purposes:

"the coupler allows study of mode-dependent fibre transmission loss and radiative loss and allows single-mode launching for bandwidth study"⁹⁷.

Though they differ slightly, the underlying principles of the two methods are the same, and the uses conceived by Midwinter may also be derived from the system described here.

It is because of the importance of the technique, firstly to demonstrate transverse coupling in fibre optics, and secondly as a fibre test and evaluation procedure in its own right, that a detailed description of the method, the results and their analysis is given.

4.2 Theory of Prism Coupling to Circular Fibres.

4.2.1 Synchronous and tilt angles of the prism coupler.

The coupling effect under study relies upon the phase matching of a near plane wave from a laser to the circular fibre mode fields. It is useful to use the relations which describe the guided mode fields in terms of locally plane waves. Restating the results of Section 2.5 we have

$$\vec{K} = k_r \hat{r} + k_\phi \hat{\phi} + \beta \hat{z} \quad 4.1$$

where

$$k_\phi = \frac{2\mu}{d} \quad 4.2$$

$$k_r = (k_{n_{\text{core}}}^2 - \beta^2 - k_\phi^2)^{\frac{1}{2}} \quad 4.3$$

$$|K|^2 = k_{n_{\text{core}}}^2 \quad 4.4$$

These equations hold where

$$k_r \frac{d}{2} \gg 1 \quad 4.5$$

As Midwinter points out,⁹⁷ the angles which represent the skew and the elevation of the local plane wave in the fibre core are given by

$$\alpha_s = \tan^{-1} \frac{k_\phi}{\beta} \quad 4.6$$

$$\alpha_e = \tan^{-1} \frac{k_r}{\beta} \quad 4.7$$

It is implicit in the above definitions that the coupling takes place by the overlap of the evanescent wave at the prism base and the evanescent radial wave of the fibre.

For the optimum launching of a particular mode the synchronous angle, θ , and the tilt angle, ϕ , of the prism coupler must be selected

to match the characteristic angles α_e and α_s . From simple geometric considerations of Figure 4.1 we find

$$\theta_m = \sin^{-1} \left[n_p \sin \left(\sin^{-1} \left[\frac{n_{\text{core}} \sin \alpha_e}{n_p} \right] - \alpha_p \right) \right] \quad 4.8$$

and

$$\phi_m = \sin^{-1} [n_p \sin \alpha_s] \quad 4.9$$

where n_p and α_p are the prism refractive index and angle, and subscript m denotes the values with the prism refraction included.

Other than this short description of the synchronism encountered in the excitation of circular fibre modes, the situation is analagous to the prism/film²⁹ or prism/ribbon coupler,⁴⁷ and there is no need to enlarge on the descriptions given in the literature. In the prism coupling experiments presented throughout this chapter, variation of the skew angle was not considered because, at the time of the work, no accurate method of doing so was devised. It is appropriate to set $\alpha_s = 0$ in equation 4.6, making $k_\phi = 0$. This further implies from equation 4.2 that

$$\mu = 0 \quad 4.10$$

throughout.

It might be expected that ^{only} modes with no azimuthal variation will ~~only~~ be set up. This was observed for large diameter fibres where equation 4.5 holds, but not for smaller fibres.

4.2.2 Launching efficiency of a prism/fibre coupler.

To a first approximation the coupling region can be divided into the xy and xz planes and the efficiency in each plane discussed (Figure 4.1a-c). The total efficiency would be the product of the two efficiencies. In the xz plane, Tien¹⁸ develops a simple expression for the efficiency of a plane wave prism/film coupler which

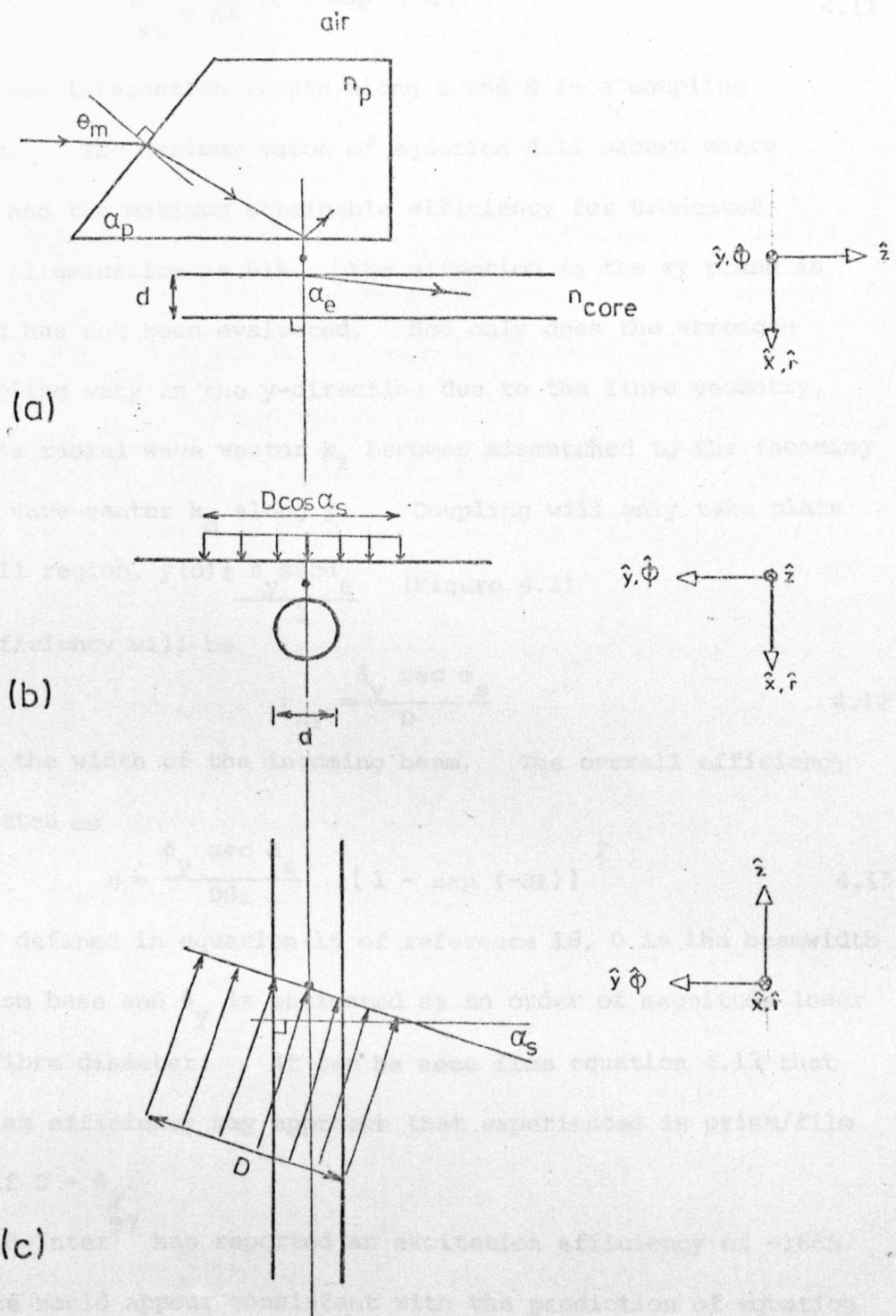


FIGURE 4.1 Geometry of prism / circular fibre
coupler : directions and
definitions.
(• denotes coordinate origin)

may be applied in this analogous situation:

$$\eta_{xz} = \frac{1}{S\ell} (1 - \exp(-S\ell))^2 \quad 4.11$$

where ℓ is the interaction length along z and S is a coupling coefficient. The maximum value of equation 4.11 occurs where $S\ell = 1.25$, and the maximum attainable efficiency for truncated plane-wave illumination is 81%. The situation in the xy plane is complex and has not been evaluated. Not only does the strength of the coupling vary in the y -direction due to the fibre geometry, but also the radial wave vector k_x becomes mismatched to the incoming evanescent wave-vector k_o along y . Coupling will only take place over a small region, $y(0) \pm \frac{\delta_y \sec \alpha_s}{2}$ (Figure 4.1) and the efficiency will be

$$\eta_{xy} = \frac{\delta_y \sec \alpha_s}{D} \quad 4.12$$

where D is the width of the incoming beam. The overall efficiency may be written as

$$\eta = \frac{\delta_y \sec \alpha_s}{DS\ell} [1 - \exp(-S\ell)]^2 \quad 4.13$$

where S is defined in equation 15 of reference 18, D is the beamwidth at the prism base and δ_y is estimated as an order of magnitude lower than the fibre diameter. It can be seen from equation 4.13 that the coupling efficiency may approach that experienced in prism/film couplers if $D \rightarrow \delta_y$.

Midwinter⁹⁷ has reported an excitation efficiency of -16dB. This figure would appear consistent with the prediction of equation 4.13, because we could assume from Midwinter's published results that $d \approx 20 \mu\text{m}$ and $D \approx 50 \mu\text{m}$. Consequently $\delta_y \approx 2 \mu\text{m}$. If a launching efficiency of 45% is assumed in the xz plane (a typical figure) equation 4.13 reveals $\eta = -17.5\text{dB}$. We can expect launching efficiencies of similar modest magnitudes.

4.3 Coupling to the High-order Modes at the Treated Region.

4.3.1 Experimental details.

The high-order modes of a circular clad glass fibre were excited at the cladding-modified region by a high-refractive-index prism coupler in the following manner. The fibres used were drawn from Schott LF5 rod as the core material and soda-lime glass tubing as the cladding. Typical fibre dimensions were a core diameter of between 50 μm and 100 μm and an accompanying overall diameter of 72 μm to 150 μm . A 20mm length of cladding at the end of a length of fibre was removed in an HF etch-bath. The exposed core region was pressed against the base of a 60° prism (refractive index 1.696 at 0.633 μm) and held in place by a soft rubber pad. Light from 5mW Spectra-Physics Helium-Neon laser operating at 0.633 μm wavelength was focused into the prism and made to reflect internally at the base immediately above the fibre. The beamwaist at the prism base was estimated as 50 μm and the tilt angle, ϕ , was zero.

4.3.2 Reflected spot m-line distribution.

Dark mode lines²⁸ were visible in the bright spot reflected from the prism base as the power coupled into the fibre modes at the particular synchronous beam angles. With the range of fibres used the normalized frequency, V , defined as⁶⁵

$$V = \frac{\pi d}{\lambda} (n_{\text{core}}^2 - n_{\text{clad}}^2)^{1/2} \quad 4.14$$

lay between 75 and 750, and many mode lines existed closely spaced. The low-order modes were difficult to separate, and the reflected spot may have contained four such lines simultaneously, indicating the excitation of that number of nearly-degenerate modes.

The higher-order modes were more spread out, and could be launched individually. Due to the refraction of the reflected beam at the prism, the spot shifted in space with prism coupling angle, and

a spectrum of dips in the reflected spot resulted. Using a time exposure for the duration of a coupling angle scan (manually operated), a section of the reflected spot m-line spectrum was photographed, and is shown in Figure 4.2. The bright centres of the spots lie below the scattering 'tails' and were omitted to prevent saturation of the photographic plate. Figure 4.2 clearly shows the dark mode-lines corresponding, as will be seen shortly, to the coupling of the $HE_{1\ell}$ modes of the fibre, where ℓ lies between approximately 26 and 33.

4.3.3 Near-field patterns of the high-order modes and relation to theory.

Observations of the near-field patterns at the cleaved termination of the clad fibre have shown the existence of pure high-order modes which were launched discretely by the prism coupler at the cladding-modified region.

The apparatus used is shown in Figure 4.3. The termination was supported and index-matched (nitrobenzene $n_D = 1.556$) using an exit cell similar in design to that of Dakin.⁶⁰ The fibre was that of Section 4.3.1, having a core diameter of 50 μm and an overall diameter of 72 μm , and an overall length of 75 mm. It was important to keep the waveguide straight to minimize bending loss and mode conversion, particularly in the study of high-order modes. A travelling microscope comprising a x20 (n.a. = 0.5) objective and a x15 eyepiece was used to focus the image of the end of the fibre on to a ground-glass screen and photographed from behind. The mode distributions observed consisted of well-defined circular interference patterns as shown in Figure 4.4a-d. As the prism was rotated from the higher-order modes to the lower-order ones (Figure 4.4a-c) the number of discernable rings decreased. At the value of θ_m where more than one mode was launched by the prism coupler, the near-field became

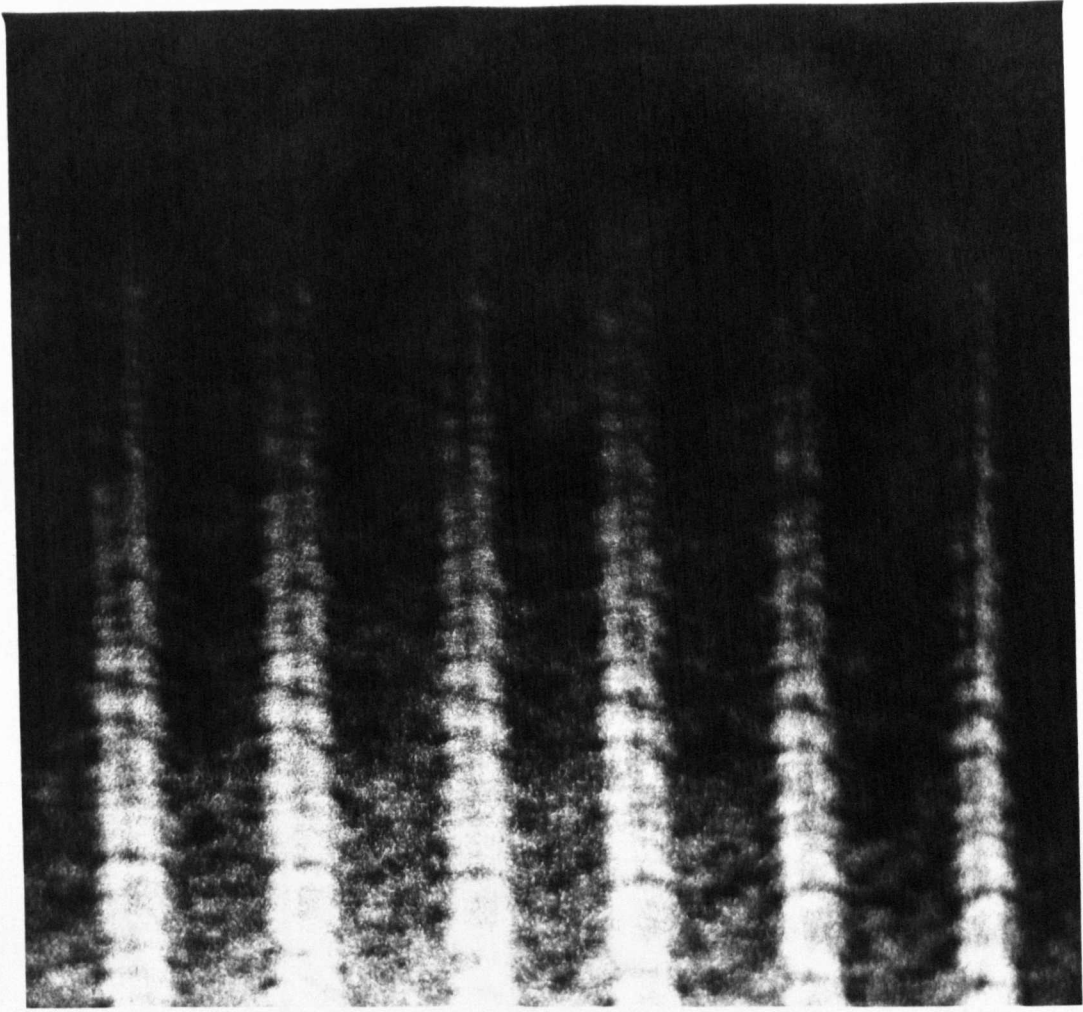


FIGURE 4.2 Part of the reflected spot m-line spectrum for the prism coupling of high - order fibre modes .

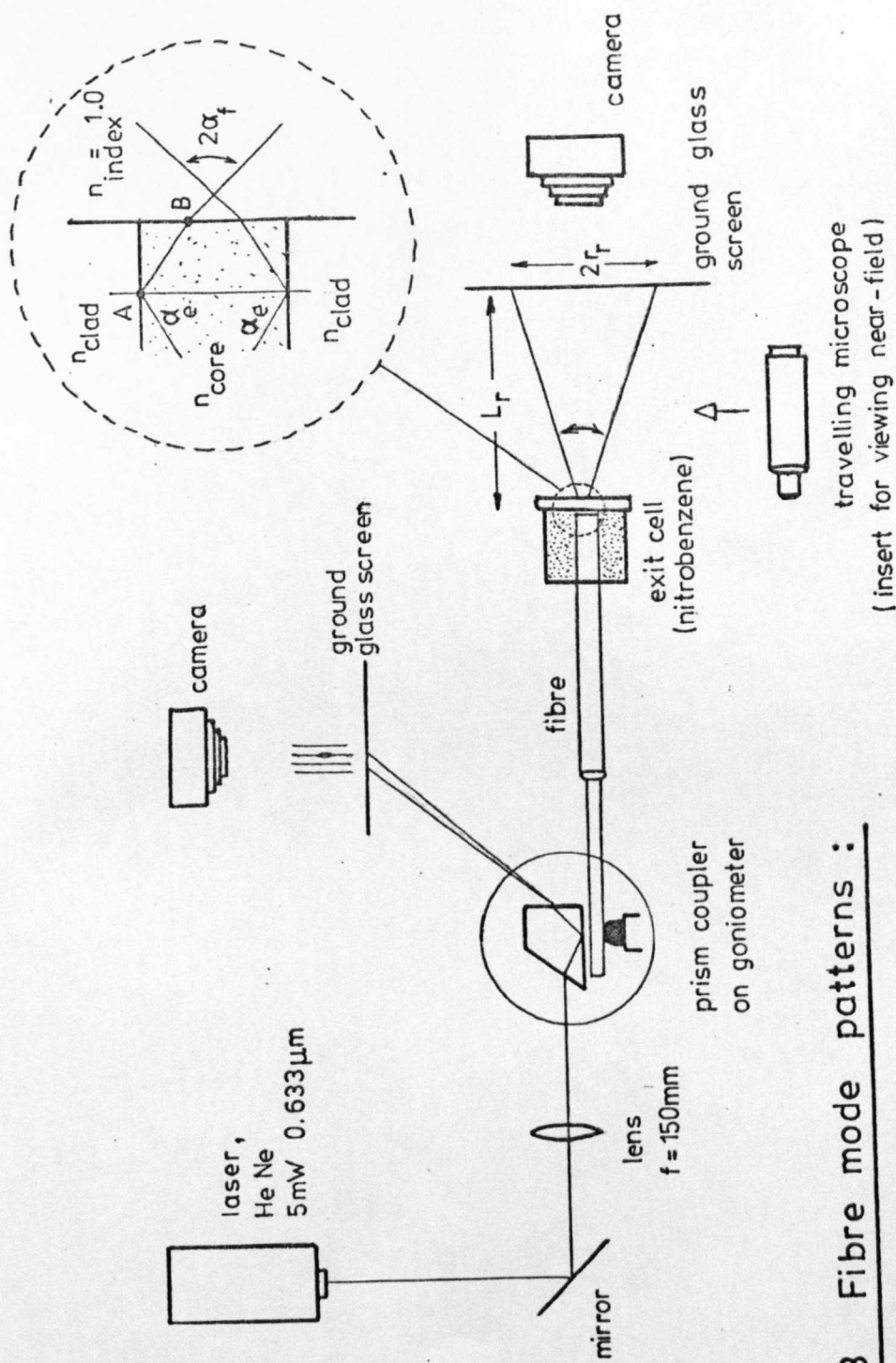


FIGURE 4.3 Fibre mode patterns : apparatus .

INSET Ray optics model of exit .

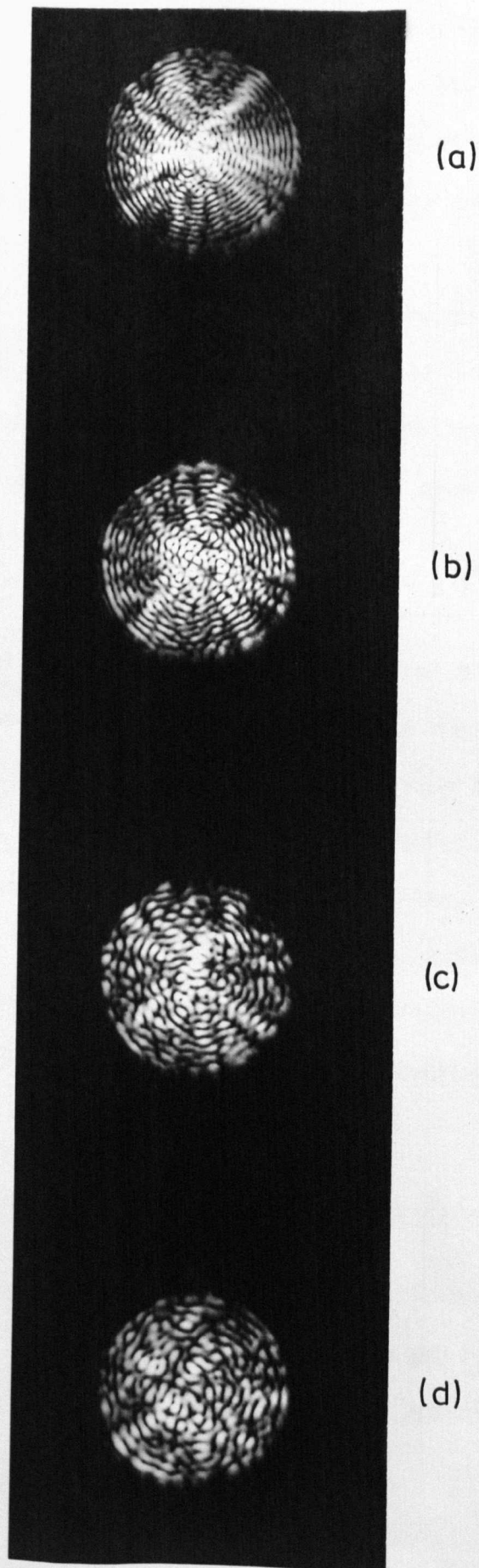


FIGURE 4.4 Near-field patterns of high-order fibre modes.

a pseudo-random interference pattern as shown in Figure 4.4d. The corresponding reflected spot pattern verified that discrete modes were no longer being launched and that the interference was due to the superposition of the nearly-degenerate modes in the near field. The highest order mode launched had approximately 30 rings and is shown in Figure 4.5.

It can be shown⁹⁸ that the power being propagated along the waveguide is characterized by the power density along the axial direction, denoted by P_z . From equation 2.42 with $\mu = 0$, we find that P_z varies with radial distance r . Within the core of radius $\frac{d}{2}$, the energy density is

$$P_z \propto E^2 = \left[J_0 \left(\frac{2(k_n^2 \text{core} - \beta^2)^{1/2}}{d} r \right) \right]^2 \text{ for } r < \frac{d}{2} \quad 4.15$$

Pure modes only have zeros in the radial direction, and are denoted (in the case of $\mu = 0$) $HE_{1\ell}$, where ℓ is the number of radial intensity maxima. Other patterns which show zeros in other than the radial direction are mixtures of degenerate modes.

The experimental results of Figures 4.4 and 4.5 show good agreement with this theoretical model, although the distributions at the centre of the patterns become slightly muddled, probably due to mode conversion down the 10^5 wavelengths of fibre to the detection point.

FIGURE 4.5 Near-field pattern of the HE_{10} mode

4.3.4 Theoretical formulation of the far-field distributions of the high-order modes.

Now that the form of the near-field distributions for high-order modes has been established, our attention must focus on the emergent far-field patterns.⁷² There are two methods of deriving the expected radiation patterns:

(i) Fourier theory of Fraunhofer diffraction.

The Fourier theory of Fraunhofer diffraction may be applied,

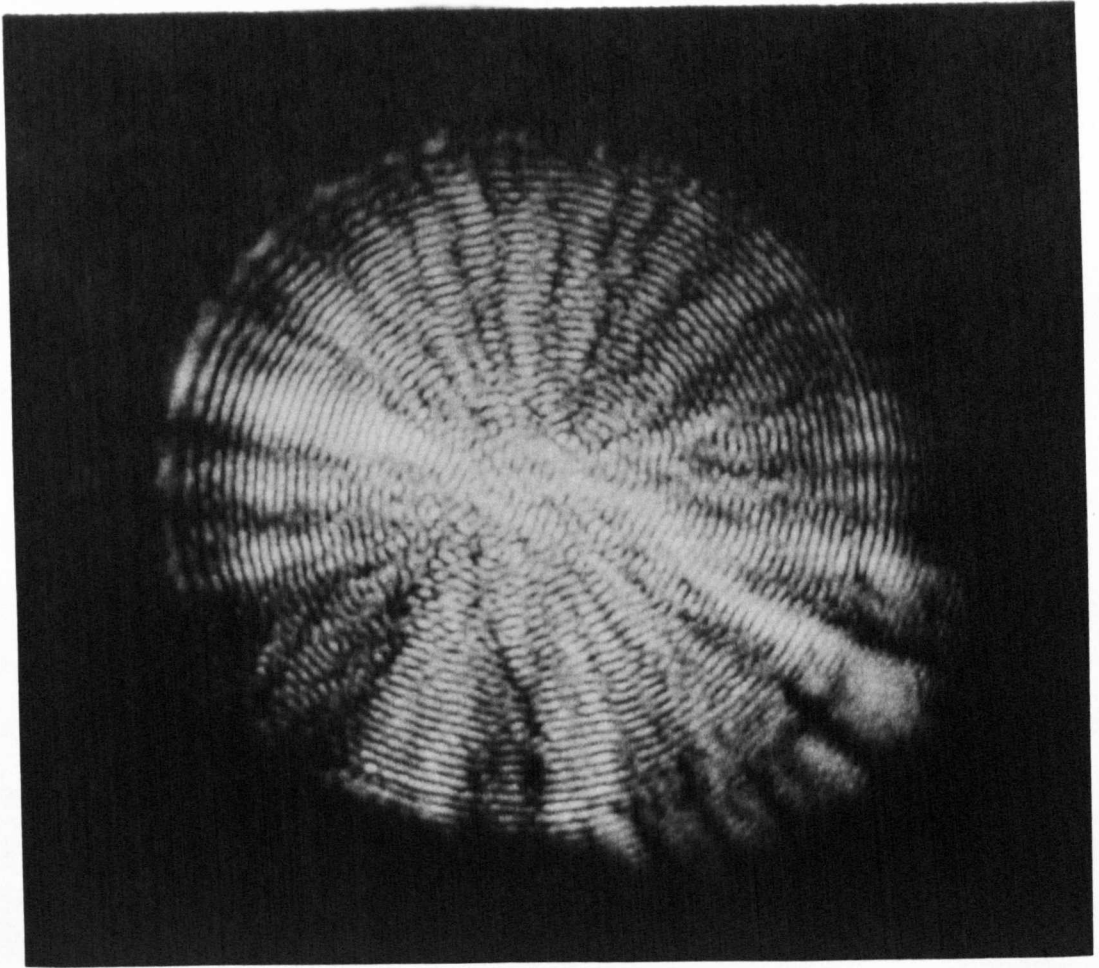


FIGURE 4.5 Near-field pattern of the $HE_{1,30}$ mode.

knowing the mode-field distributions given by equation 2.42. The situation can be thought of as the circular core aperture encoded with the amplitude and phase characteristics of the near field pattern of the mode and illuminated by plane wavefronts perpendicular to it. The far-field distribution (Fraunhofer region) is given by the Fourier transform, in r, ϕ and z coordinates, of equation 2.42. Such a calculation has been carried out by Kapany.⁷⁵

As Lipson⁹⁹ points out, the diffraction characteristics of the concentric ring patterns of equation 4.15 produce a single annular ring whose radius varies in proportion to the number of near-field rings.

(ii) Ray approach.

More simply, the geometric ray-optics model of the fibre termination may be considered. The rays of the inset of figure 4.3 represent the normals of the component wavefronts whose interference constitutes the high-order axial mode pattern. A single plane section of the fibre is shown, although, of course, the fibre is circularly symmetric. Applying Snells Law at points A and B in Figure 4.3 reveals a simple relationship between the mode propagating with characteristic angle α_e , and the emergent ray half angle α_f . It is, for refraction into air :

$$\frac{\beta}{k} = n_{\text{core}} \sin \alpha_e \quad 4.16$$

$$\sin \alpha_f = (n_{\text{core}}^2 - (\frac{\beta}{k})^2)^{1/2} \quad 4.17$$

Further, the effective refractive index, $\frac{\beta}{k}$, is normalized by

$$N_e = \frac{(\frac{\beta}{k} - n_{\text{clad}})}{(n_{\text{core}} - n_{\text{clad}})} \quad 4.18$$

Taking account of the total field in the fibre merely serves to extend α_f to the emergent cone half-angle, and we predict an annular ring pattern, having radius r_r , distance L_r away from the fibre termination, given by

$$r_r = L_r \tan \alpha_f \quad 4.19$$

4.3.5 Experimental far-field patterns of high-order modes, and comparison with theory.

Using the apparatus shown in Figure 4.3, the far-field radiation patterns were observed. As expected, the particular value of the axial propagation constant, β , determined by the input prism coupling angle, resulted in an annular ring pattern of characteristic radius. The emergent cone half-angle in air was found, using equation 4.19, for different values of $\frac{\beta}{k}$, and the result is plotted in Figure 4.6. The theoretical curve, derived from equations 4.17 and 4.18, is also included in this figure for comparative purposes.

Clearly there is excellent agreement between theory and experiment. Although it was possible to excite modes with

$$1 < \frac{\beta}{k} < n_{\text{clad}}$$

these modes were rapidly attenuated in the cladding material beyond the cladding transition and consequently did not appear at the output.

FIGURE 4.6 The graph of normalized

4.4 Further Modification of the Cladding-treated Region.

Up until this point the coupling has been restricted to large-diameter fibres supporting many modes. As pointed out in Section 4.3.2, the low-order modes were too closely bunched in $\frac{\beta}{k}$ to allow their individual excitation, and hence the preoccupation with high orders. For practical purposes the lowest orders are the

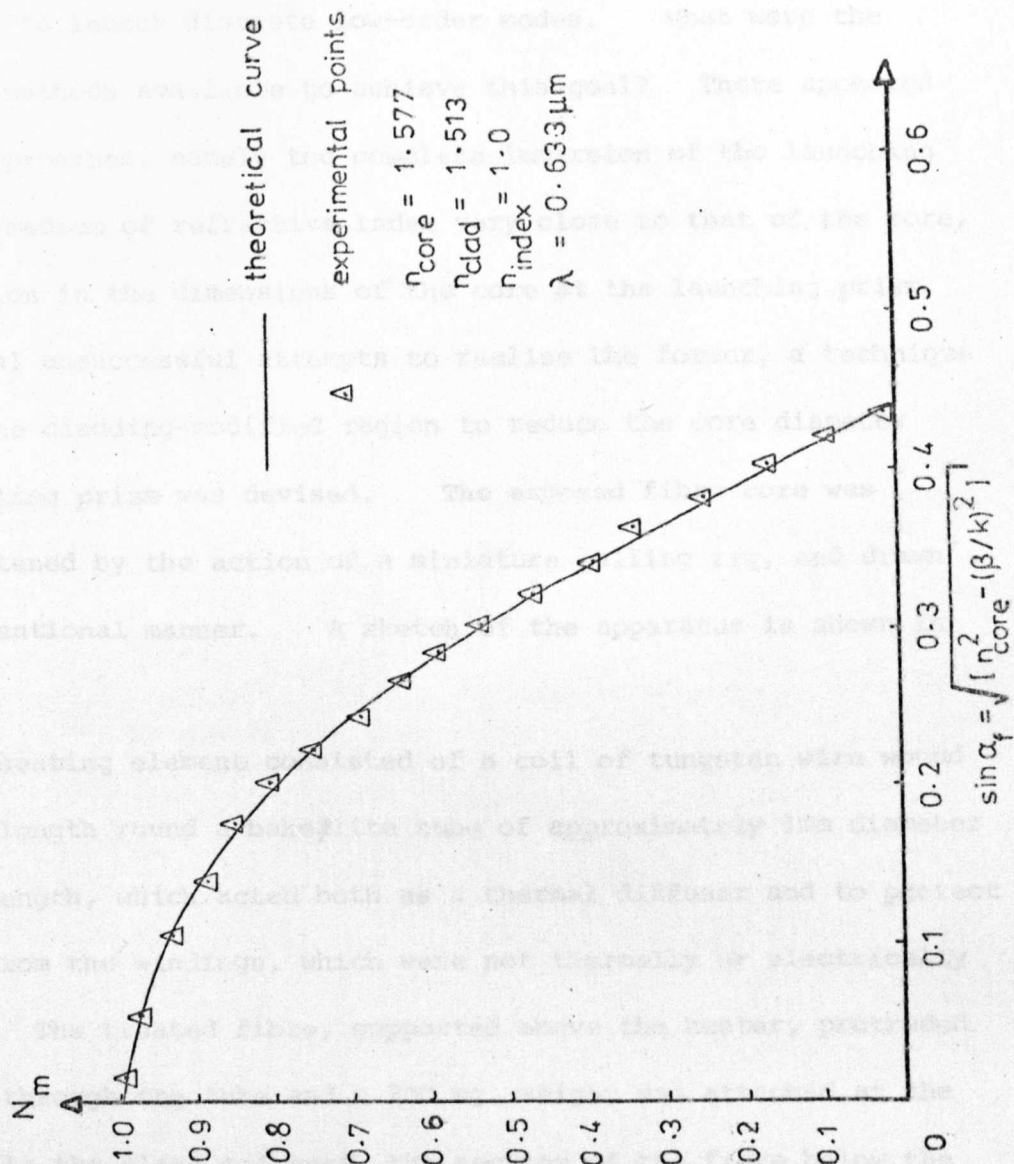


FIGURE 4.6 The graph of normalized effective refractive index against the sine of the emergent cone half-angle .

most important, particularly from the viewpoint of optical loss and mode conversion, and it was imperative that a method was developed to enable us to launch discrete low-order modes. What were the alternative methods available to achieve this goal? There appeared two basic approaches, namely the complete immersion of the launching system in a medium of refractive index very close to that of the core, or a reduction in the dimensions of the core at the launching prism. After several unsuccessful attempts to realise the former, a technique to repull the cladding-modified region to reduce the core diameter at the coupling prism was devised. The exposed fibre core was locally softened by the action of a miniature pulling rig, and drawn in the conventional manner. A sketch of the apparatus is shown in Figure 4.7.

The heating element consisted of a coil of tungsten wire wound for a 6 mm length round a bakelite tube of approximately 1mm diameter and 35 mm length, which acted both as a thermal diffuser and to protect the fibre from the windings, which were not thermally or electrically insulated. The treated fibre, supported above the heater, protruded vertically through the tube and a 200 mg. weight was attached at the bottom. As the glass softened, the section of the fibre below the hot zone slowly fell under gravity, producing a taper of the core diameter in the remaining material. Taper formation was not studied extensively though it was recognized that varying the weight varied the taper gradient, the heavier loads producing the shorter, sharper tapers. Tapers formed during the process were measured using an optical microscope and the result showed that, typically, a tenfold reduction in the diameter of the core, over some 31 mm (5×10^4 wavelengths) was achieved.

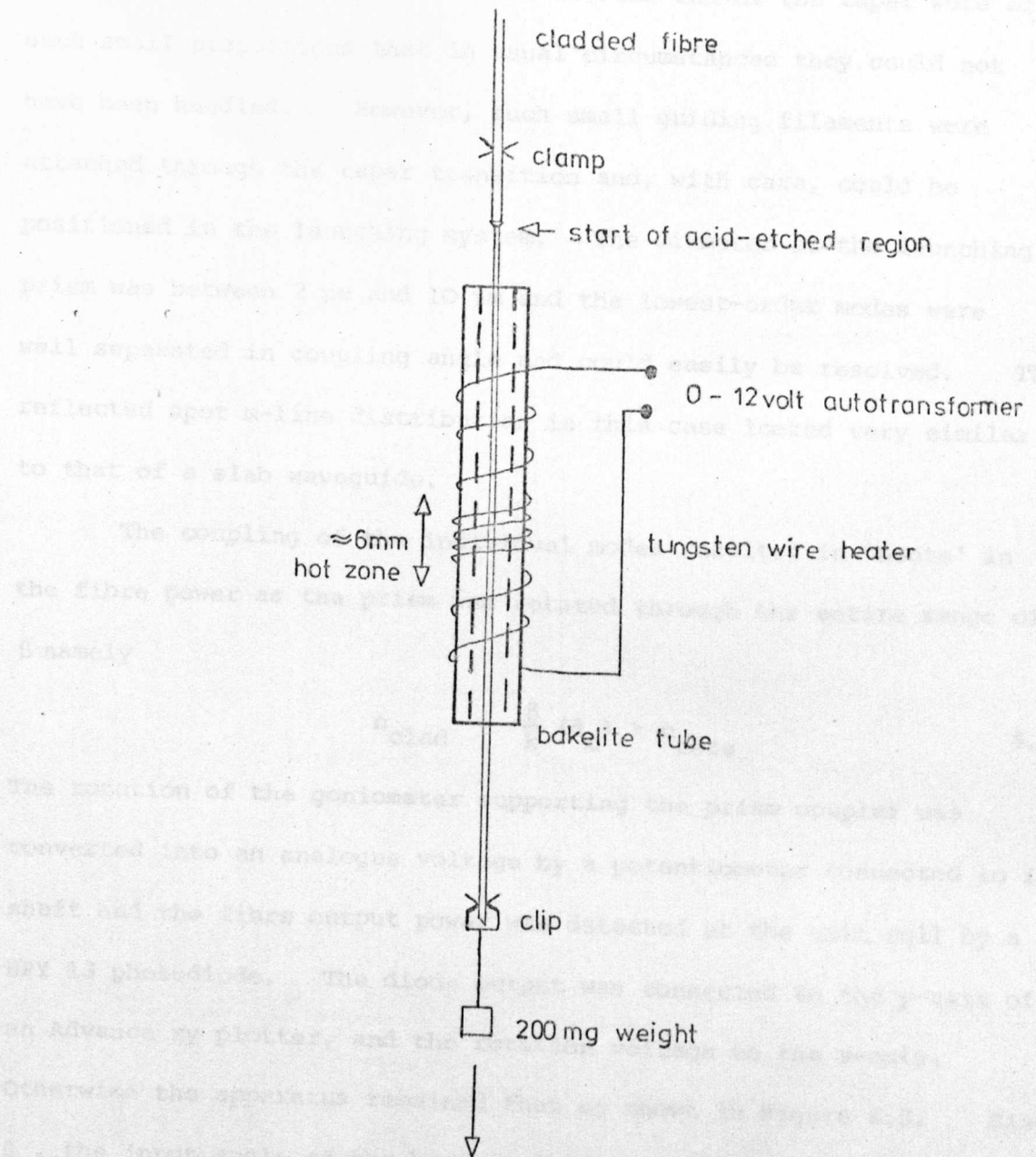


FIGURE 4.7 Fibre repulling apparatus.

4.5 Coupling to the Low-order Modes at the Treated Region with Further Modification.

4.5.1 Synchronous coupling.

The lengths of fibre at the extreme end of the taper were of such small proportions that in usual circumstances they could not have been handled. However, such small guiding filaments were attached through the taper transition and, with care, could be positioned in the launching system. The diameter at the launching prism was between 2 μm and 10 μm and the lowest-order modes were well separated in coupling angle and could easily be resolved. The reflected spot m-line distribution in this case looked very similar to that of a slab waveguide.

The coupling of the individual modes resulted in 'beats' in the fibre power as the prism was rotated through the entire range of β namely

$$n_{\text{clad}} > \frac{\beta}{k} (\theta_m) > n_{\text{core}} \quad 4.20$$

The rotation of the goniometer supporting the prism coupler was converted into an analogue voltage by a potentiometer connected to its shaft and the fibre output power was detected at the exit cell by a BPY 13 photodiode. The diode output was connected to the y-axis of an Advance xy plotter, and the rotation voltage to the x-axis. Otherwise the apparatus remained that as shown in Figure 4.3. Since θ_m , the input angle of the beam to the prism, was varied over a relatively small range given by equation 4.20 above, a linear scale of $\frac{\beta}{k}$ in the x-axis resulted. An experimental graphical output is shown in Figure 4.8, with the linear scale of $\frac{\beta}{k}$ superimposed.

Care must be taken in the interpretation of this result, as the relative heights of the peaks are uncalibrated because of:-

- (i) mode-dependent attenuation;

- (ii) mode-dependent excitation efficiency;
- (iii) movement of the input beam away from the optimum coupling region as the prism was rotated;
- (iv) inadequate plotter resolution.

The fibre used in this case had a core diameter of 25 μm which tapered over 30 mm to a diameter at the launching prism estimated at 2 μm . The laser was plane polarized. A comparison of the mode propagation constants in this example and the theory now follows.

4.5.2 Comparison with the theory of mode propagation in circular fibres.

The theory of mode propagation in circular fibres has been treated by many authors,^{79,100} and in particular by Gloge,⁶⁵ who presents theoretical curves for the normalised propagation constant in his notation 'b', our notation 'N') defined in equation 4.18, against the normalised frequency V, defined in equation 4.14, for the twenty lowest-order modes. For convenience this family of curves is shown in Appendix 4.1. The theoretical mode propagation constants N_e may be compared with the experimental values at the same normalised frequency value in order to verify the *modus operandi* and also to identify and characterise the excited modes. Figure 4.9 represents this comparison, with the experimental N_e values, obtained from the peaks in Figure 4.8, plotted against the theoretical predictions of Gloge, for a V-value of 11. The estimated V-value of the fibre at the prism was 12. Clearly there is good agreement, and identification of the modes can be obtained on this basis. For some of the higher-orders, however, the resolution of the apparatus was not sufficient to identify nearly-degenerate modes such as the HE_{51} and the HE_{81} , or the HE_{33} and the HE_{14} . The angle of skew of the beam and the fibre

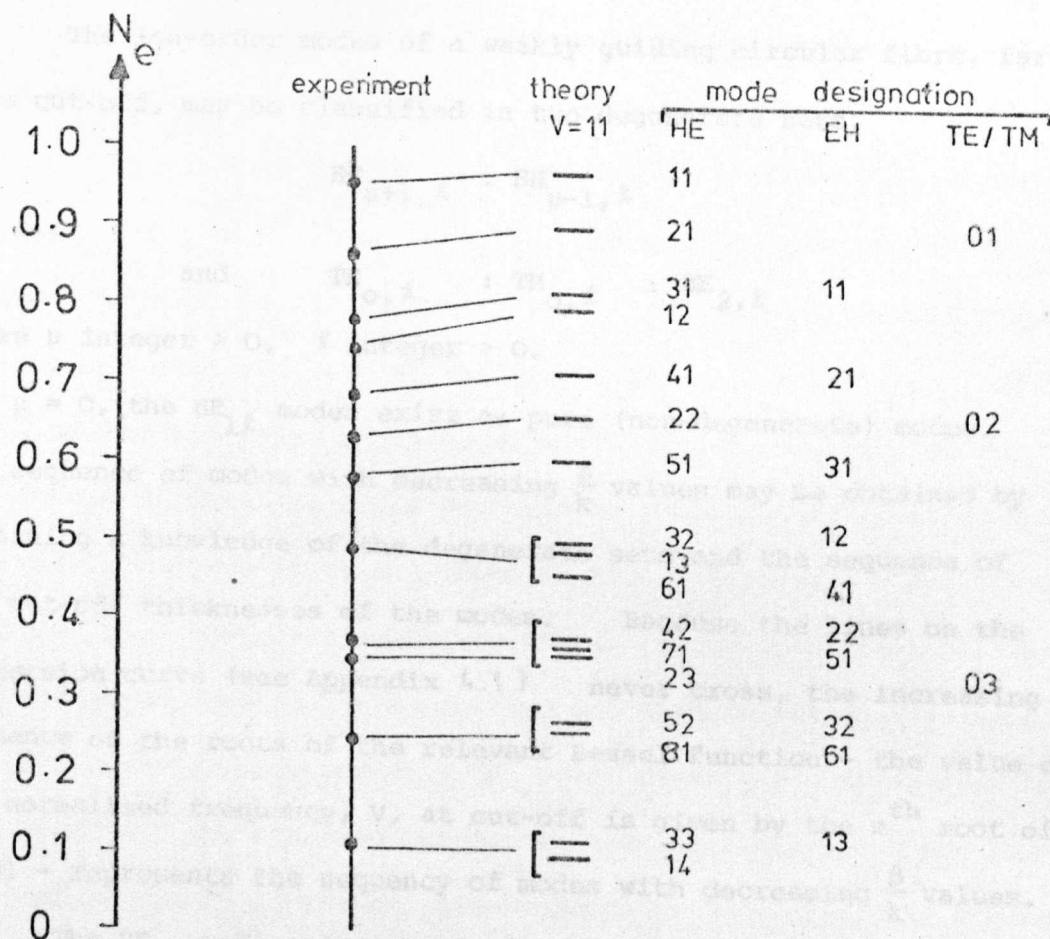


FIGURE 4.9 Comparison of theoretical and experimental propagation constants.

axis was approximately zero and variation of this angle would have undoubtedly selectively altered the coupling efficiency to the higher-order modes.

4.5.3 Near-field patterns of the low-order modes.

(i) Theory.

The low-order modes of a weakly guiding circular fibre, far from cut-off, may be classified in two degenerate sets,

$$HE_{\mu+1, \ell} : EH_{\mu-1, \ell} \quad 4.22$$

$$\text{and } TE_{0, \ell} : TM_{0, \ell} : HE_{2, \ell} \quad 4.23$$

where μ integer > 0 , ℓ integer > 0 .

For $\mu = 0$, the $HE_{1\ell}$ modes exist as pure (non-degenerate) modes.

The sequence of modes with decreasing $\frac{\beta}{k}$ values may be obtained by combining a knowledge of the degenerate sets and the sequence of the cut-off thicknesses of the modes. Because the lines on the Dispersion curve (see Appendix 4.1) never cross, the increasing sequence of the roots of the relevant Bessel function - the value of the normalised frequency, V , at cut-off is given by the m^{th} root of $J_{\mu}(0)$ - represents the sequency of modes with decreasing $\frac{\beta}{k}$ values.

The $HE_{1\ell}$ modes consist of concentric ring patterns having rings ($\ell-1$ radial zeros) and are unique in that they alone have an intensity maximum in the centre of the guide. Taking the HE_{ij} component ($i \neq 1$) of any other degenerate set, the i -value is related to the number of aximuthal zeros of the near-field distribution by

$$N_{\phi} = 2(i-1) \quad 4.24$$

and the j -value is related to the number of radial zeros by

$$N_r = (j-1) \quad 4.25$$

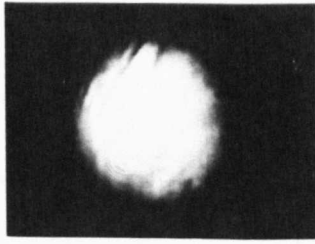
This represents a simplification of the situation because polarization effects, such as the combination of orthogonal modes,⁶⁵ (observed but not recorded here) were omitted.

(ii) Experiment.

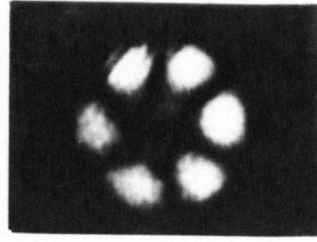
Though the technique described in the previous section adequately determined the mode structure, the most attractive and descriptive method was the direct observation of the near-field patterns of the waveguide modes. The low-order modes were excited by the prism coupler at the cladding-modified and repulled section, and, because of the gradual slope, the mode field distribution established at launching remained through the core taper and the cladding transition (assuming, of course, that $\frac{\beta}{k} > n_{\text{clad}}$) and was constructed in its original form at the fibre termination. Because of the relatively large diameter of the core at that point (25 - 50 μm) the excited mode field was visible using a low-power travelling microscope, as in Figure 4.3. The near-field patterns of the eight lowest-order modes of a clad multimode fibre are shown in Figure 4.10a-h. In this case the input beam was plane polarized and an analyser (a plane polarizer) was interposed between the microscope and the ground-glass screen. The core diameter here was 25 - 30 μm . Clearly the effects of the core taper and the cladding transition were negligible for the lower-order modes, as the observed near-field patterns recorded in Figure 4.10 were consistent with the theoretical predictions for pure or degenerate combinations of guided modes.

4.5.4 Comparison of the actual and expected intensity distributions.

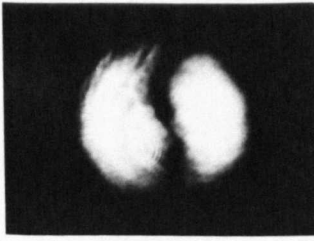
The comparison of the experimental results and the theoretical predictions are embodied in Figure 4.11 which presents in tabular form the mode sets in sequence of decreasing $\frac{\beta}{k}$, and a sketch of the expected near-field distribution, cross-referenced to the photographs of Figure 4.10.



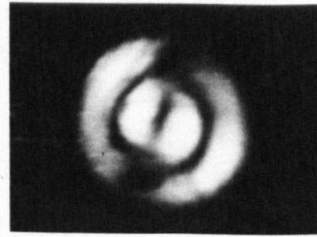
(a) HE_{11}



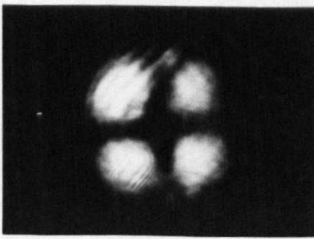
(e) HE_{41}, EH_{21}



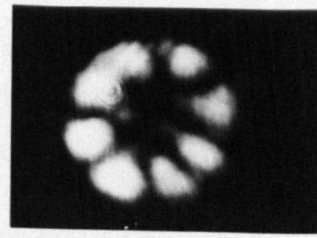
(b) $HE_{21}, TE_{01}, TM_{01}$



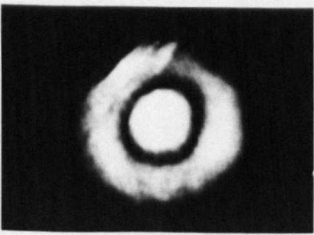
(f) $HE_{22}, TE_{02}, TM_{02}$



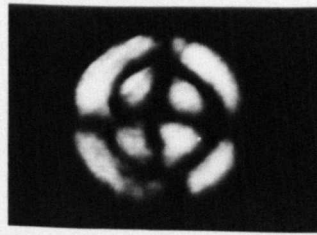
(c) HE_{31}, EH_{11}



(g) HE_{51}, EH_{31}



(d) HE_{12}



(h) HE_{32}, EH_{12}

FIGURE 4.10 NEAR - FIELD PATTERNS OF THE
LOWEST - ORDER MODES OF A
CIRCULAR FIBRE WAVEGUIDE .

mode	<div> <div>decreasing β/k</div> <div>∇</div> </div>	Bessel function zeros	expected n.f. intensity distributions	experimental n.f. intensity distributions (FIGURE 4.10)
HE_{11}		0		a
$HE_{21}, TE_{01}, TM_{01}$		2.405		b
HE_{31}, EH_{11}		3.832		c
HE_{12}		3.832		d
HE_{41}, EH_{21}		5.136		e
$HE_{22}, TE_{02}, TM_{02}$		5.520		f
HE_{51}, EH_{31}		6.380		g
HE_{32}, EH_{12}		7.016		h

FIGURE 4.11 Comparison of experimental results and theoretical predictions for the low-order fibre modes.

There is excellent agreement between Figures 4.10 and 4.11, further indicating that the evanescent wave coupling at the prism base is in accordance with the theory.

4.5.5 Fibre waveguide mode polarization and its implications.

The relation of fibre waveguide mode polarization relative to the polarization of the driving wave becomes an intriguing and complex study in a guide which is circularly symmetric, and critically important where circular fibres are to be coupled to planar or rectangular structures which have two orthogonal mode polarizations only.

An attempt was made to study the relationship between the input beam polarization and that of the observed mode field. The fundamental, HE_{11} , mode, when excited by a plane polarized beam, was 90% plane polarized after travelling 100 mm (1.58×10^5 wavelengths) along a straight fibre.

After a length of fibre, with bends and loops, we predict that there would be no way of determining the plane of polarization at the coupling point - that is assuming that the wave does remain plane polarized.

It is obvious that the coupling properties of circular fibres are complicated by the additional considerations of mode polarization, and a more complete study of the problem is regarded as a future necessity.

4.6 Summary and Conclusions.

The aim of the chapter was to extract and analyse detailed information about the evanescent field coupling of cladding-modified fibres, to help evaluate the method by which thinfilm and fibre waveguides could be coupled in a more controllable fashion.

Excitation of the modes of a multimode fibre at a cladding-modified region by a prism coupler has been studied. Phase-matching considerations led to the introduction of two synchronous angles of

the prism which define the propagating mode field. The near-field patterns, the far-field patterns, and the reflected-spot 'm-line' patterns were discussed, and favourably compared with the theoretical predictions.

The desire to excite and observe the low-order modes required a reduction in the V-value of the fibre at launch, and a technique was described of repulling the cladding modified region in a miniature electrical furnace to produce a taper with, typically, a ten-fold reduction in the core diameter over 5×10^4 wavelengths. The synchronous coupling of the quasi-multimode fibre was then investigated and the propagation behaviour of the modes were found to closely follow the established theoretical model. Finally the near-field patterns of the low order modes were recorded and explained.

The primary conclusion to be drawn from the work of this chapter is that evanescent wave coupling involving clad fibre structures is possible, given suitable cladding modification. The most serious factors limiting the practicality of couplers involving circular fibres can be concluded to be

- (i) the dimensions of a quasi-multimode fibre in air would have to be a few microns only, increasing the handling and positioning problems;
- (ii) determining and maintaining the waveguide mode polarization at the coupling regions;
- (iii) the core taper and the cladding transition necessary to make this coupler possible would ultimately lead to optical loss and a degree of unreliability and mechanical instability.

The experimental techniques will find useful application in the study of the propagation characteristics of circular fibres, and within this context there is much scope for future work.

APPENDIX 4.

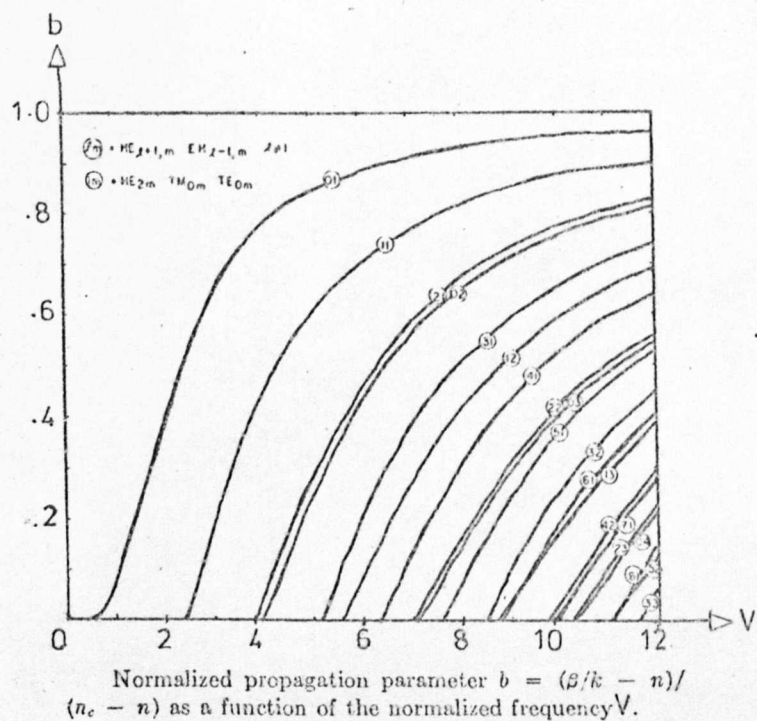


FIGURE A4.1 Normalized propagation
constant as a function of
the normalized frequency V
after Gloge⁶⁵.

5.1 General Introduction.

Circular fibre waveguides in the form envisaged for practical optical communication systems, either single-mode or multimode in design, were shown in the last chapter to be unsuitable for evanescent field coupling to integrated optical waveguides. Even in a form modified to make coupling possible, the handling difficulties of sub-micron glass filaments were considered prohibitive. Another flexible waveguiding structure would have to be found which had available evanescent fields in the interaction region, suitable for transverse coupling, yet which was large enough to be handled. It was clear that the geometry of the coupling fibre was not, at this stage, of paramount importance. For example, the coupling of the fundamental, HE_{11} , modes of two circular fibres of core diameter 'd' is not significantly different from the coupling of two rectangular fibres of equivalent refractive index and core section $2d \times d$, carrying the E_{11} modes, as shown by Marcatili,²⁰ based on results by Jones.¹⁰¹ In this simplistic argument, the rectangular fibres could be replaced by slab waveguides where the beam confinement of the fundamental mode is of the same order as the thickness d. It would, therefore, appear logical to use a fibre which was flexible analogue of the thin film waveguides and consequently of a planar or rectangular section.

Mechanical support was provided by the bulk of the waveguide in the width direction in the case of planar ribbon fibre waveguides, and by an additional supporting substrate for the sandwich ribbon fibres (Figure 5.1). At least one side of the ribbon fibres was left unclad to allow evanescent field coupling to other structures. Because the glass ribbons and the thin film guides support similar

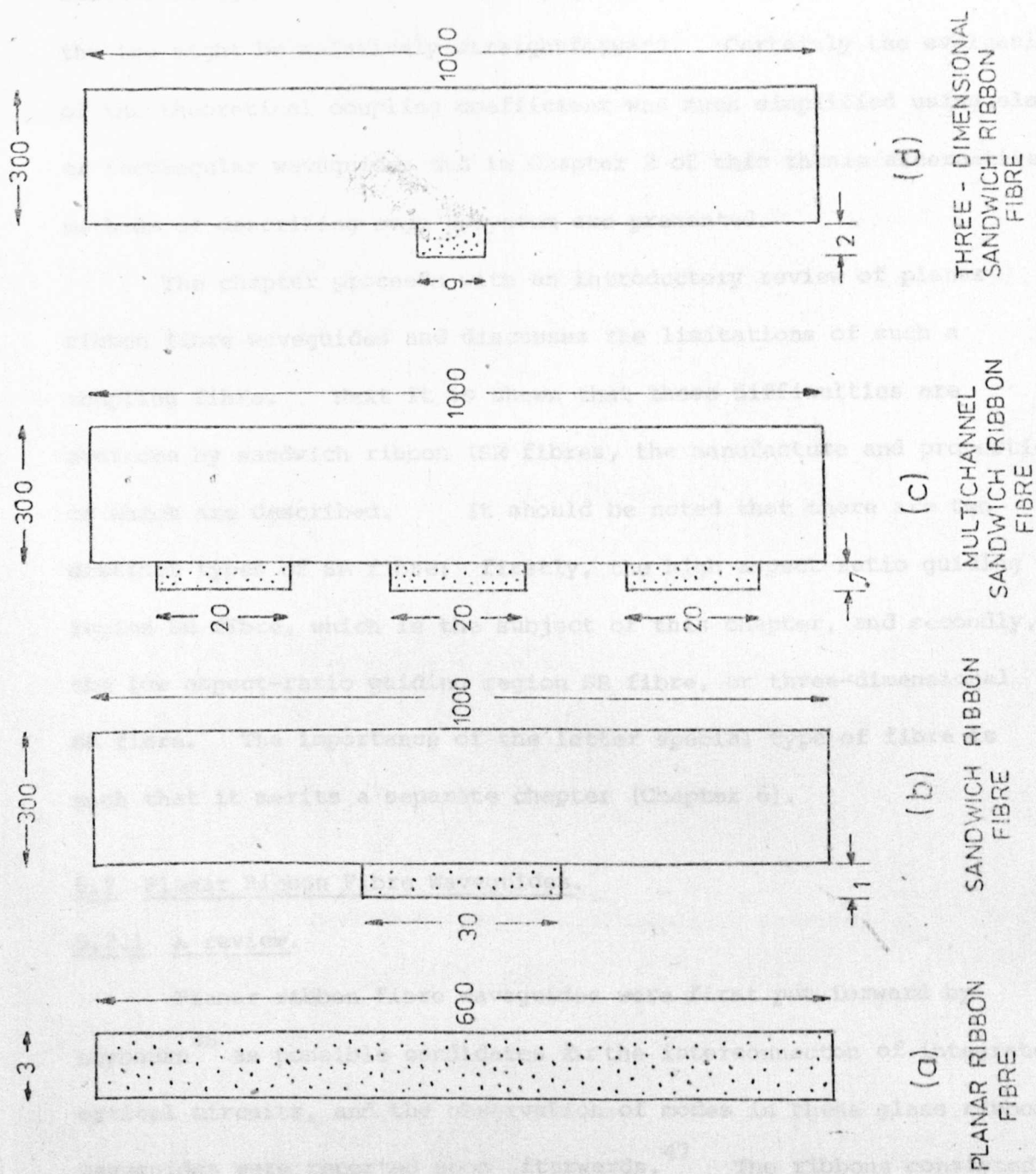


FIGURE 5.1 Cross - sections of various ribbon fibre waveguides .

The typical dimensions are in microns

similar waveguide modes, it was hoped that the coupling between the two might be relatively straightforward. Certainly the evaluation of the theoretical coupling coefficient was much simplified using slab or rectangular waveguides and in Chapter 2 of this thesis alternative methods of describing such a system are presented.

The chapter proceeds with an introductory review of planar ribbon fibre waveguides and discusses the limitations of such a coupling fibre. Next it is shown that these difficulties are overcome by sandwich ribbon (SR) fibres, the manufacture and properties of which are described. It should be noted that there are two distinct types of SR fibre: firstly, the high aspect-ratio guiding region SR fibre, which is the subject of this chapter, and secondly, the low aspect-ratio guiding region SR fibre, or three-dimensional SR fibre. The importance of the latter special type of fibre is such that it merits a separate chapter (Chapter 6).

5.2 Planar Ribbon Fibre Waveguides.

5.2.1 A review.

Planar ribbon fibre waveguides were first put forward by Laybourn⁴⁶ as possible candidates for the interconnection of integrated optical circuits, and the observation of modes in these glass ribbon waveguides were reported soon afterwards.⁴⁷ The ribbons consisted of thin unclad glass guiding filaments (Figure 5.1a) pulled by hand from sheet cover-slip glass, 200 μm thick (Pilkington Glass Ltd., refractive index of 1.522 at 0.633 μm wavelength). Since no top-feed was provided to the tubular electric pulling furnace, the width of the ribbon constantly diminished, although the original ratio of width to thickness (the aspect ratio), 200:1, was retained down to thicknesses of a few microns. The minimum thickness possible by this technique was set by the ability to handle and control the very

fine glass ribbons, and was about $1.5 \mu\text{m}$. These ribbons were assumed to be infinite in the y -direction and with no variation of the fields in that direction. With the dielectric slab approximation, Maxwell's equations were solved for propagation along the length of the ribbon.⁴⁷ The solutions for the guided modes are obtained from the eigenvalue equation for a symmetric slab waveguide (equation 2.6) given by:

$$k_1 t = 2 \tan^{-1} \xi_{10} \frac{k_o}{k_1} + m\pi \quad 5.1$$

where

$$\xi_{10} = 1 \quad \text{for TE modes}$$

$$= \left(\frac{n_1}{n_o}\right)^2 \quad \text{for TM modes}$$

$$k_1^2 = n_1^2 \omega^2 \mu_o \epsilon_o - \beta^2$$

$$k_o^2 = \beta^2 - n_o^2 \omega^2 \mu_o \epsilon_o$$

and

n_1 = refractive index of ribbon

n_o = refractive index of cladding material

t = ribbon thickness.

The plot of normalized effective refractive index, defined as

$$N_e = \frac{\frac{\beta}{k} - n_o}{n_1 - n_o} \quad 5.2$$

against the ribbon thickness, is presented on Figure 5.2 for the TE_m and TM_m modes of a glass ribbon of refractive index 1.522 in air ($n_o = 1.0$). The dispersion graph of Figure 5.2 shows that at the minimum thickness of $1.5 \mu\text{m}$ the number of modes supported was six in each of the dominant polarizations. Every planar ribbon waveguide was, therefore, multimode. For single-mode transmission at $0.633 \mu\text{m}$, the ribbon would have to be less than $0.26 \mu\text{m}$ thick, which was not a practical proposition.

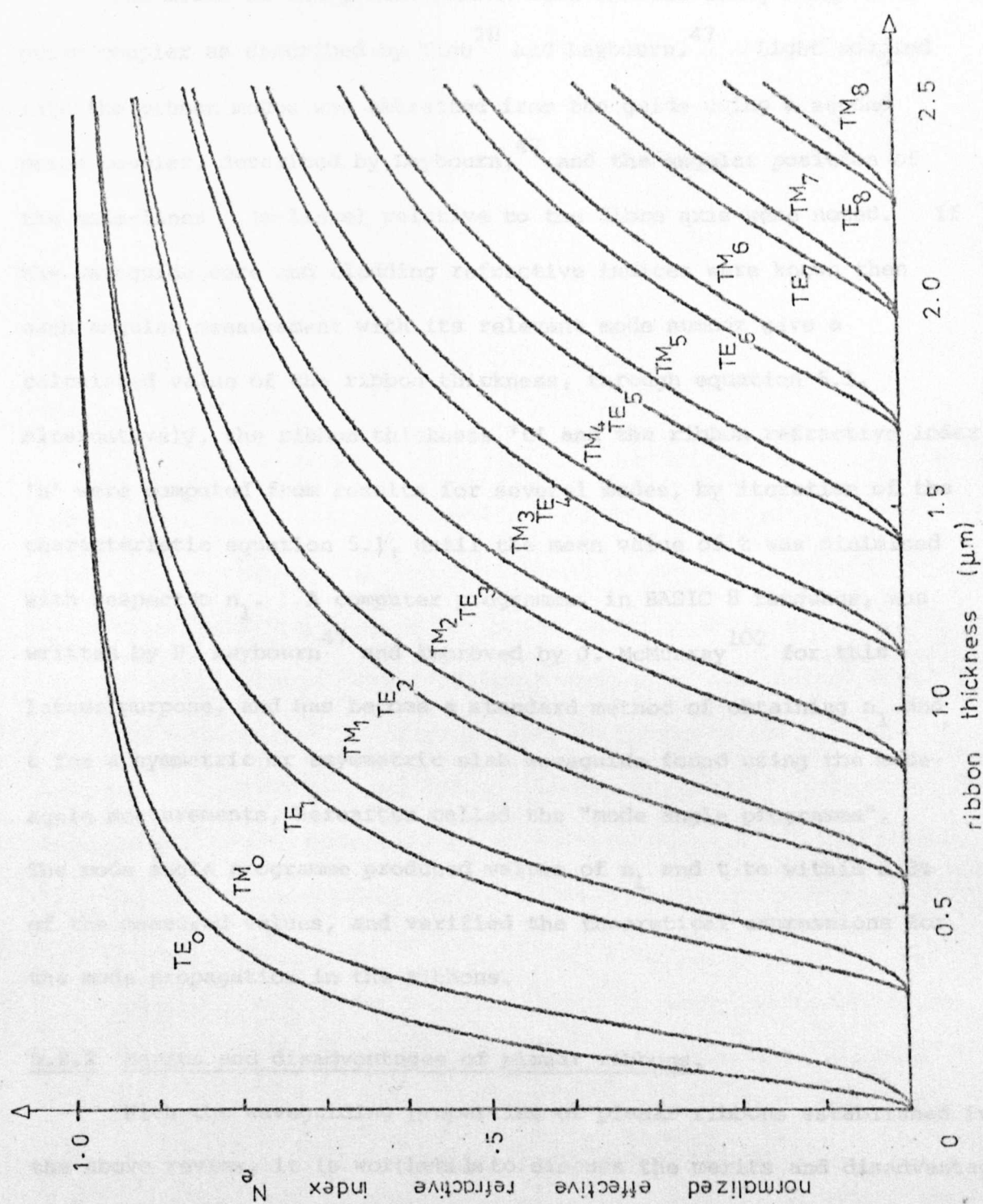


FIGURE 5.2 Dispersion graph for a planar ribbon fibre, refractive index = 1.522 at $0.633 \mu\text{m}$.

The modes of the planar ribbon were excited using a high-index prism coupler as described by Tien²⁸ and Laybourn.⁴⁷ Light coupled into the ribbon modes was extracted from the guide using a second prism coupler, described by Laybourn,⁴⁷ and the angular position of the mode-lines³⁰ (m-lines) relative to the fibre axis were noted. If the waveguide core and cladding refractive indices were known then each angular measurement with its relevant mode number gave a calculated value of the ribbon thickness, through equation 5.1. Alternatively, the ribbon thickness 't' and the ribbon refractive index 'n' were computed from results for several modes, by iteration of the characteristic equation 5.1, until the mean value of t was minimised with respect to n_1 . A computer programme, in BASIC 8 language, was written by P. Laybourn⁴⁷ and improved by J. McMurray¹⁰² for this latter purpose, and has become a standard method of obtaining n_1 and t for a symmetric or asymmetric slab waveguide found using the mode-angle measurements, hereafter called the "mode angle programme". The mode angle programme produced values of n_1 and t to within 0.3% of the measured values, and verified the theoretical expressions for the mode propagation in the ribbons.

5.2.2 Merits and disadvantages of planar ribbons.

With the waveguiding properties of planar ribbons established in the above review, it is worthwhile to discuss the merits and disadvantages of the ribbons.

The planar ribbons were simple to manufacture from readily available material. However, because they were unclad, contamination of the glass surface during and subsequent to pulling, increased the optical loss by the scattering of the evanescent wave at any inhomogeneity. Freshly manufactured ribbon fibre had an optical loss of 0.4 dB/cm for the lowest order mode in a 3 μ m thick guide, which

deteriorated as the fibre was handled. A planar ribbon fibre could seldom be removed and replaced in a particular configuration without the optical loss increasing. Another factor that increased the handling difficulties was that the thin glass filaments were prone to electrostatic charging, and sometimes adhered to, or were repelled from, other dielectric materials.

5.2.3 Planar ribbons in a coupling situation.

(i) High order modes.

As Laybourn describes,⁴⁷ a higher order axial mode of a planar ribbon guide tends to scatter into lower order modes propagating at angles to the ribbon axis such that the axial wave velocities of the lower order modes are equal to the phase velocity of the higher order mode. A significant amount of power carried by the excited mode transfers down in mode order at an estimated rate of the order of 3 dB/5cm. This factor, and the additional high attenuation of higher order modes, made even the thinnest fibre (1.5 μm) unattractive for coupling purposes using the available higher order modes.

(ii) Lowest order modes.

Let us now consider the possibility of using the lowest order mode in the 1.5 μm thick fibre for directional coupling. In this case we shall examine the coupling of two similar unclad ribbon fibres, of refractive index 1.522, with an air buffer layer of thickness 'c' between the two. The dispersion graph of Figure 5.2 indicates that for an isolated 1.5 μm thick fibre, the difference in the normalised propagation constant between the zero order and the first order TE modes, $\Delta\beta_{01}/\beta_0$, was 1.353×10^{-2} . Consider two planar ribbon guides, 1.5 μm thick, pressed together in intimate contact. The maximum power transfer between two coupled modes, having propagation constants $\Delta\beta$ apart, is given in equation 2.81. Restating this in a

rearranged form

$$K = \frac{\Delta\beta}{2} \left[\hat{\eta}^{-1} - 1 \right]^{1/2} \quad 5.3$$

The expression for the coefficient for a slab waveguide coupler is given by equation 2.86. Substituting $n_1 = 1.522$, $c=0$ and $\frac{\beta_0}{k} = 1.506$ gives $K = \frac{\pi}{2 \times 50 \mu\text{m}}$. Substituting this value of K and that of $\Delta\beta_{01}$ into equation 5.3 reveals $\hat{\eta} = 9\%$ or -10.5 dB, and represents the best value of crosstalk from the zero to the first order modes of a planar ribbon-to-planar ribbon coupler. As one might expect with ribbons in intimate contact, the phase difference between the lowest order modes is not sufficient to prevent coupling from one order to the other. The argument may be extended to the coupling of the $m = 1$ to the $m = 2$ modes of the guides, and so on. This coupling "mode crosstalk" would be apparent even for the smallest ribbon, and the coupling between the modes could result in power equalisation after an interaction of a few coupling lengths. The phenomenon of power equalisation and mode scattering was in fact the substance of the qualitative observations described previously.⁴⁶ The major disadvantage of planar ribbon fibres was, therefore, recognized to be the inherent multimode nature of the guides, and though the concept of using planar structures was firmly established, the further refinements of (i) a semi-clad structure to assist mechanical handling and reduce optical loss through contamination of the waveguide surface, and (ii) reduced waveguide thickness to support a single guided mode and eliminate crosstalk mode coupling, must now be entertained.

5.3 Sandwich Ribbon Fibre Waveguides.

5.3.1 Introduction.

The many disadvantages of unclad planar ribbon fibres were overcome by the development of a novel fibre which will be described in this section. The "sandwich ribbon fibre waveguide" was a descriptive term thought best to describe the structure. The fibre consisted of a sandwich of three dielectric materials - air, as the superstrate, a high-refractive-index glass as the guiding region, and a lower refractive index substrate as support. The guiding region consisted of a very thin ribbon of glass which, having a large width to thickness ratio, was essentially planar in construction. The substrate dimensions were much larger than the guiding region, as can be seen in Figure 5.1b. The top surface of the guiding region was left unclad (air clad) to allow evanescent field coupling to thin film waveguides or other structures such as high-index prism couplers. Similar fibres were developed by other workers at Washington University⁴² who, with the thin film interconnecting possibilities in mind, labelled the waveguide an "externally mounted fibre". This latter term embodied the recognition that the fibres were essentially flexible continuations of the thin film waveguides and were most suited to interconnect them. After a description of the manufacture and properties of sandwich ribbon (SR) fibres, the uses to which these fibres may be put are discussed, along with some other interesting developments and applications.

5.3.2 Manufacture of SR fibre waveguides.

Sandwich ribbon fibres are composite glass optical waveguides manufactured in a two-step process. The starting materials consisted of two slabs of glass, usually of microscope slide dimensions, one of high-refractive-index glass such as Schott BAK1 ($n_D = 1.5725$) and the other of lower index glass such as a Chance soda-lime glass ($n_D = 1.522$)

or Corning 7059 ($n_D = 1.530$). The initial preform of the high refractive index glass was drawn at a temperature suitable for the particular material - BAKI, for example, at 800°C . The ribbon, approximately 1 mm wide and $40\ \mu\text{m}$ thick was laid onto the surface of the low index glass slab along its axis, and retained at either end with small clips or drops of epoxy resin. This secondary preform was then mounted in the fibre pulling rig and drawn at high temperature (for example for the BAKI/7059 combination, 850°C) as previously described.⁴⁷ Our initial report of the manufacture of SR fibres⁴³ included an intermediate step in the process, where the high-index filament and the substrate preform were loosely bonded together in an electrical furnace at high temperature, prior to the last draw. However, this stage of the process was found to be unnecessary, as the glasses bonded intimately in the final draw anyway, and tended to flow naturally into each other as the pulling commenced. Using the direct technique to some extent allowed combinations of glasses slightly mismatched in their thermal expansion coefficients and softening temperatures. For example, it was possible to pull directly BAKI/7059 combinations which were found to be otherwise thermally incompatible. After the final draw, the aspect ratio of the cross-section of the secondary preform was retained, and the two parts of the sandwich became intimately attached. No preform top-feed was supplied to the pulling-rig furnace and consequently the dimensions of the fibre decreased along its length. Short lengths of fibre with effectively constant cross-section were used, and could be chosen to be multimode or single-mode in operation.

5.3.3 Cross-section of a single-mode SR fibre waveguide.

The cross-section of a single-mode sandwich ribbon fibre, produced by this technique, is shown in Figure 5.1b, and an interference microscope picture of the top surface of an SR guide, showing the

guiding layer 45 μm wide and 0.9 μm thick, is presented in Figure 5.3. The interference photograph was taken with the sample vacuum-coated with a highly reflecting gold/palladium mixture, and illuminated with sodium light ($\lambda = 0.589 \mu\text{m}$) and shows the topographical details only. The vertical separation of the fringes was 0.29 μm . The photograph indicated that the substrate and the guiding layer did not lie perfectly flat, possibly because the centre of the high-index region had sunk into the mass of the substrate or because of differential contraction when the ribbon cooled. These edge effects were not thought to be important as the guide was heavily overmoded in the width direction.

The refractive indices associated with the ribbons had to be corrected from the bulk value to take into account the compaction effects of pulling.⁵⁹ A typical reduction in refractive index from the bulk value due to the rapid-freezing-induced stress was - 0.3%, though this figure depended on the composition of the glass.

With the refractive index profile and the dimensions of the guiding region known subsequent to manufacture, it was possible to relate the theoretical propagation characteristics of SR fibres to the experimentally observed properties.

5.4. Propagation Characteristics of SR Fibre Waveguides.

5.4.1 Validity of the slab waveguide approximation.

The sandwich ribbon fibre, having a high width-to-thickness ratio guiding region, may be treated as an asymmetric slab waveguide, with modal propagation characteristics governed by the eigenvalue equation (equation 2.6).

How valid is this approximation? If the waveguide is considered as rectangular with an aspect ratio 'r', entirely embedded in a cladding medium, then there will be approximately 'r' times the number of modes

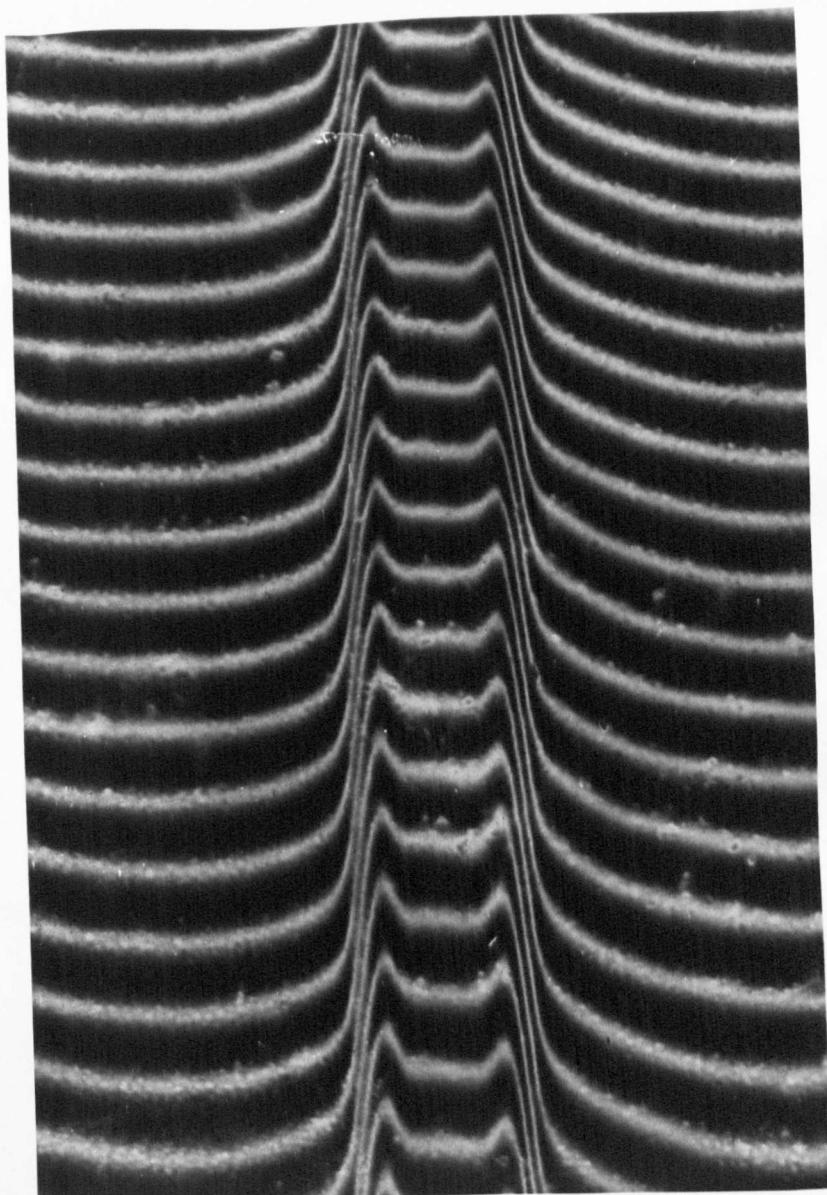


FIGURE 5.3 Interference microscope
photograph of the guiding region
of a single - mode SR fibre ,
 $45\mu\text{m} \times 0.9\mu\text{m}$.

in the thickness direction, existing in the width direction. In the case of an SR fibre the thickness-direction modes are bounded between the substrate refractive index and the guide refractive index, whereas the width-direction modes are bounded by a lower effective refractive index equal to unity. The guide is strongly asymmetrical and the ratio of the number of width modes to thickness modes becomes greater than 'r'. For example, the single-thickness-mode SR fibre shown in Figure 5.1b has some 175 width-direction modes. It has been shown⁴⁷ that such a density of modes prohibits individual excitation and therefore the assumption of a mode continuum in the width direction - the slab approximation - was considered valid.

5.4.2 The theoretical dispersion characteristics.

The modal dispersion graph, derived using the slab waveguide approximation, was calculated and plotted using a PDP8 digital computer, and is presented for a lead-glass/microscope slide SR fibre in Figure 5.4. The y-axis of this graph is in units of normalised propagation constant, defined by equation 5.2, and the x-axis is the guiding region thickness in microns. One can immediately recognise that the fundamental TE and TM modes have a finite thickness cut-off value and that the thickness for single-mode operation lies between $0.36\text{ }\mu\text{m}$ and $1.25\text{ }\mu\text{m}$ at $0.633\text{ }\mu\text{m}$ wavelength for the particular glasses used.

5.4.3 Excitation of the SR fibre waveguide modes.

Plane polarized light at $0.633\text{ }\mu\text{m}$ wavelength for a helium-neon laser was launched into SR fibres by a high-index prism coupler, in a manner similar to that described by Laybourn.⁴⁷ The ribbon was clamped by the action of a soft rubber pad with its guiding layer in contact with the base of the prism. Because the mechanical pressure was applied on the opposite side of the substrate from the guide,

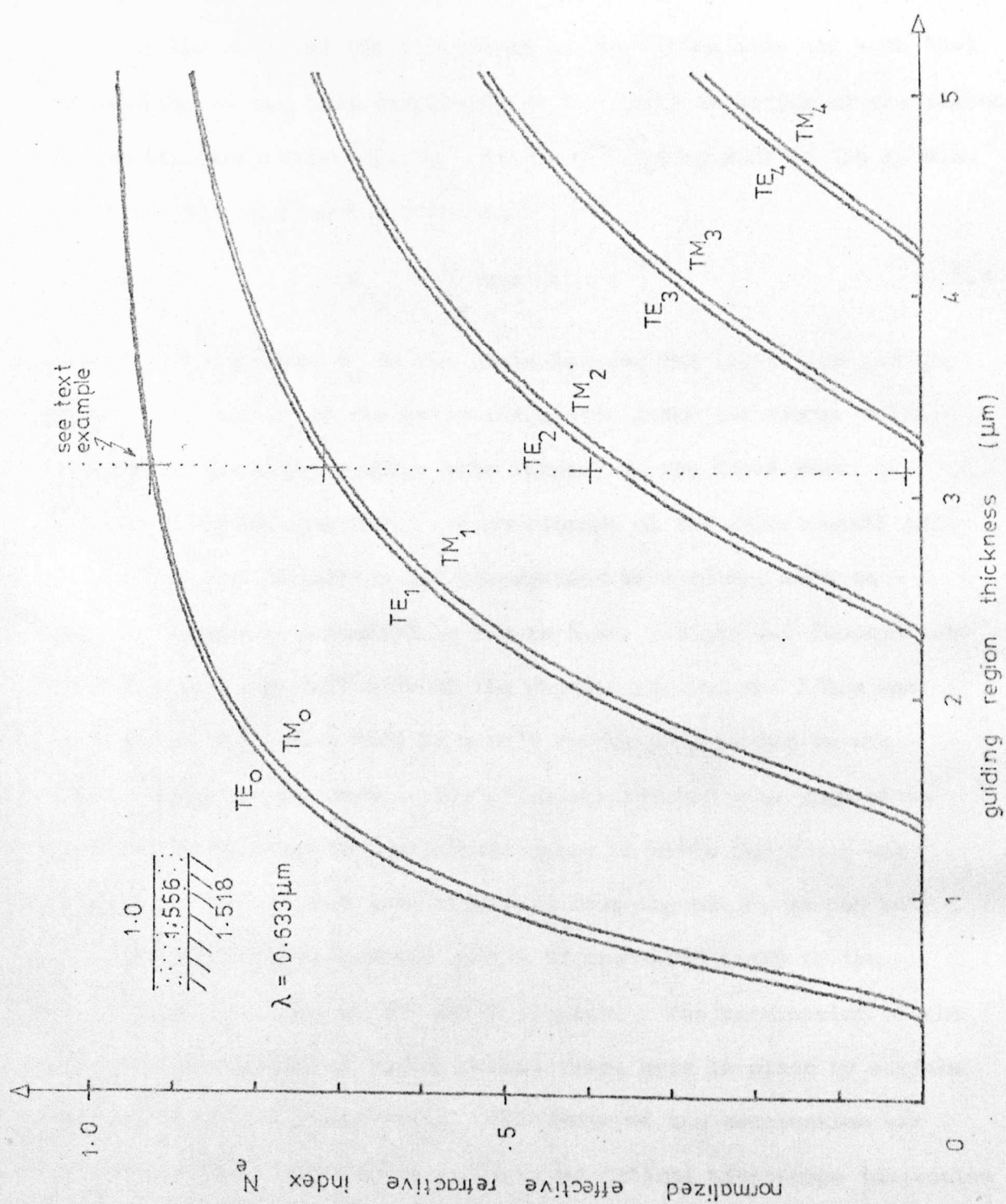


FIGURE 5.4 Dispersion graph for a sandwich -
ribbon fibre .

the support did not contribute to the optical loss.

If the angle of the input beam to the ribbon axis was such that the velocity of the beam wavefronts in the axial direction of the ribbon equaled the phase velocity, u_{p_m} of the m^{th} guided mode in the ribbon, that mode will be launched such that

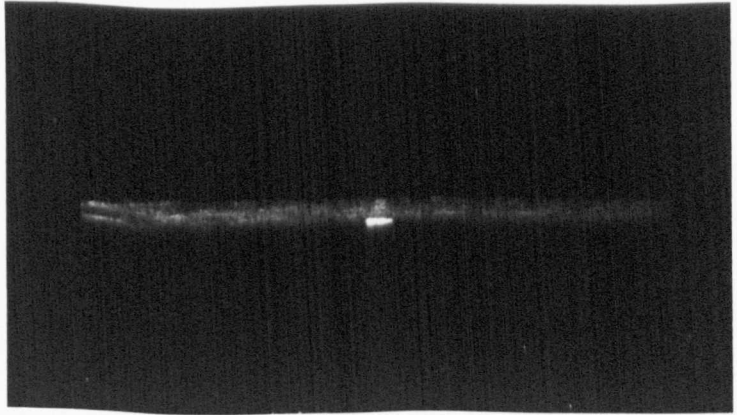
$$u_{p_m} = \frac{c}{n_p} \sec \theta_m \quad 5.4$$

where $c = 3 \times 10^8$ m/s, θ_m is the angle between the light beam and the ribbon axis, and n_p is the prism refractive index (as Figure 4.1).

By rotating the input coupler with respect to the input beam, any one mode could be launched. A photograph of the experimental set-up, showing the excitation and propagation of a guided mode in a sandwich ribbon is presented in Figure 5.5a. Light was focused into the prism from the left side of the photograph, and the fibre was pressed onto the prism face by a soft rubber pad, bonded to the aluminium bar of the clamp. The prism was rotated with respect to the input beam using the goniometer table to which the clamp was attached. The excited mode travelled down the guide, as can be seen by the bright horizontal streak of scattered light in the filament to the right of the prism coupler. The termination of the fibre was index-matched using nitrobenzene, held in place by surface tension against a glass plate. The image of the termination was reconstructed in space using a low-power optical microscope (objective 8x, n.a. 0.2, eyepiece 10x wide field) and photographed. The result is shown in Figure 5.5b. The high light density of the guiding region is visible with some scattered light, transmitted in the substrate, showing the overall cross-section of the fibre.

From the mode launching angles the thickness and refractive index of the guiding layer were computed using the mode angle programme, and compared with those obtained by direct measurement.

(b)



(a)

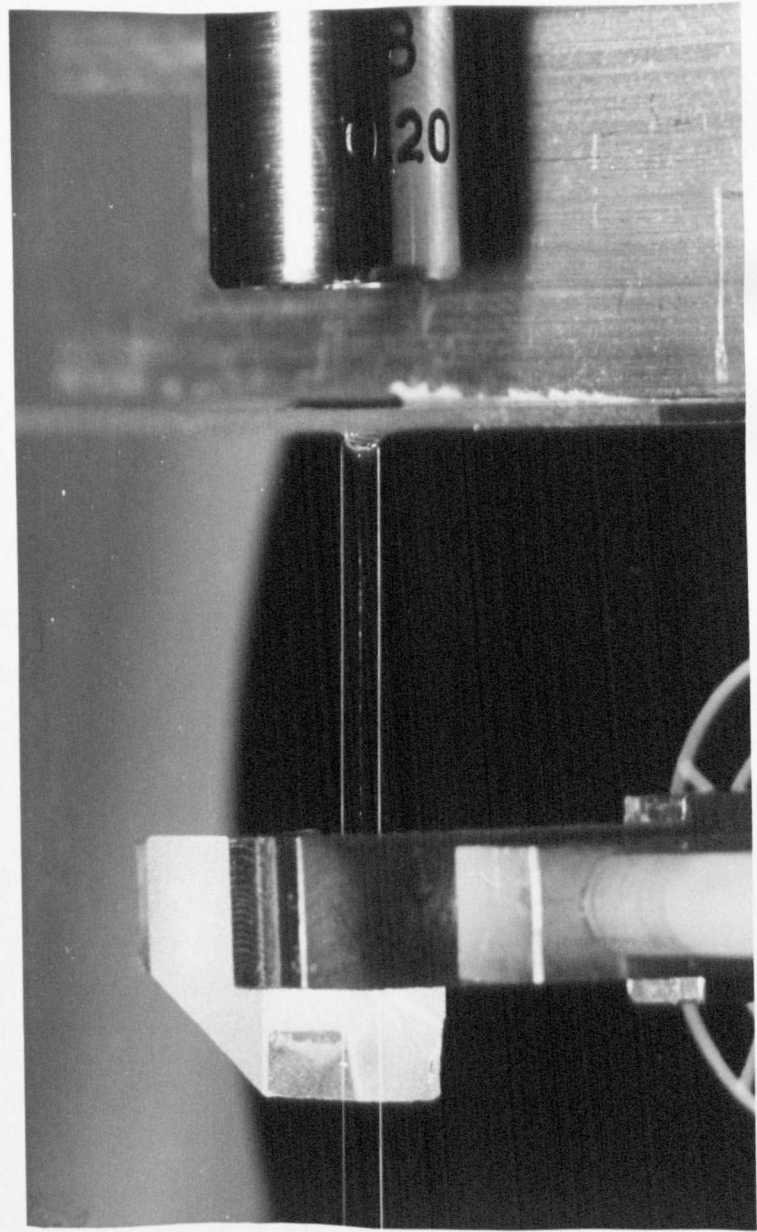


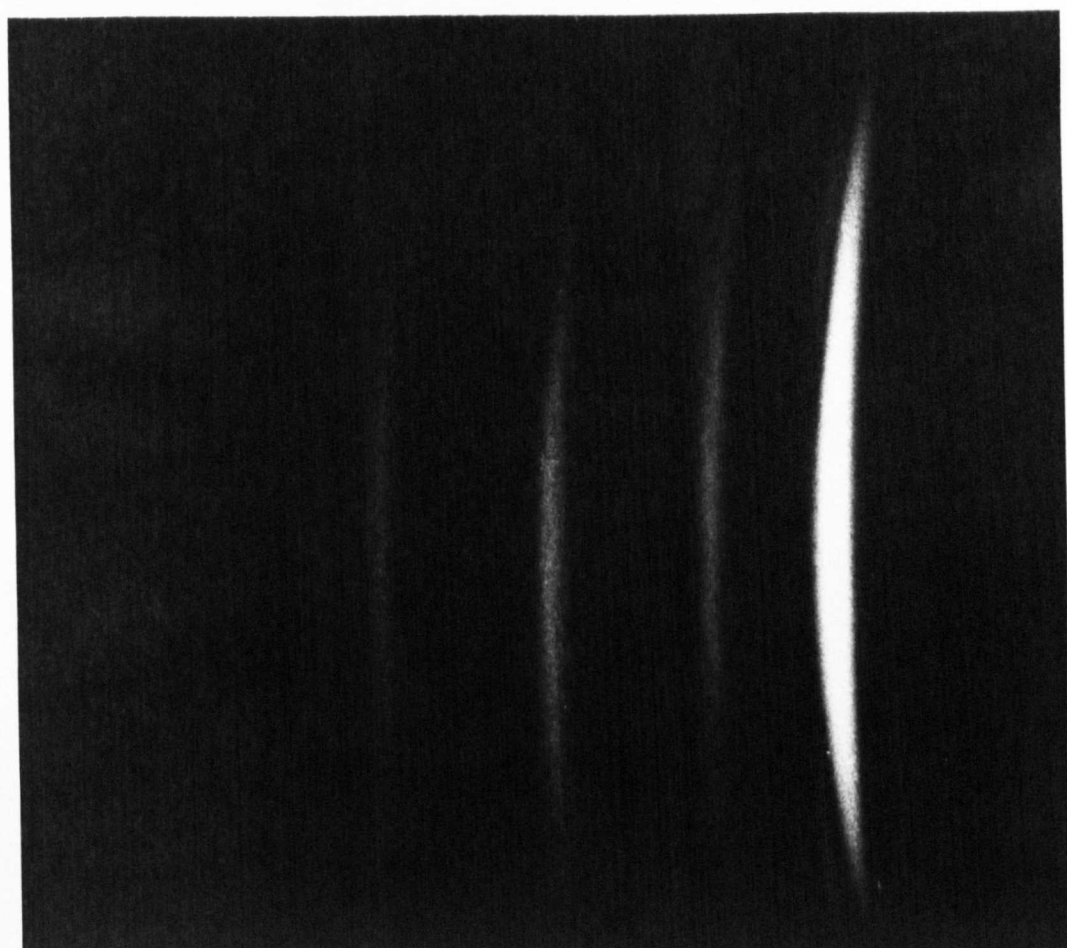
FIGURE 5.5 Excitation and propagation of a guided mode in an SR fibre .

5.4.4 Experimental example of SR fibre modes.

To illustrate the method a particular example will be presented. The SR fibre used had a lead-glass guiding filament (refractive index before pulling of 1.563 at 633 μm wavelength) of measured dimensions 85 μm x 2.93 μm , and a substrate of Chance soda-lime glass (refractive index before pulling of 1.518 at 0.633 μm) of dimensions 2200 μm x 90 μm . Using the slab equivalent model for the propagation in the waveguide, the dispersion curves of Figure 5.2 were seen to apply in this case. With the laser plane polarized at right-angles to the ribbon thickness direction, the TE modes of the guide were excited at the input prism coupler. The slab-waveguide modes propagating in the guide were studied by a second prism as an output coupler. In this example there were four such TE waveguide modes, TE_0 , TE_1 , TE_2 and TE_3 . The characteristic output mode-lines were allowed to impinge on a ground-glass screen and photographed from behind, and the resulting observation is shown on Figure 5.6. In this photograph the TE_0 mode was excited at the input coupler and the light scattered into the other modes as the energy travelled down the guide, giving rise to the fainter m-lines indicated in the figure. The scattering to the left of the TE_3 mode corresponds to the light coupled into the continuum of substrate modes of the fibre. Table 5.1 presented below, summarizes the experimental results of the prism coupling experiment. The 60° prism had a refractive index of 1.685 and the mode angles were measured to an accuracy of $\pm 4'$ arc.

Mode Order	Coupling Angle	N_e
TE_0	12° 15'	0.919
TE_1	11° 00'	0.719
TE_2	9° 10'	0.419
TE_3	7° 02'	0.035

TABLE 5.1



Δ
 TE_3 Δ
 TE_2 Δ
 TE_1 Δ
 TE_0

FIGURE 5.6 SR fibre output prism coupler m-lines.

5.4.5 Comparison of theory and experiment.

The experimentally measured N_e values are superimposed on Figure 5.2 for comparison. Substitution of this data into the mode angle programme gave the following results:

Guiding region thickness = $3.075 \mu\text{m}$

Guiding region refractive index = 1.556

Minimum variance from mean value of thickness with respect to refractive index = 5.2×10^{-15} .

Clearly there is excellent agreement of the guiding region refractive index and thickness obtained from the propagation characteristics, and these values independently measured. This agreement led us to believe that the theoretical model based on a slab dielectric waveguide was correct, and that the guiding properties of the SR fibre were completely explained and understood. The results presented in the example above serve to illustrate the method of describing the mode propagation in the fibres. In practice, single-mode waveguides were the most useful, and the analysis of them was exactly the same as above. Since the programme must have at least two sets of data, the TE_0 and TM_0 mode angles were supplied to the computer.

5.4.6 Optical loss of SR fibres.

Because of the optical loss of any coupling system must be minimised, the attenuation of the guided light in the fibre is an important practical consideration. Optical loss measurements were performed on the ribbons at $0.633 \mu\text{m}$ wavelength by the destructive method of repeatedly shortening the ribbon and plotting the increasing output light intensity. During the measurements the light input conditions were held constant and coupling of the light out of the free end of the ribbon was achieved by nullifying the scattering effects

of the ribbon end with a drop of index-matching fluid (for lead glass guiding filaments nitrobenzene, $n_D = 1.556$, was used) on the glass face of a wide-area photodiode.

The very first SR fibres reported⁴³ had high optical loss, measured by this technique. The attenuation was 0.9 dB/cm for the TE_0 mode launched in a guiding layer 0.9 μm thick, in a fibre constructed from lead glass/microscope slide materials. Although this loss was high, it must be borne in mind that the materials used were not of optical quality - in fact the lead glass used for the guiding region was obtained by collapsing a semicylindrical section of glass cut from a hollow tube (this may also explain the observation that the two glasses did not lie perfectly flat in the final fibre, as can be seen in the interference photograph, Figure 5.3). The optical loss of the composite glasses were 0.5 dB/cm and 0.35 dB/cm for the guiding layer and the substrate respectively, measured using the fundamental modes of 3 μm thick planar ribbons of each material. Cleanliness in manufacturing and the surface quality of the glasses were two very important points ignored when the first fibres were made, and it was expected that the loss figure for the SR guide would be much reduced by the use of the optical-quality low-loss bulk materials in the ribbon preparation. This indeed was the case. The use of Schott BAKI glass as the guiding region reduced the attenuation to 0.3 dB/cm with microscope slide as the substrate, and to 0.1 dB/cm with Corning 7059 glass as the substrate. The BAKI was cut from a slab of glass and the surfaces were polished to better than 1 μm finish. The further reduction in attenuation using 7059 as the substrate was thought to be due to the improved surface quality of the glass, quoted by the manufacturers¹⁰⁴ to be ground and polished to a smoothness of 130A.

The reduction in the attenuation from the initially reported value of 0.9 dB/cm to 0.1 dB/cm made the SR fibres attractive as low-loss coupling waveguides over short distances.

5.5 Uses of the SR Fibre.

Sandwich ribbon fibres are straightforward to manufacture from readily available materials and have mechanical and optical properties particularly suited to the requirements of low-loss single-mode waveguides for interconnecting thin film circuits. To what other uses can this type of structure be applied?

5.5.1 Low-loss, short-range data highway.

It was thought that the optical loss figures quoted in Section 5.4.6 could be improved with further research. A method thought to be particularly suited to this end was to use secondary preforms consisting of Chemical Vapour Deposited (CVD)¹⁰³ filaments on pure silica substrates, pulled to produce ribbons having losses equivalent to CVD fibres produced by Payne and Gambling.⁷ If the optical losses, reduced by whatever method, became better than 0.001 dB/cm it is proposed that SR fibres could act as the main data highway of short-haul communication links, such as on board ships or aircraft, and would constitute one of the first high-bandwidth, single-mode systems using integrated optics.

5.5.2 Multichannel capacity of SR fibres.

SR fibres also offer a unique multichannel facility, because the waveguide filaments may be packed side by side on the one common substrate, as in Figure 5.1c. If the spacing between each filament, of width a , is b , and the edge of the outermost filament is distance l away from the edge of the substrate, then the number of channels possible on the single substrate of width L is by simple arithmetic:

$$n = \frac{(L-2\ell + b)}{(a+b)}$$

5.5

If the spacing between each guiding filament is large enough to prevent cross-talk between adjacent guides (say 10 μm) and some typical numbers are substituted into the expression, it is seen that, for $L = 1000 \mu\text{m}$, $\ell = 200 \mu\text{m}$ and $a = 20 \mu\text{m}$, the packing density increases to 20 channels per fibre. For waveguide filaments of lower aspect ratio, the information carrying capacity of the multichannel SR fibre increases, though care must be taken in the design to isolate the electromagnetic fields of each guide from its neighbour. We have been successful in demonstrating the principle by manufacturing two-channel and three-channel SR fibres, with each guiding region having the same propagation characteristics as its neighbour. Given that single-channel directional coupling to rectangular integrated optical waveguides is possible, we can foresee the coupling of discrete integrated channels to separate guides on the single SR connecting fibre, and the formation of an optical data "busbar".

5.5.3 SR Fibre directional coupler.

An additional device which could be constructed using the multichannel facility of SR fibres is a directional coupler, where unlike the busbar, the waveguides are drawn in close proximity to one another on the substrate, such that their evanescent fields overlap and the guided modes interfere to produce a spatially periodic oscillation of power from one guide to the other. However, this proposal has not been demonstrated experimentally.

It will be shown in a subsequent chapter (Chapter 7) that the sandwich ribbon fibre may be applied principally to the interconnection of integrated optical circuits and that it is particularly successful in this respect.

5.6 Summary and Conclusions.

The chapter commenced with a discussion of the difficulties of coupling to integrated optical waveguides using multimode or monomode circular fibres, even in a modified form, and the development and use of ribbon fibres for this purpose was argued. Three types of ribbon fibre were identified: the unclad planar ribbon, the large width-to-thickness sandwich ribbon, and the three-dimensional sandwich ribbon fibre. The latter is of such importance to merit a separate chapter. The subject of the planar ribbon fibre was reviewed, and its advantages and disadvantages discussed, as well as the prohibitive handling difficulties. The inherent multimode nature of the unclad ribbons was shown to be the major factor limiting the use of the fibres to couple thin film waveguides.

Sandwich ribbon fibres were introduced and the method of manufacture described. Basing the theoretical solution on an asymmetrical slab waveguide approximation, the propagation characteristics of the fibres were investigated, and the results were supported by an experimental example. Single and multimode operation were demonstrated, and the optical attenuation was discussed. The losses have been reduced from 0.9 dB/cm for the first ribbons produced, to 0.1 dB/cm using optical-quality low-loss bulk materials in ribbon preparation. In the final section, the uses to which the SR fibre may be put, and other novel applications, were discussed.

In conclusion it may be stated that the purpose of the work of this chapter, the design, manufacture and study of a fibre capable of interconnecting thin film circuits, has been achieved, and that the properties of sandwich ribbon fibres developed for the purpose have been described. Unclad planar ribbons are unsatisfactory as inter-

connecting fibres, and the problems associated with them, described in this chapter, were overcome using SR fibres. The present high optical loss (relative to circular fibres) and their unprotected open sandwich nature make them unattractive as long distance optical data highways, although short-range high-bandwidth systems are conceivable using SR fibres with external protection, such as a low-refractive index plastic coating, coupled to fast integrated optical devices with the very high efficiencies detailed in Chapter 7.

6.1. Introduction.

The planar and sandwich ribbon fibres previously described were deliberately chosen to have large aspect-ratio guiding regions, in the former case to provide mechanical support for the otherwise flimsy structure, and in the latter to minimise the effects of mode confinement in the width direction. The waveguides were simpler to analyse as only the dominant (slab) modes were considered. However, it became apparent that the manufacture and analysis of low aspect-ratio guides was very necessary from the viewpoint of designing a practical coupling fibre for interconnecting rectangular integrated optical waveguides. In the words of Goell,¹⁹

"In many integrated optics applications it is expected that the waveguides will consist of rectangular, or near rectangular, dielectric core thus it is important to have a thorough knowledge of the properties of their modes."

In this section, the manufacture, properties and uses of three-dimensional SR fibres are described. An extensive study is presented of the method of excitation of the modes and the observation and analysis of the near- and far-field patterns obtained.

6.2 Manufacture of Three-dimensional SR Fibres.

The method of manufacture of three-dimensional SR fibre waveguides is similar to that described in Section 5.3.2. The initial filament preform consisted of a rectangular block of SCHOTT BAKI glass (refractive index before pulling = 1.5725 at 0.589 μm) of dimensions 1 mm x 4 mm x 80 mm. The four large faces were polished to a 1 μm finish. The guiding region secondary preform was then manufactured by pulling this glass at 800°C. A 75 mm length of cross-section 800 μm x 200 μm was placed on a slab of Corning 7059 (refractive index before pulling = 1.530 at 0.589 μm) of dimensions

75 mm x 25 mm x 1 mm, and the composite fibre was formed by pulling at 850°C. No preform top-feed was supplied to the pulling-rig furnace, and consequently the dimensions of the fibre decreased along its length. The measured refractive indices associated with this ribbon, $n_{\text{guide}}=1.58$, $n_{\text{substrate}}=1.528$, are those corrected for the working wavelength of 0.633 μm with the compaction effects of multiple pulling taken into account.⁵⁹ The optical loss, measured by the destructive technique for the E_{11}^Y mode in a fibre of dimensions 9 μm x 2.2 μm , was 0.05 dB/cm.

Such a fibre is shown in the electron micographs in Figures 6.1 and 6.2 .

6.3 Cross-section of Three-dimensional SR Fibres.

Figure 6.1 shows the guiding region of the fibre in relief, and Figure 6.2 shows a cross-section of the guiding region, with the boundary between the glass species evident by the contrast difference at the interface. The edges of the guiding filament have collapsed during the pulling process and though the remaining section is perhaps better described as elliptical, the aspect ratio has remained approximately 4:1. The gradual 'round-off' of the waveguide corners is beneficial as the edge reflection in the width direction is eliminated; in fact the equivalent ray-optics model would predict a serpentine progression of the wavefront in this direction. The method of manufacture ensures that the edge roughness is reduced by a factor proportional to the dimensions of the waveguide, allowing observation of the mode patterns over long distances without undue mixing or scattering.

Although the cross-section of the guiding region is not rectangular, it has been found that, in the absence of a complex

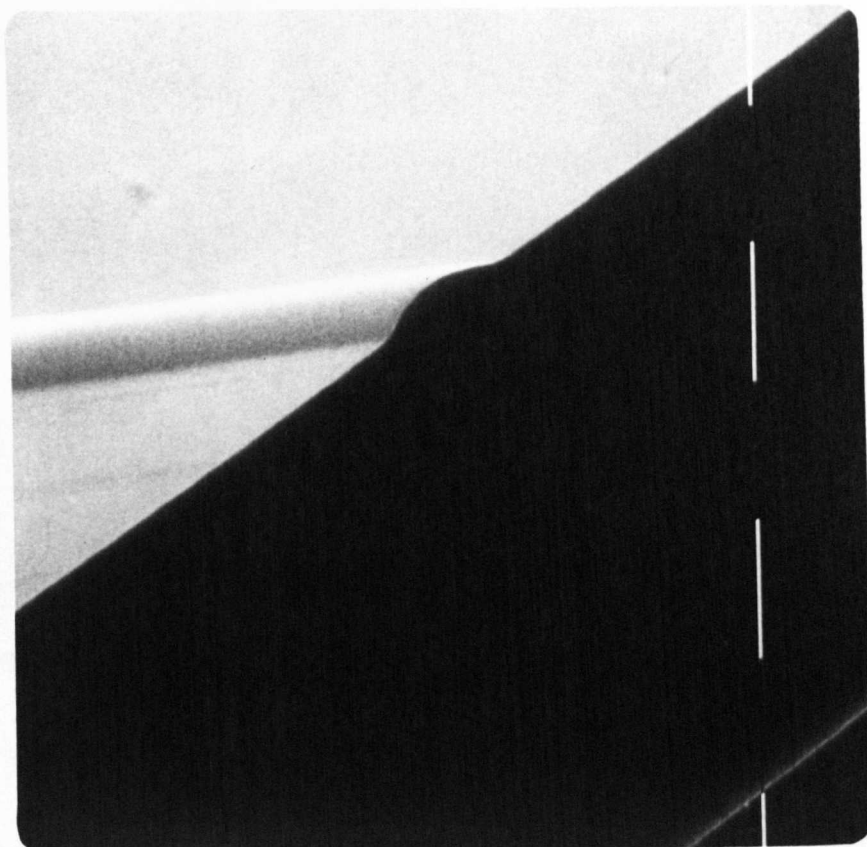


FIGURE 6.1 SEM photograph of a
3-D SR fibre : relief.
(10 μm markers)

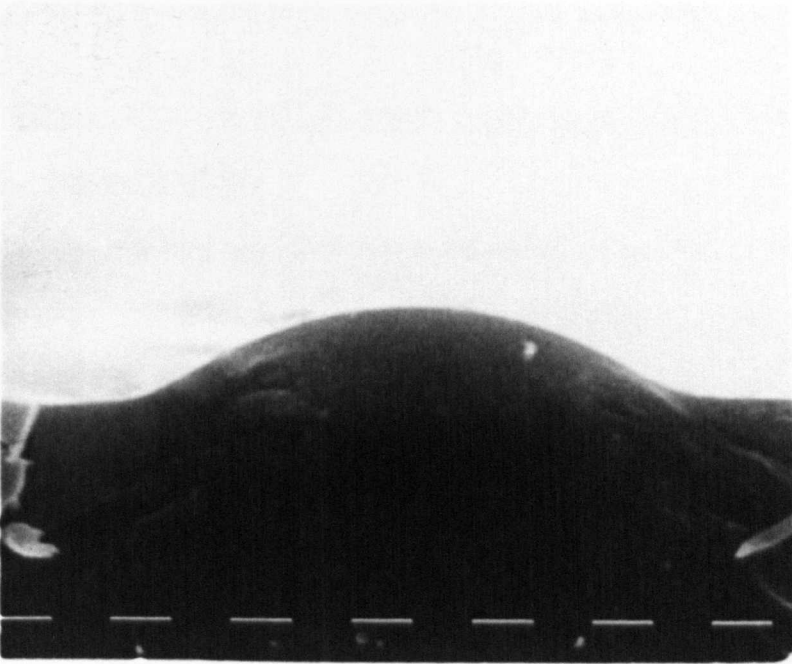


FIGURE 6.2 SEM photograph of a
3-D SR fibre : section.
(1 μ m markers)

theoretical model, the approximate solutions developed for rectangular waveguides²⁰ adequately describe the mode propagation in these fibres. Experimental results presented here for the prism coupling and the waveguide field patterns support these simplifications.

6.4 Three-dimensional SR Fibre Mode-excitation Using a Prism Coupler.

6.4.1 Introduction.

The theory and practice of mode excitation of thin film waveguides using high-index prism couplers are well established.^{18,29} Similarly the excitation of the low-order modes of circular fibres using analagous techniques are presented in Chapter 4. In this section it is demonstrated that the conventional prism coupler with an additional tilt facility may be usefully employed to excite the complete mode family of a near-rectangular SR fibre.

6.4.2 Theory of three-dimensional SR fibre mode excitation using a prism coupler.

In order to investigate the propagation characteristics of SR fibres, a launching system capable of exciting the three-dimensional modes of the structures was used. Marcatili²⁰ has shown that the field within the fibre can be described as the superposition of two orthogonal fields in x and y, the propagation constant k_x along x being independent of y, and k_y along y being independent of x. The largest field components are perpendicular to the direction of propagation (the z-axis) and the modes are essentially of the TEM kind, grouped in two families E_{pq}^y and E_{pq}^x . Associated with k_x and k_y are the characteristic angles ϵ_x and ϵ_y such that

$$\beta_x = (k_{n_1}^2 - k_x^2)^{1/2} = kn_1 \sin \epsilon_x \quad 6.1$$

$$\beta_y = (k_{n_1}^2 - k_y^2)^{1/2} = kn_1 \sin \epsilon_y \quad 6.2$$

where $k = \frac{2\pi}{\lambda}$, n_1 = guiding region refractive index.

The angles are mutually independent and for optimum launching of a particular mode, the launching angles θ and ϕ must be selected to match the characteristic angles ϵ_x and ϵ_y respectively. In addition to the usual synchronous coupling angle, defined in equation 4.8 from simple geometrical considerations as

$$\theta_m = \sin^{-1} \left[n_p \sin \left(\sin^{-1} \left(\frac{\beta_x}{kn_p} \right) - \alpha_p \right) \right] \quad 6.3$$

where n_p = prism refractive index = 1.696

α_p = prism angle = 60°

the tilt angle, $\phi_c = \frac{\pi}{2} - \epsilon_y$, must also be capable of variation. Due to refraction of the input beam at the prism face, the measured value of tilt angle, ϕ_m , differs from the correct value. Applying Snell's Law at the boundary gives

$$\phi_m = \sin^{-1} \left[n_p \sin \phi_c \right] = \sin^{-1} \left[n_p \cos \epsilon_y \right] \quad 6.4$$

or from equation 6.2

$$\phi_m = \sin^{-1} \left[n_p \left(1 - \left(\frac{\beta_y}{kn_1} \right)^2 \right)^{\frac{1}{2}} \right] \quad 6.5$$

The axial propagation constant, β_z , of the guided mode is given by

$$\beta_z^2 = k^2 n_1^2 - k_x^2 - k_y^2 = \beta_x^2 + \beta_y^2 - k^2 n_1^2 \quad 6.6$$

The phase-matching properties of the prism coupler were established through equations 6.3, 6.5 and 6.6.

6.4.3 Experimental results.

Throughout this work a BAK 1/7059 fibre of dimensions shown in Figure 6.2 was used. In order to observe the mode structure without excessive attenuation or mode mixing, the total length of the fibre was limited to 30 mm. The fibre supported eight transverse modes in the first family ($q = 1$) and four transverse modes in the second ($q = 2$), and the excited mode was identified by its characteristic far-field pattern described in Section 6.6. Light from a 5mW Spectra-

Physics 120 He-Ne laser operating at $0.633 \mu\text{m}$ and plane polarized parallel to the y-axis, was focused into the launching prism, which was mounted on a goniometer with x,y,z, θ , and ϕ calibrated positioning devices. The apparatus is shown on Figure 6.3 and the coordinates of the goniometer and fibre are presented in Figure 6.4. As the tilt angle ϕ was introduced, it was found that the synchronous angle θ had to be adjusted in order to launch the same mode. This observation was consistent with equation 6.6 where any alteration in $\beta_y(\phi)$ must be offset by an appropriate change in $\beta_x(\theta)$ to maintain β_z constant. The synchronous coupling angles for different values of tilt angle were noted for each mode, and the results are presented in Figure 6.5. It was found that the modes were excited more efficiently over distinct bands of tilt angle and the dotted lines in Figure 6.5 represent extrapolated curves where measurement was not possible. The modes formed a family of similar curves which could be described universally. The normalised phase mismatch in x,

$$\frac{\Delta\beta_x}{\beta_x(\phi=0)}$$

introduced by the tilt angle ϕ_c , is analagous to the case of Cerenkov radiation¹⁰⁴ where

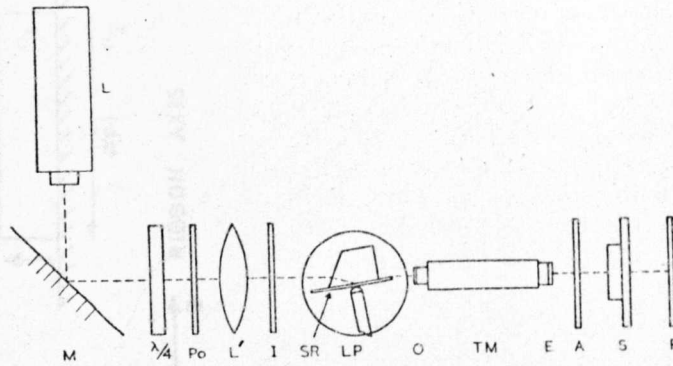
$$\frac{\Delta\beta_x}{\beta_x(\phi=0)} = \sec \phi_c - 1 = \sec \left(\sin^{-1} \left(\frac{\sin \phi_m}{n_p} \right) \right) - 1 \quad 6.7$$

β_x is obtained from the synchronous coupling angle defined in equation 6.3.

The theoretical curve of

$$\frac{\Delta\beta_x}{\beta_x(\phi=0)}$$

is plotted in Figure 6.6, along with the experimental points for the E_{11}^y , E_{51}^y and E_{22}^y modes, extracted from Figure 6.5. It is seen from Figure 6.6 that there is good agreement between theory and experiment, verifying the phasematching relations given in equations 6.3 - 6.6.



- L = laser
- M = mirror
- $\lambda/4$ = quarter-wave plate
- P_0 = polariser
- L' = lens ($f = 20$ cm)
- I = iris
- SR = sandwich-ribbon fibre
- LP = launching prism
- O = objective ($\times 100$ n.a. 1.3)
- TM = travelling microscope
- E = eyepiece, $\times 10$
- A = analyser
- S = shutter
- P = photographic plate

FIGURE 6.3 Investigation of three - dimensional
SR fibre waveguide modes :
apparatus .

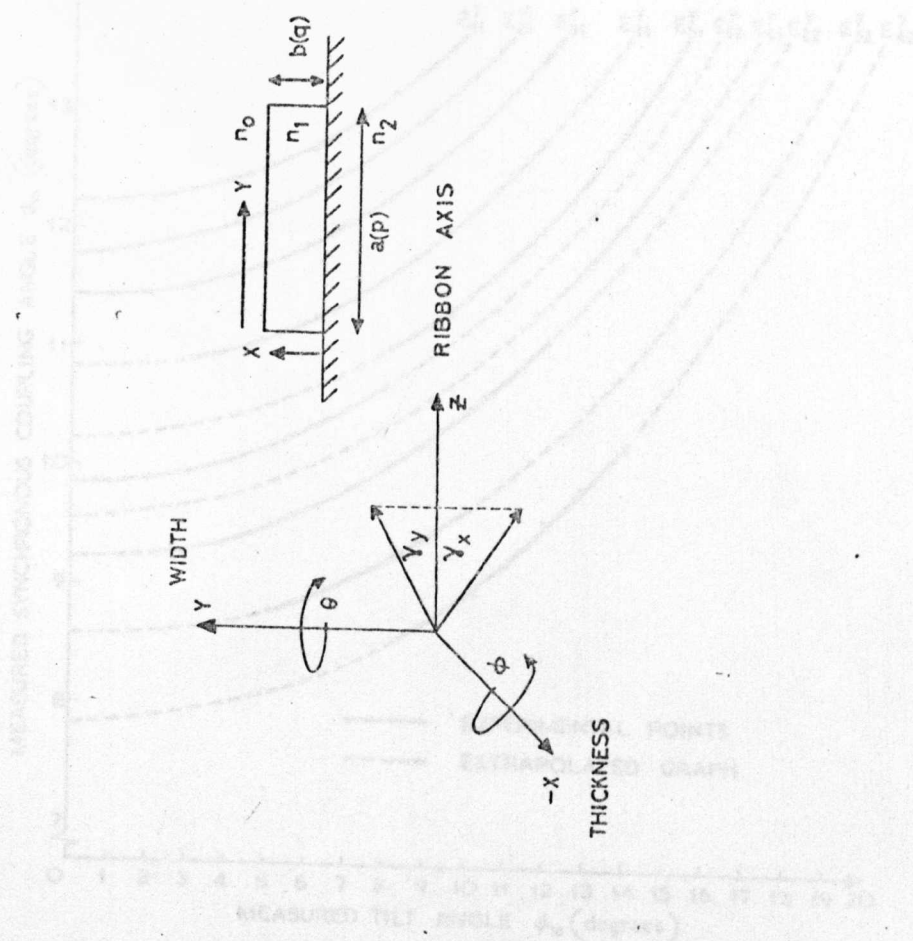


FIGURE 6.4 Definitions and directions .

FIGURE 6.5 The graph of the measured synchronous angle against measured tilt angle .

(the E_{y1}^y and E_{y1}^x are omitted for clarity)

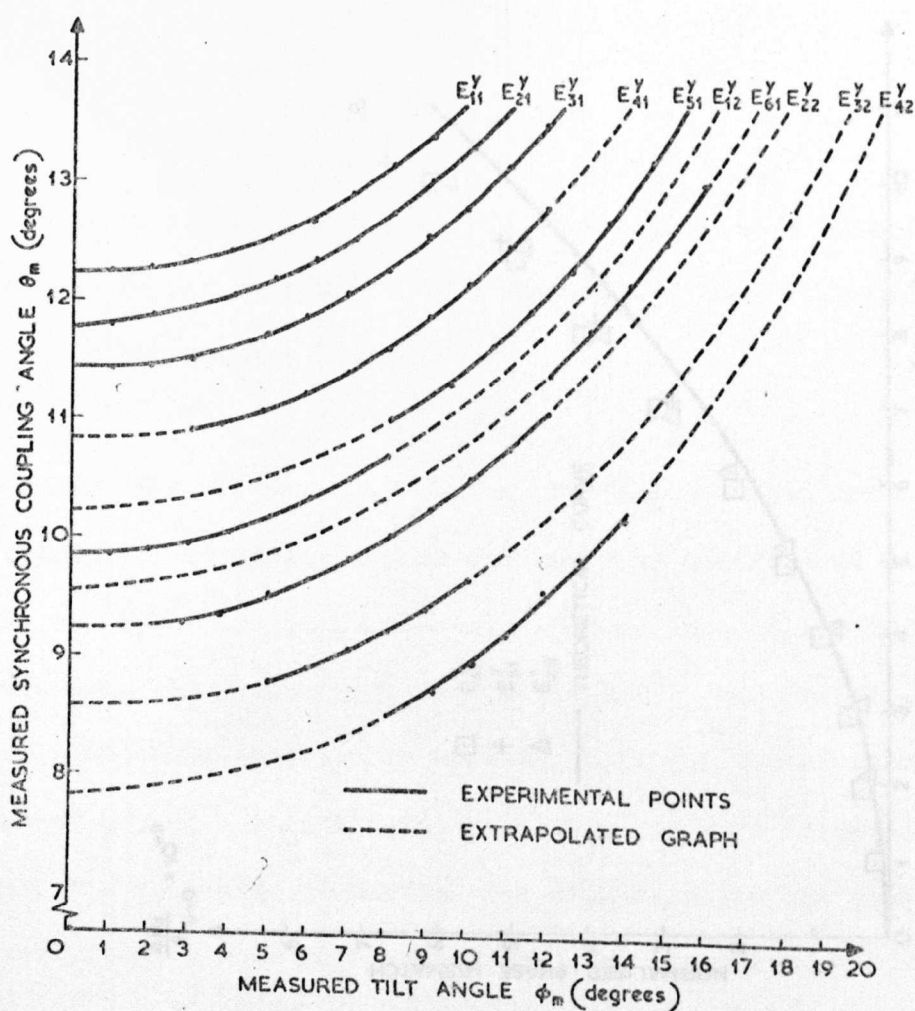


FIGURE 6.5 The graph of the measured synchronous angle against measured tilt angle .

(the E_{71}^y and E_{81}^y are omitted for clarity)

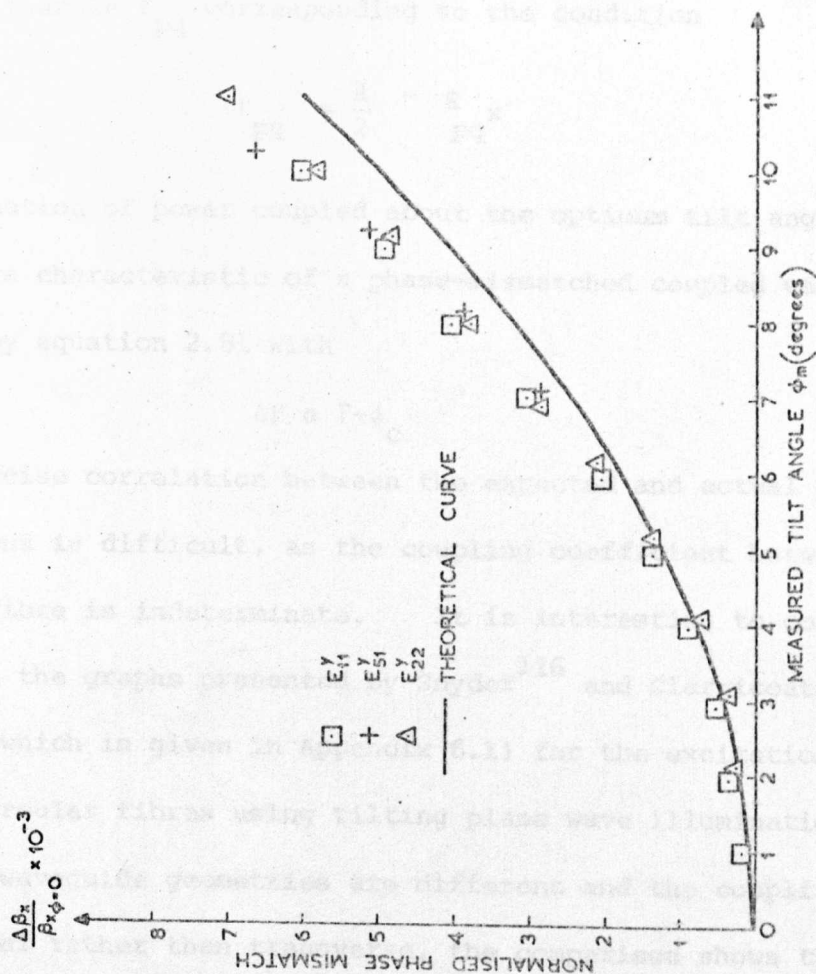


FIGURE 6.6 Normalized phase mismatch
in x plotted against the
measured tilt angle .

The power coupled into each mode, detected at the output end of the fibre, was measured as a function of the tilt angle ϕ_m , and plotted in figures 6.7a and 6.7b. They show that each mode has an optimum tilt angle Γ_{pq} corresponding to the condition

$$\Gamma_{pq} = \frac{\pi}{2} - \epsilon_{pq}^x \quad 6.8$$

The distribution of power coupled about the optimum tilt angle for each mode is characteristic of a phase-mismatched coupled wave response predicted by equation 2.81 with

$$\Delta\beta \propto \Gamma - \phi_c$$

However precise correlation between the expected and actual power distributions is difficult, as the coupling coefficient between the prism and fibre is indeterminate. It is interesting to compare these curves with the graphs presented by Snyder¹¹⁶ and Clarricoats¹⁰⁶ (an example of which is given in Appendix 6.1) for the excitation of the modes of circular fibres using tilting plane wave illumination. Though the waveguide geometries are different and the coupling is codirectional rather than transverse, the comparison shows that the experimental results were not entirely unexpected.

6.4.4 Theory of modal power variation with tilt angle.

The optimum tilt angles were determined from the peak values of the measured power curves and compared with those predicted by the following simple model. Using the effective refractive index notation, equation 6.6 becomes

$$n_1^2 + v_{pq}^z{}^2 = v_{pq}^x{}^2 + v_{pq}^y{}^2 \quad 6.9$$

where

$$v_{pq}^u = \beta_{pq}^u / k \text{ for } x, y, z, = u \quad 6.10$$

The optimum tilt angle, Γ_{pq} for the pq^{th} mode occurs where

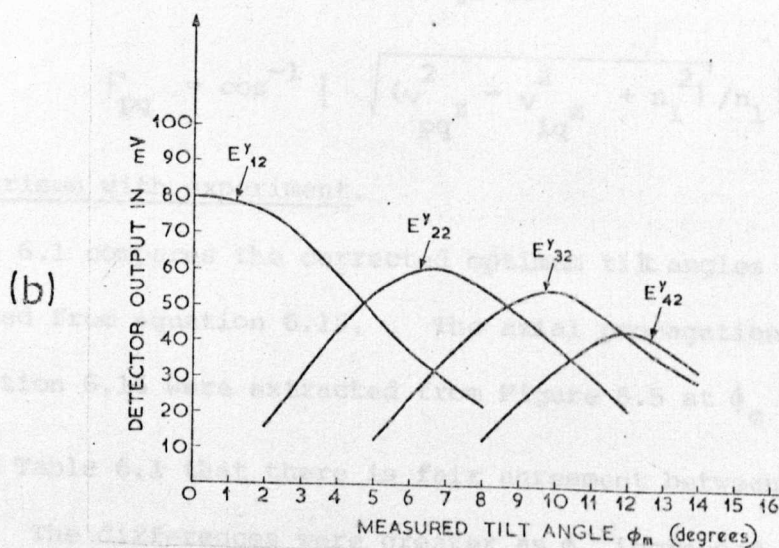
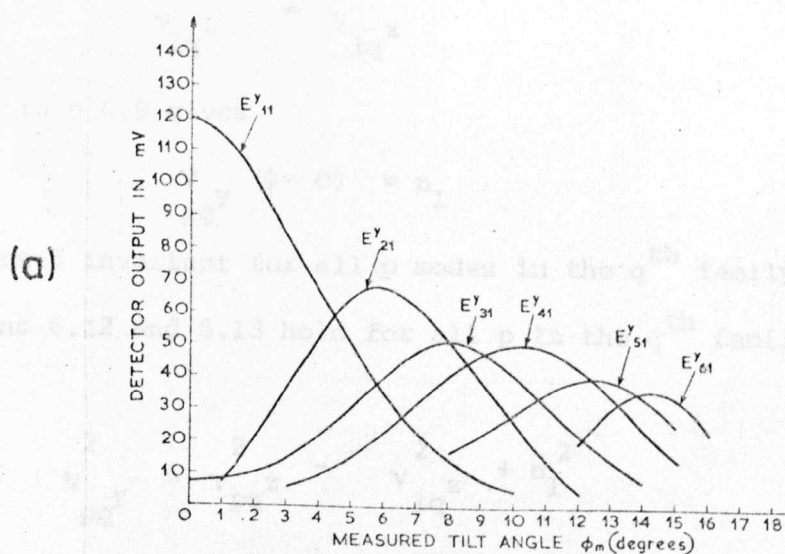


FIGURE 6.7 Power in each mode as a function of the tilt angle ,

(a) E_{p1}^y modes

(b) E_{p2}^y modes

$$\Gamma_{pq} = \cos^{-1} \left[v_{pq}^y / v_{pq}^y (\phi = 0) \right] \quad 6.11$$

When the lowest transverse order ($p=1$) is launched, $\phi = 0$, and

$$v_{1q}^z = v_{1q}^x \quad 6.12$$

substituting into 6.9 gives

$$v_{pq}^y (\phi = 0) = n_1 \quad 6.13$$

v_{pq}^x is assumed invariant for all p modes in the q^{th} family and

thus equations 6.12 and 6.13 hold for all p in the q^{th} family.

Therefore,

$$v_{pq}^y^2 = v_{pq}^z^2 - v_{1q}^z^2 + n_1^2 \quad 6.14$$

Substituting into 6.11 and 6.13 and 6.9 gives

$$\Gamma_{pq} = \cos^{-1} \left[\sqrt{(v_{pq}^z^2 - v_{1q}^z^2 + n_1^2) / n_1^2} \right] \quad 6.15$$

6.4.5 Comparison with experiment.

Table 6.1 compares the corrected optimum tilt angles with those obtained from equation 6.15. The axial propagation constants v_{pq}^z in equation 6.15 were extracted from Figure 6.5 at $\phi_c = 0$. It is seen from Table 6.1 that there is fair agreement between theory and experiment. The differences were greater as ϕ_c increased, a trend which was also noted in Figure 6.6. It would therefore appear that the error in the prism phase-matching criteria, more apparent at larger tilt angles, was the major cause of the discrepancy.

6.4.6 Conclusions.

The characteristics of the several modes supported by the ribbon have been directly measured by prism launching. Although the cross-section of the guiding region was not rectangular, it has been found that the modal characteristics were adequately described using approximate solutions developed for rectangular waveguides.

E ^y mode order pq	Axial propagation constant ν_z	Theoretical optimum tilt angles Γ_{pq}	Experimental optimum tilt angles ϕ_c
11	1.56386	0°00'	0°00'
21	1.56118	3°21'	3°25'
31	1.55869	4°39'	4°41'
41	1.55400	6°25'	5°57'
51	1.54898	7°53'	7°20'
61	1.54436	9°01'	8°29'
71	1.53991	10°00'	—
81	1.53500	10°59'	—
12	1.54757	0°00'	0°00'
22	1.54316	4°16'	3°45'
32	1.53786	6°20'	5°50'
42	1.53254	7°53'	7°00'

TABLE T6.1 Comparison of the
theoretical and
experimental optimum
tilt angles.

The higher-order modes were efficiently and selectively launched using a tilting prism coupler, allowing two synchronous coupling angles to be determined, the values of which agreed well with theory.

6.5 Near-field Patterns of Three-dimensional SR Fibre Waveguide Modes.

6.5.1 Introduction.

Efficient excitation of the complete mode family of an SR fibre using the techniques described in Section 6.4 led to the observation of the characteristic waveguide mode intensity patterns. Experiments with the prism coupler indicated that the approximate solution for rectangular waveguides was adequate for describing the propagation of modes in SR fibres. The x- and y-directions are treated independently and the total field in the cross-section can be described as the superposition of the two orthogonal fields in x and y. Modes polarized E_{pq}^y will be considered, the obvious extensions for E_{pq}^x modes being omitted.

6.5.2 Theory of approximate mode field distributions.

Marcatili²⁰ has examined the theoretical mode field distributions of a rectangular waveguide and Goell¹⁹ has presented computer-drawn intensity patterns of the same.

In Marcatili's notation the electric field within the guide cross-section is given by

$$E(y) = E_0 \cos \left[\frac{p\pi}{a} (1+A)^{-1} y + (p-1)\frac{\pi}{2} \right] \quad 6.16$$

and the magnetic field by

$$H(x) = H_0 \cos \left[\frac{q\pi}{b} (1+B)^{-1} x + (q-1)\frac{\pi}{2} \right] \quad 6.17$$

where

$$A = \frac{\frac{n_o}{2n_1}}{(n_1^2 - n_o^2)^{\frac{1}{2}} ka} \quad 6.18$$

$$B = \frac{(n_1^2 - n_0^2)^{-\frac{1}{2}} + (n_1^2 - n_2^2)^{-\frac{1}{2}}}{kb} \quad 6.19$$

Since A and B are small for well guided modes ($a, b \gg \lambda$), equations 6.16 and 6.17 may be further simplified to

$$E(y) = E_0 \cos \left[\frac{p\pi}{a} y + (p-1)\frac{\pi}{2} \right] \quad 6.20$$

$$H(x) = H_0 \cos \left[\frac{q\pi}{b} x + (q-1)\frac{\pi}{2} \right] \quad 6.21$$

The fields outside the guide are exponentially decaying and are small enough to be insignificant. Since the intensity is proportional to the square of the field, the intensity pattern of the pq^{th} mode in the fibre cross-section is

$$P_{\text{NF}}(x, y) = P_0 \cos^2 \left[\frac{p\pi}{a} y + (p-1)\frac{\pi}{2} \right] \cos^2 \left[\frac{q\pi}{b} x + (q-1)\frac{\pi}{2} \right] \quad 6.22$$

6.5.3 Description of experiment.

The fibre used throughout the following experiments is detailed in Sections 6.2 and 6.3 and has the cross-section shown in Figure 6.2. The waveguide modes were selectively excited by the prism coupler and the maximum efficiency was obtained by introducing the tilt angle as described in Section 6.44. Light travelled down the 30 mm length of fibre and the near-field distributions were observed at the cleaved exit end. The termination was index-matched using methyl salicylate, refractive index = 1.536 at 0.589 μm . A diagram of the apparatus used to observe the near-field patterns is shown in Figure 6.3.

A high-power optical microscope, mounted on a goniometer, focused the image of the fibre cross-section through a shutter onto a photographic plate set some distance behind the eyepiece. The typical dimensional magnification was $\times 10^3$ and the spatial image filled the entire frame of the photographic plate without further magnification. A quarter-wave plate and plane polarizer were used to provide input plane polarization of any orientation, and an analyser was included for the study of degenerate mode mixtures and

other polarization effects. The images of the near-field patterns were also measured using a synchronous scanning photodiode coupled to an x-y plotter, in place of the photographic plate. The photodiode[†] had an effective diameter of 618 μm , and scanned, in the y-direction, an image 20 mm long corresponding to a near-field aperture of 10 μm . The resolution was therefore better than 0.3 μm in the near-field.

Each of twelve E^Y modes was excited at its optimum tilt angle and the near-field patterns were recorded using both methods. The photographic results are presented in Figure 6.8 and the recordings of the photodiode scans are shown in Figure 6.9. Both are discussed in the following paragraphs.

6.5.4 Discussion of the results.

The results shown in Figure 6.8 clearly illustrate the confinement of the fields in both transverse directions and resemble those predicted by Goell.¹⁹ Care was taken to ensure that the composite photographs in Figure 6.8 were reproduced at the same magnification, though the exposures for each may have varied throughout the experiment and the subsequent art-work.

For each mode there are p and q intensity maxima in the y and x directions respectively, as predicted by equations 6.20 and 6.21.

The scanning measurements of Figure 6.9 were performed for the E_{pl}^Y modes ($8 \geq p \geq 1$) in the y-direction. The image plane was the same for each measurement and the abscissae of the composite graphs are therefore common. The ordinate scales are different for each mode. The scale indicated in Figure 6.9 was derived from the known magnification and scanning and plotter rates.

[†] Hewlett Packard type 5082/4205.

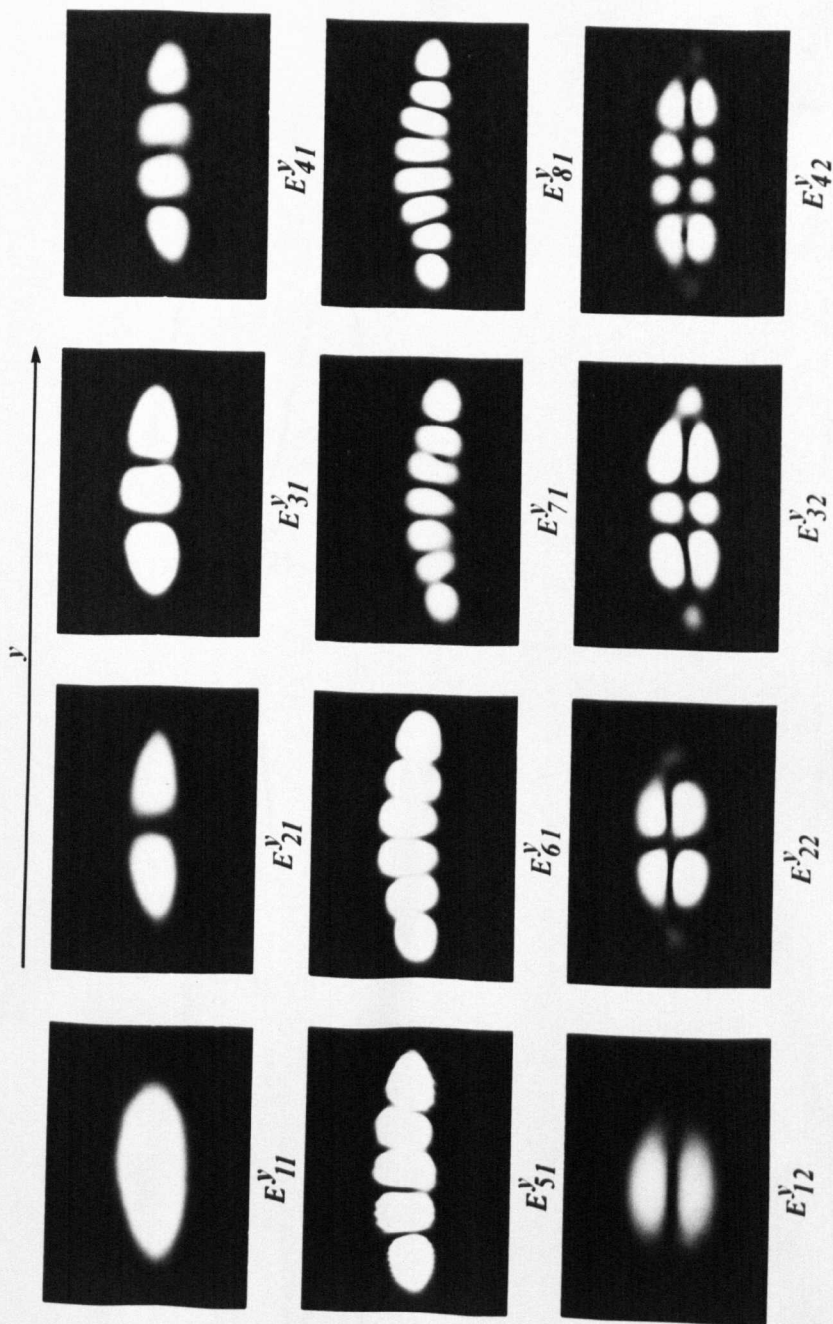


FIGURE 6.8 Near - field patterns of the E^y modes
of a 3 - D SR fibre .

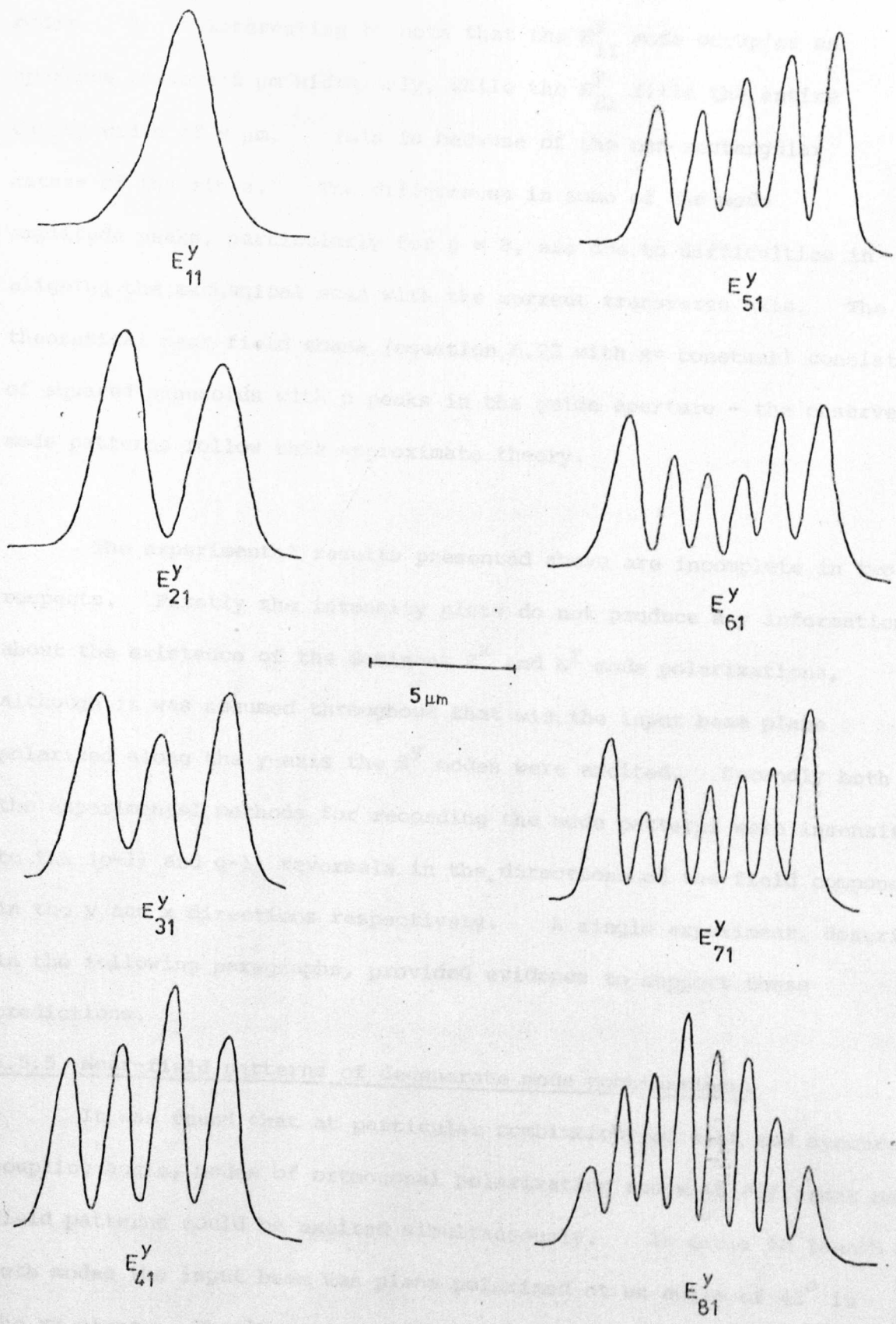


FIGURE 6.9 NEAR-FIELD PHOTODIODE SCANS IN THE
 Y-DIRECTION : E^y_{p1} MODES.

The results show the even and odd nature of the waveguide modes. It is interesting to note that the E_{11}^Y mode occupies an aperture of some $5\text{ }\mu\text{m}$ width only, while the E_{81}^Y fills the entire cavity width of $9\text{ }\mu\text{m}$. This is because of the non-rectangular nature of the fibre. The differences in some of the mode amplitude peaks, particularly for $p = 8$, are due to difficulties in aligning the mechanical scan with the correct transverse axis. The theoretical near-field scans (equation 6.22 with $x = \text{constant}$) consist of squared sinusoids with p peaks in the guide aperture - the observed mode patterns follow this approximate theory.

The experimental results presented above are incomplete in two respects. Firstly the intensity plots do not produce any information about the existence of the dominant E^X and E^Y mode polarizations, although it was assumed throughout that with the input beam plane polarized along the y -axis the E^Y modes were excited. Secondly both the experimental methods for recording the mode patterns were insensitive to the $(p-1)$ and $q-1$ reversals in the directions of the field components in the y and x directions respectively. A single experiment, described in the following paragraphs, provided evidence to support these predictions.

6.5.5 Near-field patterns of degenerate mode combinations.

It was found that at particular combinations of tilt and synchronous coupling angle, modes of orthogonal polarization and with different near-field patterns could be excited simultaneously. In order to launch both modes the input beam was plane polarized at an angle of 45° in the xy plane. The degenerate, orthogonally polarized modes interfered in the near-field and the decomposition of the observed pattern using an analyser (a plane polarizer) showed how the constituent waveguide modes were constructed. The particular combination presented in this

section was the most straightforward, and was the $(E_{51} + E_{12})$ mixture launched at a tilt angle of $8^{\circ}30'$ and a synchronous angle of $10^{\circ}30'$. Other combinations obtained were the $(E_{61} + E_{22})$ and $(E_{71} + E_{32})$ modes, and they were all characterised by annular shapes in the intensity patterns.

6.5.6 The $(E_{51} + E_{21})$ degenerate-mode near-field pattern.

The near-field pattern of the composite mode $(E_{51} + E_{12})$ was photographed, and is presented in Figure 6.10a. The analyser was positioned between the microscope eyepiece and the photographic plate, as in Figure 6.3, and the emergent patterns were recorded as a function of the position of the analyser relative to the y-axis. The results are shown in Figure 6.10b-e. When the analyser was positioned with its plane of polarization parallel to the y-axis (taken as reference zero) the E_{51}^y mode was transmitted, and when rotated perpendicular to the y-axis ($\pm \frac{\pi}{2}$), the E_{12}^x mode was transmitted. The composite mode was, therefore, the $(E_{51}^y + E_{12}^x)$, constructed from two orthogonal pure modes. Figure 6.10c and 6.10e are the transmitted patterns with the analyser set at $\frac{\pi}{4}$ and $-\frac{\pi}{4}$ respectively. They are the mirror images of each other about the y-axis, and add in intensity to produce the composite mode. The complementary nature of these patterns is a direct consequence of the sign reversals of the transverse fields in each direction and is unique to that particular theoretical model. The theoretical plots of the near-field intensity of the composite $(E_{51}^y + E_{12}^x)$ mode, as a function of analyser position, are also presented in Figure 6.10A-E.

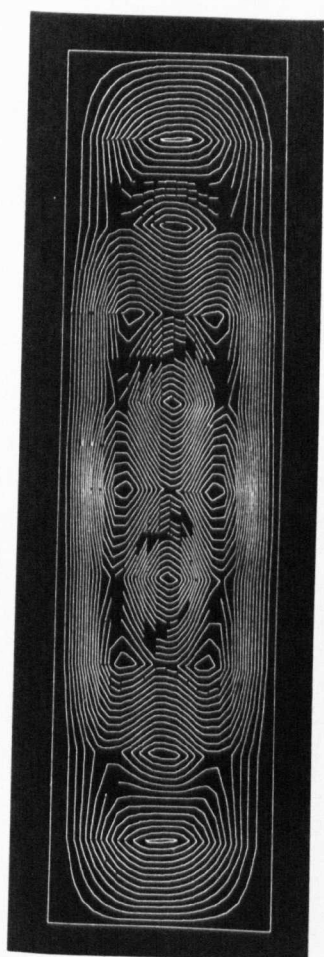
6.5.7 Theory of the approximate degenerate-mode distributions.

The plots of Figure 6.10A-E were derived from the following expressions. The equations for the field distributions of the $p_1 q_1^{\text{th}}$

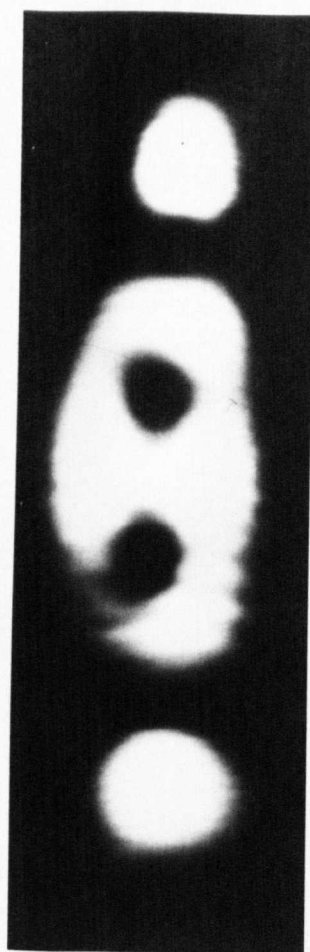
FIGURE 6.10

COMPOSITION OF THE $E_{51} + E_{12}$
DEGENERATE-MODE NEAR-FIELD PATTERN.

- A,a Near-field pattern, without analyser.
- B,b Near-field pattern, analyser setting parallel to y-axis.
- C,c Near-field pattern, analyser 45° .
- D,d Near-field pattern, analyser setting parallel to x-axis.
- E,e Near-field pattern, analyser -45° .

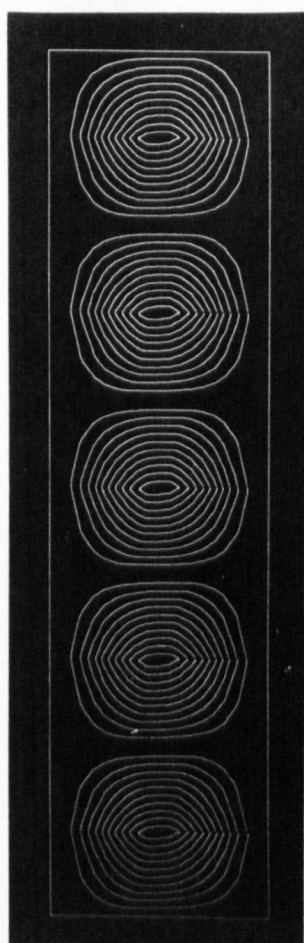


A

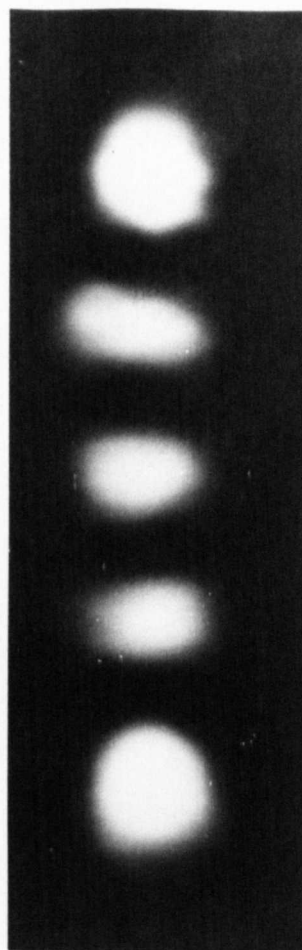


a

NO ANALYSER

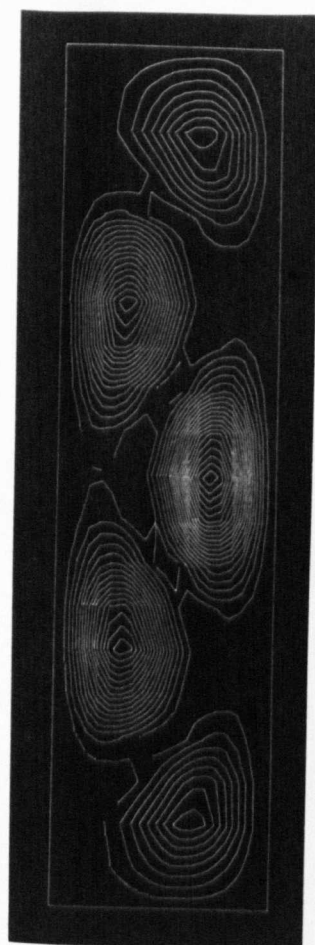


B



b

$$\alpha_a = 0$$

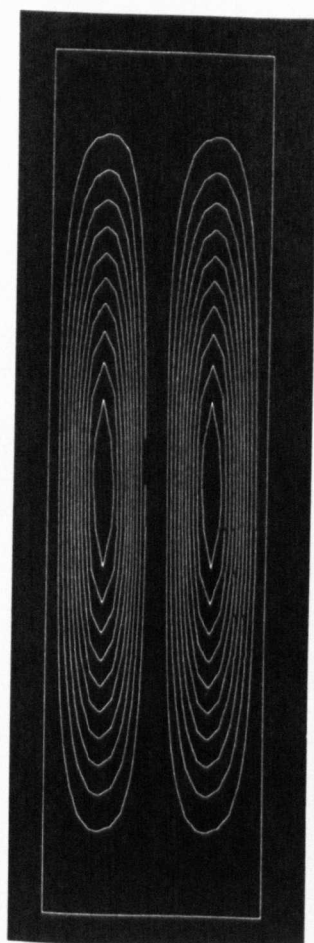


C

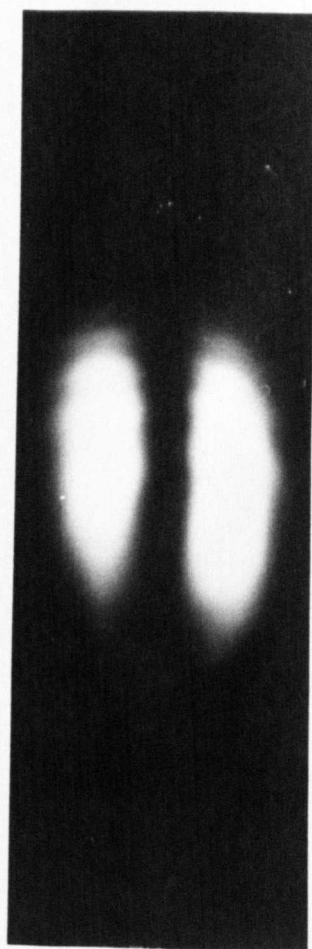


c

$$\alpha_a = \frac{\pi}{4}$$

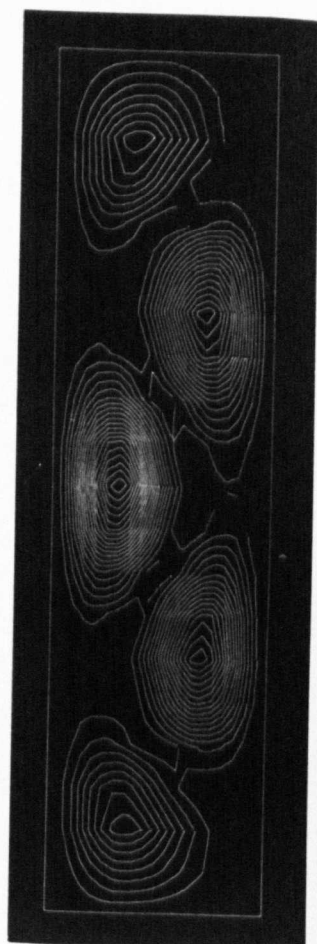


D

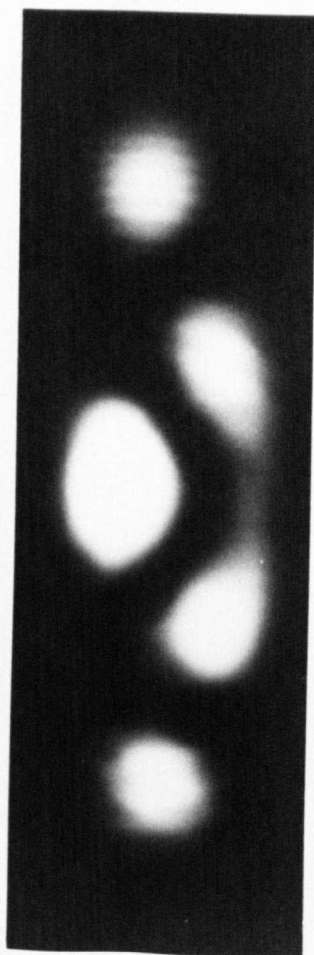


d

$$\alpha_a = \frac{\pi}{2}$$



E



e

$$\alpha_a = -\frac{\pi}{4}$$

and $p_2 q_2^{\text{th}}$ modes may be derived from equation 6.22 and are

$$\epsilon_{1 \text{ NF}}(x, y) = \cos\left(\frac{p_1 \Pi}{a} y + (p_1 - 1) \frac{\Pi}{2}\right) \cos\left(\frac{q_1 \Pi}{b} x + (q_1 - 1) \frac{\Pi}{2}\right) \quad 6.23$$

$$\epsilon_{2 \text{ NF}}(x, y) = \cos\left(\frac{p_2 \Pi}{a} y + (p_2 - 1) \frac{\Pi}{2}\right) \cos\left(\frac{q_2 \Pi}{b} x + (q_2 - 1) \frac{\Pi}{2}\right) \quad 6.24$$

The mutually perpendicular polarizations of ϵ_1 and ϵ_2 may be accounted for by the introduction of the imaginary operator such that the total field of the degenerate mode in the cross-section is

$$\epsilon_{\text{tot}}(x, y) = \epsilon_1(x, y) + j \epsilon_2(x, y) \quad 6.25$$

The phase associated with ϵ_{tot} is thus

$$\psi = \tan^{-1} \frac{\epsilon_2(x, y)}{\epsilon_1(x, y)} \quad 6.26$$

and the intensity pattern is

$$I = \epsilon_1^2(x, y) + \epsilon_2^2(x, y) \quad 6.27$$

If an analyser is placed between the image plane and the observed near-field pattern, a modulation of the intensity pattern by the function

$$T_A = \cos^2(\alpha_a - \psi) \quad 6.28$$

results, where α_a is the phase angle introduced by the analyser.

The complete expression for the near-field intensity pattern of a degenerate orthogonally polarized mode viewed through an analyser with phase angle α_a is obtained from equations 6.23 - 6.28 and is

$$\begin{aligned} & \left(\cos^2\left(\frac{p_1 \Pi}{a} y + (p_1 - 1) \frac{\Pi}{2}\right) \cos^2\left(\frac{q_1 \Pi}{b} x + (q_1 - 1) \frac{\Pi}{2}\right) + \cos^2\left(\frac{p_2 \Pi}{a} y + (p_2 - 1) \frac{\Pi}{2}\right) \right. \\ & \left. \cos^2\left(\frac{q_2 \Pi}{b} x + (q_2 - 1) \frac{\Pi}{2}\right) \right) \\ & \cos^2\left(\alpha_a - \tan^{-1} \frac{\cos\left(\frac{p_2 \Pi}{a} y + (p_2 - 1) \frac{\Pi}{2}\right) \cos\left(\frac{q_2 \Pi}{b} x + (q_2 - 1) \frac{\Pi}{2}\right)}{\cos\left(\frac{p_1 \Pi}{a} y + (p_1 - 1) \frac{\Pi}{2}\right) \cos\left(\frac{q_1 \Pi}{b} x + (q_1 - 1) \frac{\Pi}{2}\right)}\right) \quad 6.29 \end{aligned}$$

The contour plots were drawn using a standard plotting subroutine ("CONTUR") of a PDP 11 digital computer.

It can be seen from Figure 6.10 that the experimental near-field plots of the degenerate mode combinations are in complete agreement with this theory.

6.5.8 Conclusions.

The major conclusions arrived at in Section 6.5 are:

(i) The approximate solution for rectangular waveguides is adequate for describing the propagation of modes in SR fibres.

(ii) The near-field intensity patterns indicate that there is mode confinement in both transverse directions of three-dimensional SR fibres, and that the theoretical intensity distributions are in agreement with those observed. There are p and q intensity maxima in the y and x directions respectively.

(iii) Polarization studies have revealed

(a) that there are two dominant polarizations existing in the fibres, E_{pq}^x and E_{pq}^y and that these are mutually independent due to their orthogonality. The use of Marcatili's assumptions in formulating the waveguide theory, principally through equation 6.6, is thus justified experimentally.

(b) The mode fields in each transverse direction undergo $(p-1)$ or $(q-1)$ sign reversals.

The amplitude and phase characteristics of the mode fields in a near-rectangular fibre waveguide have been shown experimentally to be in accordance with the theoretical predictions.

6.6 Far-field Radiation Patterns of Three-dimensional SR Fibre Waveguide Modes.

6.6.1 Introduction.

The method of detecting a particular mode during the prism coupling experiments in Section 6.4.3 was by visual observation of the radiation patterns of the fibres. The characteristic intensity distributions observed in the far-field depended on the mode excited and the dimensions of the waveguide. It was considered worthwhile to present the results for the characteristic radiation patterns and relate them to a theoretical model. The results have some practical application to the codirectional coupling of SR fibres and circular (or other) types of fibres, where a knowledge of the "end fire" radiation pattern would be useful.

The section proceeds with the development of the theoretical model using the mode field expressions and the theoretical results are compared with the experimental results for the twelve-mode fibre used previously. Also presented are the far-field patterns of the modes of a three-dimensional SR fibre using an output prism coupler. The 'm-line' distributions, as they are alternatively called, are included in this section because they constitute a radiation pattern characteristic of the waveguide modes. They do not originate from the confined energy radiating freely from the fibre termination but via the evanescent coupling action of the output prism. The diffraction patterns obtained by this method are presented and described.

6.6.2 Theory of far-field patterns due to radiation from SR fibre termination.

The far-field patterns of low-order modes in circular fibres have been studied extensively by Kapany,⁷² and in this thesis (Chapter 4) the radiation patterns of higher-order modes of circular fibres are

discussed. The theoretical approach to the problem is well-established, involving the Fourier theory of Fraunhofer diffraction, and may be readily extended to the near-rectangular waveguide geometry. The mode fields $\epsilon(x,y)$, launched at $z = -\infty$, radiate from the waveguide aperture into the homogeneous half-space $z > 0$. The situation may be thought of as a near-rectangular aperture encoded with the amplitude and phase characteristics of the near-field of the pq^{th} mode and illuminated by plane wavefronts perpendicular to it. The far-field distribution (Fraunhofer region) is given by⁹⁹

$$\Sigma_{\text{FF}}(x,y) = \int_{-b/2}^{b/2} \int_{-a/2}^{a/2} \epsilon(x,y) e^{-j(k \sin \gamma_y y + k \sin \gamma_x x)} dx dy \quad 6.30$$

where γ_x and γ_y are the emergent half-angles in the xz and yz planes respectively. However the mode fields in x and y may be treated separately, and the total far-field can be described as the product of the diffraction patterns in x and y . Equation 6.30 may be simplified to

$$\Sigma_{\text{FF}}(x,y) = \int_{-b/2}^{b/2} H(x) e^{-j k \sin \gamma_x x} dx \int_{-a/2}^{a/2} E(y) e^{-j k \sin \gamma_y y} dy \quad 6.31$$

Each integral has the form

$$I(\gamma_w) = \int_{-l/2}^{l/2} e^{-j k \sin \gamma_w w} \cos \left[r \pi \frac{w}{l} + (r-1) \frac{\pi}{2} \right] dw \quad 6.32$$

where

$$w = x, y$$

$$r = q, p$$

$$l = b, a$$

If $v = k \sin \gamma_w$, $d = \frac{r\pi}{\ell}$ and $\alpha = (r-1)\frac{\pi}{2}$, we find

$$I(\gamma_w) = \frac{2 \cos \alpha}{d^2 - v^2} \left(d \sin \frac{d\ell}{2} \cos \frac{v\ell}{2} - v \cos \frac{d\ell}{2} \sin \frac{v\ell}{2} \right) \\ - \frac{2 \sin \alpha}{d^2 - v^2} \left(d \cos \frac{d\ell}{2} \sin \frac{v\ell}{2} - \sin \frac{d\ell}{2} \cos \frac{v\ell}{2} \right) \quad 6.33$$

The amplitude distribution in the far-field in the w-direction, as a function of γ_w , is given by $|I(\gamma_w)|^2$. The complete intensity pattern in the far-field is therefore;

$$P_{FF}(x, y) = |I(\gamma_x)|^2 |I(\gamma_y)|^2 \quad 6.34$$

Equation 6.34 was solved using a PDP8 digital computer.

6.6.3 Observation of far-field patterns and comparison with theory.

(i) radiation from fibre termination.

The far-field patterns were studied using the same apparatus as Figure 6.3 but with the eyepiece of the travelling microscope removed and the emergent patterns focused at infinity. The radiation patterns of the twelve E^Y modes were recorded using a photographic plate positioned behind the microscope, and the result for each mode is shown in Figure 6.11. For each mode there are p and q intensity maxima in the y and x directions respectively. In particular the patterns for the $q = 1$ family of modes consist of two dominant outer lobes enveloping $(p-2)$ inner lobes of lower amplitude. As with the near-field patterns, the far-field patterns were recorded using a scanning photodiode, and the result of one such scan for the E_{41}^Y mode is compared with the theoretical prediction (equation 6.34 with $x = \text{constant}$) in Figure 6.12a,b.

Comparison of the two results show that the measured level of the inner lobes relative to the outer lobes is larger than one might

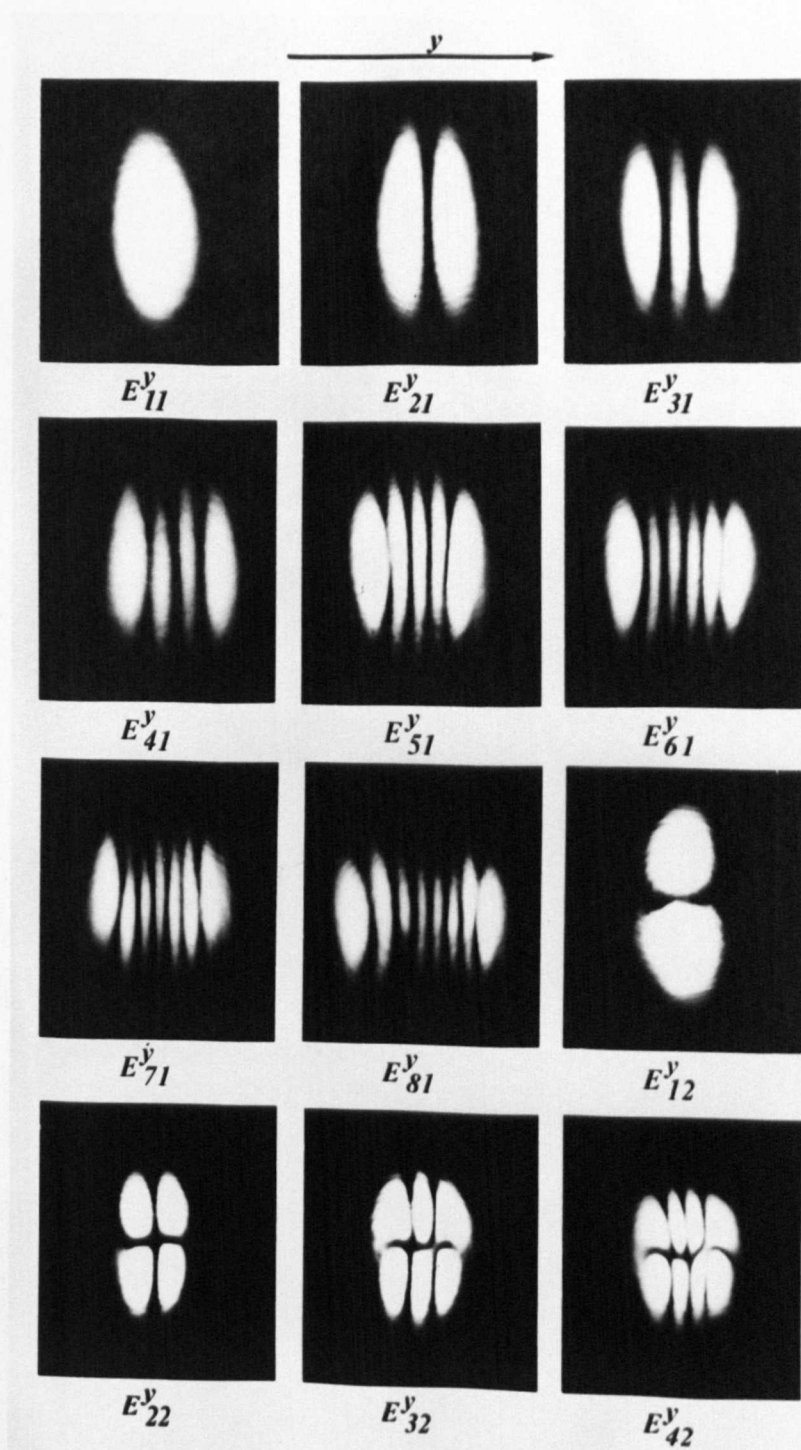


FIGURE 6.11 Far-field patterns of the E^y modes of a 3-D SR fibre.

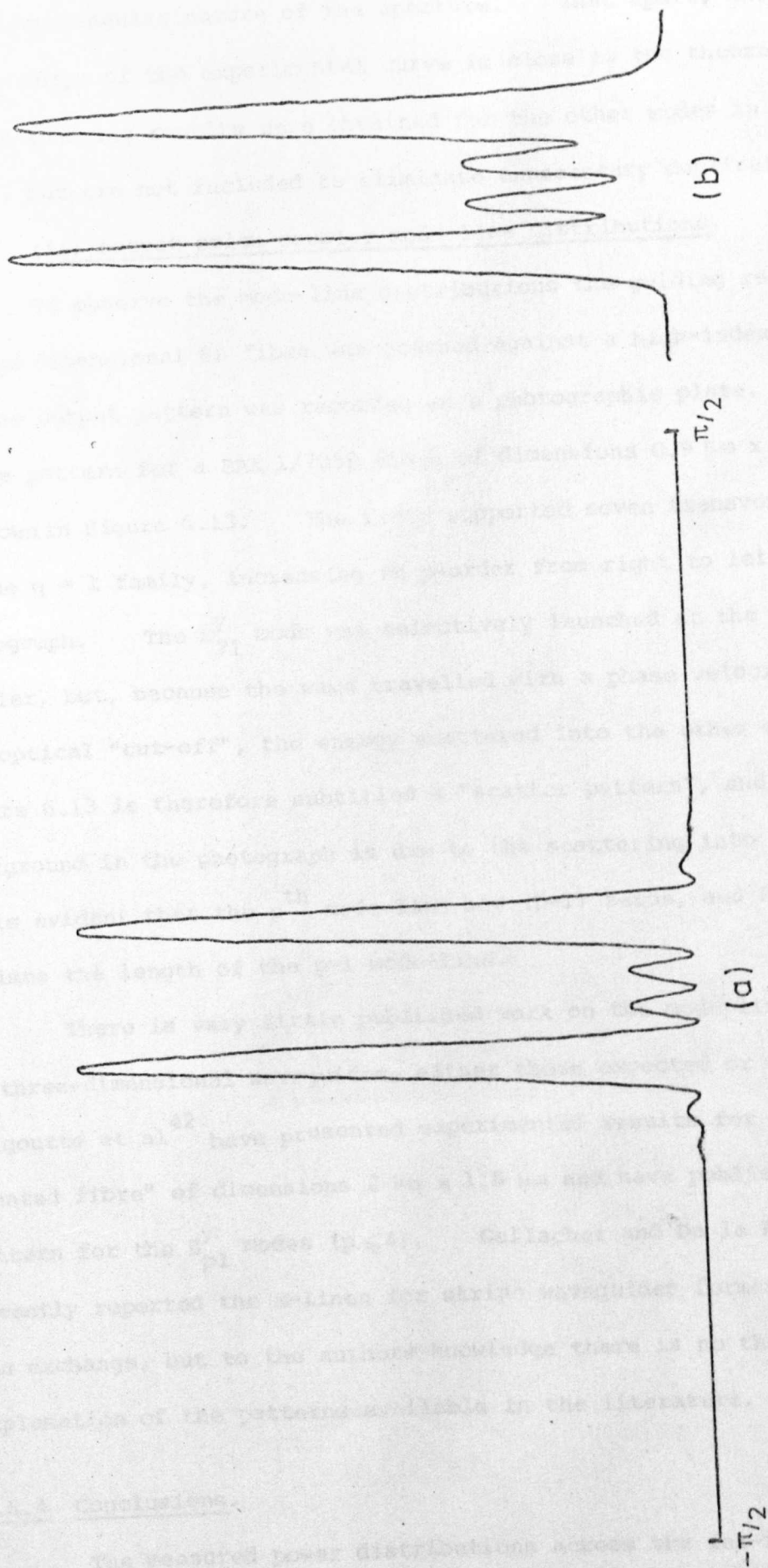


FIGURE 6.12 Far-field radiation pattern of the E_{41}^y mode.
 (a) theory (b) experimental scan in y-direction.

expect, perhaps due to phase errors at the waveguide termination or the non-rectangular nature of the aperture. That apart, the periodicity and the shape of the experimental curve is close to the theoretical curve. Similar scanning results were obtained for the other modes in the E_{pl}^y family, but are not included to eliminate unnecessary duplication.

(ii) output prism coupler mode-line distributions.

To observe the mode-line distributions the guiding region of a three-dimensional SR fibre was pressed against a high-index prism and the output pattern was recorded on a photographic plate. The m-line pattern for a BAK 1/7059 fibre of dimensions $0.9 \mu\text{m} \times 3.7 \mu\text{m}$ is shown in Figure 6.13. The fibre supported seven transverse modes in the $q = 1$ family, increasing in p-order from right to left in the photograph. The E_{71}^y mode was selectively launched at the input prism coupler, but, because the wave travelled with a phase velocity very near the optical "cut-off", the energy scattered into the other modes. Figure 6.13 is therefore subtitled a "scatter pattern", and the noisy background in the photograph is due to the scattering into the substrate. It is evident that the p^{th} mode-line has $(p-1)$ zeros, and is approximately p times the length of the $p=1$ mode-line.

There is very little published work on the mode-line distributions of three-dimensional waveguides, either those expected or encountered. Dalgoutte et al.⁴² have presented experimental results for an "externally mounted fibre" of dimensions $2 \mu\text{m} \times 1.5 \mu\text{m}$ and have published the m-line pattern for the E_{pl}^y modes ($p \leq 4$). Gallacher and De la Rue¹⁰⁶ have recently reported the m-lines for stripe waveguides formed by silver ion exchange, but to the authors knowledge there is no theoretical explanation of the patterns available in the literature.

6.6.4 Conclusions.

The measured power distributions across the far-field patterns

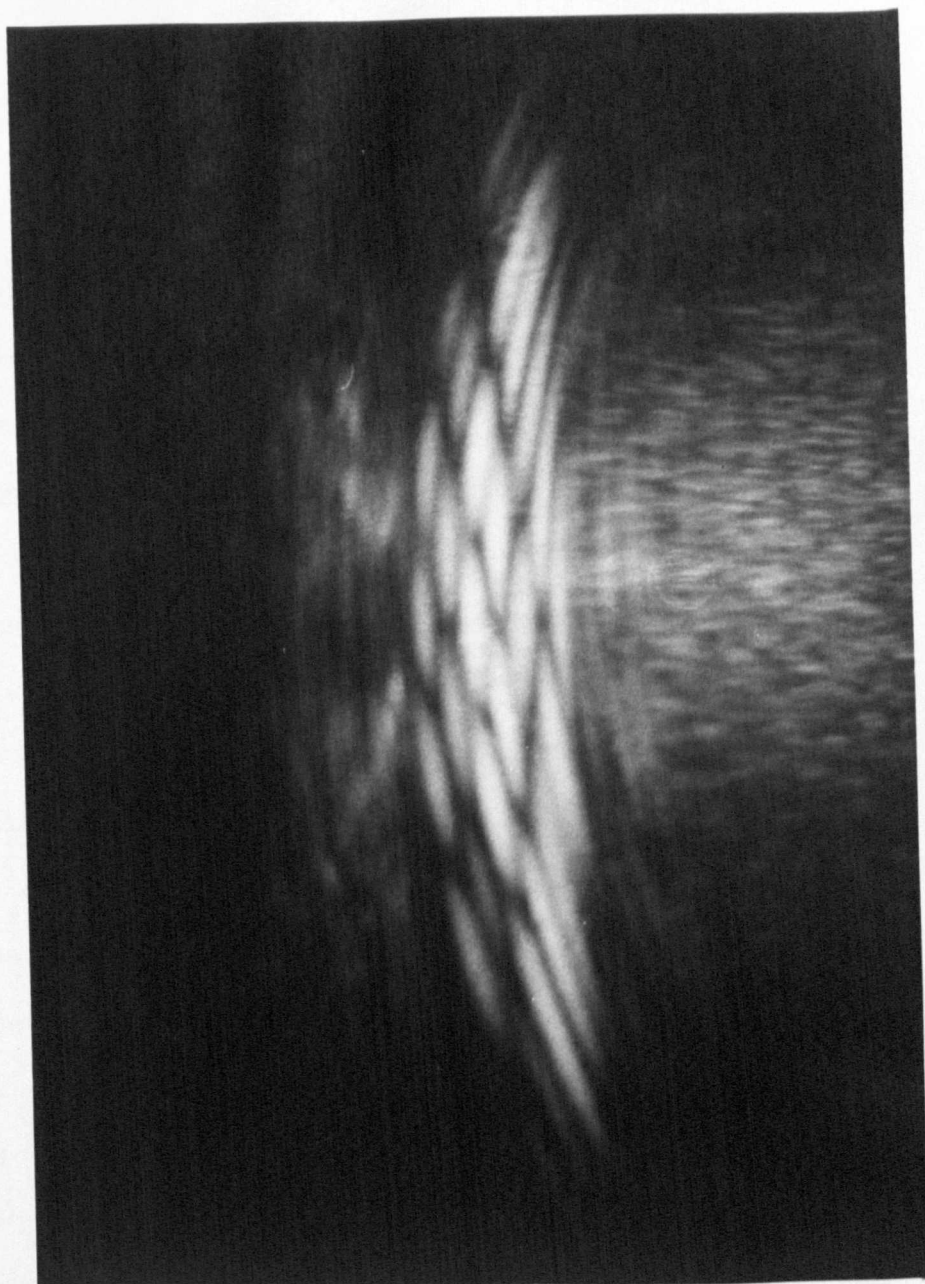


FIGURE 6.13 m-line scatter pattern of
a 3-D SR fibre,
 $3.7\mu\text{m} \times 0.9\mu\text{m}$.

emerging from the SR fibre waveguide termination was as predicted by the approximate theoretical model based on the Fourier theory of Fraunhofer diffraction of the near-field distribution through the waveguide aperture. The use of the theory would seem sufficient to calculate the radiation fields needed in the design of butt joints using SR fibres.

6.7 Summary and General Conclusions.

The recognition of the practical importance of rectangular or near-rectangular waveguides has led to the study, both theoretical and experimental, of the properties of three-dimensional SR fibre waveguides. The aim was to produce a fibre capable of coupling the envisaged integrated optical waveguides. The method of manufacture of the fibres was described, and it was shown that a three-dimensional fibre, of low optical loss, can be manufactured simply and inexpensively using established glass pulling techniques. It was further shown that the complete mode family of an SR fibre could be excited by a prism coupler. Knowledge of the mode structure of the fibres was central to the design of a coupler constructed from them and in Section 6.4 we discussed the experimental results of an extensive study of mode excitation, and related these results to the theoretical predictions. It was found that the approximate model was valid, and that it could be further successfully applied to the observations of the near-field patterns. The amplitude and phase characteristics of the guided wave mode patterns were verified experimentally. The far-field patterns of the fibre waveguide modes were studied: two such characteristic patterns were dealt with, the "end fire" radiation pattern and the exit prism coupler mode-line distribution. The former was shown to be in accordance with our understanding of wave propagation in SR fibres.

It can therefore be concluded that the initial objectives of

the manufacture and understanding of a three-dimensional waveguide, capable of coupling practical integrated optical waveguides, have been realised.

The major results of this chapter have been published.¹¹⁷

APPENDIX 5

APPENDIX 6.

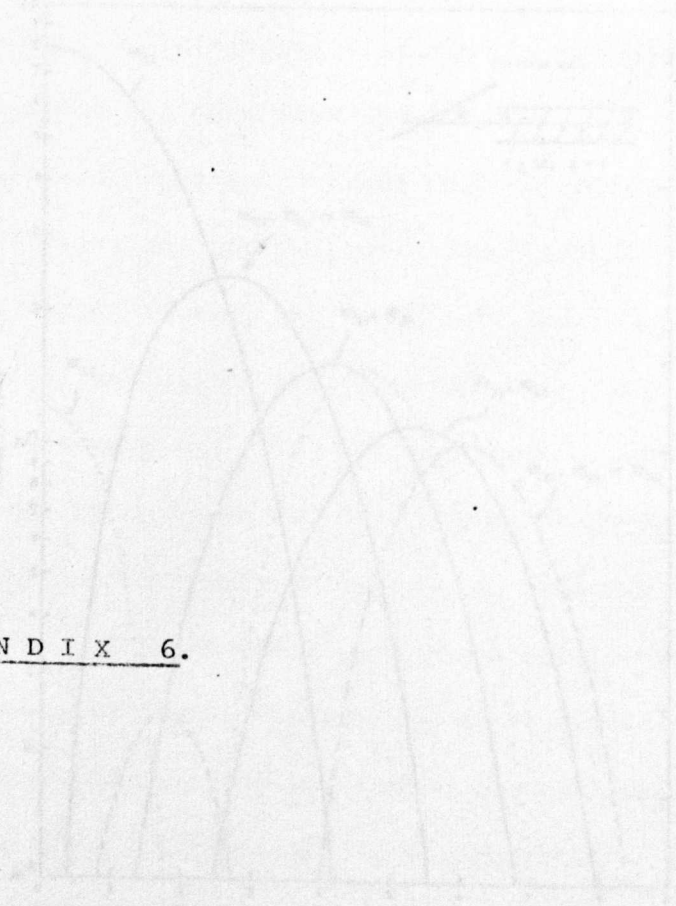
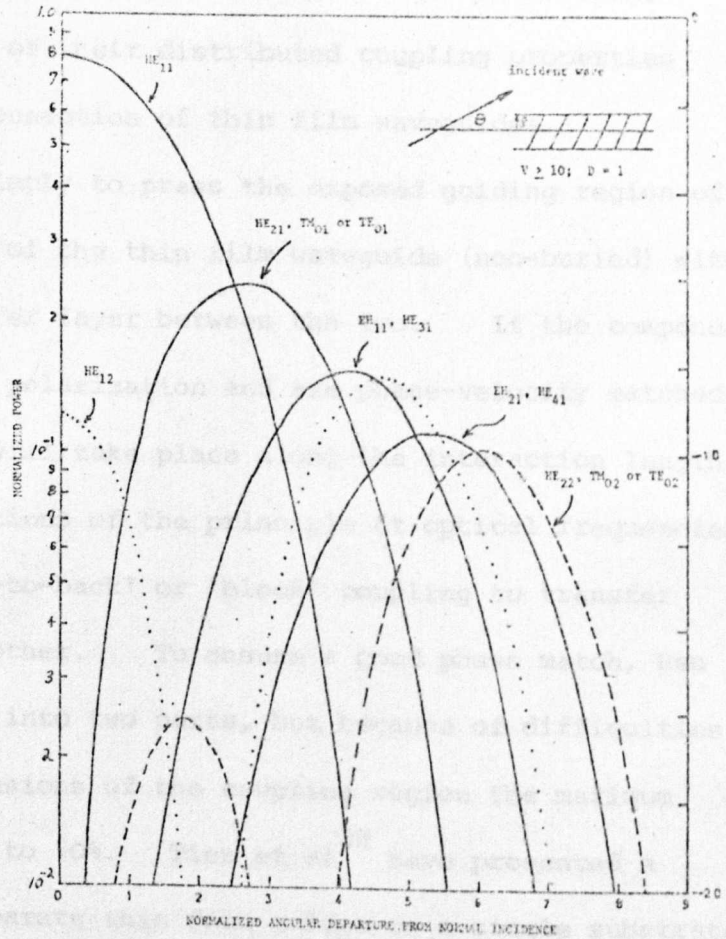


FIGURE A50. Excitation of circular fibre
with linearly polarized light
using a waveguide.



Power of modes excited by a uniform source when the aperture $d = \rho$ and $V \geq 10$. δ and θ are assumed small. λ is the wavelength in an ϵ_1 medium.

FIGURE A6.1 Excitation of circular fibre waveguide modes using tilting plane - wave illumination, after Snyder.¹¹⁶

CHAPTER 7. EVANESCENT FIELD COUPLING OF RIBBON FIBRES AND THIN FILM WAVEGUIDES.

7.1. Introduction.

The development of fibre guides with an exposed core, such as planar or three-dimensional ribbons of open sandwich construction, leads to the consideration of their distributed coupling properties principally for the interconnection of thin film waveguides.

The principle is simply to press the exposed guiding region of the fibre onto the surface of the thin film waveguide (non-buried) with or without a low index buffer layer between the two. If the component guided modes have the same polarization and are phase-velocity matched, then directional coupling will take place along the interaction length. One of the first demonstrations of the principle at optical frequencies was by Hsu⁸⁵ who used 'back-to-back' or 'block' coupling to transfer energy from one film to another. To ensure a good phase match, Hsu used the same film divided into two parts, but because of difficulties in defining the exact dimensions of the coupling region the maximum power transfer was limited to 70%. Tien et al³⁸ have presented a technique to couple two separate thin film guides on a single substrate, which involved the transition of the wave into a gradual taper of an overlay guide. McMurray and Stanley¹⁰⁸ have successfully used the method to transfer optical energy in a thin glass film into and out of a thin film modulator in cadmium sulphide. The use of taper transitions has been studied theoretically by Wilson and Teh,⁴⁵ Smith¹⁰⁹ and Louisell.⁴⁴ Dalgoutte,⁴² using fibres similar in construction to three-dimensional SR fibres, has reported the observation of transverse coupling from thin film waveguides, utilizing a tapered velocity coupler to overcome the phase mismatch, and has proposed methods whereby coupling might be possible from high refractive index films to glass sandwich ribbons. A power transfer from a sputtered film to the fibre of 70% was noted.

The realisation that external methods and devices to overcome any inherent mismatch of the coupled waves, such as a thickness taper or a periodic grating might of themselves be lossy or inefficient, leads us to the adoption of a slightly different approach. The proposal, sketched in Figure 7.1, shows that the guiding regions of the fibre and film are brought into intimate contact such that the evanescent waves of the guided modes interact. The figure illustrates the coupling of an integrated optical device, such as a modulator, via the SR fibre to either a semiconductor laser, another thin film or a taper or a butt joint to a circular fibre. The waveguide structures are phase matched along the entire region of interaction, allowing a return to the classical model of directional coupling outlined in Chapter 2 (Part ii). The matching of the phase velocities of the guiding structures is achieved in this case by resorting to silver/sodium ion-exchanged waveguides where the modal propagation constants, β_m , are precisely determined by the fabrication parameters. The waveguiding properties of thin films used in this work must of necessity be examined, firstly to ensure a phase-matched configuration and secondly to obtain a theoretical coupling coefficient for the waves in a coupled system.

7.2 Silver/Sodium Ion-Exchanged Thin Film Waveguides.

7.2.1 Advantages of silver/sodium ion-exchanged waveguides.

Thin film optical waveguides have been manufactured by a variety of techniques,⁷³ but at present there is considerable interest in guides formed by various types of diffusion processes, including the exchange and diffusion of Ag^+ ions in soda-lime glass.¹¹⁴ The major advantages of Ag^+/Na^+ ion-exchanged (IE) waveguides can be listed as follows:

- TO: (a) TAPER OR BUTT JOINT TO CIRCULAR FIBRE
 (b) OTHER THIN FILM
 (c) SEMICONDUCTOR LASER

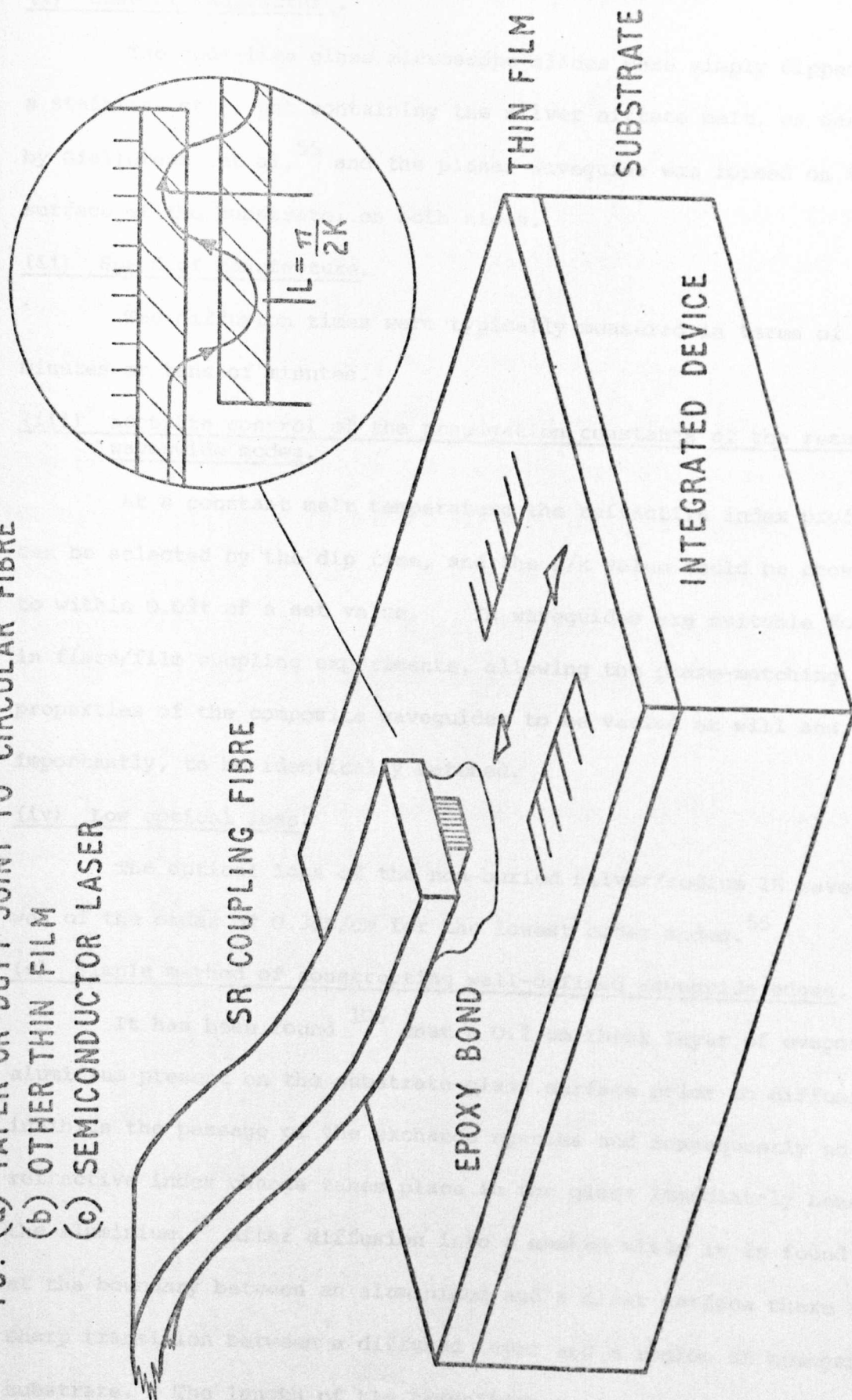


FIGURE 7.1 Coupling of integrated optical circuits using sandwich ribbon fibres : Proposal

(i) Ease of manufacture.

The soda-lime glass microscope slides were simply dipped in a stainless steel pot containing the silver nitrate melt, as described by Giallorenzi et al,⁵⁵ and the planar waveguide was formed on the surface of the substrate, on both sides.

(ii) Speed of manufacture.

The diffusion times were typically measured in terms of minutes or tens of minutes.

(iii) Accurate control of the propagation constants of the resulting waveguide modes.

At a constant melt temperature the refractive index profile can be selected by the dip time, and the β/k value could be chosen to within 0.03% of a set value. IE waveguides are suitable for use in fibre/film coupling experiments, allowing the phase-matching properties of the composite waveguides to be varied at will and, most importantly, to be identically matched.

(iv) Low optical loss.

The optical loss of the non-buried silver/sodium IE waveguides was of the order of 0.3dB/cm for the lowest order modes.⁵⁵

(v) Simple method of constructing well-defined waveguide edges.

It has been found¹⁰⁶ that a 0.2 μm thick layer of evaporated aluminium present on the substrate glass surface prior to diffusion inhibits the passage of the exchange species and consequently no refractive index change takes place in the glass immediately beneath the aluminium. After diffusion into a masked slide it is found that at the boundary between an aluminized and a clear surface there is a sharp transition between a diffused layer and a region of homogeneous substrate. The length of the transition region is, to a first approximation, the diffusion depth ' d_d '. Using this technique, Gallacher and De la Rue¹⁰⁶ have found it possible to define three-

dimensional waveguide patterns for integrated optical circuits.

If IE waveguides with the advantages listed above are to be used in experimental coupling configurations, the refractive index profile of the waveguide, its dependence on the fabrication conditions and the coupling coefficient associated with its particular geometry and mode-field configuration, must all be examined. Working in collaboration with Mr. George Stewart of this department, the study of planar optical waveguides formed by silver-ion migration in glass was undertaken.⁵⁶ The following section is a short description of the refractive index profile and shows how the definition of an effective diffusion depth leads to a universal mode dispersion graph, applicable over a wide range of fabrication conditions. The construction of an appropriate eigenvalue equation will be shown to lead to an expression for the coupling coefficient for such a waveguide.

7.2.2 The refractive index profile.

Using a non-destructive optical technique,⁵⁶ the refractive index profile of a silver/sodium IE guide has been found to follow a quadratic variation with depth into the host glass as

$$\begin{aligned} n(x) &= n_s - \Delta \left(\frac{x}{d_d} + f \left(\frac{x}{d_d} \right)^2 \right) & x \leq d_1 \\ &= n_2 & x > d_1 \end{aligned} \quad 7.1$$

where x is the depth into the sample perpendicular to the surface, n_s and n_2 are the surface and substrate refractive indices respectively, $\Delta = n_s - n_2$, $f = 0.64$ and d_d is a constant which depends on the melt temperature and the diffusion time. The graph of $n(x)$ against $\left(\frac{x}{d_d}\right)$ is shown in Figure 7.2. The depth d_1 is defined by the condition

$$\left. \left(\frac{x}{d_d} + 0.64 \left(\frac{x}{d_d} \right)^2 \right) \right|_{x=d_1} = 1 \quad 7.2$$

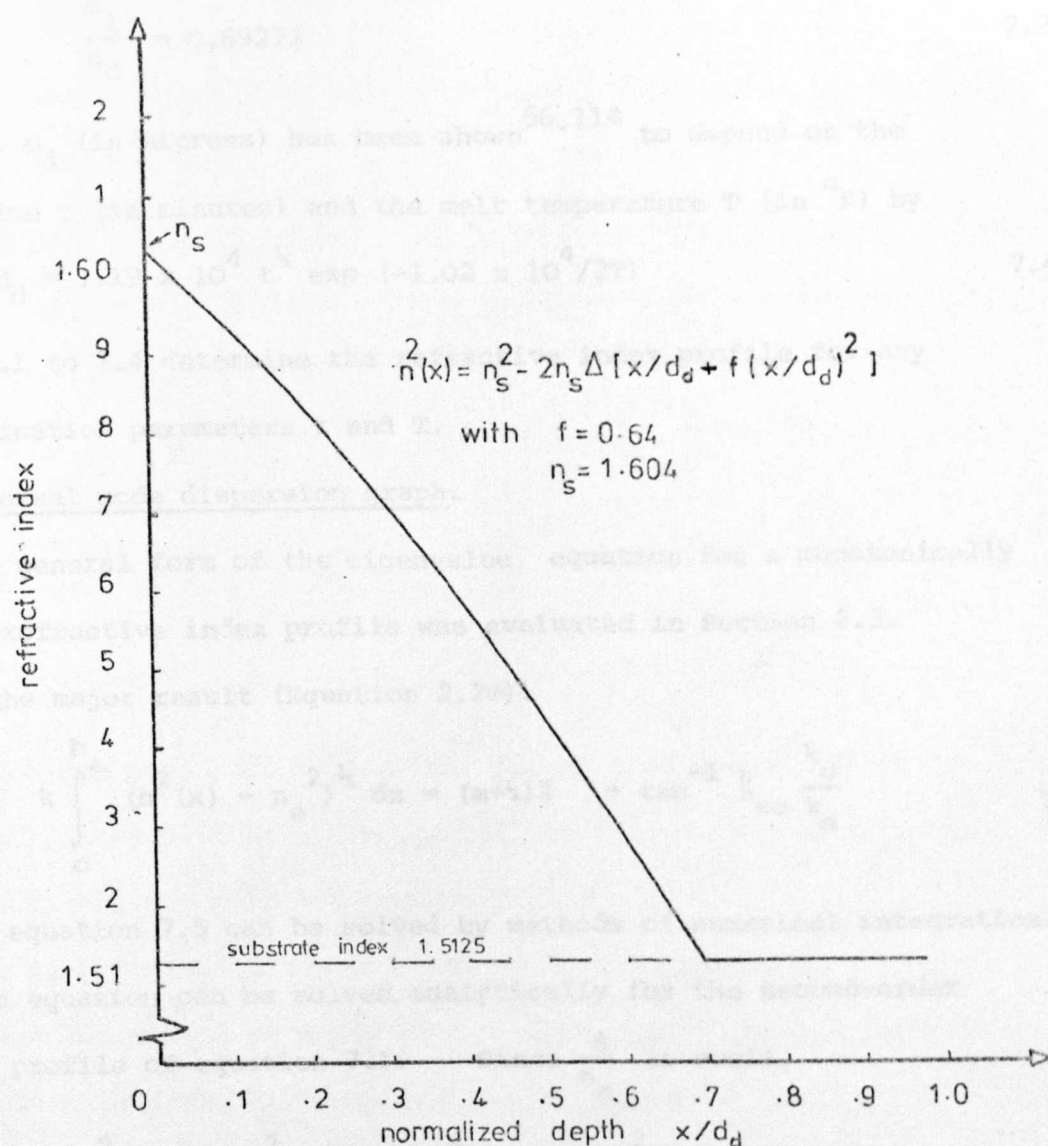


FIGURE 7.2 Second order polynomial
refractive index profile
against normalized depth.

or

$$\frac{d_1}{d_d} = 0.69273 \quad 7.3$$

The constant d_d (in microns) has been shown^{56,114} to depend on the diffusion time t (in minutes) and the melt temperature T (in $^{\circ}\text{K}$) by

$$d_d = 1.19 \times 10^4 t^{\frac{1}{2}} \exp(-1.02 \times 10^4/2T) \quad 7.4$$

Equations 7.1 to 7.4 determine the refractive index profile for any set of fabrication parameters t and T .

7.2.3 Universal mode dispersion graph.

The general form of the eigenvalue equation for a monotonically decreasing refractive index profile was evaluated in Section 2.3.

Restating the major result (Equation 2.20):

$$k \int_0^b (n^2(x) - n_e^2)^{\frac{1}{2}} dx = (m + \frac{1}{4})\pi + \tan^{-1} \xi_{so} \frac{k_o}{k_s} \quad 7.5$$

In general equation 7.5 can be solved by methods of numerical integration.

However the equation can be solved analytically for the second-order

polynomial profile of equation 7.1. Since $\frac{\Delta}{n_s}$ is small,

$$n^2(x) \approx n_s^2 - 2n_s \Delta \left(\frac{x}{d_d} + f \left(\frac{x}{d_d} \right)^2 \right) \quad 7.6$$

With this approximation a solution may be found.⁵⁶

It may be seen from the profile (Figure 7.2) that a linear approximation with $f = 0$ may suffice. Equation 7.6 becomes

$$n^2(x) = n_s^2 - 2n_s \Delta \left(\frac{x}{d_1} \right) \quad 7.7$$

with

$$d_1 = d_d \times 0.69273 \quad 7.8$$

For the profile of equation 7.9, equation 7.5 may be readily evaluated in a simple, though approximate, form:

$$kd_1 \frac{(n_s^2 - n_e^2)^{3/2}}{3n_s \Delta} = (m + \frac{1}{4})\pi + \tan^{-1} \xi_{so} \frac{k_o}{k_s} = \psi \quad 7.9$$

which, along with equation 7.8, is the universal description of the mode dispersion curves.

7.2.4 Particular solution of the mode dispersion against diffusion time.

If only one silver nitrate melt temperature is considered, at say 250°C, equation 7.8 becomes

$$d_1 \Big|_{T = 250^\circ\text{C}} = 0.69269 t_{250}^{1/2} \times 0.69273 \quad 7.10$$

Substitution into equation 7.9 gives

$$0.69273 \times 0.69269 k t_{250}^{1/2} \frac{(n_s^2 - n_e^2)^{3/2}}{3n_s \Delta} = \psi \quad 7.11$$

which defines any propagation constant, $\beta = kn_e$, of the m^{th} TE or TM mode of the IE waveguide as a function of the diffusion time t_{250} , in minutes, at a constant melt temperature of 250°C.

The graphical solution of equation 7.11 is presented in Figure 7.3 for the first two TE and TM modes of the waveguide. Superimposed on the graph are experimentally measured points for the TM modes.

7.2.5 Selection of the film-mode propagation constant.

The results of Figure 7.3 indicate that choice of the diffusion time at a constant temperature allows us to vary, to within fractions of one percent, the phase velocity of the guided mode in the film, and so produce a match at the coupling region to the known velocity of the wave in the ribbon fibre. The 'tuning' of a film mode to a particular n_e was made less critical because of a slight variation in n_e along the length of the diffused slide, due to a slight temperature gradient in the melting pot. In fact the mounting base had a larger thermal capacity than the pot lid and this resulted in a gradient in n_e of about $1.5 \times 10^{-4} \text{ cm}^{-1}$ over 3 cm.

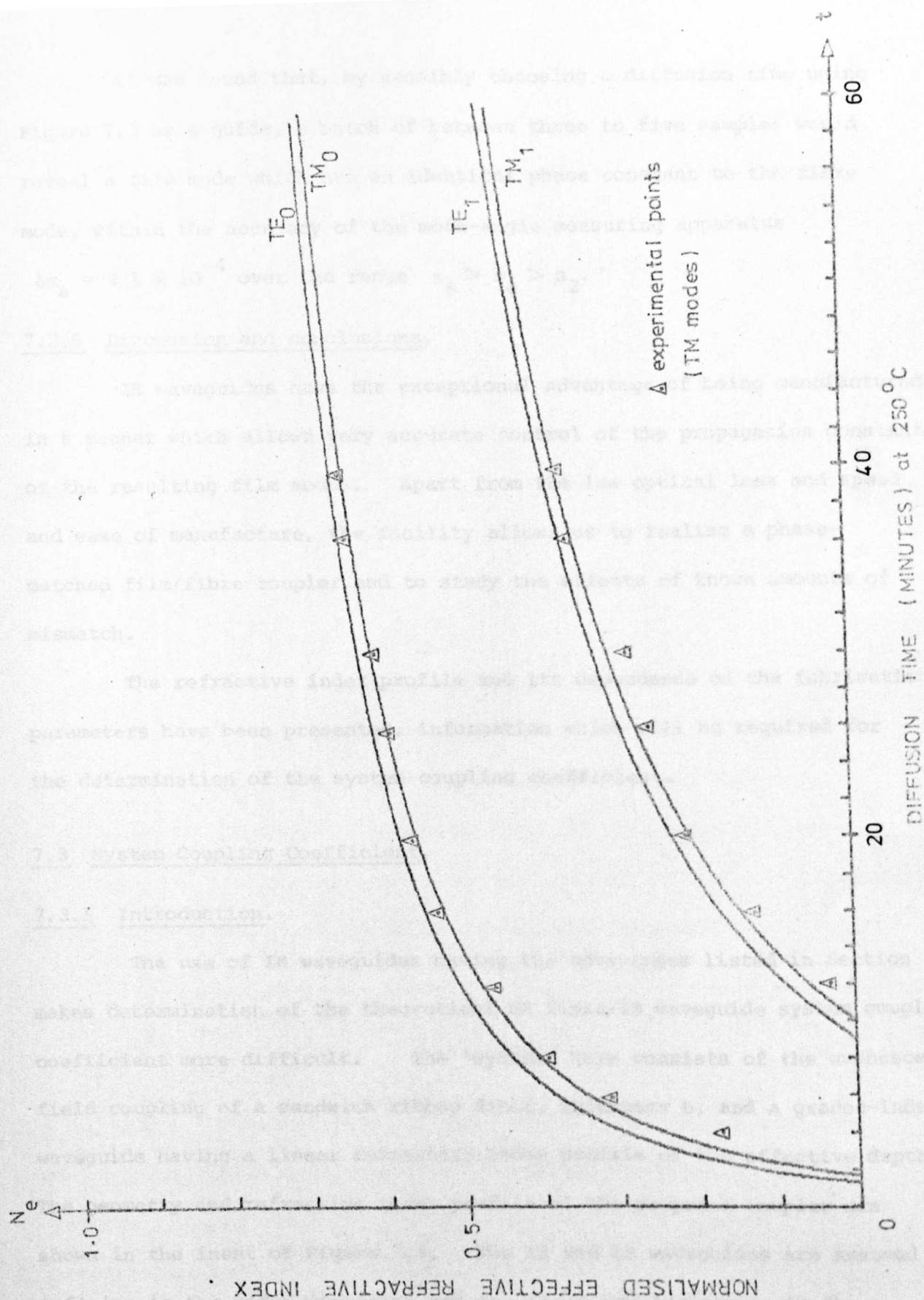


FIGURE 7.3 Mode dispersion ($m=0,1$) of an IE waveguide against diffusion time at 250°C.

It was found that, by sensibly choosing a diffusion time using Figure 7.3 as a guide, a batch of between three to five samples would reveal a film mode which had an identical phase constant to the fibre mode, within the accuracy of the mode-angle measuring apparatus

$$\delta n_e = \pm 1 \times 10^{-4} \text{ over the range } n_s > n_e > n_2.$$

7.2.6 Discussion and conclusions.

IE waveguides have the exceptional advantage of being manufactured in a manner which allows very accurate control of the propagation constants of the resulting film modes. Apart from the low optical loss and speed and ease of manufacture, the facility allows us to realise a phase-matched film/fibre coupler and to study the effects of known amounts of mismatch.

The refractive index profile and its dependence on the fabrication parameters have been presented, information which will be required for the determination of the system coupling coefficient.

7.3 System Coupling Coefficient.

7.3.1 Introduction.

The use of IE waveguides having the advantages listed in Section 7.2, makes determination of the theoretical SR fibre/IE waveguide system coupling coefficient more difficult. The 'system' here consists of the evanescent field coupling of a sandwich ribbon fibre, thickness b , and a graded-index waveguide having a linear refractive index profile of the effective depth d_1 . The geometry and refractive index profile of the proposed coupler are shown in the inset of Figure 7.4. The IE and SR waveguides are assumed infinite in the width direction and the field overlap occurs in the region of material n_o .

An expression for the coupling coefficient will be derived and examined in the following subsections.

7.3.2 Determination of the IE waveguide self-coupling coefficient.

The self-coupling coefficient for the SR fibre section of the coupler is a simple matter to evaluate, as this is merely the coupling coefficient of two identical asymmetric slab waveguides. An outline of the procedure is given in Section 2.8 and the result, for TE modes is,

$$K_{SR} = \frac{2k_o \exp(-ck_o)}{\beta(b + 1/k_o + 1/k_3)(1 + (k_o/k_1)^2)} \quad 7.12$$

where

$$k_o^2 = \beta^2 - k_{n_o}^2$$

$$k_1^2 = k_{n_1}^2 - \beta^2$$

$$k_3^2 = \beta^2 - k_{n_3}^2$$

b = waveguide thickness

c = interguide spacing

It should be noted that equation 7.12 can be made independent of the waveguide thickness by resubstituting the characteristic equation 2.6. Equation 7.12 becomes a function of the material refractive indices, the interguide spacing and the modal propagation constant:

$$K_{SR} = \frac{2k_o \exp(-ck_o)}{\beta \left[\frac{1}{k_1} (\tan^{-1} \frac{k_o}{k_1} + \tan^{-1} \frac{k_3}{k_1} + m_1 \pi) + 1/k_o + 1/k_3 \right] \left[1 + \left(\frac{k_o}{k_1} \right)^2 \right]} \quad 7.13$$

The expression for the self-coupling coefficient for the graded index guide, K_{IE} , is rather more complex. The novel technique, presented in Section 2.10, of obtaining the self-coupling coefficient by differentiation of the characteristic (eigenvalue) equation may be used. Differentiating both sides of equation 7.9 with respect to n_o gives, for TE modes,

$$\frac{d}{dn_o} \left(\frac{kd_1}{3n_s \Delta} (n_s^2 - n_e^2)^{3/2} \right) = \frac{d}{dn_o} \left[\tan^{-1} \frac{k_o}{k_s} \right] \quad 7.14$$

where k_s is defined in equation 2.19.

After differentiation, terms in $\frac{d}{dn_o}$ are collected to give

$$\frac{d\beta}{dn_o} = \frac{n_o k^2}{\beta k_o \left[\frac{1}{k_o} + \frac{d_1 k_s^2}{n_s \Delta k^2} \right] \left[1 + \left(\frac{k_o}{k_s} \right)^2 \right]} \quad 7.15$$

Multiplying equation 7.15 by the perturbation term, from equation 2.120

$$\delta n_o = \frac{2k_o^2 \exp(-ck_o)}{k^2 n_o} \quad 7.16$$

leads to the expression for K_{IE} ,

$$K_{IE} = \delta\beta = \frac{d\beta}{dn_o} \delta n_o = \frac{2k_o \exp(-ck_o)}{\beta \left[\frac{1}{k_o} + \frac{d_1 k_s^2}{n_s \Delta k^2} \right] \left[1 + \left(\frac{k_o}{k_s} \right)^2 \right]} \quad 7.17$$

It is interesting to compare in passing equation 7.17 and 7.12.

The term $(\frac{1}{k_o} + \frac{1}{k_3})$ has been recognised by Gedeon⁸⁹ as the effective thickness of a slab waveguide, and that the terms $\frac{1}{k_o}$ and $\frac{1}{k_3}$ represent the effects of the Goos-Hanchen shift. By direct comparison it may be seen that the "effective thickness" of the linear IE profile is

$$d_e = \frac{d_1 k_s^2}{n_s \Delta k^2} + \frac{1}{k_o} \quad 7.18$$

At cut-off, $n_e \rightarrow n_2$ and, for the refractive indices of Figure 7.4,

$$d_e \rightarrow 2d_1 \quad 7.19$$

The condition that the effective thickness of the waveguide at cut-off should be infinite is clearly not obeyed, and the breakdown of the theory is thought to be a consequence of the WKB approximation used to formulate equation 7.5. Equation 7.17 may be rendered independent of d_1 by the substitution of equation 7.9, giving

$$K_{IE} = \frac{2k_o \exp(-ck_o)}{\beta \left[\frac{1}{k_o} + \frac{3}{k_s} \left(m_2 \Pi + \frac{\Pi}{4} + \tan^{-1} \frac{k_o}{k_s} \right) \right] \left[1 + \left(\frac{k_o}{k_s} \right)^2 \right]} \quad 7.20$$

7.3.3 Complete expression for the system coupling coefficient.

Using equations 7.20, 7.13 and 2.85, the final expression for the coupling coefficient is obtained:

$$K = \frac{2k_o}{\beta} \exp(-ck_o) \cdot \left\{ \left(1 + \left(\frac{k_o}{k_s} \right)^2 \right) \left(\frac{3}{k_s} \left(m_2 \Pi + \frac{\Pi}{4} + \tan^{-1} \frac{k_o}{k_s} \right) + \frac{1}{k_o} \right) \right\}^{-\frac{1}{2}} \cdot \left\{ \left(1 + \left(\frac{k_o}{k_1} \right)^2 \right) \left(\frac{1}{k_1} \left(m_1 \Pi + \tan^{-1} \frac{k_o}{k_1} + \tan^{-1} \frac{k_3}{k_1} + \frac{1}{k_o} + \frac{1}{k_3} \right) \right) \right\}^{-\frac{1}{2}} \quad 7.21$$

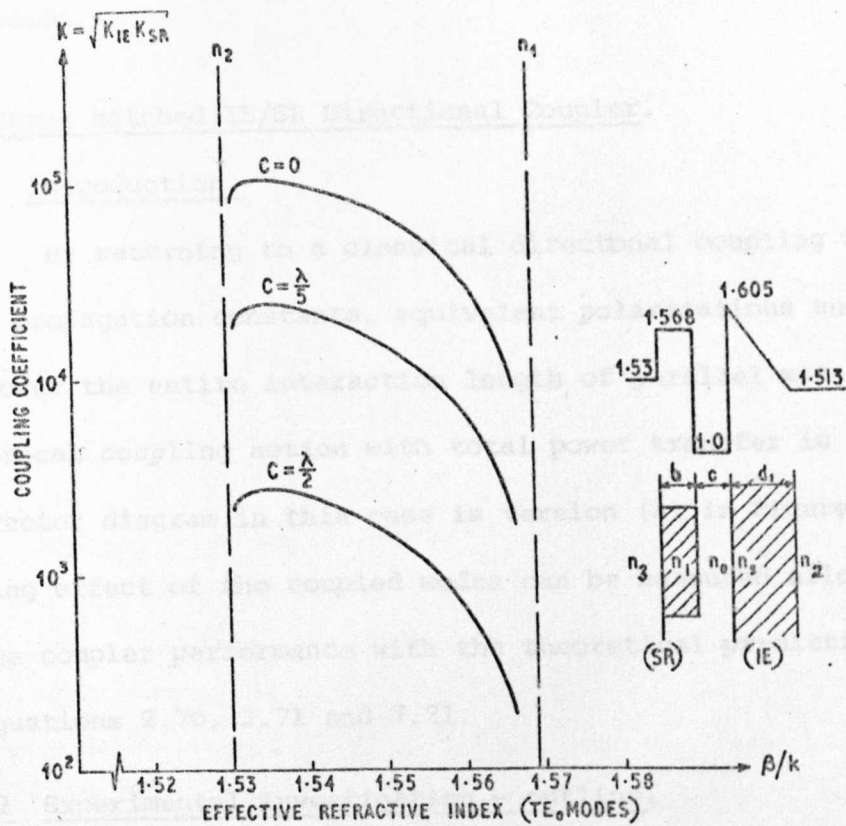
valid except where $\beta/k \rightarrow n_2$

β/k in the above equation ranges from the highest substrate index to the lowest guide index. Equation 7.21 has been solved for the refractive index distribution of the SR/IE system and with the fundamental modes coupling ($m_1 = m_2 = 0$). The graph of the system coupling coefficient against the propagation constant is shown in Figure 7.4, for different values of interguide spacing.

7.4 The experimental coupler - preamble.

In the previous two sections the IE waveguide characteristics and the phase-matching or tuning of the coupler were discussed and an expression for the coupling coefficient was evaluated. We would therefore appear to be prepared to investigate the coupling experimentally. In the event it was discovered that the experimental work could be divided into three distinct sections,

- (i) phase-matched directional coupling.
- (ii) phase-mismatched directional coupling.
- (iii) phase-mismatched leakage coupling.



$$K_{SR} = \frac{2k_0 \exp(-ck_0)}{\beta \left(b + \frac{1}{k_0} + \frac{1}{k_3} \right) \left(1 + \left(\frac{k_0}{k_1} \right)^2 \right)} ; K_{IE} = \frac{2k_0 \exp(-ck_0)}{\beta \left(\frac{1}{k_0} + d_1 R \right) \left(1 + \left(\frac{k_0}{k_s} \right)^2 \right)}$$

$$\text{WHERE } R = \frac{k_s^2}{k^2 n_s (n_s - n_2)}$$

FIGURE 7.4 System coupling coefficient

against propagation constant

for the fundamental modes,

for different values of

interguide spacing.

characterised by the vector diagrams of Figure 7.5a-c. Each will be considered in turn, and the results unified by a concluding discussion.

7.5 Phase Matched IE/SR Directional Coupler.

7.5.1 Introduction.

By returning to a classical directional coupling situation - equal propagation constants, equivalent polarizations and low optical loss over the entire interaction length of parallel waveguides - reciprocal coupling action with total power transfer is assured. The vector diagram in this case is version (a) in Figure 7.5. The beating effect of the coupled modes can be measured allowing comparison of the coupler performance with the theoretical predictions, embodied in equations 2.70, 2.71 and 7.21.

7.5.2 Experimental investigation - outline.

The experimental set-up, devised to study film/fibre coupling, is shown in Figures 7.6 and 7.7. Light ($\lambda = 0.633 \mu\text{m}$) was launched into the fundamental mode of a three-dimensional SR fibre waveguide. The energy travelled down the guide with minimal optical loss (0.05 dB/cm) and with little mode scattering. The IE waveguide was manufactured according to Section 7.2 such that the two fundamental modes were very nearly degenerate. The guiding region of the SR fibre was pressed onto the surface of the thin film using a soft semicylindrical rubber pad which expanded along the axis of the fibre as it was pushed against the film, and the variation of the fibre power with applied pressure was recorded. A direct calibration between the micropositioner setting and the coupling region profile in three dimensions was obtained by observing the interference fringes between the fibre substrate and the bulk of the film. The Fizeau interferometer consisted of a sodium lamp and the beam-splitting objective of the travelling microscope.

NOTES

subscript 1 \equiv film

subscript 2 \equiv fibre

assume for simplicity that

$$n_1 \approx n_2 = n$$

For 'leakage' coupling a mirror image of (c) exists about the xz plane. For 'edge' coupling the mirror image is discounted.

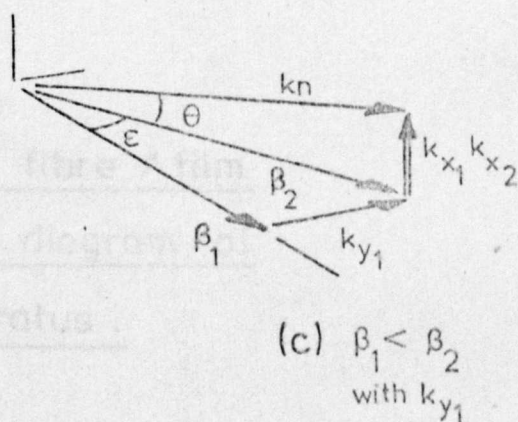
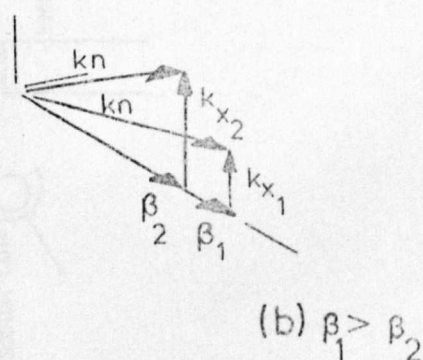
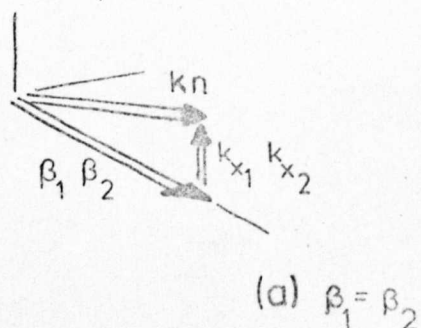
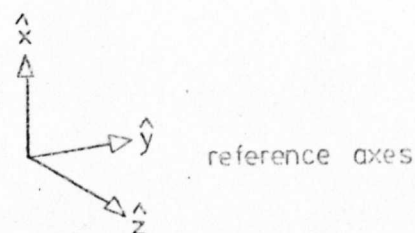


FIGURE 7.5 Coupled-wave vector diagrams.

- (a) phase-matched directional coupler
- (b) mismatched directional coupler
- (c) mismatched leakage coupler

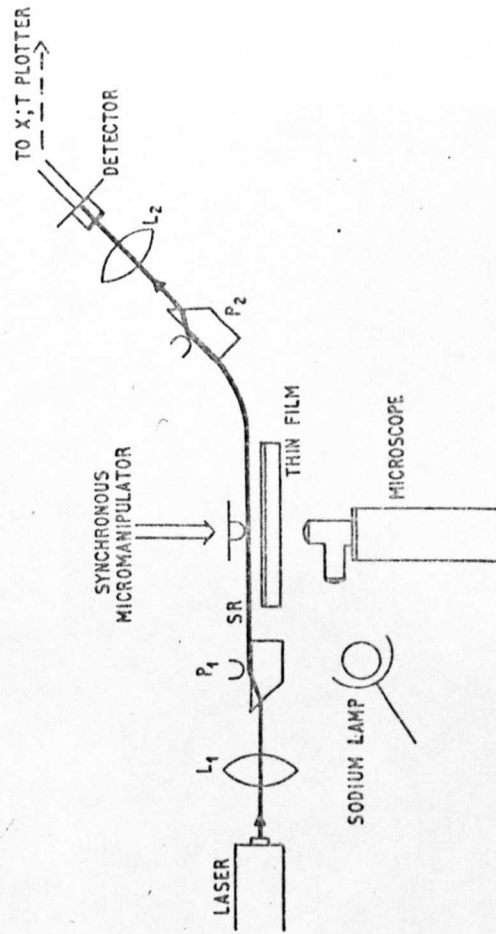
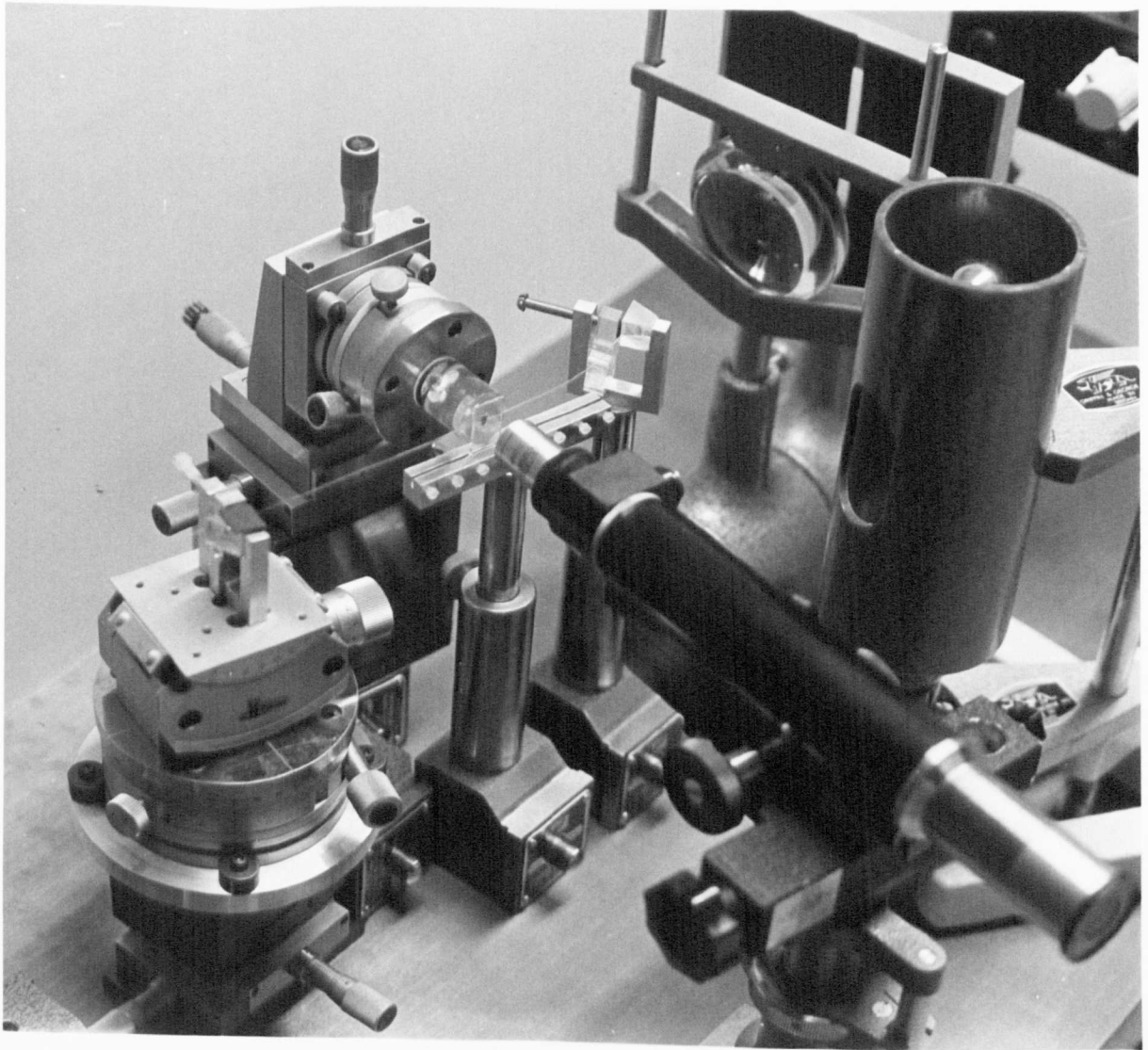


FIGURE 7.6 Study of fibre / film
coupling : diagram of
the apparatus .

FIGURE 7.7 Apparatus for the study of
fibre / film coupling .



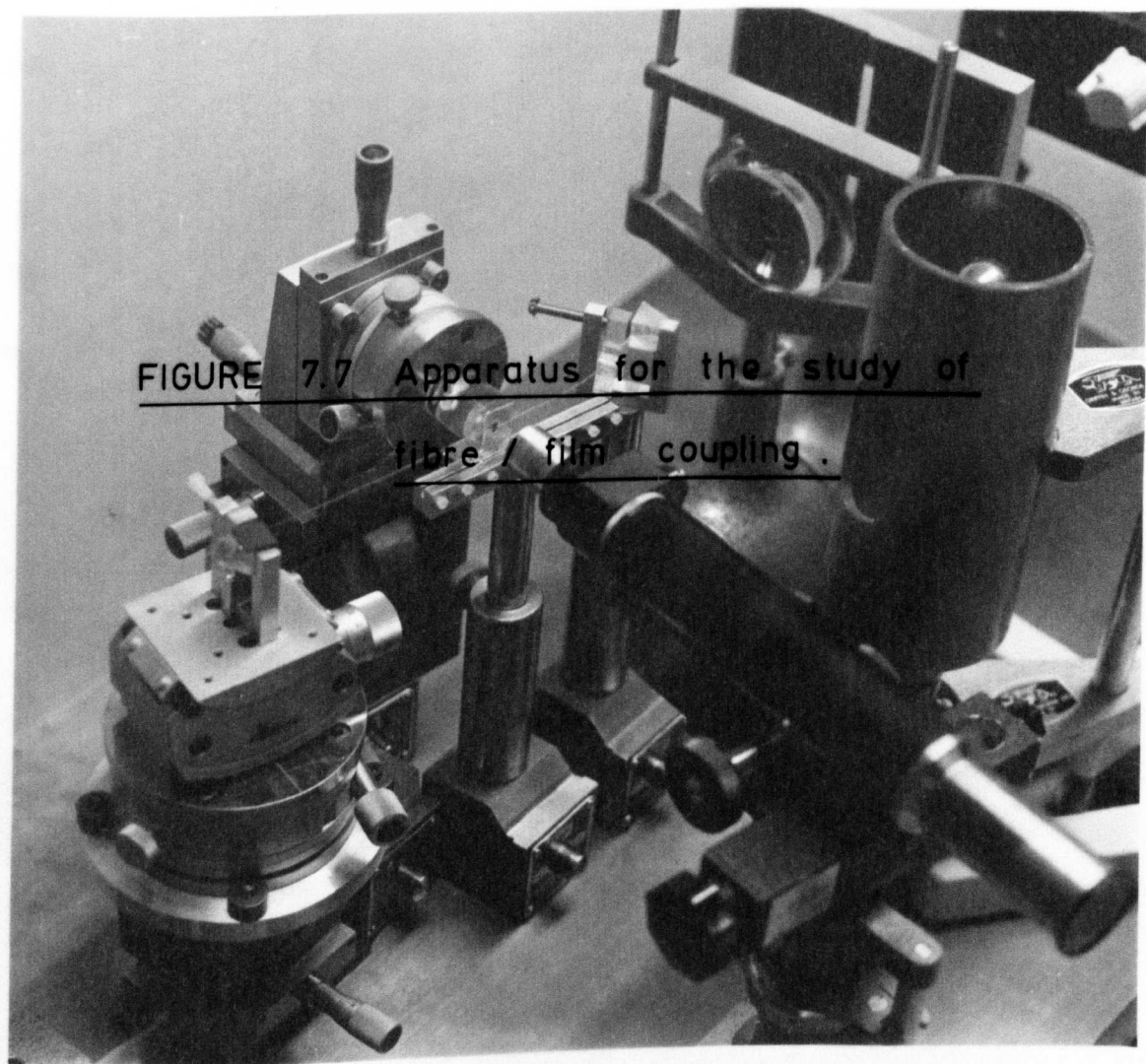


FIGURE 7.7 Apparatus for the study of
fibre / film coupling .

In this manner the periodicity of the observed beats was related to a measured length. The coupling coefficient was thereby obtained.

7.5.3 Experimental investigation - details.

(i) material specification.

The material specification of the system to be described was as follows. The fibre was a BAK 1/7059 three-dimensional SR fibre, having a cross-section, shown in Figure 6.2 of $9\text{ }\mu\text{m} \times 2.1\text{ }\mu\text{m}$. The width of the substrate was $1100\text{ }\mu\text{m}$ and the fundamental E_{11}^x mode, $\beta_{\text{SR}}/k = 1.563 \pm 2 \times 10^{-4}$, was excited. The film was an Ag^+/Na^+ IE waveguide fabricated by an 8 minute diffusion at 250°C , with a TE_0 mode, $\beta_{\text{IE}}/k = 1.562 \pm 2 \times 10^{-4}$.

(ii) calibration of the coupling region.

While it was realised that the calibration of the coupling region was peculiar to this particular experimental configuration, an explanation of the methodology is appropriate, as there is no reason why the technique could not be universally applied.

Light ($\lambda_D = 0.589\text{ }\mu\text{m}$) from a 500W sodium lamp (Griffen and George Ltd) flooded the coupling region and illuminated the beam-splitting objective of the x70 travelling microscope (Figure 7.7). Interference fringes between the fibre substrate and the bulk of the thin film occurred and a typical interference photograph is shown in Figure 7.8. The bright horizontal streak is scattered light from the waveguides at the coupling region. The known width of the fibre substrate allows us to calibrate the region in the plane of the photograph, while the fringes detail the separation in the direction perpendicular to the plane of the photograph (the x-direction). The dark fringes were used to give better resolution and they were defined in the following manner.

The first fringe was called the 'zero-order fringe' and

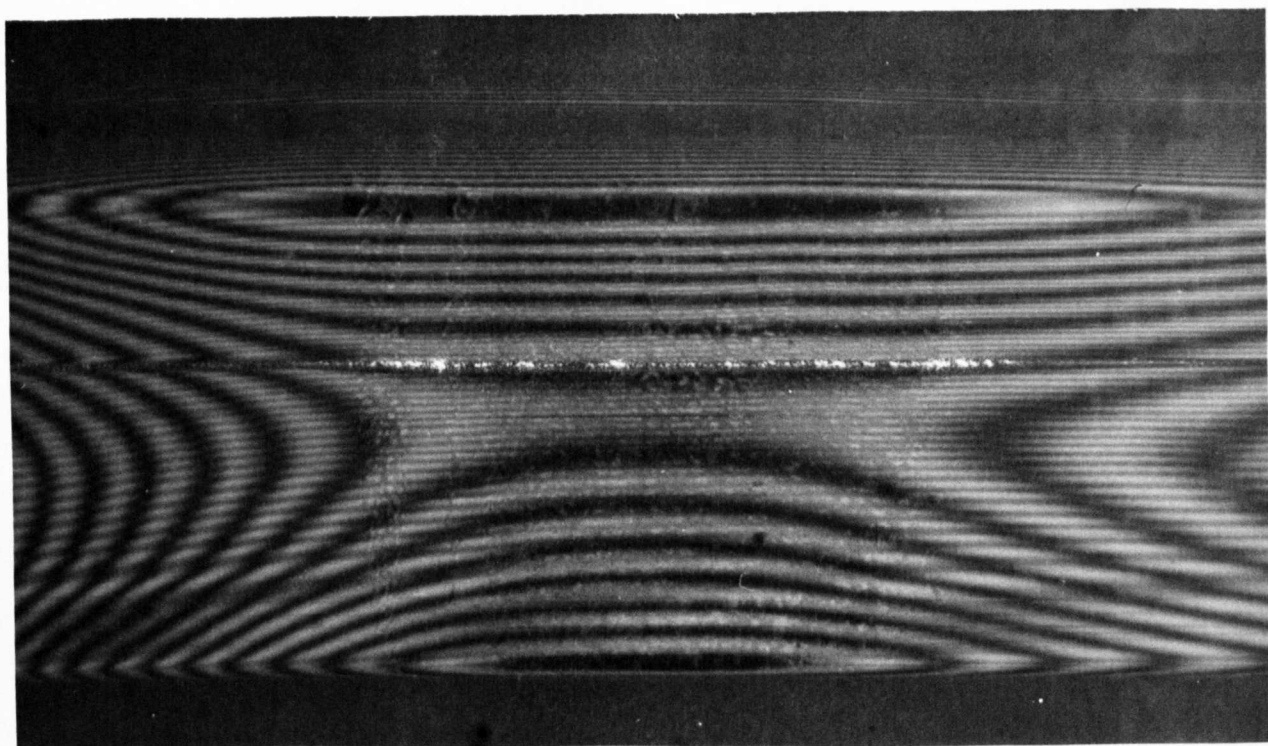


FIGURE 7.8 Interference pattern used to calibrate
the coupling region .

corresponded to zero spacing in x between the fibre substrate and the film. Note that the reaction to the applied force must be located at the junction of the two guides. This implies that they must be in intimate contact at one point, at least. Subsequent fringes were labelled 1^{st} , 2^{nd} m^{th} etc. The m^{th} order fringe is

$$x_m = \frac{m\lambda_D}{2} \quad 7.22$$

above contact of the film and the fibre substrate. Taking a line along the axis of the SR fibre waveguide filament a plot of fringe order, or, from equation 7.22, the separation of the fibre substrate from contact, may be constructed as a function of applied pressure, shown in Figure 7.9a. Knowing the height of the fibre filament above the fibre substrate (in this case $1.8 \mu\text{m}$ due to a burying effect of the high-index guiding region of about $0.3 \mu\text{m}$, seen in Figure 6.2) an accurate picture of the waveguide coupling region, and how it varied with the position of the synchronous micromanipulator, was constructed. The sixth order fringe would appear in this case to correspond to zero interguide spacing. What can be considered to be the interaction length? First, it is interesting to note that the e^{-1} penetration depth of the evanescent wave in air is only $\frac{\lambda_D}{8}$, making the effect of the two hyperbolic 'tails' of the coupling region negligible. From considerations of Figure 7.9a, the interaction length is seen to be equal to the distance between the sixth order fringe intersects with the SR waveguide axis. A check for this deduction is to return to Figure 7.8, where it is seen that the level of light scattering - indicative of the perturbation of the evanescent fields - increases in the coupling region between the sixth fringe intersects.

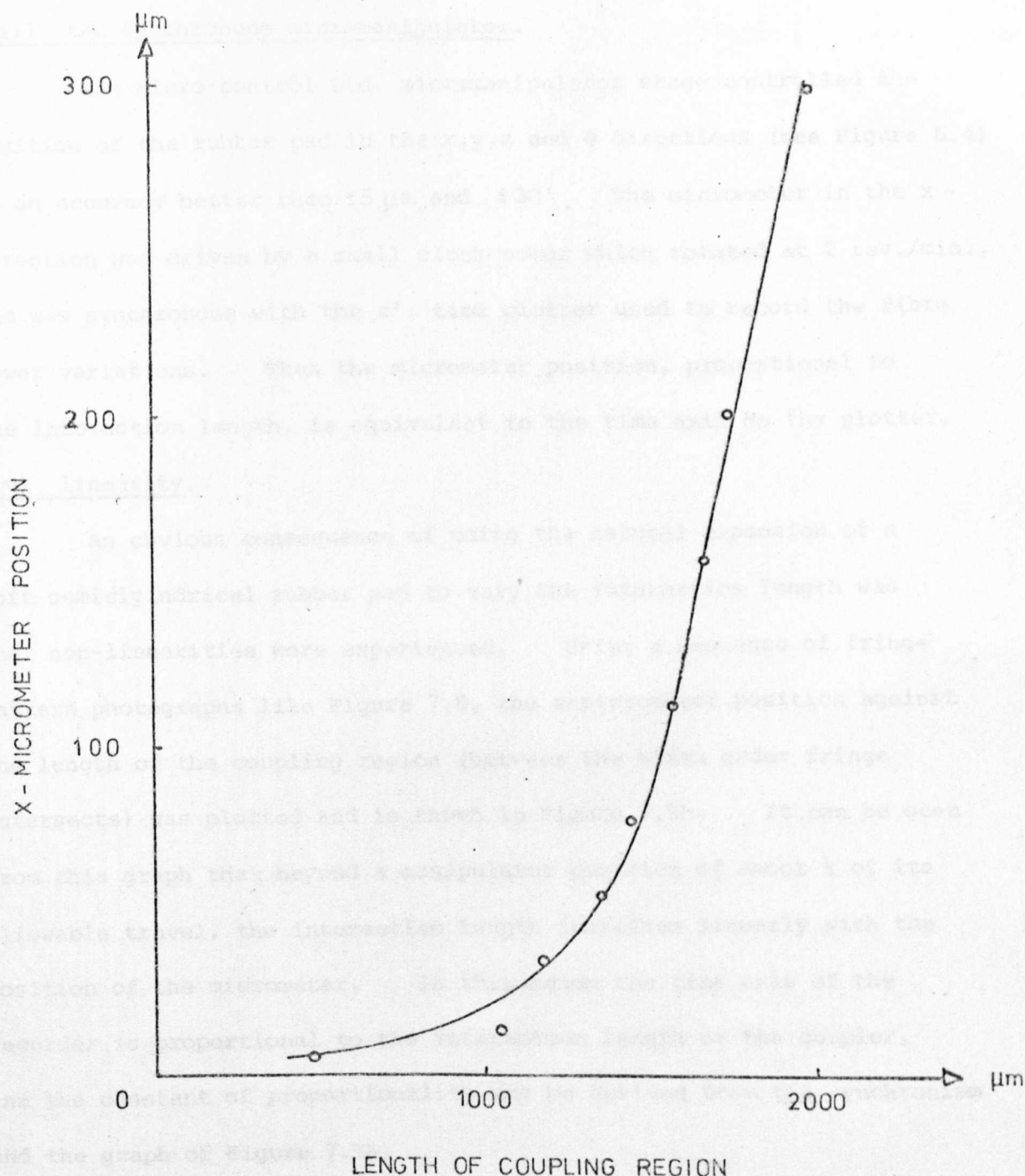


FIGURE 7.9b The x-micrometer position plotted against the length of the coupling region (between the sixth fringe intersects) .

(iii) the synchronous micromanipulator.

The Micro-contrôl Ltd. micromanipulator stage controlled the position of the rubber pad in the x, y, z and ϕ directions (see Figure 6.4) to an accuracy better than $\pm 5 \mu\text{m}$ and $\pm 30'$. The micrometer in the x -direction was driven by a small clock motor which rotated at 2 rev./min., and was synchronous with the x' : time plotter used to record the fibre power variations. Thus the micrometer position, proportional to the interaction length, is equivalent to the time axis on the plotter.

(iv) linearity.

An obvious consequence of using the natural expansion of a soft semicylindrical rubber pad to vary the interaction length was that non-linearities were experienced. Using a sequence of fringe pattern photographs like Figure 7.8, the x -micrometer position against the length of the coupling region (between the sixth order fringe intersects) was plotted and is shown in Figure 7.9b. It can be seen from this graph that beyond a manipulator position of about $\frac{1}{4}$ of its allowable travel, the interaction length increases linearly with the position of the micrometer. In this region the time axis of the recorder is proportional to the interaction length of the coupler, and the constant of proportionality may be derived from the synchronism and the graph of Figure 7.9b.

7.5.4 Results and analysis.

The light remaining in the fibre beyond the coupling region (see Figures 7.6 and 7.7) was extracted using a second prism coupler and focused onto a large-area BPY 13 photodiode connected through a DC amplifier to the x' -axis of the plotter. Consequently the final result was a plot of the power in the SR fibre as a function of the coupler interaction length, for which the theory predicts a $\cos^2 Kz$ response. The experimental result for the coupling of the SR fibre

and the IE waveguide specified in Section 7.5.3(i) is shown in Figure 7.10.

Let us consider several important points in turn.

(i) linearity.

Clearly the \cos^2 beats of the fibre power are evident. The non-linearity of the plotter trace was due to the non-linear pad expansion and the slight initial variation in the interguide spacing 'c'. In accordance with Figure 7.9b the linearity is acceptable beyond the first quarter of the manipulator's allowable travel.

(ii) coupling efficiency.

It would appear from Figure 7.10 that there was a coupling loss of about 10% from the initial value. However, the fact that this loss did not increase with increasing interaction length indicated that it had nothing to do with the coupling mechanism. Furthermore the loss was incurred even if the film was replaced by a plane glass slab of substrate material. We conclude that the loss represented the radiation of the power carried by the fibre substrate modes and should be largely discounted. Of the total power available for coupling, the transfer efficiency was 97%, maintained over many spatial power oscillations.

(iii) reciprocity.

One of the advantages of the experiment is that the result of Figure 7.10 immediately accounts for the coupling of energy between the structures in both directions, because the energy transferred from the fibre to the film couples back to the fibre at a later point.

(iv) the experimental coupling coefficient.

By relating the beat length observed in the linear portion of the plotter trace to a measured distance in the coupling region via the calibration information, an experimental value for the coupling coefficient of

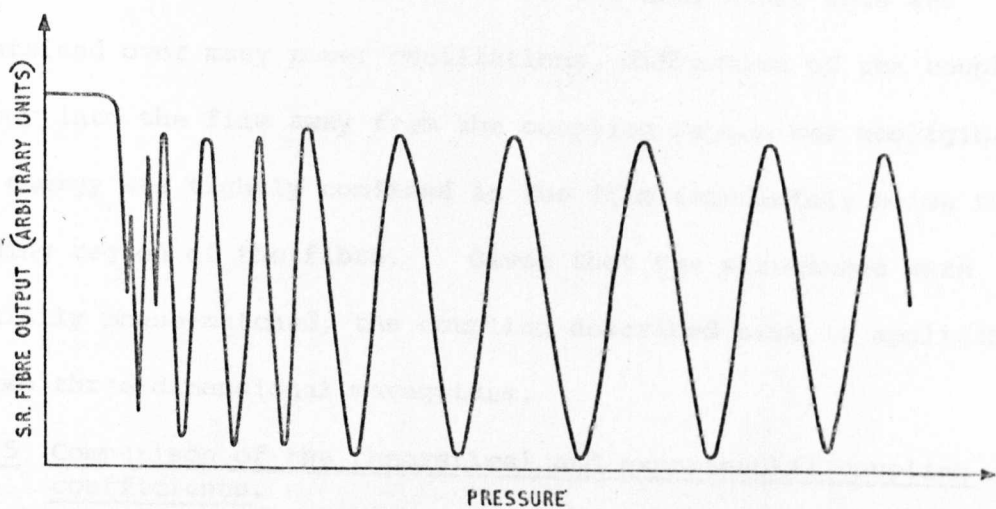


FIGURE 7.10 SR fibre output against pad
pressure : phase matched coupler .

7.5.6 Summary and conclusions.

An experiment has been carried out showing that a return to directional coupling with optical fibre couplers results in a highly efficient fibre-to-fibre coupling. The system was shown to be reciprocal and the measured coupling efficiency was 50%, obtained over many optical realizations of phase-matching. The directional and reciprocal coupling efficiencies were found

$$K_{\text{exp}} = \frac{\Pi}{2L_c} = \frac{\Pi/2}{47 \mu\text{m}}$$

7.23

was obtained.

(v) further note.

An important point should be noted. The coupling from the film to the fibre was of the order of 97% and, since this was maintained over many power oscillations, diffraction of the coupled energy into the film away from the coupling region was negligible. The energy was tightly confined in the film immediately below the guiding region of the fibre. Given that the structures were initially phase-matched, the coupling described here is applicable to two three-dimensional waveguides.

7.5.5 Comparison of the theoretical and experimental coupling coefficients.

Figure 7.4 indicates that for an interguide spacing of zero and $\beta/k = 1.562$, the theoretical coupling coefficient of 2.4×10^4 rads. m^{-1} or

$$K_{\text{th}} = \frac{\Pi/2}{65 \mu\text{m}} \quad 7.24$$

was expected.

It may be seen that the agreement between the theoretical and experimental coupling coefficients is acceptable, bearing in mind the normal experimental inexactitudes ($\pm 10\%$) and the approximate nature of the theory, particularly for $c = 0$.

7.5.6 Summary and conclusions.

An experiment has been devised and presented which shows that a return to classical directional coupling with single waveguide modes results in a highly efficient film-to-fibre couple. The system was shown to be reciprocal and the measured transfer efficiency was 97%, maintained over many spatial oscillations of power transfer. The theoretical and experimental coupling coefficients were in fair

agreement.

The first realisation of quasi-single-mode directional coupling between an optical fibre waveguide and a thin film waveguide constitutes a major result of the work of this thesis.

A photograph of the coupling device in operation is presented in Figure 7.15. The fibre was pressed against the thin film at the point arrowed, and the pressure adjusted until the interaction length was equal to an odd number of coupling lengths. The light couples from the fibre to the film with 95% efficiency. The beam in the film was discontinued by a surface scratch, showing that the light was indeed guided as a surface wave.

7.6 Phase Mismatched Directional Coupler.

7.6.1 Introduction.

In the following section we shall be concerned with the effects on the coupling of a deliberate amount of phase mismatch, introduced by the relative reduction of the film mode propagation constant β_{IE}/k . This constant, set by the diffusion time, must be chosen such that

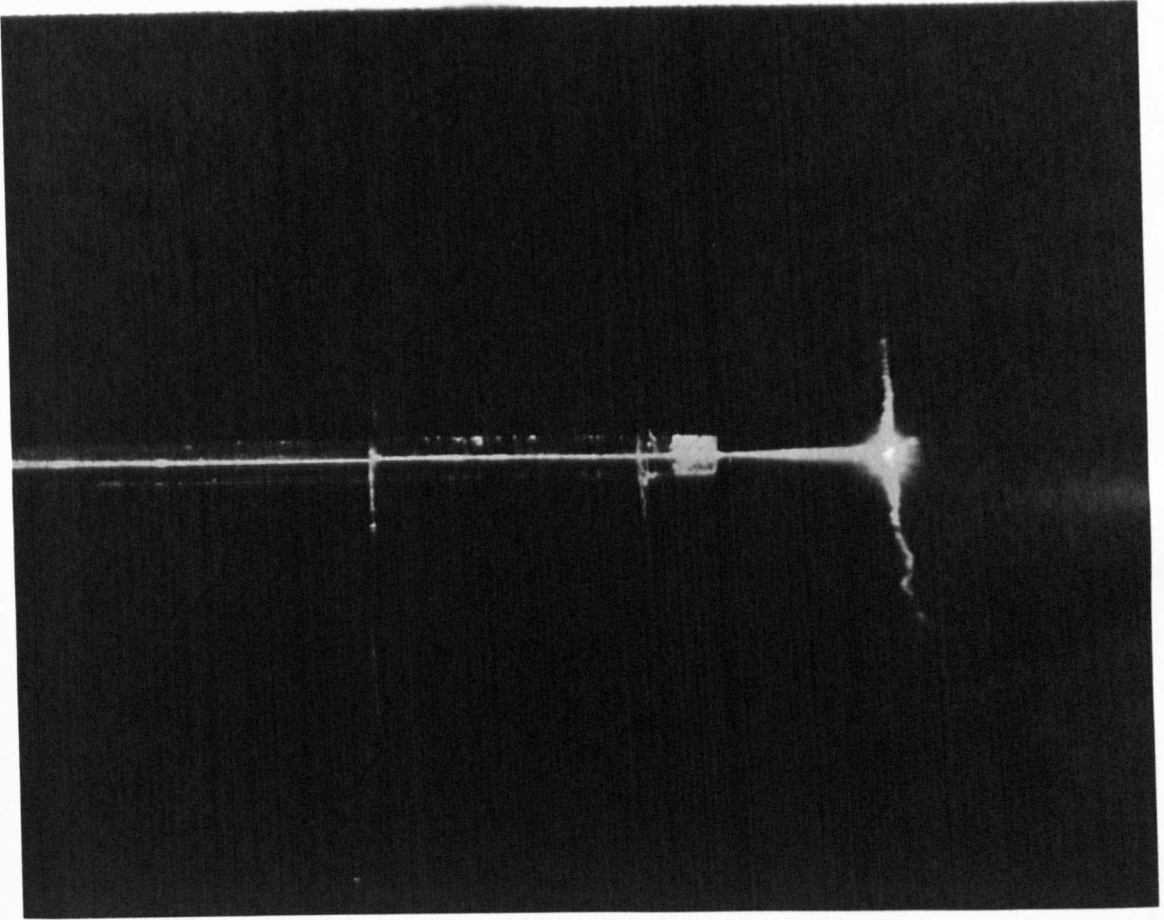
$$\beta_{\text{film}} < \beta_{\text{fibre}} \quad 7.25$$

as in the vector diagram of Figure 7.5b. Measuring the response of the coupler to the magnitude of the change $(\beta_{SR} - \beta_{IE}) = \Delta\beta$ will be shown to result in an independent measurement of the experimental coupling coefficient, as well as further confirmation of the theory of coupled waves.

7.6.2 Phase mismatched system response: the method of obtaining the coupling coefficient.

Investigation of the solution of the coupled wave equation for the coupling of parallel waves shows that the maximum power transfer efficiency $\hat{\eta}$ and the beat length L are a function of the parameter $\frac{\Delta\beta}{2K}$ and, from equation 2.81

$$\hat{\eta} = (1 + (\frac{\Delta\beta}{2K})^2)^{-1} \quad 7.26$$



Δ

FIGURE 7.15 Phase matched fibre - to - film
directional coupler in operation .
The device is viewed through
the substrate of the thin film .

$$L = \hat{\eta}^{-1/2} L(\Delta\beta = 0) \quad 7.27$$

Concentrating on equation 7.26, it may be seen that the response of the system transfer efficiency, $\hat{\eta}$, to changes in $\Delta\beta$ leads to a value for the coupling coefficient, which is assumed constant. The measurement is one of amplitude not beat separation, and is therefore independent of the experimental uncertainties introduced in Section 7.5.3. Normalising equation 7.26 gives

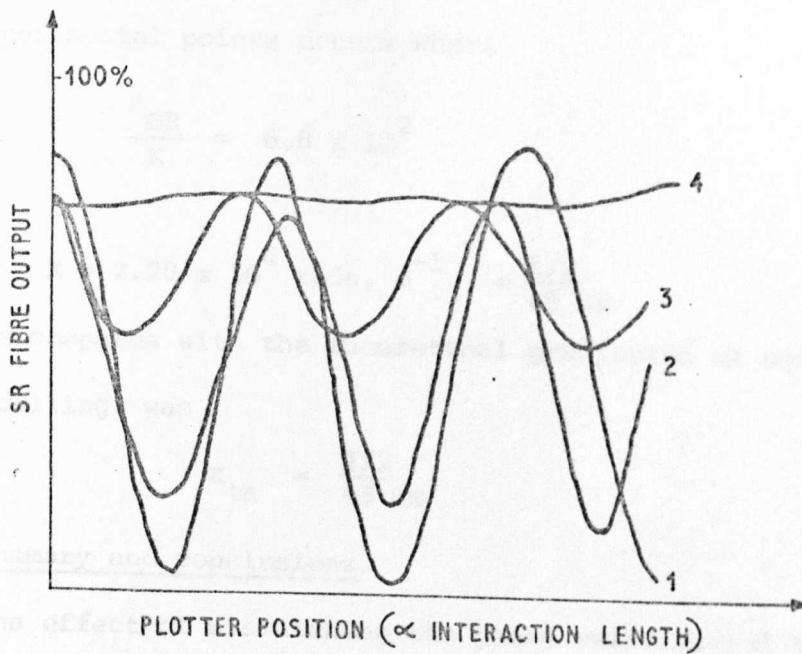
$$\hat{\eta} = (1 + 0.25 \frac{(\beta_{SR} - \beta_{IE})^2}{\beta_{SR}^2} \cdot \frac{\beta_{SR}^2}{K^2})^{-1} \quad 7.28$$

The method is to plot experimental points of $\hat{\eta}$ against $\log(\frac{\beta_{SR} - \beta_{IE}}{\beta_{SR}})$ and choose a value of $\frac{\beta_{SR}}{K}$ to produce a best fit between those and the theoretical curve given by equation 7.28.

7.6.3 Results and analysis.

Throughout this work the fibre and the experimental apparatus remain unchanged from Section 7.5. The phase mismatch was introduced by choosing diffusion times less than 8 minutes at 250°C, with the propagation constants calculated using mode angle measurements. As before, the SR fibre output was recorded as a function of the interaction length for the different amounts of mismatch, and the results are summarised in Figures 7.11. Figure 7.11a shows the superposition of four curves extracted from the linear portion of the response, while Figure 7.11b tabulates the corresponding phase mismatch and a best estimate of the transfer efficiency. The value of 100% on the fibre output axis in Figure 7.11a represents the initial power before coupling including the fibre substrate mode content. The similarity in shape and form of these curves to the theoretical predictions of Figures 2.6 and 2.7 should be noted, particularly the reduction in transfer efficiency and beat length with increasing phase mismatch.

To obtain the coupling coefficient, the graph of $\hat{\eta}$ against



(a)

β_{film}/k_0	$\Delta\beta/\beta_{\text{SR}}$	$\frac{\Delta}{\eta}(\%)$
1 — 1.5618	~ 0	97.2
2 — 1.5595	-1.47×10^{-3}	76.8
3 — 1.5548	-4.48×10^{-3}	36.0
4 — 1.5484	-8.58×10^{-3}	6.0

(b)

FIGURE 7.11

- (a) SR fibre output against pad pressure:
effect of phase mismatch.
- (b) Table summarizing the results
of (a).

$\frac{\Delta\beta}{\beta_{SR}}$ on a logarithmic scale is constructed (Figure 7.12). Superimposing the theoretical curve of equation 7.28, it was found that the best fit to the experimental points occurs where

$$\frac{\beta_{SR}}{K} = 6.8 \times 10^2 \quad 7.29$$

or

$$K = 2.28 \times 10^4 \text{ rads, m}^{-1} = \frac{\pi/2}{69 \text{ } \mu\text{m}} \quad 7.30$$

This value compares with the theoretical prediction of equation 7.24 which, recalling, was

$$K_{th} = \frac{\pi/2}{65 \text{ } \mu\text{m}} \quad 7.31$$

7.6.4 Summary and conclusions.

The effect of mismatching the phase velocities of the coupled waves was studied. The method of obtaining the coupling coefficient by measuring the transfer efficiency was described, and the results were shown to be in complete agreement with the theoretical expectations.

7.7 Phase Mismatched Leakage Coupler.

7.7.1 Introduction.

The third and final form of coupling to be described has alternatively been called "mode sinking" by Arnaud⁹⁰ though used in the slightly different context of sinking unwanted modes of a circular fibre. The effect has also been noted by Bulmer⁴⁰ in a situation similar to the preliminary coupling experiments of Chapter 3. In the case of a three-dimensional fibre coupling to a two-dimensional film, there is one less degree of confinement - one additional degree of freedom - in the thin film over the fibre. The phase-matching conditions of Figure 7.5c are possible in the Z-plane where the coupling is via the evanescent wave in the x-direction. The condition

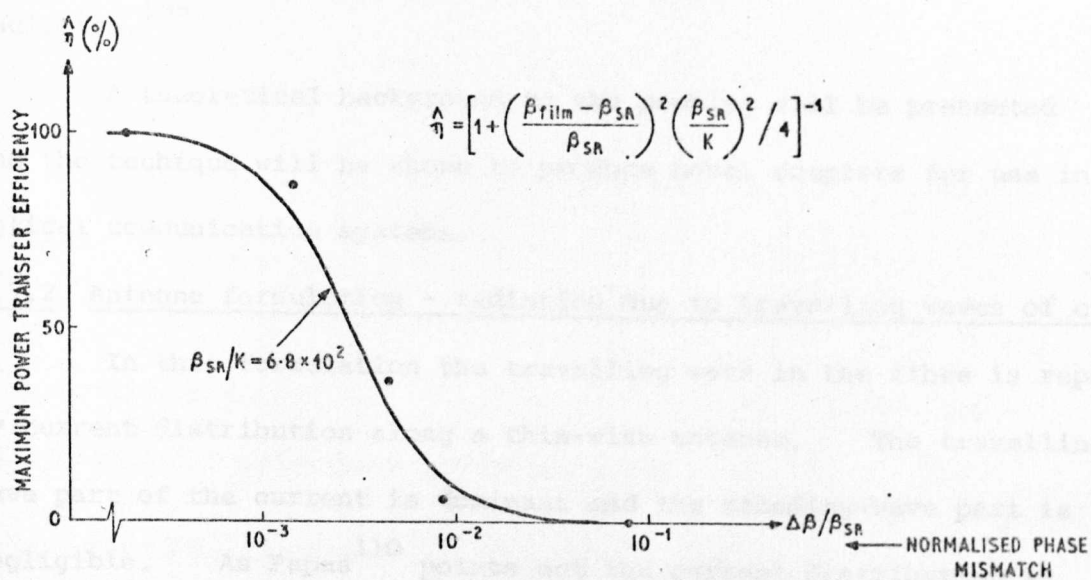


FIGURE 7.12 The graph of the maximum power transfer efficiency against the normalized phase mismatch.

$$\beta_{\text{film}} > \beta_{\text{fibre}}$$

7.32

holds in this case. A transfer of energy occurs by virtue of the coupling of the evanescent waves, but the phase-matching results in leakage of the coupled energy away from the coupling region at an angle $\pm \epsilon$ (Figure 7.5c). The situation is analagous to Cerenkŏv radiation.¹⁰⁵

A theoretical background to the problem will be presented and the technique will be shown to produce novel couplers for use in optical communication systems.

7.7.2 Antenna formulation - radiation due to travelling waves of current.

In this formulation the travelling wave in the fibre is replaced by current distribution along a thin-wire antenna. The travelling-wave part of the current is dominant and the standing-wave part is negligible. As Papas¹¹⁰ points out the current distribution is given by

$$\vec{J} = \hat{z} I_0 \delta_x \delta_y f(z) \quad \left(\frac{l}{2} \geq z \geq -\frac{l}{2}\right) \quad 7.33$$

where I_0 is the reference current, \hat{z} is the unit vector in z , δ_m is the Kronecker delta and $f(z)$ is a complex function of the real variable z . Further, in the case of a travelling wave in a loaded antenna (coupled waveguide) the distribution is

$$\vec{J} = \hat{z} I_0 \delta_x \delta_y e^{j p z} \quad \left(\frac{l}{2} \geq z \geq -\frac{l}{2}\right) \quad 7.34$$

where the index p is the ratio of the wave velocities of the radiating and travelling waves:

$$p = \frac{\beta_{\text{fibre}}}{\beta_{\text{film}}} \quad 7.35$$

Applying the integral relation between the antenna current and the radiation pattern^{110,111}

$$F(\epsilon) = k \int_{-\frac{l}{2}}^{\frac{l}{2}} e^{-j k z \cos \epsilon} \sin \epsilon \cdot f(z) dz \quad (0 \leq \epsilon \leq 2\pi)$$

$$= k \sin \epsilon \int_{-\ell/2}^{\ell/2} e^{-jkz(\cos \epsilon - p)} dz \quad 7.36$$

In our case the energy is restricted in the x-direction in both waveguides and ϵ is therefore the emergent radiation angle in the zy plane. Evaluating the integral gives

$$F(\epsilon) = \sin \epsilon \cdot \frac{\sin \frac{k\ell}{2} (\cos \epsilon - p)}{(\cos \epsilon - p)} \quad (0 \leq \epsilon \leq 2\pi) \quad 7.37$$

The maximum radiation of the travelling wave for $k\ell \rightarrow \infty$ appears at an angle

$$\cos \epsilon = p = \frac{\beta_{\text{fibre}}}{\beta_{\text{film}}} \quad 7.38$$

in the forward direction. A typical radiation pattern, predicted by equation 7.37, is shown in Figure 7.13.

7.7.3 Rate of leakage.

To obtain a theoretical prediction for the rate of leakage of the coupler, the near-rectangular fibre is divided into the system of two sets of orthogonal plane waves and each is considered in turn. The coupling is due to the field overlap in the x-direction, but the leakage is result of the mode confinement in the fibre in the y-direction. Looking along the x-axis at a plan view of the coupling region (Figure 7.14a) we find

$$\bar{n}_s = \bar{n}_g \cos (\pm \epsilon) \quad 7.39$$

The bar over the variable n denotes an effective refractive index and subscripts s and g denote the sink (thin film) and the guide (three-dimensional SR fibre) respectively. Using equation 2.36 we may write

$$\bar{n}_s = \bar{n}_{gy} \cos (\pm \epsilon) \left[1 + \frac{\bar{n}_{gx}^2 - n_1^2}{\bar{n}_{gy}^2} \right]^{1/2} \quad 7.40$$

$$\text{If} \quad n_1 \approx \bar{n}_{gx}, \quad 7.41$$

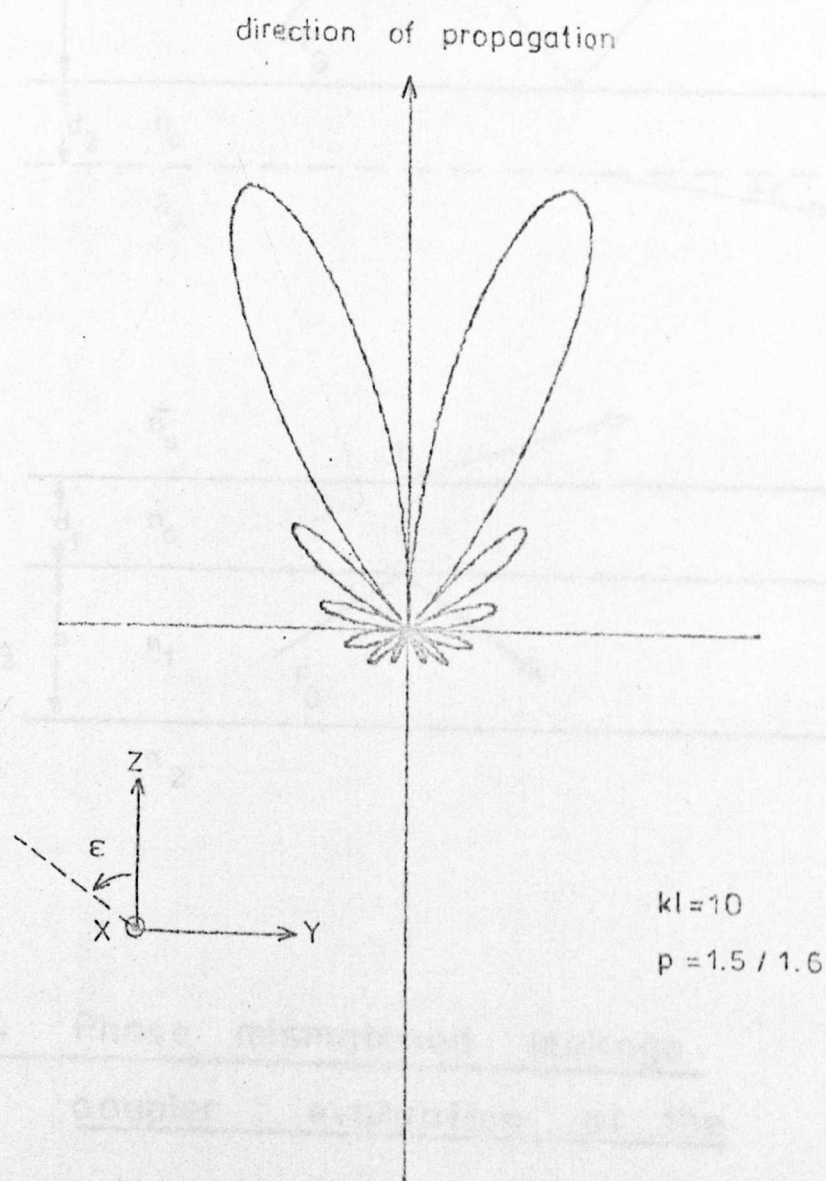


FIGURE 7.13 Radiation pattern of a travelling wave.

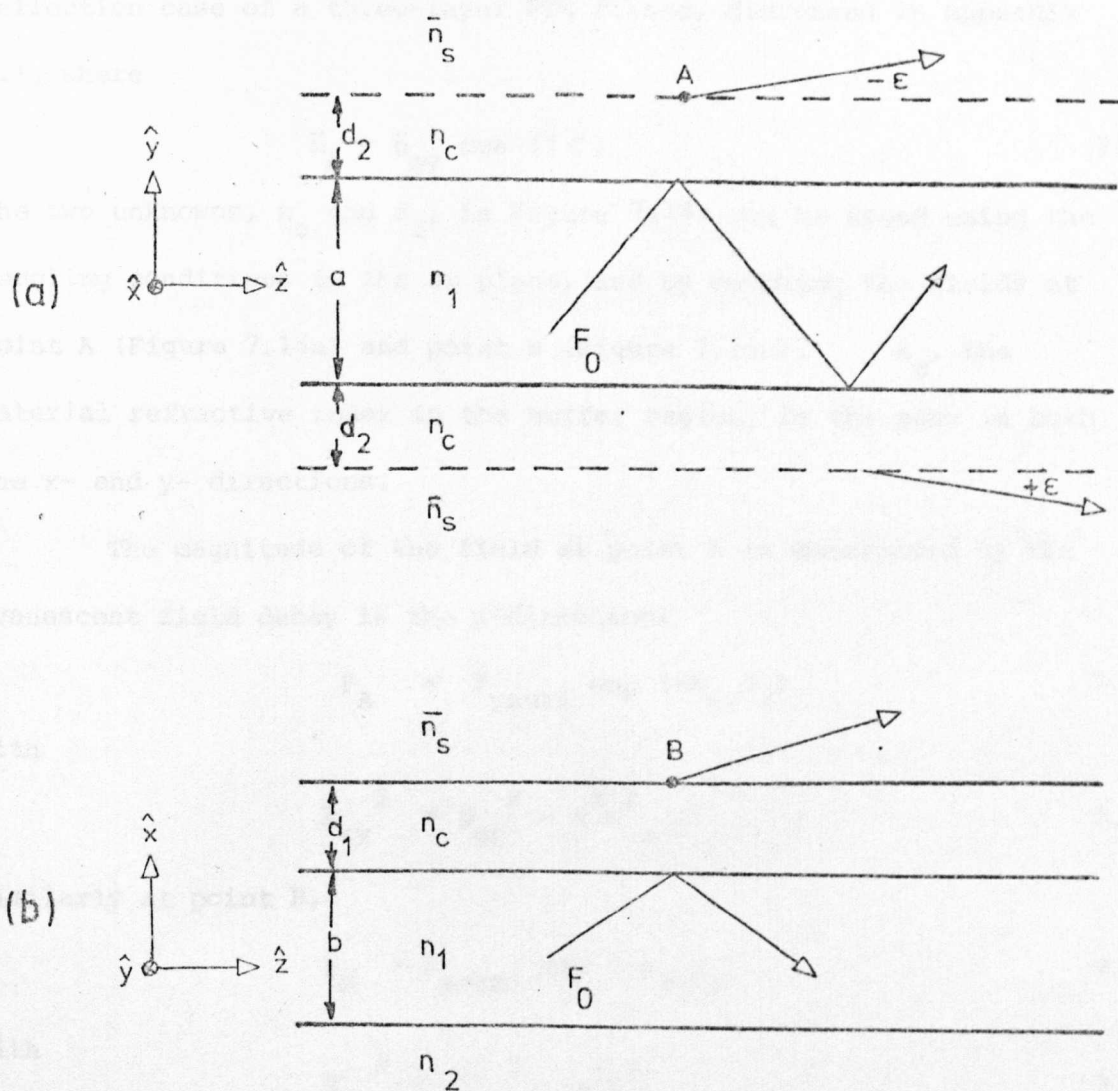


FIGURE 7.14 Phase mismatched leakage
coupler : evaluation of the
rate of leakage .

the situation of Figure 7.14a reduces to a straightforward Fresnel reflection case of a three-layer FTR filter, discussed in Appendix 2.1, where

$$\bar{n}_s \approx \bar{n}_{gy} \cos(\pm \varepsilon) \quad 7.42$$

The two unknowns, n_c and d_2 , in Figure 7.14a can be found using the coupling conditions in the xz plane, and by matching the fields at point A (Figure 7.14a) and point B (Figure 7.14b). n_c , the material refractive index in the buffer region, is the same in both the x- and y- directions.

The magnitude of the field at point A is determined by the evanescent field decay in the y-direction:

$$F_A = F_{ysurf} \exp(-k_{cy} d_2) \quad 7.43$$

with

$$k_{cy}^2 = \beta_{gy}^2 - k_c^2 n_c^2 \quad 7.44$$

Similarly at point B,

$$F_B = F_{xsurf} \exp(-k_{cx} d_1) \quad 7.45$$

with

$$k_{cx}^2 = \beta_{gx}^2 - k_c^2 n_c^2 \quad 7.46$$

Matching the fields at points A and B we find

$$u = \exp(-k_{cy} d_2) = \frac{F_{xsurf}}{F_{ysurf}} \exp(-k_{cx} d_1) \quad 7.47$$

The surface fields may be found using equation 2.8. For a mode polarized E^y we have

$$F_{ysurf} = F_o \left(1 + \left[\frac{k_{cy}}{k_{ly}} \right]^2 \right)^{-1/2} \quad 7.48$$

$$F_{xsurf} = F_o \left(1 + \left[\frac{n_1}{n_c} \right]^4 \left[\frac{k_{cx}}{k_{lx}} \right]^2 \right)^{-1/2} \quad 7.49$$

$$\text{where } k_{ly}^2 = k_{n_1}^2 - \beta_{gy}^2 \quad 7.50$$

$$\text{and } k_{lx}^2 = k_{n_1}^2 - \beta_{gx}^2 \quad 7.51$$

Substituting into equation 7.47 gives

$$u = \frac{\sqrt{1 + \left(\frac{k_{cy}}{k_{ly}}\right)^2}}{\sqrt{1 + \left(\frac{n_1}{n_c}\right)^4 \left(\frac{k_{cx}}{k_{lx}}\right)^2}} \cdot \exp(-k_{cx}d_1) \quad 7.52$$

From simple geometric considerations of Figure 7.14a it is seen that the distance between consecutive edge reflections is

$$\frac{\beta_{gy} a}{k_{ly}} \approx \frac{\beta_g a}{k_{ly}} \quad (\text{from equation 7.41}) \quad 7.53$$

The transmission loss per reflection is determined from the Fresnel equations of the three-layer FTR filter⁹³ (see also Appendix 2.1, equations A2.21, A2.19, A2.2, A2.3)

$$T = \frac{k_{ly}}{k_s} \cdot \frac{16k_s k_{ly} k_{cy}^2 u^2}{[(k_{ly} + k_{cy})(k_{ly} + k_s) + u(k_{ly} - k_{cy})(k_{cy} - k_s)]^2} \quad 7.54$$

$$\text{where } k_s^2 = (\bar{n}_s^2 - \bar{n}_g^2) k^2 \quad 7.55$$

For $u \ll 1$ equation 7.54 can be reduced to

$$T = \frac{16k_{ly}^2 k_{cy}^2 u^2}{(k_{ly} + k_{cy})^2 (k_{ly} + k_s)^2} \quad 7.56$$

Using equations 7.56, 7.53 and 7.52, the distance rate of power loss α_p is given by

$$\alpha_p = \frac{16 k_{ly}^3 k_{cy}^2 \left(1 + \left(\frac{k_{cy}}{k_{ly}}\right)^2\right) \exp(-2k_{cx}d_1)}{\beta_g a \left(1 + \left(\frac{n_1}{n_c}\right)^4 \left(\frac{k_{cx}}{k_{lx}}\right)^2\right) (k_{ly} + k_{cy})^2 (k_{ly} + k_s)^2} \quad 7.57$$

The power in the fibre decays as

$$P(z) = P_0 \exp(-\alpha_p z) \quad 7.58$$

What are typical order-of-magnitude results for α_p ?

Clearly if k_s , k_{cy} and $\frac{k_{cx}}{k_{lx}}$ are small, with $k_{ly} \approx \frac{11P}{a}$, equation 7.57 becomes approximately;

$$\alpha_p \approx \frac{16 \Pi p \exp(-2k_{cx} d_1)}{\beta_g a^2} \quad 7.59$$

For a $10 \mu\text{m} \times 2.5 \mu\text{m}$ BAKI/7059 fibre carrying the E_{11}^y mode (p, the transverse mode order = 1) at $0.633 \mu\text{m}$ wavelength we estimate

$$\begin{aligned} \alpha_p &\approx \frac{1}{10 \mu\text{m}} & (2k_{cx} d_1 = 0) \\ &\approx \frac{1}{100 \mu\text{m}} & (2k_{cx} d_1 = 2.303) \end{aligned} \quad 7.60a,b$$

It can be seen that the rate of leakage is expected to be high, typically between the bounds of equation 7.60 a,b. It is interesting to compare the result of equation 7.57 to that of Arnaud,⁹⁰ who predicted the loss coefficient of a mode-sinking coupler as

$$\alpha_p = \Pi N K^2 \quad 7.61$$

where K is the coupling coefficient and N is the density of the substrate modes. Recalling equation 2.129, it is clear that a dependence of the form

$$\alpha_p \propto k_{ly} \exp(-2k_{cx} d_1)$$

was not unexpected.

7.7.4 The experimental leakage coupler.

The theory predicts that when a three-dimensional fibre is coupled to a two-dimensional film such that $\beta_{\text{film}} > \beta_{\text{fibre}}$ the power in the fibre will leak out into the film at an angle,

$$\pm \epsilon = \cos^{-1} \frac{\beta_{\text{fibre}}}{\beta_{\text{film}}}$$

and at a rate governed by equation 7.57. Experimental observations agree with these predictions.

Figure 7.16 shows the coupling of a BAKI/7059 SR fibre and an IE thin film, viewed through the substrate of the film. The

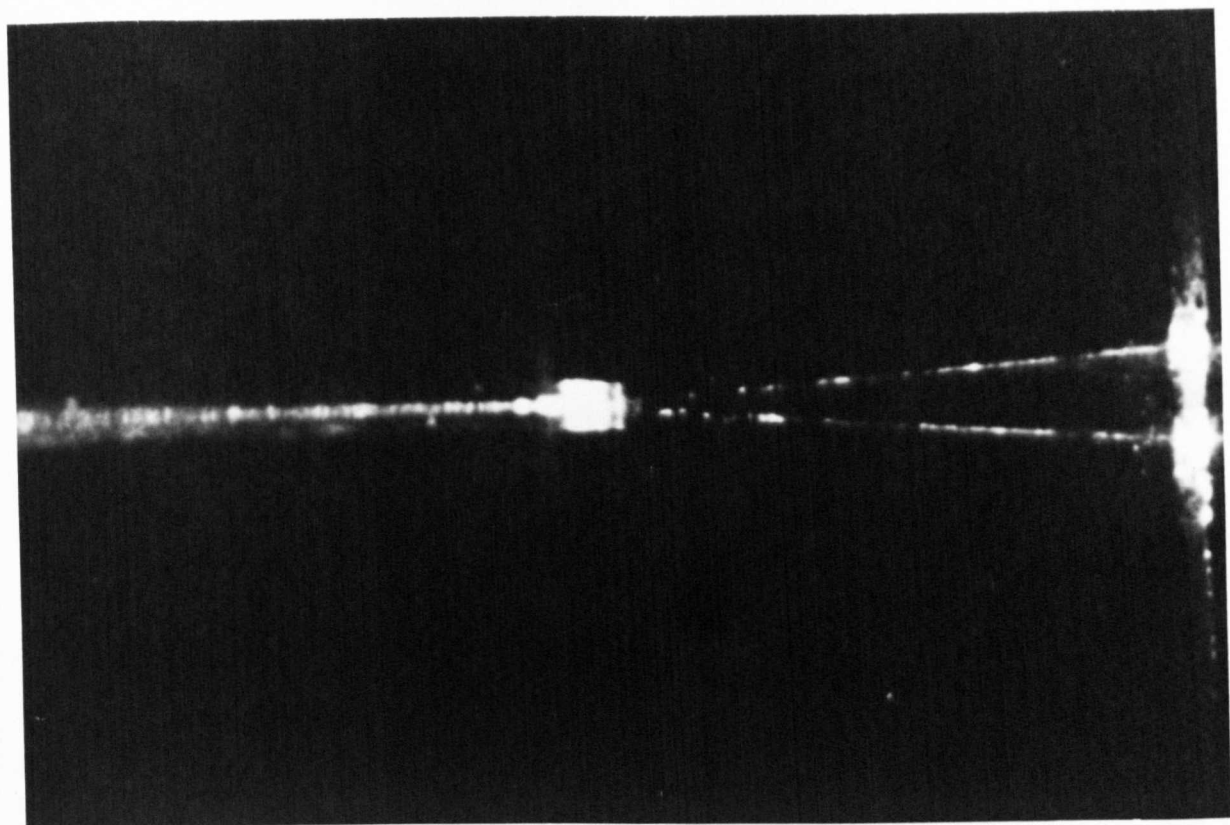


FIGURE 7.16 Phase mismatched leakage coupling,
viewed through the substrate of
the thin film.

light enters the left-hand side of the photograph in the $9\text{ }\mu\text{m} \times 2.1\text{ }\mu\text{m}$ core of the fibre, as the E_{11}^Y mode ($\beta_{\text{SR}} = 1.562k$). On contact with the film the light couples at the -ve and +ve synchronous angle ϵ , which, for $\beta_{\text{IE}}(\text{TE}_0) = 1.568k$, is $5^\circ 00'$. The power in the SR guide decays exponentially to zero and the transfer efficiency tends to 100% minus scattering losses. Coupling efficiencies greater than 94% from fibre to film have been measured using the apparatus of Figure 7.6.

If there is a single film mode with a higher β -value than the fibre, then a fibre-to-film guided mode beam splitter is obtained with approximately 50% of the power in each of the film beams. This effect may find useful application in thin film devices such as phase modulators, where a stable internal reference beam may be required for homodyne detection.

The theoretical leakage rate of approximately $(10\text{ }\mu\text{m})^{-1}$ compared favourably with experimental value, which was estimated visually.

The coupling action in the reverse direction, from a single film beam to the fibre at the phase-matching angle was attempted, but the results were inconclusive due to micropositioning difficulties. By the reciprocity theorem, both beams must be reconstructed in the film to make total transfer to the fibre possible, and by using a single beam alone the maximum transfer in this direction was limited to 50%. How can a practical single-beam device be devised? Clearly elimination or reflection of one of the film beams is required, and one method of doing so - the use of a film edge - will be discussed briefly.

7.7.5 The leakage coupler at a film edge.

As described by Ulrich and Martin,¹⁴ 'internally' reflecting one of the coupled beams at the edge of the light-guiding film, lying parallel to the fibre axis, resulted in two parallel film beams slightly displaced. In the limit as the fibre axis and the film edge became colinear, the in-phase wavefronts combined to produce a single beam, emanating at an angle $+\epsilon$ to the fibre axis. The possibility of a phase matched interaction in the $-\epsilon$ direction was eliminated, and although the analysis of the coupler remains the same as sections 7.7.2 and 7.7.3, the rate of leakage is halved.

The well-defined film edge was prepared using an evaporated aluminium barrier to the diffusion, and tapered linearly in effective refractive index over a length of a few microns. Figure 7.17 is a view of the coupling region through the film substrate, where the leakage coupler of Figure 7.16 is placed along a film edge. The coupling is indeed into a single beam in the film, with a measured transfer efficiency greater than 94%.

Reversing the coupler has not been attempted, although it is anticipated that the coupling will not be straightforward. Energy coupled into the fibre from the film may readily leak out again, and in fact the situation is very similar to prism/film coupling using a truncated plane wavefront.

7.7.6. Discussion and conclusions.

Section 7.7 has introduced phase mismatched leakage coupling as a method of achieving a transfer of optical energy between the modes of a three-dimensional fibre and a thin film waveguide. If the interaction length is sufficiently long, the efficiency from fibre to film is very high because the energy radiates away from the coupling region at the synchronous angles $\pm \epsilon$. The major advantage of the method is that the phase mismatch is always

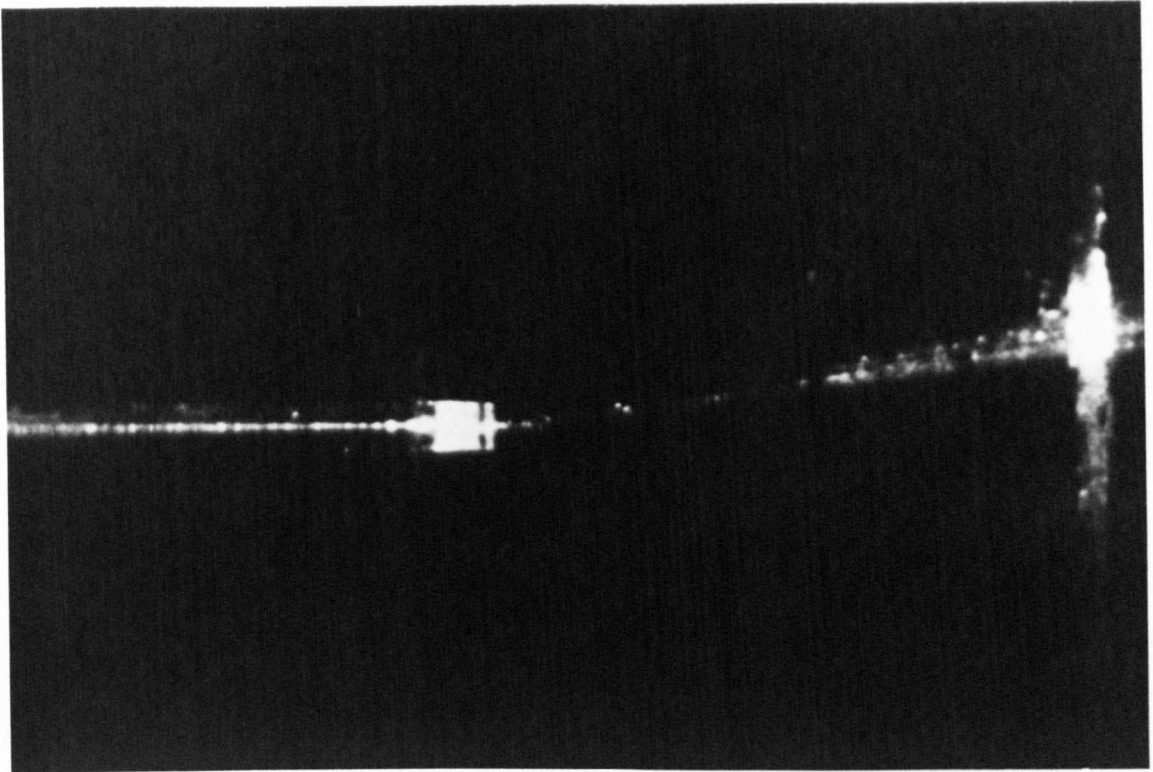


FIGURE 7.17 Phase mismatched leakage coupling
of figure 7.16 at a film edge .

accommodated by the synchronous angle and the manufacturing tolerances of the component waveguides decrease.

A more practical arrangement has been demonstrated where one of the synchronous conditions was nullified by deploying the coupler at a sharp film edge. The transfer efficiency again approached 100%, this time into a single film beam.

The most important factors limiting the application of the leakage-type coupler were considered to be:

- (1) Coupling in the reverse direction, that is from the film to the rectangular fibre, might not be as efficient.
- (2) Practical integrated optical waveguides will undoubtedly be three-dimensional, and the techniques described in this section would not strictly apply.

It is interesting to consider the situation where a three-dimensional fibre couples to a three-dimensional integrated waveguide, where $\beta_{\text{film}} \neq \beta_{\text{fibre}}$ and $k_{y_{\text{film}}} \neq k_{y_{\text{fibre}}}$. Clearly a synchronous angle would exist to uphold a phase-matching condition in the yz plane. An off-axis type of leakage coupler for three-dimensional waveguides is predicted, though such ideas must be relegated to the category of topics for further research.

Though the leakage coupler cannot compete with the parallel phase-matched situation it exists as an interesting alternative, with the attractive properties of being simple to construct, non-critical in design and, in one direction at least, highly efficient.

7.8 Summary and General Conclusions.

This chapter was concerned with the evanescent field coupling of thin film waveguides and the ribbon fibres developed for that purpose. "Tuning" of the film waveguide mode to match the β -value of the coupling fibre was achieved by resorting to ion-exchanged waveguides, the properties of which were briefly discussed, including

the refractive index profile and the dispersion characteristics.

An expression for the theoretical coupling coefficient was developed.

The chapter was then divided into three sections according to the distinctive coupling situations: phase-matched directional coupling, phase-mismatched directional coupling, and phase-mismatched leakage coupling. The first case was shown to be described by the classical model of directional coupling and the experimental results could be directly and accurately compared with the theoretical prediction. The coupler was entirely reciprocal, the measured transfer ratio was 97% and the theoretical and experimental coupling coefficients were in close agreement.

The conditions for the second situation, $\beta_{\text{fibre}} < \beta_{\text{film}}$, were shown to lead to a reduction in the maximum transfer efficiency $\hat{\eta}$ and in the beat length L . Measurement of the functional dependence of $\hat{\eta}$ with $(\beta_{\text{fibre}} - \beta_{\text{film}})$ led to a second experimental evaluation of the coupling coefficient, again found to be in agreement with the theory.

Finally, phase-mismatched leakage coupling was presented as a novel method of transferring optical energy between waveguiding structures and a theoretical explanation of the coupling was presented. The experimental realisation of this type of device was outlined, and a further development - leakage coupling at a film edge - was described.

The foremost conclusion to be drawn from the work of this chapter is that ribbon fibres, in the form of three-dimensional SR fibres, offer a solution to the coupling problem. By achieving a phase-velocity match along the entire length of the interaction region a highly efficient, reciprocal coupler has been shown to result, and in this manner the goal of interconnecting thin film waveguides has been realised.

The major results of this chapter have been published.¹¹⁵

8.1. General Conclusions.

The main body of this thesis has been concerned with the treatment of conventional fibres, or the development of new fibres, for the purposes of coupling to and from planar integrated circuits. Various methods of coupling have been successfully demonstrated, and the propagation characteristics of the coupled modes have been studied. Some of the conclusions reached have been presented with the relevant section as occasion and need arose. These will now be generalized and further observations will be made.

The simple ray-optics approach was found to suffice in the description of the waveguides used throughout this work, and was useful to describe the coupled wave interactions between circular (large diameter) planar and rectangular fibres structures, and prisms. The coupling of waveguide modes has been explained using the coupled wave equations, the solution of which depended on three parameters; the complex propagation constants of each guide and the complex system coupling coefficient. For a lossless exchange of power between the modes the system coupling coefficient κ must be purely imaginary and for the coupling of two dissimilar guides $\kappa = |\kappa|$ was the geometric mean of the self-coupling coefficients. The determination of the system coupling coefficient was thereby rendered independent of any differences in the propagation constants of the coupled modes, which entered into the calculation of the solution of the coupled first-order system of differential equations 2.54. The most flexible method of obtaining the solution was by the simulation of equation 2.54 using digital computing techniques, which produced the result in the form of a direct graphical output for any combination of propagation constants and any number of coupled waves. At a later

stage of the work (Chapter 4.5.5) mode polarization was found to play an important role in the coupling of waveguides, in particular those of circular cross-section where rotation and variation of the mode fields are probable over lengths of fibre. It was concluded that the maintenance of mode polarization and its effect on the coupling of structures of different geometry may be a limiting factor not accounted for in the theoretical descriptions presented in Chapter 2. It is maintained that ribbon fibres have the advantage of propagating only two well-defined dominant mode polarizations and are therefore best suited to interconnecting planar waveguide structures.

Existing circular optical fibres having a protective glass cladding can be treated by acid-etching or ion-diffusion to expose the guided mode fields for evanescent field coupling. The better general method was acid-etching, which was applied in two experimental coupling configurations; from a thin film to a circular clad fibre and from a prism to a circular clad fibre. The coupled wave interactions occurred at regions where the cladding was locally modified, and the transition between modified and unmodified cladding regions was virtually lossless for low-order core modes. From the initial film/circular fibre coupling experiments, we can conclude that, while cladding modification enables the desired interaction of the evanescent waves, the remaining large diameter circular core is unsuitable for coupling to single-mode thin film waveguides. The word 'unsuitable' here must be tempered in the knowledge that a high efficiency spiralling mode coupler has been produced by simply pressing a fibre on top of a film and observing the phase-matching criteria set out in Chapter 3. However, as far as a practical communication system is concerned there exist doubts as to the practicalities of such a coupler. Prism

coupling experiments have shown that for low-order fibre-mode excitation the cladding-modified region must be further adjusted to lower the V-value of the fibre at the coupling region. The accompanying reduction in fibre diameter to micron dimensions leads to many handling and positioning problems, considered prohibitive for most practical coupling situations.

Coupling light into treated circular fibres using a high-index prism was found to be less critical and has allowed identification of the mode structure and quantified the coupling to the guided modes of a clad fibre via the evanescent waves. We can conclude, as Midwinter⁹⁷ has done, that the techniques described in Chapter 4 will find useful application in the study of mode-dependent phenomena in circular fibres.

Three types of waveguide were identified as candidates for coupling fibres; the unclad planar ribbon, the large width-to-thickness SR fibre, and the three-dimensional SR fibre.

Planar unclad ribbons, because of their inherent multimode nature and their undesirable handling properties, were considered to be unsuitable for the purposes in mind.

The observation of single-mode operation in a sandwich ribbon fibre - a flexible fibre of macroscopic dimensions - led to the conclusion that SR fibres were ideally suited for coupling to or from planar waveguides, although the exposed core of the SR fibre makes them unsuitable for transmission over long distances. The large width-to-thickness ratio guiding region of the SR fibre allowed the use of the slab waveguide approximation to apply in the description of the mode fields, and the propagation constant, determined by prism coupling experiments, was found to be adequately predicted by this method. These fibres were developed still further to produce three-dimensional SR fibre structures capable of coupling to rectangular waveguides, envisaged as the building-blocks of integrated optic components.

The characteristics of the several modes supported by this ribbon in the width direction have been directly measured by prism launching and observation of the waveguide field patterns. Although the cross-section of the guiding region was not rectangular, it has been found that the modal characteristics were adequately described using approximate solutions developed for rectangular waveguides. The modes were efficiently and selectively excited using a tilting prism coupler, allowing two synchronous coupling angles to be determined, the values of which agreed well with the theory. The measured power distributions across the near- and far-field mode patterns emerging from the fibre were also as predicted by the approximate theory. The use of the theory seems sufficient to calculate the mode parameters needed in the design of SR fibre-to-integrated circuit couplers.

Transverse coupling arrangements using SR fibres have been conceived and demonstrated, operating between selected modes in the guiding structures. Ion-exchanged waveguides were chosen as the thin films, having many advantageous properties, principally the facility to 'tune' the waveguide mode to within fractions of one percent of a set value of phase velocity. This property permitted investigation of a variety of coupling configurations. The first case, that of phase matched directional coupling, has been shown to be described by the established model presented in Chapter 2 (Part II) and has resulted in the development of a reciprocal integrated optic-fibre waveguide coupler which is virtually lossless and has a measured transfer efficiency of 97%. We can conclude that the first single-mode fibre-film optical directional coupler has been realised by the application of sandwich ribbon fibres to the coupling problem. The theoretical and experimental estimates for the system coupling coefficient were in fair agreement.

The effect of an amount of phase mismatch deliberately introduced into the system was analysed, leading to a further verification of the coupled wave solutions and a second experimental measure of the system coupling coefficient which agreed to within 6% of the theoretical value.

Novel coupling configurations have been described which further reinforce the concepts of coupled propagating waves. Phase mismatched leakage coupling has been shown to be non-critical in design and application and has produced a fibre to film coupler which is 100% efficient (into two film beams) in that direction. Introducing a sharp film edge lying colinear with the fibre axis has resulted in a single-beam device which is analogous to a two-dimensional guided-mode version of a prism/film coupler. Clearly much theoretical and experimental work has still to be done in the study of these devices but we are able to conclude that new avenues of research are apparent and the realisation of film-to-fibre couplers incorporating new techniques are foreseen.

8.2. Relation of the Results and Future System Development.

What are the projected component technologies? Electro-optic modulation has been successfully demonstrated in high-refractive-index birefringent materials such as gallium arsenide, lithium niobate and cadmium sulphide. Gallium arsenide technology enables the manufacture of thin film semiconductor lasers, and waveguides and passive components can be produced in all these materials. The working wavelength will be in the infrared or near-infrared region of the spectrum. The transmission waveguide will undoubtedly be a low-refractive-index circular glass fibre, and, because of bandwidth requirements, probably single-mode. How can the demands of simplicity and high coupling efficiency and the developing technologies in fibres and integrated devices be related to the results of this work?

An immediate difficulty which can be foreseen in the application of phase matched directional coupling using SR fibres is the inherent phase mismatch existing between a high-refractive-index film (refractive index ≈ 2.2) and a low-refractive-index glass fibre (refractive index ≈ 1.6). There are two possible methods of overcoming this mismatch. Firstly, as has been pointed out by McMurray and Stanley,¹⁰⁸ the use of overlay layers³⁸ to produce low-refractive-index waveguide input and output sections tapering into and out of high-refractive-index active devices would allow the efficient coupling of a low-refractive-index SR fibre in a phase matched configuration at the entrance and exit ports (Figure 8.1). As will be described in Section 8.3, the connection to the long-distance optical fibre cable could be made through a butt-joint (now isolated from the active thin film device) or a section of SR fibre tapering into a guide of circular cross-section. The second solution is to use a high-refractive-index SR fibre and proceed exactly as in Section 7.5 (Figure 7.1), selecting the phase velocity of the guided fibre-mode to be equal to that of the thin film device. We presume that the device $\frac{\beta}{k}$ will be the determining factor in the choice of the system mode velocity, and that the fibre $\frac{\beta}{k}$ will have to be chosen from a length of slowly tapering coupling waveguide, or alternatively locally modified by other means. If such a high-refractive-index fibre were successfully manufactured, the leakage coupling devices described in Chapter 7 would also enable the transfer of optical energy into and out of thin film components, via the SR coupling fibre, to the circular fibre data highway.

The spiralling mode coupler of Chapter 3 does not appear to offer a solution because of the projected system requirement of single-mode operation.

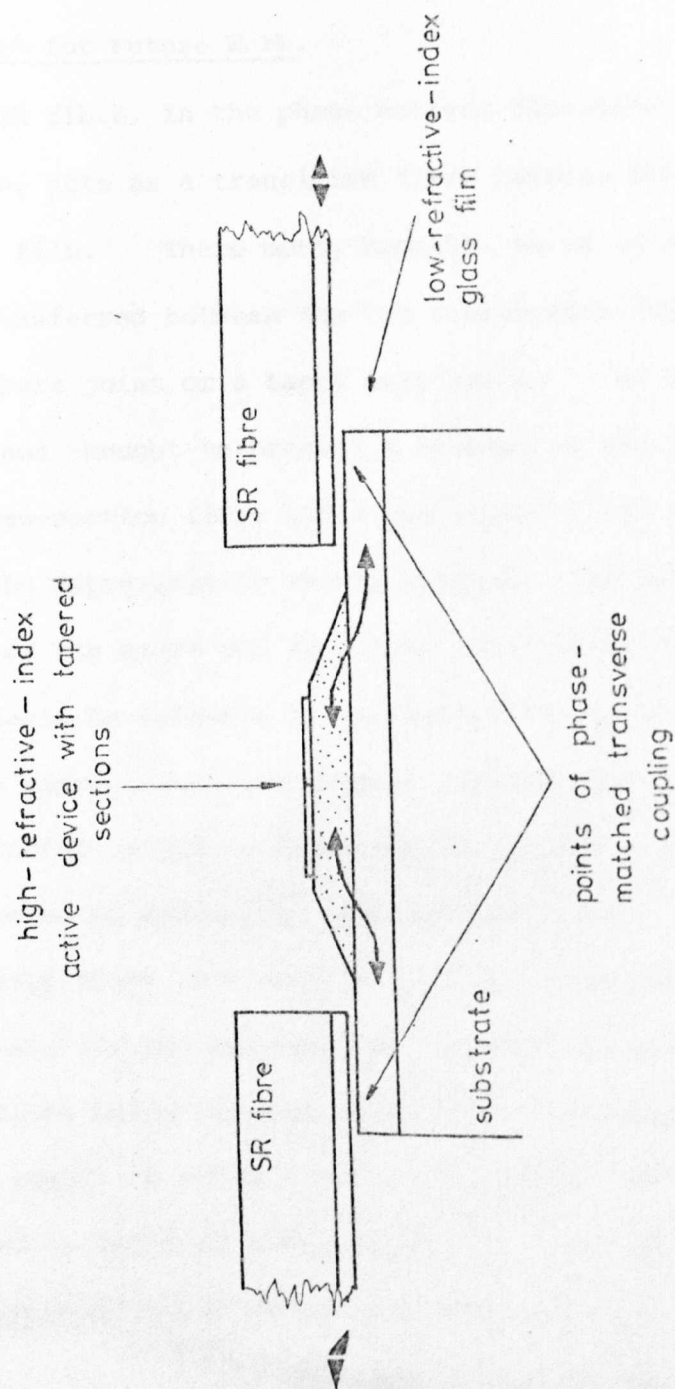


FIGURE 8.1 Coupling to and from a
high-refractive-index
active thin film device
using glass SR fibres.

8.3 Proposals for Future Work.

The SR fibre, in the phase matched directional coupling configuration, acts as a transition fibre between the circular fibre and the thin film. There must, however, be an arrangement whereby energy is transferred between the two single-mode fibres consisting of either a butt joint or a taper transition. Of these, butt jointing is not thought to present a problem as the apertures of a circular cross-section fibre and a low aspect-ratio SR fibre can be designed to be approximately evenly matched; the theoretical description of the near- and far-field patterns of three-dimensional SR fibres should be valuable in the design of such a codirectional coupler. A taper transition from a circular clad fibre to an open-sandwich structure would be difficult to engineer, and is not considered to be an attractive alternative.

Clearly there is a need to develop SR fibres using high-refractive-index materials for the purposes of coupling directly to high-refractive-index thin films using infrared radiation. A suitable material for the guiding region is arsenic trisulphide (refractive index=2.4) which has been used in infrared fibre optics. Short lengths of unclad arsenic trisulphide fibre can be drawn through an orifice at $280^{\circ}\text{C}^{\dagger}$ to produce the guiding region filament of a secondary preform. One possible compatible material for the SR fibre substrate is a plastic (nylon for example melts in an inert atmosphere at 270°C) although the adherence of the two species is a subject of speculation and future experimentation.

A continuation of the research is proposed into the novel forms of couplers introduced in this thesis; the spiralling mode coupler and the leakage coupler, to determine their theoretical and experimental properties and examine their range of application.

[†] prepared by Mr. R.H. Hutchins.

Further investigations are necessary into the feasibility of short-range communication networks using SR fibres and SR fibre devices, in particular on board ships and aircraft, within single building units, and in computers. A further reduction in the loss figure for these waveguides is an important goal for future research.

APPENDIX 8.

List of Published Work.

- (i) LAYBOURN, P.J.R., MILLAR, C.A.
Sandwich-ribbon optical waveguides.
EL. LETT., 10, 10, p.175, 1974.
- (ii) LAYBOURN, P.J.R., WILKINSON, C.D.W., MILLAR, C.A.
Optical waveguide coupling arrangements.
UNITED KINGDOM PATENT 46974/74, 1974.
- (iii) LAYBOURN, P.J.R., MILLAR, C.A., STEWART, G., WILKINSON, C.D.W.
Optical coupling between thin films and circular fibres.
EL. LETT., 11, 1, p.2, 1975.
- (iv) MILLAR, C.A., LAYBOURN, P.J.R.
Coupling between optical fibres and thin film waveguides.
Presented orally at 2nd NAT. QUANT. EL. CONF., OXFORD,
2-4 Sept., 1975.
- (v) LAYBOURN, P.J.R., MILLAR, C.A., STEWART, G., WILKINSON, C.D.W.
Coupling to optical fibres from prisms and thin films.
PAPER PD2, TOP. MEETING OPT. FIBRE TRANSM., WILLIAMSBURG,
VIRGINIA, 7-9 Jan., 1975.
- (vi) STEWART, G., MILLAR, C.A., LAYBOURN, P.J.R., WILKINSON, C.D.W.,
DE LA RUE, R.M.
Planar optical waveguides fabricated by silver ion migration
in glass.
PAPER PD2, CONF. INTEGRATED OPT., SALT LAKE CITY, 12 - 14 Jan., 1976.
- (vii) STEWART, G., MILLAR, C.A., LAYBOURN, P.J.R., WILKINSON, C.D.W.,
DE LA RUE, R.M.
Planar optical waveguides formed by silver-ion migration in glass.
Accepted for publication, IEEE J. QUANT. EL., SPRING 1977.
- (viii) MILLAR, C.A., LAYBOURN, P.J.R.
Coupling of integrated optical circuits using sandwich ribbon fibres.
OPT. COMM., 18, 1, p.80, 1976.
and
PAPER I3, IXth INT. QUANT. EL. CONF., AMSTERDAM, 14-18 June, 1976.
- (ix) MILLAR, C.A., HUTCHINS, R.H., LAYBOURN, P.J.R.
Modes of a 3-dimensional sandwich ribbon optical waveguide.
MICROWAVES, OPTICS, ACOUSTICS, 1, 1, p.27, 1976.
- (x) LAYBOURN, P.J.R., MILLAR, C.A., STEWART, G., HUTCHINS, R.H.
Coupling fibres to integrated optical circuits.
INT. IEEE/AP-S SYMP. and USNC/URSI MEETING.
UNIV. of MASSACHUSETTS, AMHERST, 11-15 Oct., 1976.

R E F E R E N C E S

1. MAIMAN, T.H.
Stimulated optical radiation in ruby.
NATURE, 187, p.493, 1960.
2. KAPANY, N.S.
Fibre optics principles and applications.
ACADEMIC PRESS, NEW YORK, 1967.
3. KAO, K.C., HOCKHAM, G.A.
Dielectric fibre surface waveguides for optical frequencies.
PROC. IEEE, 113, 7, p.1151, 1966.
4. KAPRON, F.P., KECK, D.B., MAURER, R.D.
Radiation losses in glass optical waveguides.
APP. PHYS. LETT., 17, 10, p.423, 1970.
5. OGILVIE, G.J., ESDAILE, R.S., KIDD, G.P.
Transmission loss of tetrachloroethylene-filled liquid-core-fibre light guides.
EL. LETT., 8, 22, p.533, 1972.
6. KECK, D.B., MAURER, R.D., SCHULTZ, P.C.
On the ultimate lower limit of attenuation in glass optical waveguides.
APP. PHYS. LETT., 22, 7, p.307, 1973.
7. PAYNE, D.N., GAMBLING, W.A.
New silica-based low-loss optical fibre.
EL. LETT., 10, 15, p.289, 1974.
8. SANDBANK, C.P.
Fibre transmission system research in the United Kingdom.
PAPER TUBI-I, CONF. ON OPT. FIBRE TX., WILLIAMSBURG, VIRGINIA.
7-9 Jan., 1975.
9. D'AURIA, L.,
Communications optiques guidees.
BULLETIN BNM, July 1975, p.20.
10. MILLER, S.E.
Integrated optics: an introduction.
BSTJ, 48, 7, p.2059, 1969.
11. TAYLOR, H.F., YARIV, A.
Guided wave optics.
PROC. IEEE, 62, p.1044, 1974.
12. SHUBERT, R., HARRIS, J.H.
Optical surface waves on thin films and their application to integrated data processors.
IEEE TRANS. MTT - 16, p.1048, 1968.
13. SHUBERT, R., HARRIS, J.H.
Optical guided-wave focussing and diffraction.
J. OPT. SOC. AM., 61, p.154, 1971.

14. ULRICH, R., MARTIN, R.J.
Geometrical optics in thin film light guides.
APP. OPT., 10, p.2077, 1971.
15. HONDROS, D., DEBYE, P.,
Elektromagnetische wellen an dielektrischen drahten.
ANN.PHYS., 32, p.456, 1960.
16. HATKIN, L.
Analysis of propagating modes in dielectric sheets.
PROC. IRE., 42, p.1565, 1954.
17. LOTSCH, H.K.V.
Physical optics theory of planar dielectric waveguides.
OPTIK, 27, 4, p.239, 1968.
18. TIEN, P.K.
Light waves in thin films and integrated optics.
APP. OPT., 10, p.2395, 1971.
19. GOELL, J.E.
A circular harmonic computer analysis of rectangular dielectric waveguides.
BSTJ, 48, p.2133, 1969.
20. MARCATILI, E.A.J.
Dielectric rectangular waveguide and directional coupler integrated optics.
BSTJ, 48, p.2071, 1969.
21. GOELL, J.E.
Electron resist fabrication of bends and couplers for integrated optical circuits.
APP. OPT., 12, 4, p.729, 1973.
22. IHAYA, A., FURUTA, H., NODA, H.
Thin film optical directional coupler.
IEEE J. QUANT. EL., 8, p.546, 1972.
23. PAPUCHON, M., et al.
Electrically switched optical directional coupler: COBRA.
APP.PHYS.LETT., 27, 5, p.289, 1975.
24. HAMMER, J.M., CHANNIN, D.J., DUFFY, M.T.
Fast electro-optic waveguide deflector modulator.
APP.PHYS.LETT., 23, p.176, 1973.
25. NAKAMURA, M., et al.
Laser oscillation in epitaxial Ga.As.waveguides with corrugation feedback.
APP.PHYS.LETT., 23, p.224, 1973.
26. TSANG, W.T., WANG, S.
Ga.As. - $\text{Ga}_{1-x}\text{Al}_x\text{As}$ double heterostructure injection lasers with distributed Bragg reflectors.
PAPER B3, OPT. COMM., 18, 1, p.38, 1976.

27. OSTROWSKY, D.B., POIRER, R., REIBER, L.M., DEVERDUN, C.
Integrated optical photodetector.
APP.PHYS. LETT., 22, p.463, 1973.
28. TIEN, P.K., ULRICH, R., MARTIN, R.J.
Modes of propagating light waves in thin deposited semiconductor films.
APP.PHYS. LETT., 14, p.291, 1969.
29. MIDWINTER, J.E.
Evanescent field coupling into a thin film waveguide.
IEEE J. QUANT. EL., 6, p.583, 1970.
30. TIEN, P.K., MARTIN, R.J.
Experiments on light waves in a thin tapered film and a new light-wave coupler.
APP.PHYS. LETT., 18, p.398, 1974.
31. DALGOUTTE, D.G.
A high efficiency thin grating coupler for integrated optics.
OPT. COMM., 8, 2, p.124, 1973.
32. ASH, E.A., et al.
Holographic coupler for integrated optics.
APP. PHYS. LETT., 24, 4, p.207, 1974.
33. ARNAUD, J.
Transverse coupling in fibre optics, Part I: coupling between trapped modes.
BSTJ, 53, 2, p.217, 1974.
34. BOIVIN, L.P.
Thin film laser-to-fibre coupler.
APP. OPT., 13, 2, p.391, 1974.
35. SUGIMOTO, S., et al.
Light coupling from a DH Laser into a SELFOC fibre using slab SELFOC lenses.
Paper WD1-1, TOP.MEETING OPT.FIBRE TRANS., WILLIAMSBURG, VIRGINIA, 7-9 Jan., 1975.
36. AURACHER, F.
A photoresist coupler for optical waveguides.
OPT.COMM., 11, 2, p.191, 1974.
37. TIEN, P.K., SMOLINSKY, G., MARTIN, R.J.
Radiation fields of a tapered film and a noval film to fibre coupler.
IEEE TRANS., MTT-23, 1, p.79, 1975.
38. TIEN, P.K., MARTIN, R.J., SMOLINSKY, G.
Formation of light-guiding interconnections in an integrated optical circuit by composite tapered film coupling.
APP. OPT., 12, 8, p.1909, 1973.

39. HARVEY, A.F.
Microwave engineering.
ACADEMIC PRESS, LONDON, 1963.
40. BULMER, C., WILSON, M.G.F.
Distributed coupling between a singlemode fibre and a planar waveguide.
PAPER WB3-1, CONF. INT. OPT., SALT LAKE CITY, 12-14 Jan., 1976.
41. HAMMER, J., et al.
Optical grating coupling between low-index fibres and high-index film waveguides.
APP.PHYS.LETT., 28, 4, p.192, 1976.
42. DALGOUTTE, D.G., SMITH, R.B., ACHUTARAMAYYA, G., HARRIS, J.H.
Externally mounted fibres for integrated optics interconnections.
APP.OPT., 14, 3, p.1860, 1975.
43. LAYBOURN, P.J.R., MILLAR, C.A.
Sandwich-ribbon optical waveguides.
EL. LETT., 10, 10, p.175, 1974.
44. LOUISELL, W.H.
Analysis of the single tapered mode coupler.
BSTJ, 34, p.853, 1955.
45. WILSON, M.F.G., TEH, G.A.
Improved tolerance in optical directional couplers.
EL. LETT., 9, 19, p.453, 1973.
46. LAYBOURN, P.J.R.
Paper presented at IEE meeting on thin film optical waveguides.
LONDON, 1973.
47. LAYBOURN, P.J.R.
Observation of modes in a glass ribbon waveguide.
OPTO ELECT., 5, p.539, 1973.
48. SOMEKH, et al.
Channel optical waveguides and directional couplers in Ga As imbedded and ridged.
APP.OPT., 13, 2, p.327, 1974.
49. KAPANY, N.S., BURKE, J.J., FRAME, K.L., WILCOX, R.E.
Coherent interactions between optical waveguides and lasers.
J. OPT. SOC. AM., 58, 9, p.1176, 1968.
50. KRASNUSHKIN, P.E., KHOKHLOV, R.V.
Spatial beating in coupled waveguides.
ZU.TEKH.FIZ., 19, p.931, 1949. (in Russian).
51. HAIDLE, L.L.
Power transfer between Goubau lines with unequal phase velocities.
EL. LETT., 6, 19, p.599, 1970.

52. CLARRICOATS, P.J.B., ed.
Optical fibre waveguides.
IEE REPRINT SERIES 1, PEREGRINUS LTD., STEVENAGE, 1975.
53. MILLER, S.E.
Coupled wave theory and waveguide applications.
BSTJ, 33, 3, p.661, 1954.
54. LAYBOURN, P.J.R., WILKINSON, C.D.W.
Optical waveguide coupling arrangements.
UNITED KINGDOM PATENT 49775/74, 1974.
55. GIALLORENZI, T.D., et al.
Optical waveguides formed by thermal migration of ions in glass.
APP.OPT., 12, 6, p.1240, 1973.
56. STEWART, G., MILLAR, C.A., LAYBOURN, P.J.R., WILKINSON, D.C.W.,
DE LA RUE, R.M.
Planar optical waveguides fabricated by silver ion migration in glass.
PAPER PD2, CONF. INT. OPT., SALT LAKE CITY, 12-14 Jan., 1976.
57. LAYBOURN, P.J.R., MILLAR, C.A., STEWART, G., WILKINSON, C.D.W.
Optical coupling between thin films and circular fibres.
EL. LETT., 11, 1, p2, 1975.
58. SUZUKI, Y., KASHIWAGI, H.
Polymer-clad fused silica optical fibre.
APP. OPT, 13, 1, p.1, 1974.
59. OTTO, H.H.
Compaction effects in glass fibres.
J. AM. CERAM. SOC., 44, 68, p.68, 1961.
60. DAKIN, J.P., GAMBLING, W.A., PAYNE, D.N., SUNAK, H.R.D.
Launching into glass fibre optical waveguides.
OPT. COMM., 4, 5, p.354, 1972.
61. CRANK, J.
The mathematics of diffusion.
OXFORD UNIVERSITY PRESS, LONDON, 1956.
62. DOREMUS, R.H.
Exchange and diffusion of ions in glass.
J. PHYS. CHEM., 68, p.2212, 1964.
63. BURGRAAF, A.J.
The mechanical strength of alkali-alumino silicate glasses after ion-exchange.
PHILIPS RESEARCH REPORT, No.3., 1966.
64. UCHIDA, T., et al.
Optical characteristics of a light-focusing fibre guide and its applications.
IEEE J.QUANT. EL., 6, p.606, 1970.

65. GLOGE, D.,
Weakly guiding fibres.
APP. OPT., 10, p.2252, 1970.
66. GINZTON, E.L., GOODWIN, P.S.
A note on coaxial Bethe-hole directional couplers.
PROC. IRE, 38, p.305, 1950.
67. LAYBOURN, P.J.R., WILKINSON, C.D.W., MILLAR, C.A.
Optical waveguide coupling arrangements.
UNITED KINGDOM PATENT 46974/74, 1974.
68. JACKSON, G.N.
RF sputtering.
THIN SOLID FILMS, 5, p.209, 1970.
69. MARCUSE, D.
Cut-off condition of optical fibres.
J. OPT. SOC. AM., 63, 11, p.1369, 1973.
70. McLACHLAN, N.W.
Bessel functions for engineers.
SECOND EDITION, OXFORD CLARENDON PRESS, NEW YORK, 1955.
71. STEWART, W.J.
A new technique for determining the V-values and refractive index profiles of optical fibres.
PAPER TUD8-1, CONF. OPT. FIBRE TRANSM. , WILLIAMSBURG, VIRGINIA, 7-9 Jan., 1975.
72. KAPANY, N.S., BURKE, J.J.
Optical waveguides.
ACADEMIC PRESS, LONDON, 1972.
73. MARCUSE, D., ed.
Integrated optics.
IEEE PRESS, NEW YORK, 1973.
74. COLLIN, R.E.
Field theory of guided waves.
McGRAW HILL, LONDON, 1960.
75. As reference 2, Chapter 14, Part 3.
76. JACOBSSON, R.
Progress in Optics, V.
E. WOLF, Ed., NORTH HOLLAND, AMSTERDAM, 1966, p.249.
77. GEDEON, A.
Comparison between rigorous theory and WKB analysis of modes in graded index waveguides.
OPT. COMM., 12, 3, p.329, 1974.
78. LOTSCH, H.K.V.
Reflection and refraction of a beam of light at a plane interface.
J. OPT. SOC. AM., 58, 4, p.551, 1968.

79. SNYDER, A.W.
Asymptotic expressions for eigenfunctions and eigenvalues of a dielectric or optical waveguide.
IEEE TRANS., MTT-17, 12, p.1130, 1969.
80. THOMPSON, E.C.
A digital simulation of a boiler and turbine in conjunction with a model power system.
Ph.D. THESIS, UNIVERSITY OF GLASGOW, 1976.
81. ROSKO, J.S.
Digital simulation of physical systems.
ADDISON WESLEY, LONDON, 1972.
82. AURACHER, F., WITTE, H.H.
New directional coupler for integrated optics.
J. APP. PHYS., 45, 11, p.4997, 1974.
83. ALBERSHEIM, W.J.
Propagation of TE_{01} waves in curved waveguides.
BSTJ, 27, p.1, 1949.
84. MARCUSE, D.
The coupling of degenerate modes in two parallel dielectric waveguides.
BSTJ, 50, 6, p.1791, 1971.
85. HSU, H.P.
Block coupler/directional coupler for hybrid integrated optical circuit.
D.Sc. DISSERTATION, WASHINGTON UNIV., 1974.
86. WILSON, L.O., REINHART, F.K.
Coupling of nearly degenerate modes in parallel asymmetric dielectric waveguides.
BSTJ, 53, 4, p.717, 1974.
87. GAMBLING, W.A., PAYNE, D.N., MATSUMURA, H., MEDLICOTT, M.
Optical fibres and the Goos-Hanchen shift.
EL. LETT., 10, 7, p.99, 1974.
88. KOGELNIK, H., WEBER, H.P.
Rays, stored energy and power flow in dielectric waveguides.
J. OPT. SOC. AM., 64, 2, p.174, 1974.
89. GEDEON, A.
Effective thickness of optical waveguides in tunable directional couplers.
J. OPT. SOC. AM., 64, 5, p.615, 1974.
90. ARNAUD, J.
Transverse coupling in fibre optics: Part II, coupling to mode sinks.
BSTJ, 53, 4, p.675, 1974.

91. ARNAUD, J.
Transverse coupling in fibre optics: Part III, bending losses.
BSTJ, 53, 7, p.1379, 1974.
92. DUNSMUIR, R., WILKINSON, C.D.W., DE LA RUE, R.M.
Thin film dielectric waveguides and prism film couplers.
TO BE PUBLISHED, IEEE J. QUANT. EL.
93. HANSEN, W.H.
Electric fields produced by the propagation of plane coherent
electromagnetic radiation in a stratified medium.
J.OPT. SOC. AM., 58, 3, p.380, 1965.
94. MONTGOMERY, C.G. et al.
Principles of microwave circuits.
McGRAW HILL, NEW YORK, 1948.
95. SNITZER, E., OSTERBERG, H.
Observed dielectric waveguide modes in the visible spectrum.
J. OPT. SOC. AM., 51, 5, p.499, 1961.
96. LAYBOURN, P.J.R., MILLAR, C.A., STEWART, G., WILKINSON, C.D.W.
Coupling to optical fibres from prisms and thin films.
PAPER PD2, TOP. MEETING OPT. FIBRE TRANSM., WILLIAMSBURG,
VIRGINIA, 7 - 9 Jan. 1975.
97. MIDWINTER, J.E.
The prism-taper coupler for the excitation of single modes in
optical transmission fibres.
OPT. QUANT. EL., 7, p.297, 1975.
98. BIERNSON, G., KINGLSEY, D.J.
Generalized plots of mode patterns in a cylindrical dielectric
waveguide applied to retinal cones.
IEEE TRANS., MTT-13, p.345, 1965.
99. LIPSON, S.G., LIPSON, H.
Optical physics.
CAMBRIDGE UNIV.PRESS, 1969.
100. CLARRICOATS, P.J.B.
Propagation behaviour of cylindrical-dielectric-rod waveguides
PROC. IEEE, 120, 11, p.1371, 1973.
101. JONES, A.L.
Coupling of optical fibres and scattering in fibres.
J. OPT. SOC. AM., 55, 3, p.261, 1965.
102. McMURRAY, J.A.
Electrooptic modulation of infrared radiation in planar cadmium
sulphide waveguides.
Ph.D. THESIS, UNIVERSITY OF GLASGOW, 1976.

103. HUTCHINS, R.H., Private communication.
104. CORNING GLASS INTERNATIONAL S.A.
Product Information "7059 ground and polished photomask substrates",
15th February, 1972.
105. JELLEY, J.V.
Cerenkov radiation and its applications.
PERGAMON PRESS, LONDON, 1958.
106. GALLACHER, J.G., DE LA RUE, R.M.
Single mode stripe optical waveguides formed by silver ion
exchange.
EL.LETT., 12, 16, p.397, 1976.
107. As reference 18, equation 23.
108. McMURRAY, J.A., STANLEY, C.R.
Taper coupling between 7059-glass and Cd.S films and phase
modulation in the composite waveguide structure.
APP.PHYS. LETT., 28, 3, p.126, 1976.
109. SMITH, R.B.
Coupling efficiency of the tapered coupler.
EL. LETT, 11, 10, p.204, 1975.
110. PAPAS, C.H.
Theory of electromagnetic wave propagation.
McGRAW HILL, NEW YORK, 1965, CHAPTER 3.
111. RAMO, S., WHINNERY, J.R., VAN DUZER, T.
Fields and waves in communication electronics.
JOHN WILEY INC., NEW YORK, 1967, CHAPTER 12.
112. ABRAMOWITZ, M., STEGUN, I.A.
Handbook of mathematical functions.
DOVER, NEW YORK, 1965.
113. BORN, M., WOLF, E.
Principles of optics.
4th EDT., PERGAMON PRESS, NEW YORK, 1970.
114. STEWART, G., et al.
Planar optical waveguides formed by silver-ion migration in
glass.
ACCEPTED FOR PUBLICATION, IEEE J.QUANT. EL., SPRING 1977.
115. MILLAR, C.A., LAYBOURN, P.J.R.
Coupling of integrated optical circuits using sandwich ribbon
fibres.
OPT. COMM., 18, 1, p.80, 1976.
116. SNYDER, A.W.
Excitation and scattering of modes on a dielectric or optical fibre.
IEEE TRANS., MTT-17, 12, p.1138, 1969.
117. MILLAR, C.A., HUTCHINS, R.H., LAYBOURN, P.J.R.
Modes of a 3-dimensional sandwich ribbon optical waveguide.
MICR.,OPT. AND ACOUS., 1, p.27, 1976.